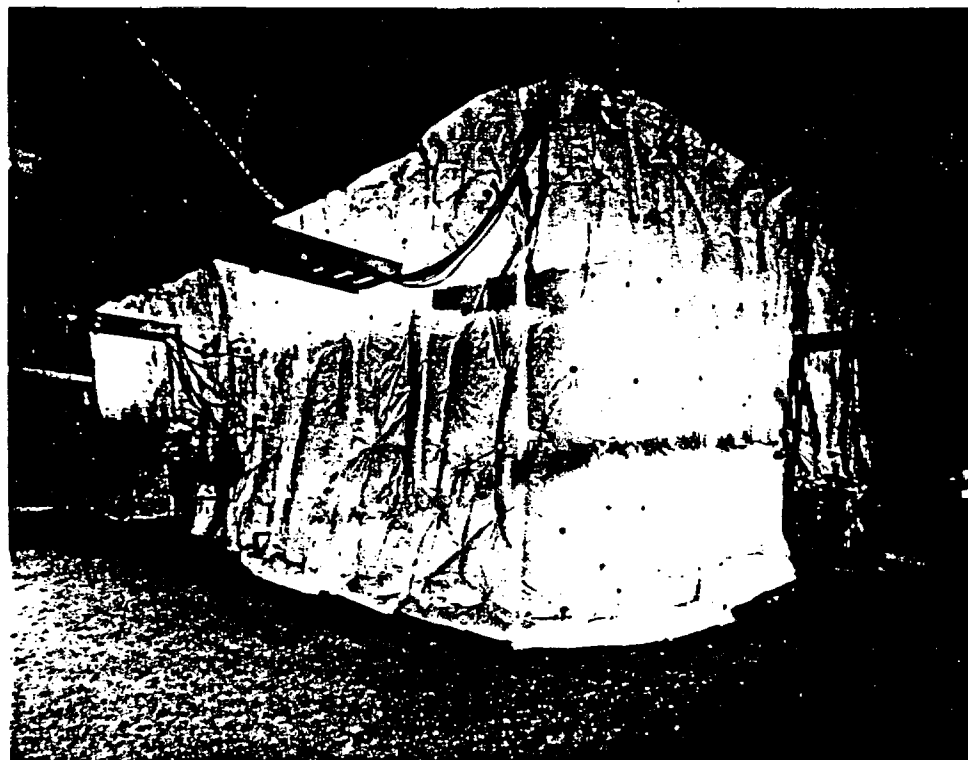


**EVALUATION AND COMPARATIVE ANALYSIS  
OF SINGLE HEATER TEST  
THERMAL AND THERMOMECHANICAL DATA:  
THIRD QUARTER RESULTS  
(8/26/96 through 5/31/97)**

Sandia National Laboratories  
Albuquerque, NM 87185

18 July 1997



# EVALUATION AND COMPARATIVE ANALYSIS OF SINGLE HEATER TEST THERMAL AND THERMOMECHANICAL DATA: THIRD QUARTER RESULTS (8/26/96 through 5/31/97)

## ABSTRACT

The Yucca Mountain Project is conducting a Single Heater Test (SHT) in the Exploratory Studies Facility at Yucca Mountain. This report describes the thermal and thermomechanical data collected for the SHT through the third quarter of heating (through 31 May 1997) and compares the data with numerical predictions in order to gain insight into the coupled Thermal-Mechanical-Hydrologic-Chemical processes. The SHT was energized on 26 August 1996 with the nominal heater power set at 4 kW. The heater was deactivated on 28 May 1997 at 20:31 Universal Coordinated Time, after being on for 275 days, 2 hours. Thermomechanical instrumentation was installed within and on the rock mass encompassed by the SHT. This thermomechanical instrumentation includes temperature measurements using thermocouples, resistance temperature devices, and thermistors. Mechanical measurements include multiple-point-borehole extensometers (MPBXs), tape extensometers, surface-mounted wire extensometers, load cells on rock bolts, and the NX borehole jack. Data for both thermal and mechanical measurements are presented and discussed. Major findings and recommendations include:

- The temperature distribution around the heater is radially symmetric; conduction appears to be the primary mode of heat transfer.
- Temperature gages in open boreholes exhibit erratic temperature behavior as their temperatures pass through the boiling point of water. Because gages grouted into sealed boreholes do not exhibit this type of behavior, it is attributed to intra-borehole vapor phase heat transfer effects.
- Fifteen of 319 temperature gages (almost 5%) have failed so far.
- Four mechanical gages in MPBX-1 have failed for unknown reasons. Two mechanical gages in MPBX-3 have failed.
- Several temperature gages on probe TMA-RTD-15 exhibit anomalous behavior that cannot be dismissed as attributable to failed gages. The data from these gages may indicate convective heat transport in fractures.
- Thermal data indicate the formation of a dry-out zone extending radially outward from the heater to approximately the 100°C isotherm located roughly 1 m from the heater.
- Numerical simulations of thermal behavior do not accurately predict observed thermal data. This is likely due to limitations imposed by the Equivalent Continuum Model, which is the conceptual model on which the numerical simulations are based.
- The expansion of the rock mass is not explained by elastic continuum models; therefore, it is strongly recommended that thermomechanical discrete block modeling be performed.
- The calculated rock mass thermal expansion from selected MPBX data is between about 4 and  $6 \times 10^{-6}/^{\circ}\text{C}$ .
- The rock mass modulus measured in the SHT using a borehole jack is significantly lower than the intact modulus. Measured rock mass moduli between about 3 and 23 GPa have been measured.
- Data from a single rock mass modulus test using a borehole jack show thermally induced stiffening of the rock mass in the region near the heater. Rock mass moduli in this region have increased from about 8 GPa on 26 November 1996 to about 23 GPa on 18 March 1997. This modulus increase is likely due to closing of fractures by rock matrix thermal expansion.

The data presented in this report should be considered indeterminate until the procurement/calibration issues related to Yucca Mountain Project deviation report YM-97-D-025 have been resolved.

Page intentionally blank .

## CONTENTS

1. Introduction .....	1
1.1 Background.....	1
1.2 Test Description .....	1
2. Layout.....	9
3. Thermal Measurements .....	13
3.1 Heater Power .....	13
3.2 Temperature.....	15
4. Displacement Measurements.....	71
4.1 Extensometers .....	71
4.2 Borehole Jack .....	86
4.3 Rock Bolt Load Cells .....	88
4.4 Miscellaneous Instrumentation.....	94
5. Performance of Measuring Systems .....	95
6. Discussion .....	97
6.1 Thermal Data Discussion .....	97
6.2 Displacement Data Discussion.....	107
7. Summary and Recommendations .....	119
8. References .....	121
Appendix A: Available DAS-Acquired Data for the SHT (through 28 February 1997).....	A-1
Appendix B: Thermomechanical Gage Specifications for the SHT.....	B-1
Appendix C: As-built Gage Locations .....	C-1
Appendix D: Goodman Jack Data for Measurements Taken on 26 August 1996, 10 October 1996, 26 November 1996, and 18 March 1997 .....	D-1

## FIGURES

Figure 1-1. General location of the ESF Thermal Test. ....	3
Figure 1-2. Plan view of ESF Thermal Test Facility.....	4
Figure 1-3. Conceptual layout for the SHT, views in plan and cross-section. ....	5
Figure 2-1. Layout of Single Heater Test, plan. ...	10
Figure 2-2. Layout of Single Heater Test, cross-section. ....	11
Figure 3-1a. Heater power summary through 31 May 1997.....	14
Figure 3-1b. Average weekly power output of heater through 31 May 1997.....	14
Figure 3-2. Map and cross section views of the SHT block showing the locations of interior temperature gages. ....	17
Figure 3-3. Data from gage TMA-H-1-TCB-4.....	19
Figure 3-4. Data from gage TMA-TC-2A-4.....	19
Figure 3-5. Data from gage TMA-TC-4A-1.....	20
Figure 3-6. Data from gage TMA-BX-1-TC-9.....	20
Figure 3-7. Data from gage TMA-BX-3-TC-1.....	21
Figure 3-8. Data from gage TMA-BX-3-TC-2.....	21
Figure 3-9. Data from gage TMA-BX-3-TC-7.....	22

## (continued) FIGURES (continued)

Figure 3-10. Data from gage TMA-BX-3-TC-9.....	22
Figure 3-11. Data from gage TMA-BX-4-TC-10.....	23
Figure 3-12. Data from gage TMA-RTD-15-20.....	23
Figure 3-13. Data from gage TMA-RTD-15-23.....	24
Figure 3-14. Data from gage TMA-RTD-17-26.....	24
Figure 3-15. Data from gage TMA-RTD-23-19.....	25
Figure 3-16. Data from gage TMA-RTD-23-11.....	25
Figure 3-17. Temperature profiles for thermocouple probe TMA-TCT ( $x=-0.005$ m, $z=0.04$ m) every 10 days since heater activation. ....	26
Figure 3-18. Temperature versus time for the temperature gages in probe TMA-TCT. ....	26
Figure 3-19. Temperature profiles for thermocouple probe TMA-TCS ( $x=-0.038$ m, $z=-0.006$ m) every 10 days since heater activation. ....	27
Figure 3-20. Temperature versus time for the temperature gages in probe TMA-TCS. ....	27
Figure 3-21. Temperature profiles for thermocouple probe TMA-TCB ( $x=-0.005$ m, $z=-0.027$ m) every 10 days since heater activation. ....	28
Figure 3-22. Temperature versus time for the temperature gages in probe TMA-TCB. ....	28
Figure 3-23. Temperature profiles for thermocouple probe TMA-TC-1 ( $x=-0.237$ m, $z=0.342$ m) every 10 days since heater activation. ....	29
Figure 3-24. Temperature versus time for the temperature gages in probe TMA-TC-1. ....	29
Figure 3-25. Temperature profiles for thermocouple probe TMA-BX-1 ( $x=0.148$ m, $z=0.306$ m) every 10 days since heater activation. ....	30
Figure 3-26. Temperature versus time for the temperature gages in probe TMA-BX-1. ....	30
Figure 3-27. Temperature profiles for thermocouple probe TMA-TC-2 ( $x=0.613$ m, $z=0.263$ m) every 10 days since heater activation. ....	31
Figure 3-28. Temperature versus time for the temperature gages in probe TMA-TC-2. ....	31
Figure 3-29. Temperature profiles for thermocouple probe TMA-BX-2 ( $x=-0.628$ m, $z=0.263$ m) every 10 days since heater activation. ....	32
Figure 3-30. Temperature versus time for the temperature gages in probe TMA-BX-2. ....	32
Figure 3-31. Temperature profiles for thermocouple probe TMA-TC-4 ( $x=-0.083$ m, $z=-0.724$ m) every 10 days since heater activation. ....	33
Figure 3-32. Temperature versus time for the temperature gages in probe TMA-TC-4. ....	33
Figure 3-33. Temperature profiles for thermocouple probe TMA-TC-5 ( $x=-0.038$ m, $z=0.699$ m) every 10 days since heater activation. ....	34
Figure 3-34. Temperature versus time for the temperature gages in probe TMA-TC-5. ....	34
Figure 3-35. Temperature profiles for thermocouple probe TMA-TC-3 ( $x=-0.734$ m, $z=1.318$ m) every 10 days since heater activation. ....	35
Figure 3-36. Temperature versus time for the temperature gages in probe TMA-TC-3. ....	35
Figure 3-37. Temperature profiles for thermocouple probe TMA-BX-3 ( $x=0.759$ m, $z=1.295$ m) every 10 days since heater activation. ....	36
Figure 3-38. Temperature versus time for the temperature gages in probe TMA-BX-3. ....	36
Figure 3-39. Temperature profiles for thermocouple probe TMA-TC-6 ( $y=5.434$ m, $z=-0.001$ m) every 10 days since heater activation. ....	37
Figure 3-40. Temperature versus time for the temperature gages in probe TMA-TC-6. ....	37

## FIGURES (continued)

Figure 3-41. Temperature profiles for thermocouple probe TMA-BX-4 ( $y=3.461$ m, $z=-0.139$ m) every 10 days since heater activation. ....	38
Figure 3-42. Temperature versus time for the temperature gages in probe TMA-BX-4. ....	38
Figure 3-43. Temperature profiles for thermocouple probe TMA-TC-7 ( $y=3.408$ m, $z=0.011$ m) every 10 days since heater activation. ....	39
Figure 3-44. Temperature versus time for the temperature gages in probe TMA-TC-7. ....	39
Figure 3-45. Temperature profiles for thermocouple probe TMA-RTD-15 ( $y=4.25$ m) every 10 days since heater activation. ....	40
Figure 3-46. Temperature versus time for the temperature gages in probe TMA-RTD-15. ....	40
Figure 3-47. Temperature profiles for thermocouple probe TMA-RTD-17 ( $y=4.27$ m) every 10 days since heater activation. ....	41
Figure 3-48. Temperature versus time for the temperature gages in probe TMA-RTD-17. ....	41
Figure 3-49. Temperature profiles for thermocouple probe TMA-RTD-22 ( $y=4.38$ m, $z=-0.66$ m) every 10 days since heater activation. ....	42
Figure 3-50. Temperature versus time for the temperature gages in probe TMA-RTD-22. ....	42
Figure 3-51. Temperature profiles for thermocouple probe TMA-RTD-23 ( $y=4.39$ m) every 10 days since heater activation. ....	43
Figure 3-52. Temperature versus time for the temperature gages in probe TMA-RTD-23. ....	43
Figure 3-53. Temperature profiles for thermocouple probe TMA-TEMP-16 ( $y=4.275$ m) every 10 days since heater activation. ....	44
Figure 3-54. Temperature versus time for the temperature gages in probe TMA-TEMP-16. ....	44
Figure 3-55. Temperature profiles for thermocouple probe TMA-TEMP-18 ( $y=4.25$ m, $z=-0.22$ m) every 10 days since heater activation. ....	45
Figure 3-56. Temperature versus time for the temperature gages in probe TMA-TEMP-18. ....	45
Figure 3-57. Temperature plotted as a function of distance from the center point of the heater. ....	48
Figure 3-58. Temperature plotted as a function of distance from the center point of the heater. ....	49
Figure 3-59. Comparison of data from TMA-RTD-15-1 and TMA-RTD-15-2. ....	51
Figure 3-60. Comparison of data from TMA-RTD-15-9 and TMA-RTD-15-10. ....	52
Figure 3-61. Location of temperature gages on the three rock faces and in the insulation material. ....	54
Figure 3-62. Temperature versus time for the thermocouples mounted on the Thermomechanical Alcove face of the SHT block. ....	55
Figure 3-63. Temperature versus time for the thermocouples mounted on the Observation Drift face of the SHT block. ....	56
Figure 3-64. Temperature versus time for the thermocouples mounted on the Thermomechanical Alcove Extension face of the SHT block. ....	57
Figure 3-65. Temperature versus time for the thermistors installed in the insulation covering the Thermomechanical Alcove face of the SHT block. ....	58
Figure 3-66. Temperature versus time for the thermistors installed in the insulation covering the Observation Drift face of the SHT block. ....	59
Figure 3-67. Temperature versus time for the thermistors installed in the insulation covering the Thermomechanical Alcove Extension face of the SHT block. ....	60

## FIGURES (continued)

Figure 3-68. Temperature as a function of radial distance from the heater borehole collar for the surface and insulation temperature gages on the front face of the SHT block. ....	61
Figure 3-69. Temperature drop across the insulation for surface-insulation temperature gage pairs at four locations on the front face of the SHT, as a function of radial distance from the heater borehole collar. ....	61
Figure 3-70. Vertical slice perpendicular to the heater axis at Y=4.5 m showing temperature contours (interval = 25°C) after 275 days of heating. ....	62
Figure 3-71. Vertical slice perpendicular to the heater axis at Y=3.5 m showing temperature contours (interval = 25°C) after 275 days of heating. ....	63
Figure 3-72. Vertical slice perpendicular to the heater axis at Y=5.5 m showing temperature contours (interval = 25°C) after 275 days of heating. ....	64
Figure 3-73. Vertical slice parallel to the heater axis at X=0 m showing temperature contours (interval = 25°C) after 275 days of heating. ....	65
Figure 3-74. Horizontal slice parallel to the heater axis at Z=0 m showing temperature contours (interval = 25°C) after 275 days of heating. ....	66
Figure 3-75. Horizontal slice parallel to the heater axis at Z=0.3 m showing temperature contours (interval = 25°C) after 275 days of heating. ....	67
Figure 3-76. Horizontal slice parallel to the heater axis at Z=0.7 m showing temperature contours (interval = 25°C) after 2754 days of heating. ....	68
Figure 3-77. Temperature as a function of radial distance from the heater after 275 days of heating. ....	69
Figure 3-78. Increase in temperature during the time interval from 186 to 275 days. ....	69
Figure 4-1. Plan view showing locations of boreholes, MPBX anchors, wire extensometers, rock bolt load cells, borehole jack, and tape extensometers in the SHT block. ....	73
Figure 4-2. Cross-section showing locations of boreholes, MPBX anchors, wire extensometers, rock bolt load cells, borehole jack, and tape extensometers in the SHT block. ....	73
Figure 4-3. Displacement history for ESF-TMA-MPBX-1 (corrected for rod thermal expansion; extension positive).....	74
Figure 4-4. Displacement history for ESF-TMA-MPBX-2 (corrected for rod thermal expansion; extension positive).....	74
Figure 4-5. Displacement history for ESF-TMA-MPBX-3 (corrected for rod thermal expansion; extension positive).....	75
Figure 4-6. Displacement history for ESF-TMA-MPBX-4 (corrected for rod thermal expansion; extension positive).....	75
Figure 4-7. Displacement history for wire extensometer ESF-TMA-WX-1 (extension positive). ....	81
Figure 4-8. Displacement history for wire extensometer ESF-TMA-WX-2 (extension positive). ....	81
Figure 4-9. Displacement history for wire extensometer ESF-TMA-WX-3 (extension positive). ....	82
Figure 4-10. Displacement history for wire extensometer ESF-TMA-WX-4 (extension positive). ....	82
Figure 4-11. Displacement history for wire extensometer ESF-TMA-WX-5 (extension positive). ....	83

## FIGURES (continued)

Figure 4-12. Displacement history for wire extensometer ESF-TMA-WX-6 (extension positive) .....	83
Figure 4-13. Rock bolt load history for TMA-RB-LC-1 (average).....	90
Figure 4-14. Rock bolt load history for TMA-RB-LC-2 (average).....	90
Figure 4-15. Rock bolt load history for TMA-RB-LC-3 (average).....	91
Figure 4-16. Rock bolt load history for TMA-RB-LC-4 (average).....	91
Figure 4-17. Rock bolt load history for TMA-RB-LC-5 (average).....	92
Figure 4-18. Rock bolt load history for TMA-RB-LC-6 (average).....	92
Figure 6-1. Temperature-time history at the heater mid-plane for gage TMA-TC-1A-7.....	98
Figure 6-2. Temperature-time history at the heater mid-plane for gage TMA-TC-5A-7.....	99
Figure 6-3. Temperature-time history at the heater mid-plane for gage TMA-TC-4A-6.....	99
Figure 6-4. Radial temperature distribution in the vertical plane that intersects the heater at its midpoint, after 275 days of heating.....	100
Figure 6-5. Comparison of measured data and numerical models, after 266 days of heating.....	102
Figure 6-6a. Amount by which the temperature increased between day 186 and day 266 as a function of the temperature measured on day 186; data only.....	103
Figure 6-6b. Amount by which the temperature increased between day 186 and day 266 as a function of the temperature measured on day 186; data and model predictions. ....	103
Figure 6-7. Initial pre-heating condition and layout for descriptive thermomechanical conceptual model.....	113
Figure 6-8. Descriptive conceptual model of MPBX behavior shortly after heater startup.....	113
Figure 6-9. Descriptive conceptual model of MPBX behavior midway through heating.....	114
Figure 6-10. Descriptive conceptual model of MPBX behavior near the end of heating.....	115
Figure 6-11. Descriptive conceptual thermomechanical model applied to MPBX-3 behavior....	116

## TABLES

Table 1-1. List of Milestone Criteria Satisfied by this Document.....	2
Table 1-2. Data and Information Needs Addressed by the Single Heater Test .....	6
Table 3-1. Unreliable Temperature Gages from the SHT Block.....	18
Table 4-1. MPBX Displacement History (mm) (Corrected for Rod Thermal Expansion; Extension Positive).....	76
Table 4-2. Wire Extensometer Data (mm) (Extension Positive).....	80
Table 4-3. Tape Extensometer Measurements for the SHT (Extension Positive).....	86
Table 4-4. Estimated Rock Mass Modulus in Borehole ESF-TMA-BJ-1 Using the Borehole Jack .....	88
Table 4-5. Rock Bolt Load Cells, Load Versus Time .....	89
Table 4-6. Change in Rock Bolt Load Cell Readings (8/26/96 – 5/31/97) .....	94
Table 5-1. Failed, Unreliable, and Suspect Thermomechanical Gages Installed in the SHT.....	95
Table 6-1. Calculated Rock Mass Thermal Expansion Coefficient from SHT Data through Day 90.....	108
Table 6-2. Thermal Expansion Coefficients for Longest Available Gage Lengths Near Heating Cycle Culmination.....	109

**Page intentionally blank**

# 1. Introduction

## 1.1 Background

This document presents data and results of temperature and mechanical measurements conducted by Sandia National Laboratories (SNL) for the Single Heater Test (SHT) in the Exploratory Studies Facility (ESF) at Yucca Mountain, NV. Data through 31 May 1997 are presented. This report also presents temperature data from resistance temperature devices (RTDs) installed by Lawrence Livermore National Laboratory (LLNL) for the SHT. Other measurements, including hydrology and chemistry, were performed by other project participants and are not presented in this document. The data presented in this document were collected using (1) an automated data acquisition system (DAS) operated by the Los Alamos National Laboratory (LANL) Test Coordination Office and (2) manual recording methods. Manual data presented in this document include tape extensometer and NX borehole jack readings. The raw data recorded by the DAS through 31 May 1997 are described in Appendix A.

The work was performed by SNL under Yucca Mountain Project WBS number 1.2.3.14.2. SNL work agreements WA-0310 (SNL, 1995) and WA-0334 (SNL, 1996) detail the installation and conduct of SNL responsibilities and measurements, respectively, in the SHT. The completion of this document satisfies CRWMS M&O Level 4 Milestones. Table 1-1 outlines the criteria for these milestones and shows where they are met in this document.

## 1.2 Test Description

The SHT is part of the ESF Thermal Test being conducted underground at the potential high-level nuclear waste repository at Yucca Mountain, NV. This experiment will evaluate in situ the coupled thermal-mechanical-hydrologic-chemical (T-M-H-C) processes expected to occur during waste emplacement at Yucca Mountain. The ESF Thermal Test includes the SHT and a larger drift-scale thermal test. The SHT is a straightforward modification of the canister-scale heater test described in Section 8.3.1.15.1.6 of the Site Characterization Plan (DOE, 1988).

The canister-scale heater test was designed to simulate a single waste package for borehole emplacement with the primary objective of measuring rock mass response in the near field. Although borehole emplacement is not considered likely at this time, the geometry of the test is useful for directly measuring rock mass thermal and thermomechanical properties such as thermal conductivity, thermal expansion, and rock mass modulus.

The SHT is being conducted in the Topopah Spring Welded Tuff lithologic unit (middle-nonlithophysal) in a specially constructed facility located south of the North Ramp and east of the North-South main drift. The location of the Thermal Testing Facility is shown schematically in Figures 1-1 and 1-2. The SHT block is bounded on the north by the Observation Drift (declining at about 10%), on the west by the Thermomechanical Alcove, and on the south by the Thermomechanical Alcove Extension. The dimensions of the excavations are given in Figure 1-3. Refer to TRW (1996a) for specific details regarding the test and facility design.

Figure 1-3 shows the conceptual layout for the SHT in plan and cross-section views. The SHT consists of emplacing a long (5-m) heater at a slight upward incline in a borehole in the west face of the test block, as shown in Figure 1-3. The test configuration includes the heater in roughly the

center (plan view) of the test block, with instrumentation access from all three free surfaces bounded by the excavations.

**Table 1-1. List of Milestone Criteria Satisfied by this Document**

<b>Level 4 Milestone SP9261 M4 is a TDIF submitted by 7/18/97. This milestone will be satisfied on submission to the technical database under a TDIF the results of heater power and temperature measurements from the start of the SHT to 5/31/97, including ambient temperature measurements before the start of heating.</b>	
<b>Criteria for SP9261 M4</b>	<b>Location</b>
Heater power and all temperature sensor data will be tabulated	Section 3.1, 3.2; Appendix C
Measurements of 15 temperature sensors will be plotted	Section 3.2
Preliminary evaluation of the results	Section 3.1, 3.2, 6.1
Performance of measuring systems and anomalous readings	Section 3.1, 3.2, 5
<b>Level 4 Milestone SP9271 M4 is a TDIF submitted by 7/18/97. This milestone will be satisfied on submission to the technical database under a TDIF the results of thermal-mechanical measurements from the start of the SHT to 5/31/97, including ambient temperature measurements before the start of heating.</b>	
<b>Criteria for SP9271 M4</b>	<b>Location</b>
Displacements measured by MPBXs will be tabulated	Section 4.1; Table 4-1; Appendix C
Displacements measured by wire and tape extensometers will be tabulated	Section 4.1; Tables 4-2 & 4-3; Appendix C
Rock bolt load cell readings will be tabulated	Section 4.3; Tables 4-5 & 4-6; Appendix C
Goodman (NX borehole) jack measurements will be reported	Section 4.2; Table 4-4
Preliminary evaluation of the results	Sections 4.1, 4.2, 4.3, 6.2
Performance of measuring systems and anomalous readings	Sections 4.1, 4.2, 4.3, & 5.
<b>Level 4 Milestone SP9268 M4 is a deliverable submitted by 7/18/97. This milestone will be satisfied on submission to the M&amp;O a report documenting the results of integrated analyses of the heating phase and early cooling phase of the Single Heater Test through 5/31/97.</b>	
<b>Criteria for SP9268 M4</b>	<b>Location</b>
Document as-builts	Appendix C
Document test thermomechanical results through 5/31/97	Section 3; Section 4
Document results of an integrated analysis and interpretations of SHT results through the heating phase (5/27/97)	Section 3; Section 4; Section 6
Document derived rock mass thermal expansion coefficient from thermal and mechanical measurements	Section 6
Document rock mass deformation modulus measurements	Section 4; Section 6

The SHT is intended to provide data and information on the rock mass thermal and thermomechanical properties, preliminary information on coupled T-M-H-C responses, and preliminary information on ground support/rock interaction at elevated temperature (see Table 1-2). The SHT will also serve to evaluate equipment and instrumentation, evaluate predictive numerical models, and develop and evaluate procedures.

The SHT was constructed, instrumented, and initiated during the summer of 1996, with the heater being started on 26 August. This report documents the data collected through the third quarter of heating (31 May 1997). This report will present temperature data from all sensors as well as SNL

# 1. Introduction

## 1.1 Background

This document presents data and results of temperature and mechanical measurements conducted by Sandia National Laboratories (SNL) for the Single Heater Test (SHT) in the Exploratory Studies Facility (ESF) at Yucca Mountain, NV. Data through 31 May 1997 are presented. This report also presents temperature data from resistance temperature devices (RTDs) installed by Lawrence Livermore National Laboratory (LLNL) for the SHT. Other measurements, including hydrology and chemistry, were performed by other project participants and are not presented in this document. The data presented in this document were collected using (1) an automated data acquisition system (DAS) operated by the Los Alamos National Laboratory (LANL) Test Coordination Office and (2) manual recording methods. Manual data presented in this document include tape extensometer and NX borehole jack readings. The raw data recorded by the DAS through 31 May 1997 are described in Appendix A.

The work was performed by SNL under Yucca Mountain Project WBS number 1.2.3.14.2. SNL work agreements WA-0310 (SNL, 1995) and WA-0334 (SNL, 1996) detail the installation and conduct of SNL responsibilities and measurements, respectively, in the SHT. The completion of this document satisfies CRWMS M&O Level 4 Milestones. Table 1-1 outlines the criteria for these milestones and shows where they are met in this document.

## 1.2 Test Description

The SHT is part of the ESF Thermal Test being conducted underground at the potential high-level nuclear waste repository at Yucca Mountain, NV. This experiment will evaluate in situ the coupled thermal-mechanical-hydrologic-chemical (T-M-H-C) processes expected to occur during waste emplacement at Yucca Mountain. The ESF Thermal Test includes the SHT and a larger drift-scale thermal test. The SHT is a straightforward modification of the canister-scale heater test described in Section 8.3.1.15.1.6 of the Site Characterization Plan (DOE, 1988).

The canister-scale heater test was designed to simulate a single waste package for borehole emplacement with the primary objective of measuring rock mass response in the near field. Although borehole emplacement is not considered likely at this time, the geometry of the test is useful for directly measuring rock mass thermal and thermomechanical properties such as thermal conductivity, thermal expansion, and rock mass modulus.

The SHT is being conducted in the Topopah Spring Welded Tuff lithologic unit (middle-nonlithophysal) in a specially constructed facility located south of the North Ramp and east of the North-South main drift. The location of the Thermal Testing Facility is shown schematically in Figures 1-1 and 1-2. The SHT block is bounded on the north by the Observation Drift (declining at about 10%), on the west by the Thermomechanical Alcove, and on the south by the Thermomechanical Alcove Extension. The dimensions of the excavations are given in Figure 1-3. Refer to TRW (1996a) for specific details regarding the test and facility design.

Figure 1-3 shows the conceptual layout for the SHT in plan and cross-section views. The SHT consists of emplacing a long (5-m) heater at a slight upward incline in a borehole in the west face of the test block, as shown in Figure 1-3. The test configuration includes the heater in roughly the

center (plan view) of the test block, with instrumentation access from all three free surfaces bounded by the excavations.

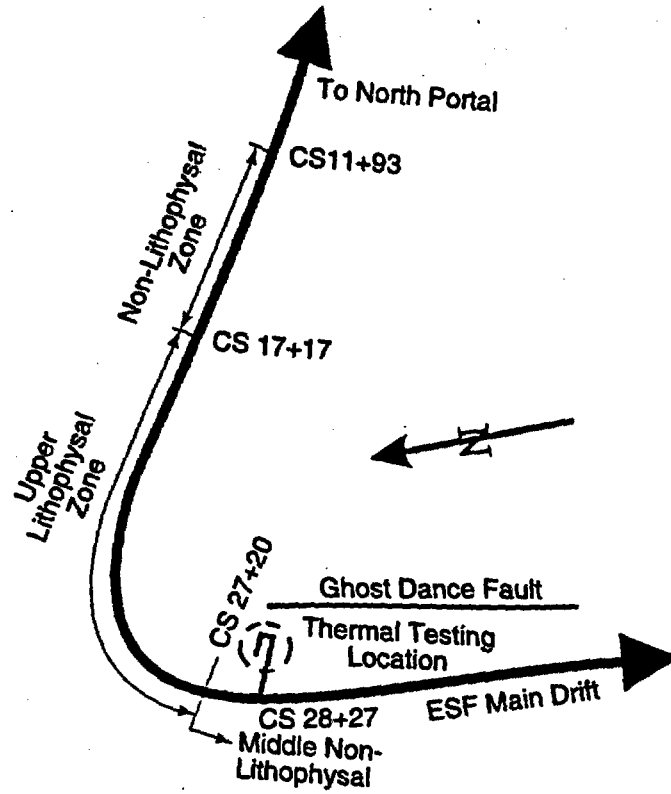
Table 1-1. List of Milestone Criteria Satisfied by this Document

Level 4 Milestone SP9261 M4 is a TDIF submitted by 7/18/97. This milestone will be satisfied on submission to the technical database under a TDIF the results of heater power and temperature measurements from the start of the SHT to 5/31/97, including ambient temperature measurements before the start of heating.	
Criteria for SP9261 M4	Location
Heater power and all temperature sensor data will be tabulated	Section 3.1, 3.2; Appendix C
Measurements of 15 temperature sensors will be plotted	Section 3.2
Preliminary evaluation of the results	Section 3.1, 3.2, 6.1
Performance of measuring systems and anomalous readings	Section 3.1, 3.2, 5
Level 4 Milestone SP9271 M4 is a TDIF submitted by 7/18/97. This milestone will be satisfied on submission to the technical database under a TDIF the results of thermal-mechanical measurements from the start of the SHT to 5/31/97, including ambient temperature measurements before the start of heating.	
Criteria for SP9271 M4	Location
Displacements measured by MPBXs will be tabulated	Section 4.1; Table 4-1; Appendix C
Displacements measured by wire and tape extensometers will be tabulated	Section 4.1; Tables 4-2 & 4-3; Appendix C
Rock bolt load cell readings will be tabulated	Section 4.3; Tables 4-5 & 4-6; Appendix C
Goodman (NX borehole) jack measurements will be reported	Section 4.2; Table 4-4
Preliminary evaluation of the results	Sections 4.1, 4.2, 4.3, 6.2
Performance of measuring systems and anomalous readings	Sections 4.1, 4.2, 4.3, & 5.
Level 4 Milestone SP9268 M4 is a deliverable submitted by 7/18/97. This milestone will be satisfied on submission to the M&O a report documenting the results of integrated analyses of the heating phase and early cooling phase of the Single Heater Test through 5/31/97.	
Criteria for SP9268 M4	Location
Document as-builts	Appendix C
Document test thermomechanical results through 5/31/97	Section 3; Section 4
Document results of an integrated analysis and interpretations of SHT results through the heating phase (5/27/97)	Section 3; Section 4; Section 6
Document derived rock mass thermal expansion coefficient from thermal and mechanical measurements	Section 6
Document rock mass deformation modulus measurements	Section 4; Section 6

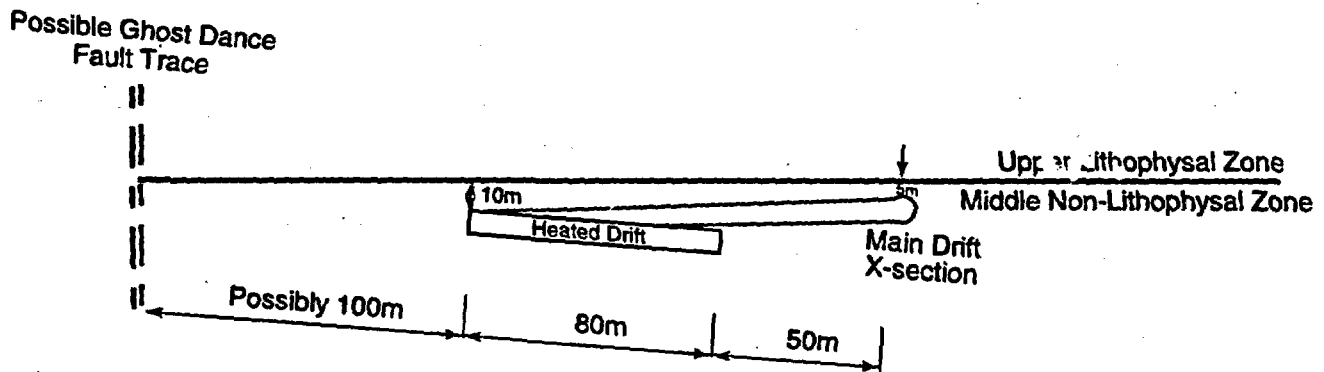
The SHT is intended to provide data and information on the rock mass thermal and thermomechanical properties, preliminary information on coupled T-M-H-C responses, and preliminary information on ground support/rock interaction at elevated temperature (see Table 1-2). The SHT will also serve to evaluate equipment and instrumentation, evaluate predictive numerical models, and develop and evaluate procedures.

The SHT was constructed, instrumented, and initiated during the summer of 1996, with the heater being started on 26 August. This report documents the data collected through the third quarter of heating (31 May 1997). This report will present temperature data from all sensors as well as SNL

thermomechanical gage data, borehole jack results, and heater power. Additional data collected by other participants (including water saturations, chemistry, and air pressure) will not be presented in this report; those data are expected to be presented by the various other participants.



(a) Plan View

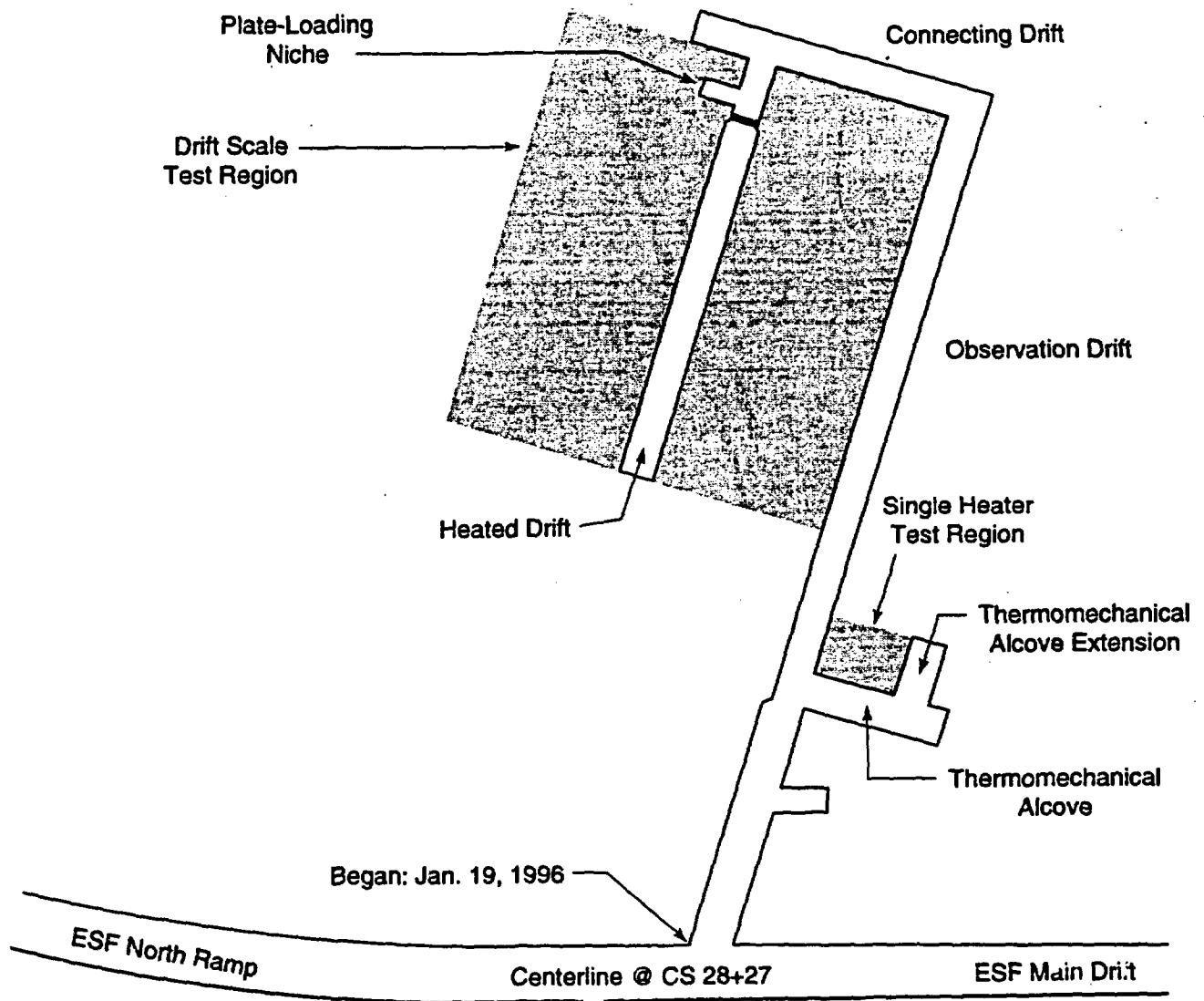


(b) Profile View

Reference Only  
(Not to Scale)

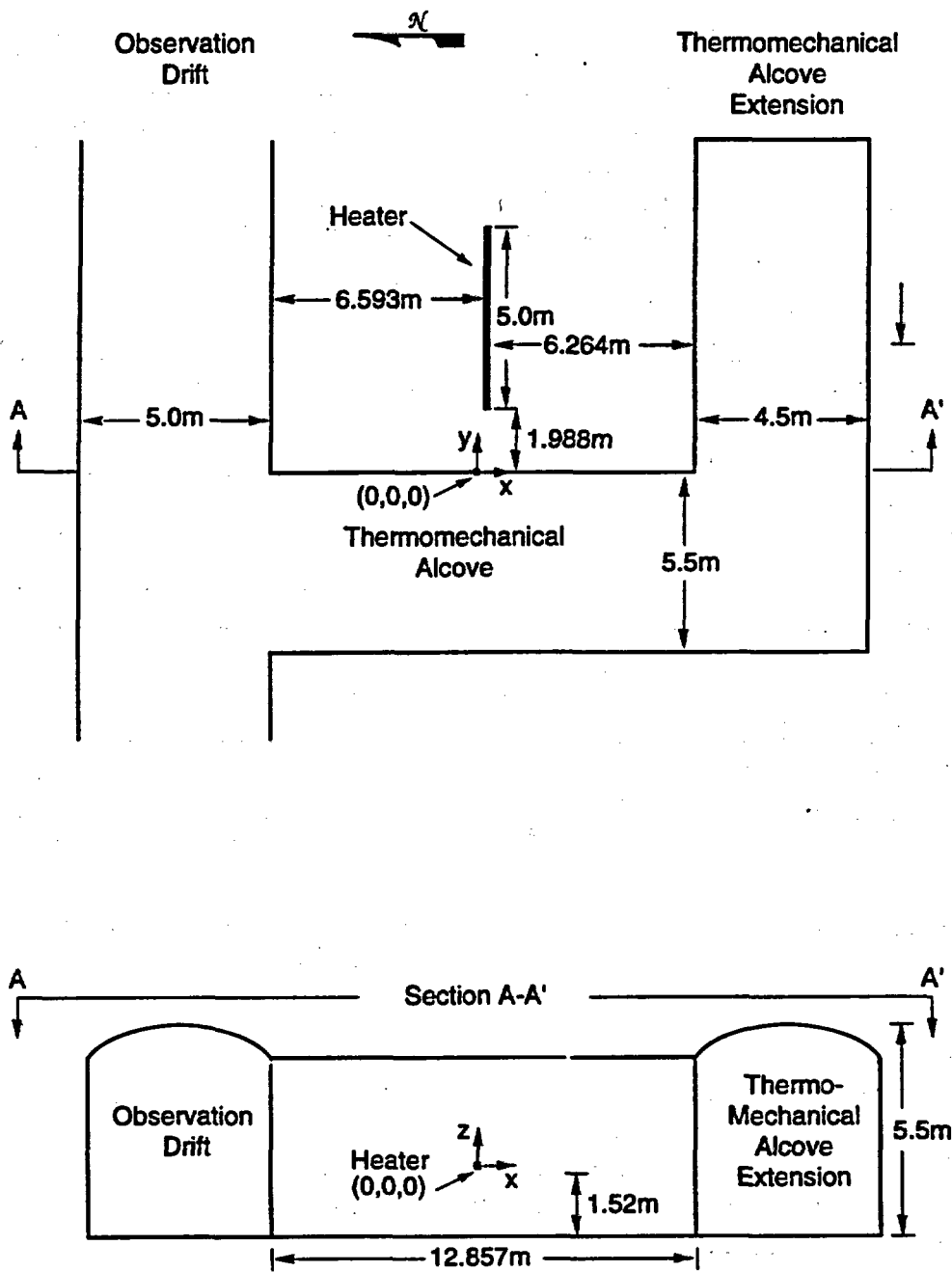
Figure 1-1. General location of the ESF Thermal Test.

TRI-6852-002-0



TRI-6852-005-0

Figure 1-2. Plan view of ESF Thermal Test Facility.



TRI-6852-001-0

Figure 1-3. Conceptual layout for the SHT, views in plan and cross-section.

Table 1-2. Data and Information Needs Addressed by the Single Heater Test

<b>Data/Information Needs</b>	<b>Single Heater Test</b>
<b>NEAR FIELD T-M-H-C ENVIRONMENT</b>	
Changes in rock saturation	Primary
Water chemistry (liquid reflux)	Secondary
Mineralogic changes	Secondary
Propagation of "drying" front	Primary
Residual water saturation in "dry" zone	Primary
Drainage/reflux of liquid by fracture flow (heterogeneity, heat pipe, fast paths)	Secondary
Rock mass and fracture permeability changes	Primary
Conductive/convective heat transfer	Primary
<b>ROCK MASS PROPERTIES OVER A RANGE OF TEMPERATURES</b>	
Thermal capacity or specific heat	Primary
Thermal conductivity	Primary
Thermal expansion	Primary
Deformation modulus	Secondary
Strength	Only by inference
<b>GROUND SUPPORT AND DESIGN FEATURES INTERACTIONS AT ELEVATED TEMPERATURES</b>	
Rock mass/ground support interactions	Secondary
Effect of materials on near-field water chemistry	Secondary
Effect of near-field environment on ground support components	Secondary

Note: Primary and secondary refer to the purpose of the experiment relative to the data to be collected.

The data and information recognized in Table 1-2 are collected through in situ measurements made from instrumentation installed in boreholes within the SHT block and from instruments installed on the SHT block surface. Actual measurements include:

- heater power
- temperature on the heater canister surface,
- temperature within the SHT block,
- temperature on the three free surfaces of the SHT block,
- temperatures within the insulation applied to the three free surfaces of the SHT block,
- displacement within the SHT block,
- displacement of the three free surfaces of the SHT block,
- rock mass modulus using a borehole jack,
- water saturation within the SHT block,
- air pressure within the SHT block, and
- water chemistry.

Additionally, the SHT block was characterized prior to heater startup by conducting air permeability measurements, rock mass quality assessments, and laboratory tests of thermal

conductivity, thermal expansion, and initial water saturation. These characterization data are described in detail in TRW (1996b).

The SHT represents the combined efforts of a number of organizations, which include Sandia National Laboratories (SNL), Lawrence Livermore National Laboratory (LLNL), Lawrence Berkeley Laboratory (LBL), Los Alamos National Laboratory (LANL), The Managing and Operating (M&O) contractor, the Department of Energy (DOE), and Yucca Mountain Project (YMP) site contractor personnel. Each organization had distinct responsibilities. SNL was responsible for heater design and installation and in situ thermomechanical measurements, as well as rock mass quality assessment of the SHT block and laboratory thermal conductivity and thermal expansion measurements. LLNL was primarily responsible for in situ thermohydrologic measurements. LBL was primarily responsible for bulk permeability characterization of the SHT block and laboratory testing of initial matrix saturation and permeability. LANL was responsible for the test coordination, scheduling, and data acquisition system design and construction. The DOE was responsible for test oversight. The M&O contractor was responsible for creation of borehole and SHT block as-builts (geometric locations of boreholes and rock surfaces) as well as construction support.

Page intentionally blank

## 2. Layout

As noted in Section 1, the layout for the SHT includes the block of the Topopah Spring Welded Tuff bounded by the Observation Drift on the north, the Thermomechanical Alcove on the west, and the Thermomechanical Alcove Extension on the south. Thirty-one boreholes are drilled in the SHT block, eight holes are drilled on the heated and ambient side of the Thermomechanical Alcove for rock bolt evaluation, and six surface extensometer arrays (including tape extensometer pins and wire extensometer stations) are located on the three free surfaces of the SHT block. Figures 2-1 and 2-2 show the general borehole layout in plan and cross-section views. Figure 2-2 includes a table listing the heater and instrumentation boreholes. Also listed are the types of instruments installed, borehole diameter and length, and additional information related to the instrument.

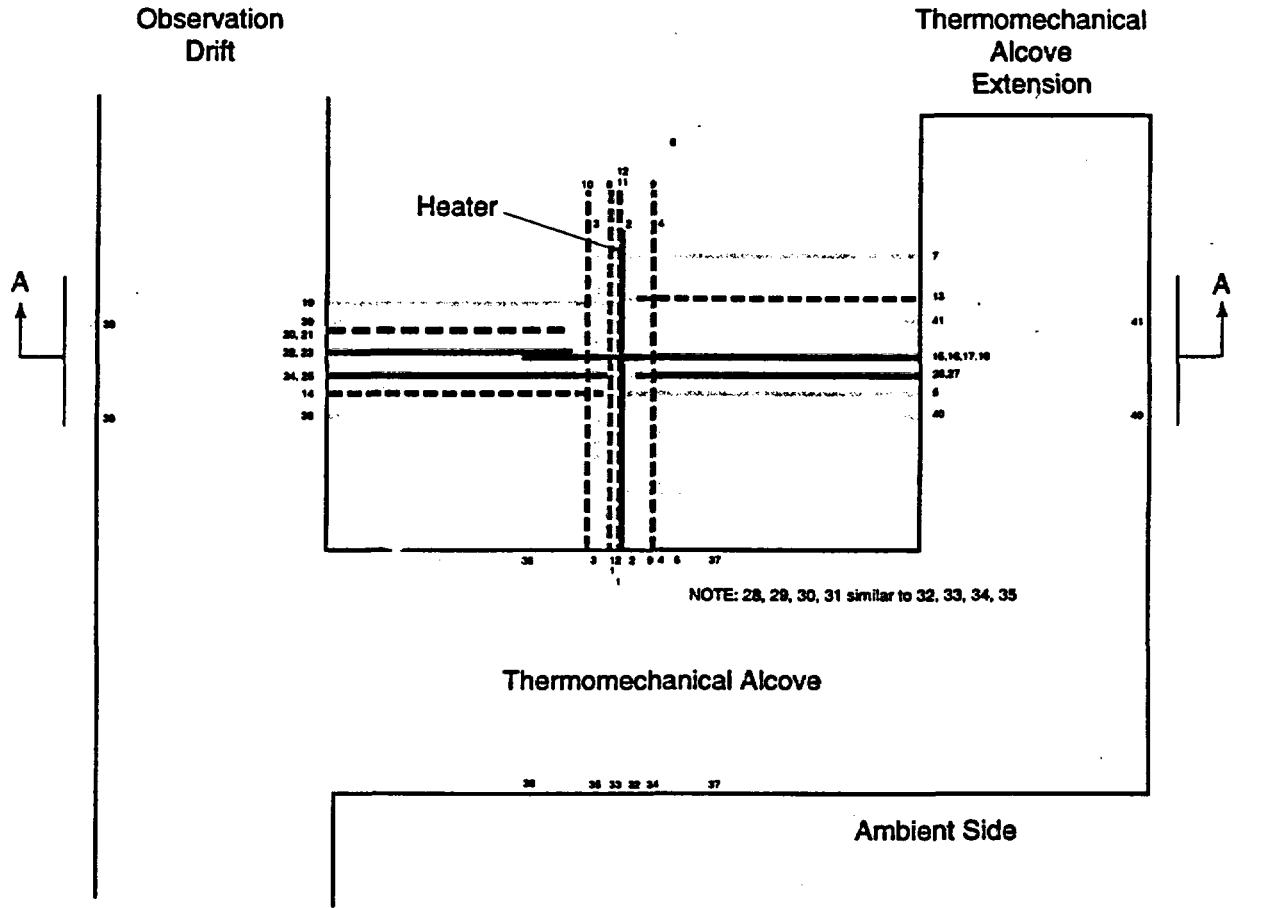
In Section 3 data will be presented for each sensor. The gage locations are given in x,y,z coordinates in Appendix C. The gages included thermocouples (TCs), resistance temperature devices (RTDs), thermistors, multiple point borehole extensometers (MPBXs), wire extensometers (WXs), tape extensometers (WXM), rock bolt load cells (RBLCs), borehole jack measurements, and heater power. Gage specifications are given in Appendix B.

The gage location table in Appendix C presents each gage relative to the center of the heater borehole collar at x=0, y=0, and z=0 (all measurements in meters). The gage locations for all SNL-installed gages have previously been reviewed by SNL and submitted under TDIF # 305721 (DTN: SNF35110695001.001).

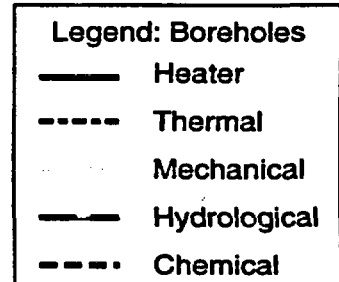
In Appendix C, the gages are identified based on the borehole in which they are installed (if applicable), the other gages they are related to (if applicable), and the gage type and gage number. For instance, thermocouples are installed in dedicated boreholes, on the heater surface, in conjunction with MPBXs, and on the rock surface. The following list is intended to serve as a guide to reading the gage table in Appendix C.

Gage Identifier	Description:
(Drift)-(Borehole #)-(gage type)-(gage #) TMA-H-1-TCT-(1-9)	TMA = Thermomechanical Alcove H-1 = Heater borehole TCT = Thermocouple top (of heater) (1-9) = TCs #1-9 with TC #1 bottom and TC #9 nearest the collar
TCS	TCS = Thermocouple side (of heater)
TCB	TCB = Thermocouple bottom (of heater)

The other "gage type" designators are clarified in Appendix C.



Reference Only  
(Not to Scale)



TRI-6852-004-0

Figure 2-1. Layout of Single Heater Test, plan.

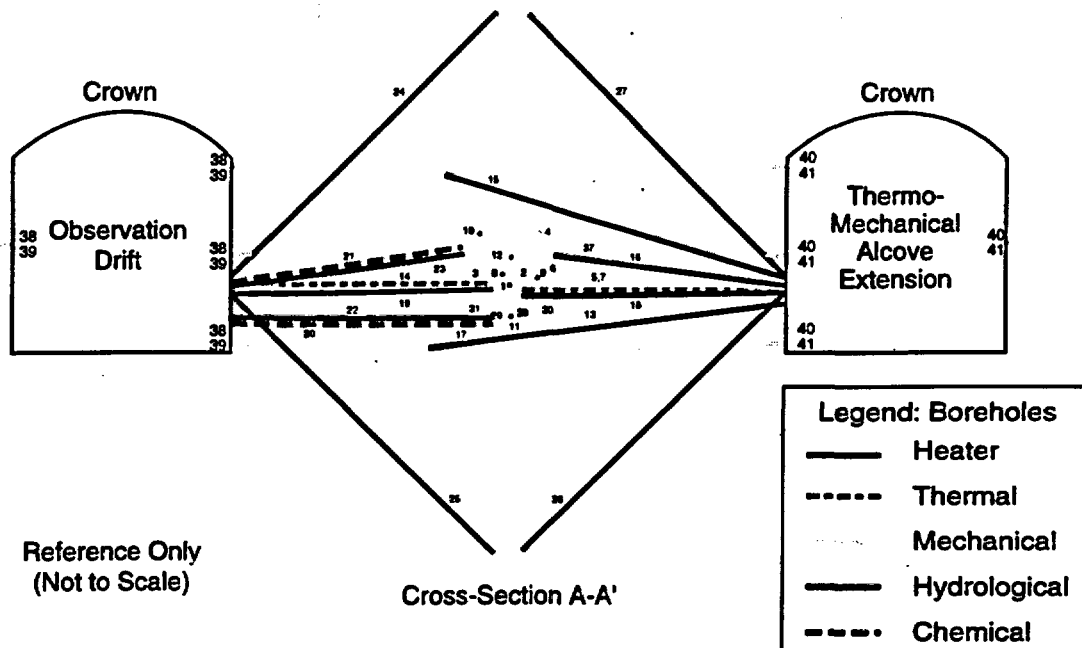


Fig. ID #	Borehole Instrument	Dia. (cm)	Length (m)	Additional Instrument Information
1	Heater	9.6	7.00	5m Long Heater w/Metallic Spring Centralizers
2	MPBX	7.57	7.00	6-pt Extensometers
3	MPBX	7.57	7.00	6-pt Extensometers
4	MPBX	7.57	7.00	6-pt Extensometers
5	MPBX	7.57	6.20	6-pt Extensometers
6	Optical MP	7.57	12.00	Laser Reflection MPBX System
7	Optical MP	7.57	6.20	Laser Reflection MPBX System
8	Thermocouple	4.80	8.00	Thermocouple Probes Grouted in Hole
9	Thermocouple	4.80	8.00	Thermocouple Probes Grouted in Hole
10	Thermocouple	4.80	8.00	Thermocouple Probes Grouted in Hole
11	Thermocouple	4.80	8.00	Thermocouple Probes Grouted in Hole
12	Thermocouple	4.80	8.00	Thermocouple Probes Grouted in Hole
13	Thermocouple	4.80	6.20	Thermocouple Probes Grouted in Hole
14	Thermocouple	6.00	6.20	Thermocouple Probes Grouted in Hole
15	Neutron Probe & Temp	7.57	8.50	Temp Probe Grouted Between Hole and Small Pipe
16	Hydrology	7.57	5.50	Humidity Sensors (Humicaps) in Packer Systems
17	Neutron Probe & Temp	7.57	8.50	Temp Probe Grouted Between Hole and Small Pipe
18	Hydrology	7.57	5.00	Humidity Sensors (Humicaps) in Packer Systems
19	Borehole Jack	7.57	6.20	Open Hole for Borehole Jack
20	Chemistry - SEAMIST	7.57	5.00	SEAMIST System with Chemical Sensors
21	Chemistry - SEAMIST	7.57	5.50	SEAMIST System with Chemical Sensors
22	Neutron Probe & Temp	7.57	5.00	Temp Probe Grouted Between Hole and Small Pipe
23	Neutron Probe & Temp	7.57	5.50	Temp Probe Grouted Between Hole and Small Pipe
24	Electrical Resistivity Tomography	7.57	8.70	Electrical Resistivity Tomography
25	Electrical Resistivity Tomography	7.57	8.70	Electrical Resistivity Tomography
26	Electrical Resistivity Tomography	7.57	8.70	Electrical Resistivity Tomography
27	Electrical Resistivity Tomography	7.57	8.70	Electrical Resistivity Tomography
28	Rock Bolt w/ Load Cell	6.67	5.00	Vibrating Wire Load Cell on Head of Rock Bolt
29	Rock Bolt w/ Load Cell	6.67	5.00	Vibrating Wire Load Cell on Head of Rock Bolt
30	Rock Bolt w/ Load Cell	6.67	5.00	Vibrating Wire Load Cell on Head of Rock Bolt
31	Rock Bolt w/ Load Cell	6.67	5.00	Vibrating Wire Load Cell on Head of Rock Bolt
32	Rock Bolt w/ Load Cell	6.67	5.00	Vibrating Wire Load Cell on Head of Rock Bolt
33	Rock Bolt w/ Load Cell	6.67	5.00	Vibrating Wire Load Cell on Head of Rock Bolt
34	Rock Bolt w/ Load Cell	6.67	5.00	Vibrating Wire Load Cell on Head of Rock Bolt
35	Rock Bolt w/ Load Cell	6.67	5.00	Vibrating Wire Load Cell on Head of Rock Bolt
36	Tape Extensometer Array 3	2.54	Up to 0.5	4-pin Tape Extensometer Array
37	Tape Extensometer Array 3	2.54	Up to 0.5	4-pin Tape Extensometer Array
38	Tape Extensometer Array 3	2.54	Up to 0.5	4-pin Tape Extensometer Array
39	Tape Extensometer Array 3	2.54	Up to 0.5	4-pin Tape Extensometer Array
40	Tape Extensometer Array 3	2.54	Up to 0.5	4-pin Tape Extensometer Array
41	Tape Extensometer Array 3	2.54	Up to 0.5	4-pin Tape Extensometer Array

TRI-6852-003-0

Figure 2-2. Layout of Single Heater Test, cross-section.

**Page intentionally blank**

### 3. Thermal Measurements

This section presents measurements of heater power and temperature. These measurements primarily represent SNL-installed gages and activities; however, temperature data from LLNL-installed RTDs are also presented. Selected data from measurements of heater power and temperature are presented. Figures summarizing plan and SHT block surface views of gage locations are presented for each type of measurement. Data are presented through 31 May 1997. A brief description of instruments and equipment is given in Appendix B. Specific details regarding serial numbers, calibration records, etc. can be found in the Scientific Notebook covering this work.

#### 3.1 Heater Power

The heater assembly for the SHT consisted of two single-ended 4000-watt heating elements centered in a 5.4-cm (2.125-in.) diameter copper tube with a copper end cap at the bottom end. The two heating elements were contained in a nominally 2.5-cm (1-in.) diameter carbon steel inner casing. The heating elements were made of nicrome and were each 5-m long with a 180° bend at the bottom end. The design of the SHT heater allowed for one of the heating elements to act as a secondary heating source in the event that the other failed, or if additional heat needed to be added to the rock. The heater included a control loop that allowed for automatic switching from the primary element to the secondary element if the heater power dropped below a prescribed set point. Throughout the test only one of the heating elements was operated at a time.

The heater assembly also included four 1.3-cm (0.5-in) diameter copper sheaths brazed onto the outer surface of the copper canister at 90° intervals around the circumference. These small tubes served as guides for 0.6-cm (0.25-in) diameter thermocouple probes intended to measure the temperature of the surface of the heater canister. Three such probes were installed in three of the four guide tubes. One TC-probe was inserted on the top of the heater canister (ESF-TMA-TCT), one was located on the left side (north) of the heater assembly (ESF-TMA-TCS), and one was located on the bottom of the heater canister (ESF-TMA-TCB). Each of these probes included nine Type-K thermocouples. The intent of placing the TC-probes on the heater canister as described was to evaluate potential temperature anomalies lengthwise and from the bottom to the top of the heater assembly.

The heater power, voltage, and current were monitored using a Magtrol power monitor. The SHT called for the heater power to be nominally 4000 watts for a period of 9 to 12 months, followed by a cooldown period where the heater is off completely.

The heater power data are tabulated in Appendix C and are illustrated in Figure 3-1a. Power was applied to the heater starting on 26 August 1996 at 18:30:30 Universal Coordinated Time. Time zero in Figure 3-1a corresponds to the time of activation of the heater. During the few hours immediately prior to powering up the heater, the heater power readings averaged about -4.5 watts, reflecting zero power. Between the time of activation and 31 May 1997, but omitting the anomalous data intervals and heater down times discussed below, the heater power output averaged about 3760 watts. The heater power was not perfectly stable over the course of the test, however, as can be seen in Figure 3-1b, which illustrates the average weekly power output of the heater, omitting heater down time and anomalous data.

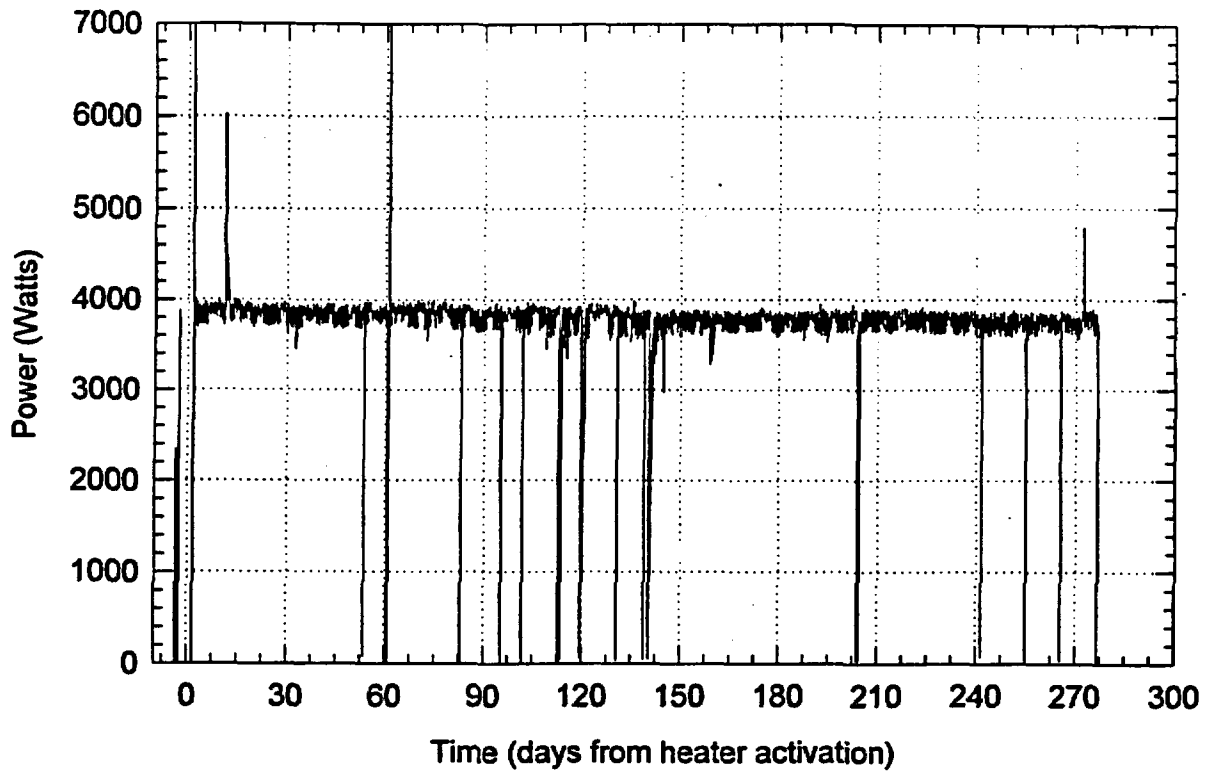


Figure 3-1a. Heater power summary through 31 May 1997.

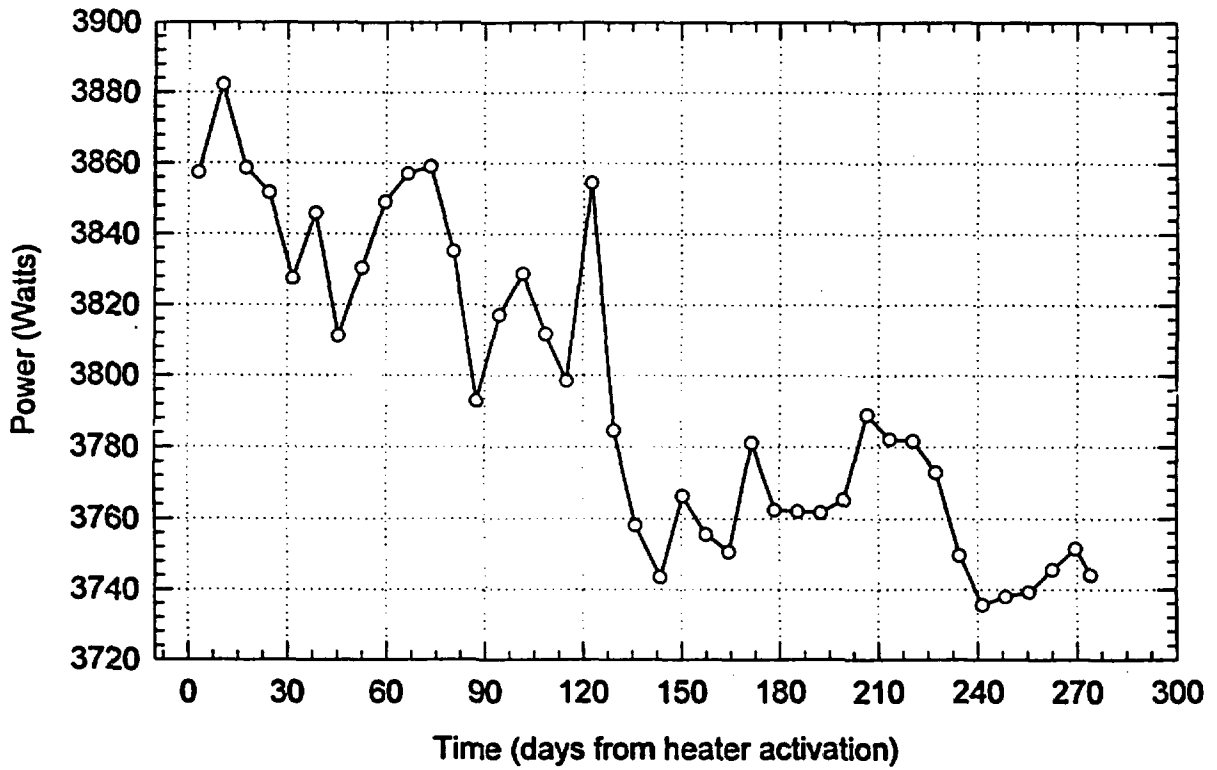


Figure 3-1b. Average weekly power output of heater through 31 May 1997.

The data indicate that the power output of the heater under normal operation declined by about 100 watts (2.5%) over the 9 months that it was in operation. The heater was deactivated on 28 May 1997 at 20:31 Universal Coordinated Time after being on for 275 days and 2 hours.

During the roughly 9 months that the heater was in operation, there were a few time intervals during which anomalous data were observed or when the power to the heater was temporarily interrupted. During the first two hours of heater operation, the heater was turned on and off a few times primarily to test the switching mechanism for heating elements #1 and #2. The heater power data collected during this interval appear to be accurate because the temperatures measured by the thermocouples on the heater tracked the heater power in a predictable manner. On day 9, the heater power data suggest that the heater power jumped abruptly from about 3900 watts to 6000 watts, then quickly decayed to about 4500 watts in a few hours. Then a gap of approximately 24 hours appears in the heater power data. This power fluctuation was caused by a power outage, and when data collection resumed late on day ten, the heater power had returned to about 3850 watts. These anomalous readings do not appear accurate because the temperatures measured by the thermocouples on the heater did not record the degree of temperature change that would be expected for heater power variations of this magnitude. Following this event, the heater power remained quite steady, varying with high frequency between about 3700 and 3950 watts for about 40 days. Late on day 51 one heater power reading is missing and the next reading is near zero, suggesting that the power was off for a period up to 45 minutes. This outage is also reflected in the thermocouple data from the heater, which dropped about 100°C but quickly recovered when heater power was restored. Early on day 59 the power went off for about 2.5 hours. This outage resulted in a significant temperature drop, recorded on the thermocouples mounted on the heater. A small drop was observed on the thermocouples on probe ESF-TMA-TC-1, located some 40 cm away from the heater. The temperatures recovered quickly after power was restored. Similar events occurred on days 81 and 93. In both these cases the heater power was off for 15 to 45 minutes and the thermocouples on the heater showed modest temperature drops but quickly recovered when heater power was restored. A 15.8-hour power outage occurred on day 112, followed by a 12-minute interruption on day 116. Longer heater down times were experienced on days 118 (23.1 hours), 139 (24.6 hours), and 202 (13.6 hours). The four longest power outages were sufficiently severe as to noticeably influence the temperatures recorded by the temperature gages in nearby boreholes.

### **3.2 Temperature**

The TC probes used in the SHT consist of Type-K thermocouples enclosed within 304 stainless steel, 0.64-cm (0.25-in.) diameter sheaths that were manufactured by STI in Houston, TX. The thermocouples within the sheaths were insulated from each other with magnesium oxide. The TC probes were installed in seven boreholes in the rock mass around the heater to monitor temperature changes away from the heater. Three additional TC probes were installed on the top, side, and bottom of the heater canister to monitor heater surface temperatures. Five of the boreholes were drilled roughly parallel to the heater axis to a depth slightly exceeding the planned heater installation depth. Within these five boreholes, probes TMA-TC-1, TMA-TC-2, TMA-TC-3, TMA-TC-4, and TMA-TC-5 were located at nominal radial distances from the heater borehole of 0.33 m, 0.66 m, and 1.48 m, roughly corresponding with the numerically

predicted temperature isotherms of 200°C, 150°C, and 100°C respectively (TRW, 1996a). Within each of these five boreholes, two TC probes were installed. Two probes were required during test planning because it was feared that the drift width was too narrow (about 5.5 m) to allow installation of 8-m long TC probes. Therefore, for each of these boreholes, two probes were used: one about 6 m long with ten Type-K thermocouple junctions spaced along its length (designated probe "A" for each borehole), and one about 2 m long with five Type-K thermocouple junctions spaced along its length (designated probe "B" for each borehole). The other two TC probes (TMA-TC-6 and TMA-TC-7) were drilled perpendicular to the heater borehole from the Observation Drift and the Thermomechanical Alcove Extension. Each of these two boreholes included a single TC probe with ten Type-K thermocouple junctions spaced along its length. The locations of the individual thermocouple junctions within each borehole were determined from (1) the survey and corrected borehole collar coordinates, (2) the field notes for installation (e.g., installed depth to various points on the probes), and (3) manufacturer and SNL specifications for the probes. Throughout the remainder of this document, the "A" and "B" designations have been dropped.

Temperatures were also measured on each of the free surfaces of the SHT block using individual Type-K thermocouple junctions. Twelve individual thermocouples were installed on each face of the SHT block. The locations for each of these thermocouples were measured manually in the field using a metric tape measure.

Temperatures were also measured between the two layers of insulation on each of the three free surfaces of the SHT block using individual thermistors. Five individual thermistors were installed between the layers of insulation on each face of the SHT block. The locations for each of these thermistors were measured manually in the field using a metric tape measure.

The locations of the 319 temperature gages being reported here are listed in Appendix C and illustrated in Figure 3-2. The median daily temperature recorded by each of the gages is presented in Appendix C, Table C-2 for day zero and every 14 days thereafter. The median daily temperature is used instead of the mean daily temperature because the median value is less affected by isolated anomalous values such as temperature spikes caused by electrical glitches, etc. Note that time is measured relative to the time of heater activation (26 August 1996 at 18:31 Universal Coordinated Time). In Table C-2, day zero refers to the twenty-four-hour period that ended when the heater was activated, day 14 refers to the 14<sup>th</sup> twenty-four-hour period after heater activation, etc.

Although all temperature gages are included in Appendix C, Table C-2, fifteen of the 319 temperature gages (<5%) are judged to be unreliable. These gages are listed in Table 3-1, and the data obtained from them are illustrated in Figures 3-3 through 3-16. Although in most cases the reasons for these gage failures are not known, it is possible that the failures represent either fabrication or installation errors. For gage TMA-BX-4-TC-3, the thermocouple extension wire was broken during installation of the probe, so the gage was never connected to the data acquisition system (DAS) and no data were ever collected. For TMA-H-1-TCB-4, something happened when the power was applied to the heater and no temperature data are available for that gage after heater activation.

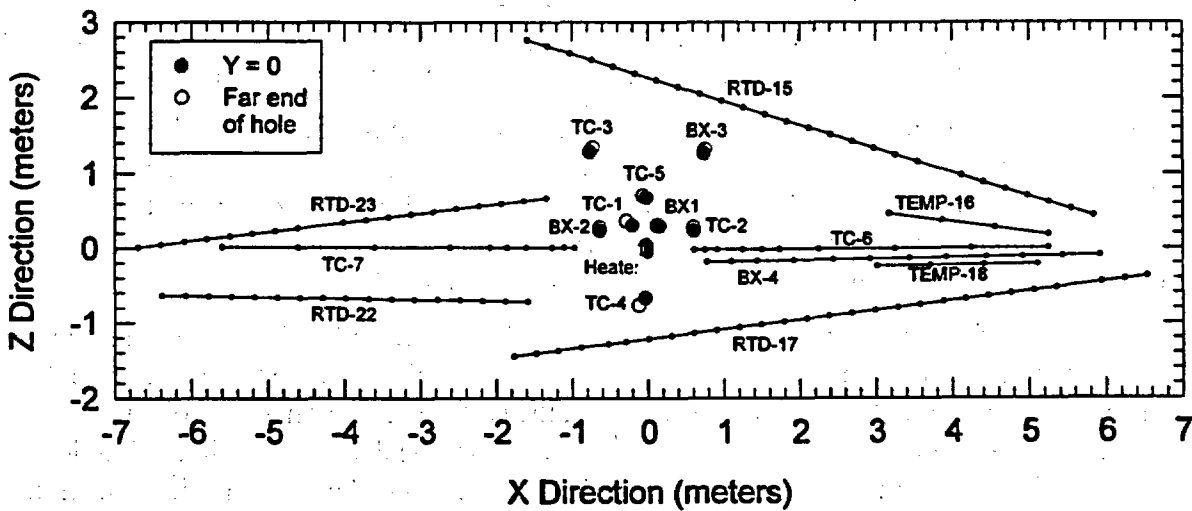
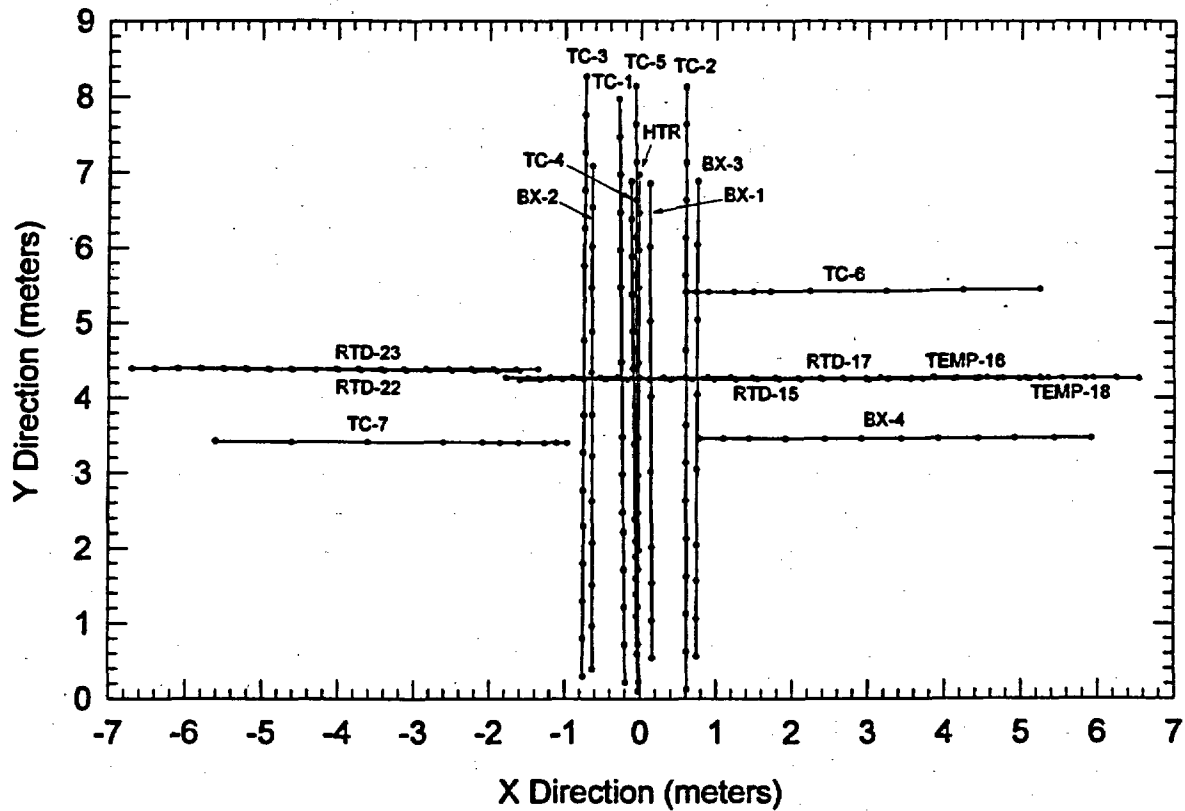


Figure 3-2. Map and cross section views of the SHT block showing the locations of interior temperature gages.

Table 3-1. Unreliable Temperature Gages from the SHT Block

Gage	Reason for Omission
TMA-H-1-TCB-4	No data after heater activation
TMA-TC-2A-4	Erratic temperature readings
TMA-TC-4A-1	Erratic temperature readings
TMA-BX-1-TC-9	Erratic or missing temperature readings starting on day 210
TMA-BX-3-TC-1	Erratic temperature readings starting on day 122
TMA-BX-3-TC-2	Erratic temperature readings starting on approximately day 210
TMA-BX-3-TC-7	Erratic temperature readings starting on day 140
TMA-BX-3-TC-9	Erratic temperature readings; no data after day 90
TMA-BX-4-TC-3	TC extension wire broken during installation
TMA-BX-4-TC-10	Missing data after day 120
TMA-RTD-15-20	Erratic temperature readings
TMA-RTD-15-23	Erratic temperature readings
TMA-RTD-17-26	Erratic temperature readings
TMA-RTD-23-11	Erratic temperature readings
TMA-RTD-23-19	Erratic temperature readings

The remaining thirteen unreliable temperature gages are deemed unreliable because either they ceased to function altogether (no data recorded in the DAS) or they exhibited erratic behavior, which is defined as very abrupt changes in temperature that are not recorded by other nearby temperature gages. In most but not all cases, the temperatures recorded are also clearly implausible, such as impossibly hot or cold temperatures, etc.

Because of the small percentage of gages yielded unreliable data, a conservative approach was adopted for dealing with suspect data: If a gage exhibited any erratic behavior, it was excluded from all analyses, even if prior or later data from that gage appeared to be reliable. The data from gage TMA-TEMP-16-4, discussed later in this section, are the only exception to this rule.

It is important that good judgment be applied in the determination of the reliability of suspect gages because anomalous behavior may also be evidence of important phenomena that should not be ignored. For the fifteen unreliable gages identified above, it is quite clear that the data are unreliable and that—even if some “good” data are available—it is unlikely that any anomalous data would be missed by ignoring all the data from these gages.

For the purpose of creating summary data plots, the 304 gages considered reliable were divided into 27 different sets. Each set contains the gages from a single probe, a single borehole, or, in the case of the surface thermocouples and the thermistors in the surface insulation, data from a particular rock face. Figures 3-17 through 3-56 illustrate the data from the data sets within the interior of the SHT block. The curves in Figures 3-17 through 3-56 illustrate (1) the median daily temperature as a function of spatial position along one of the coordinate directions every ten days, starting with the 24-hour period that preceded heater activation; and (2) for each data set, the median daily temperature as a function of time, with one curve for each temperature gage in the set. Time zero refers to the time of heater activation. The median temperature of the data collected during the first 24-hour period following heater activation is plotted at time 0.5 days, and so forth. The dots along the bottom of the spatial plots indicate the location of each gage in the borehole.

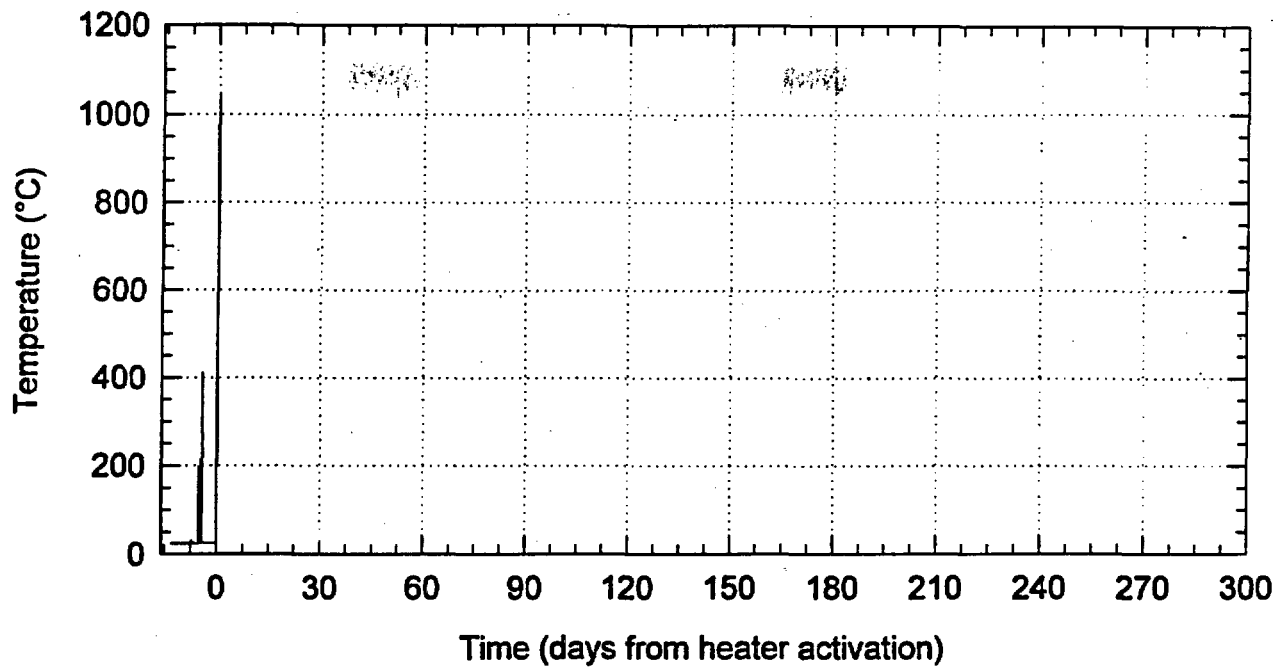


Figure 3-3. Data from gage TMA-H-1-TCB-4.

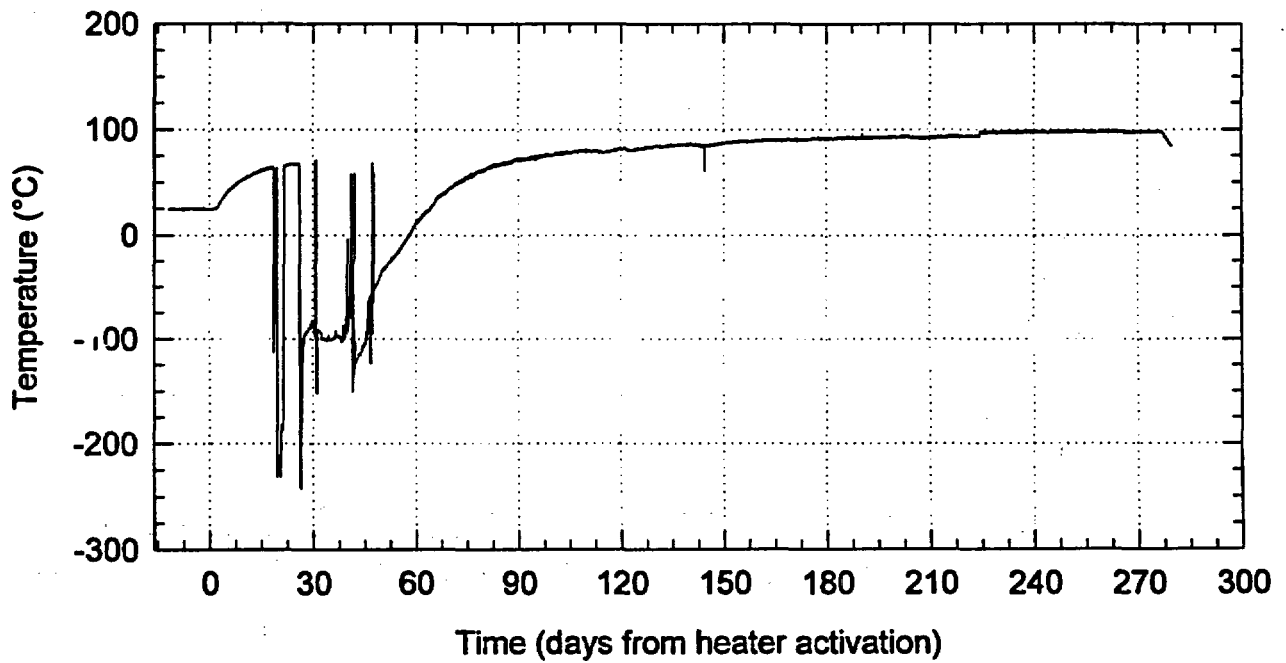


Figure 3-4. Data from gage TMA-TC-2A-4.

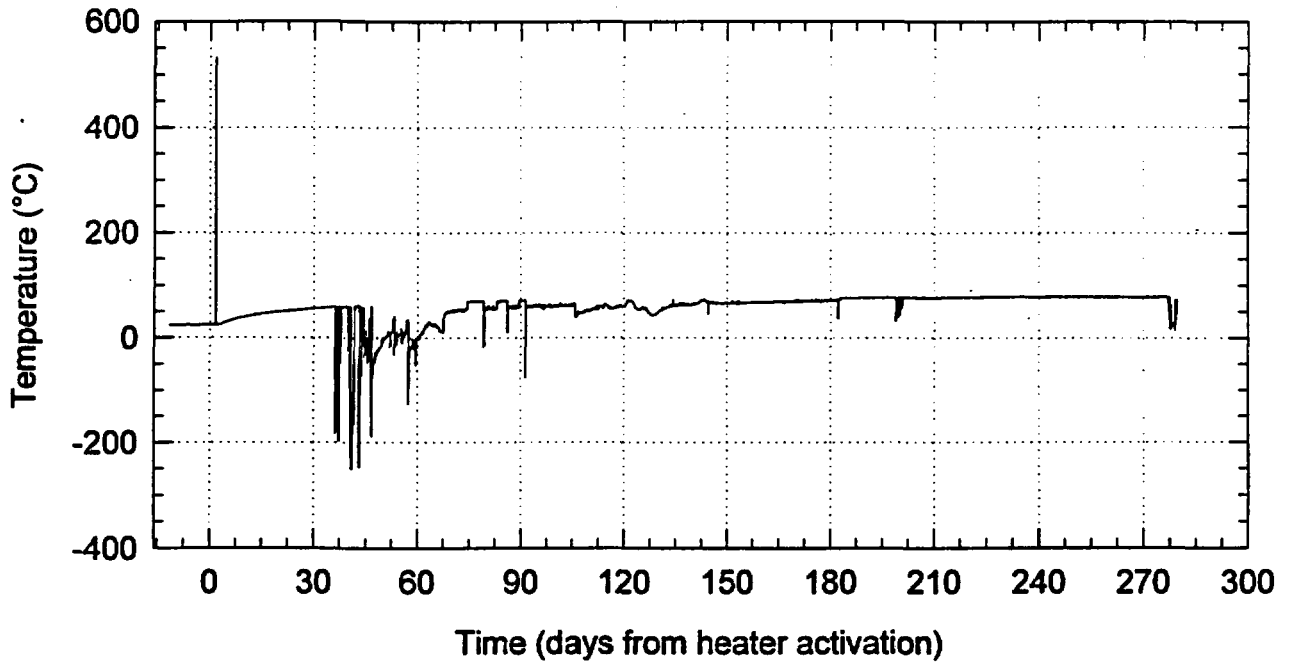


Figure 3-5. Data from gage TMA-TC-4A-1.

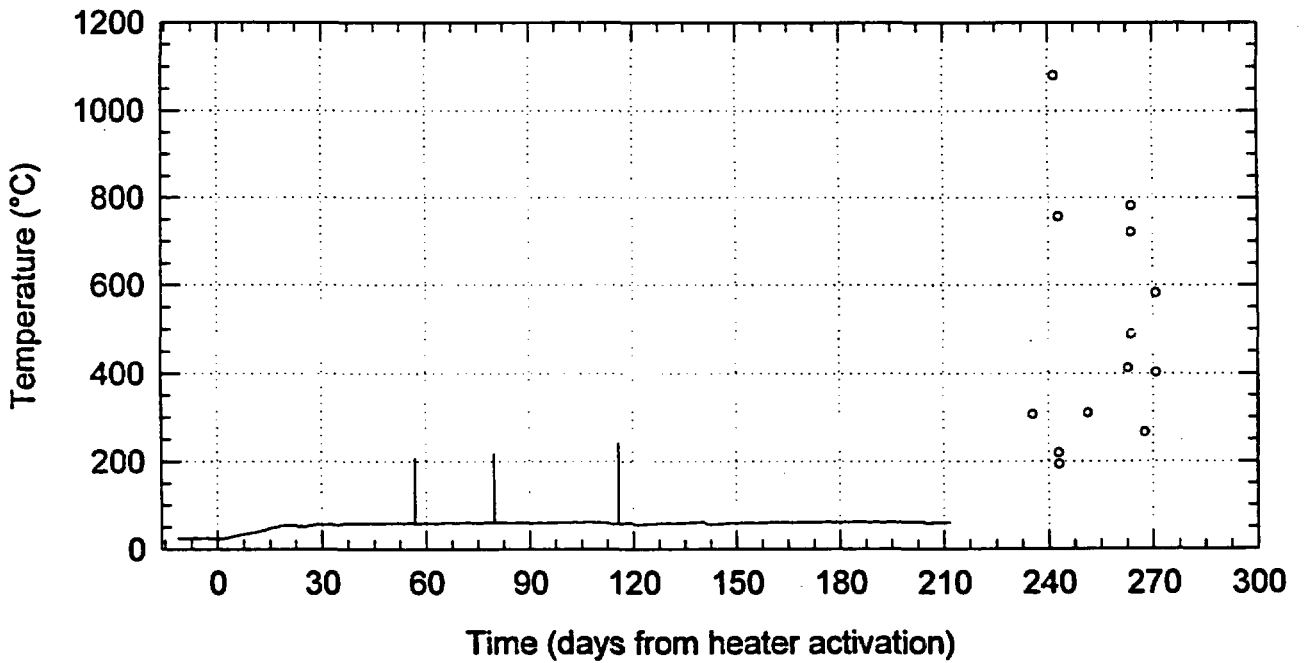


Figure 3-6. Data from gage TMA-BX-1-TC-9.

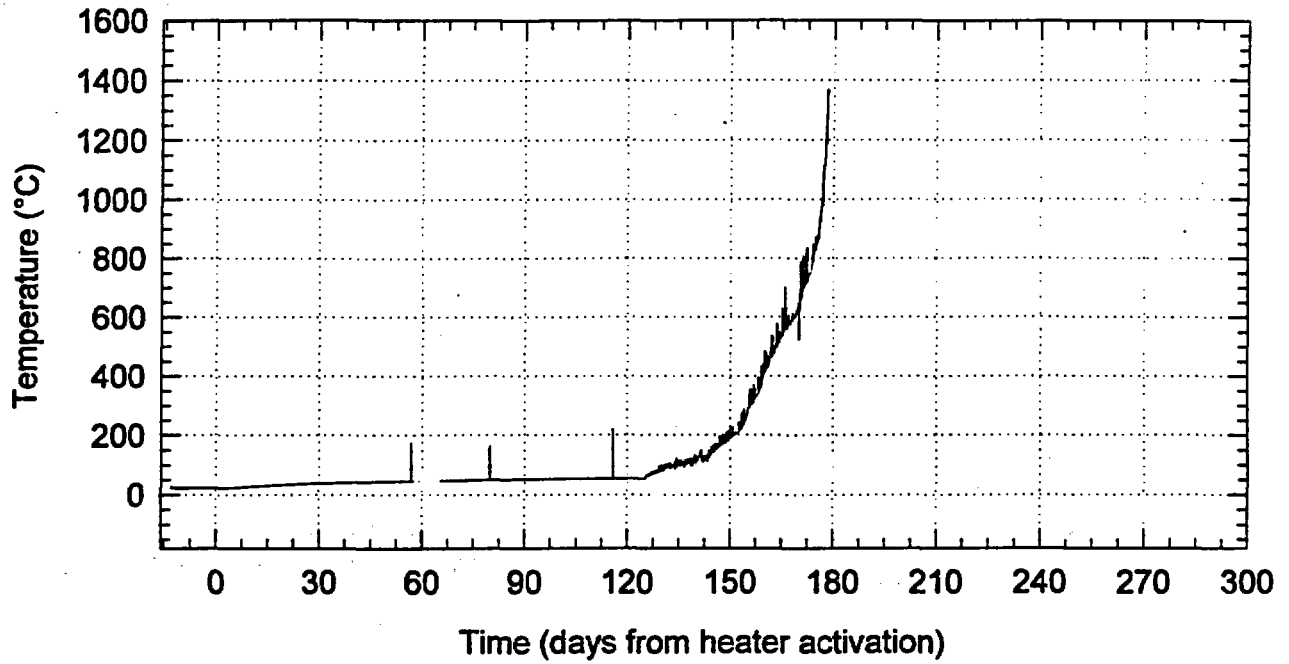


Figure 3-7. Data from gage TMA-BX-3-TC-1.

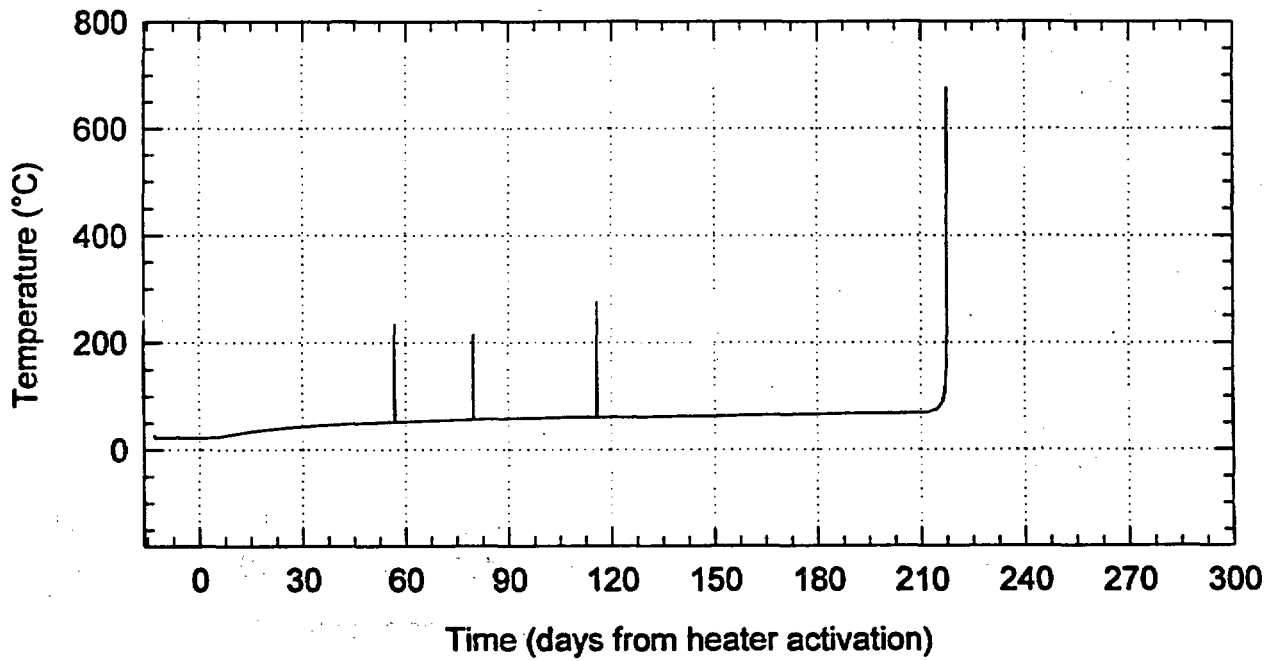


Figure 3-8. Data from gage TMA-BX-3-TC-2.

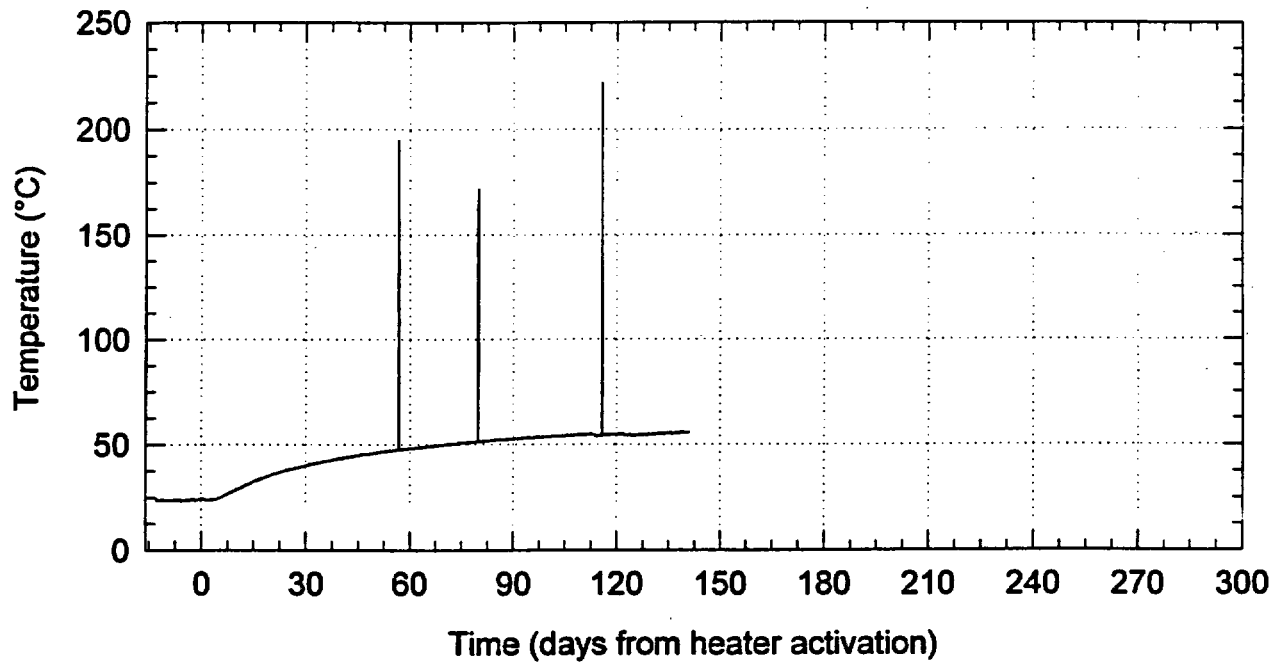


Figure 3-9. Data from gage TMA-BX-3-TC-7.

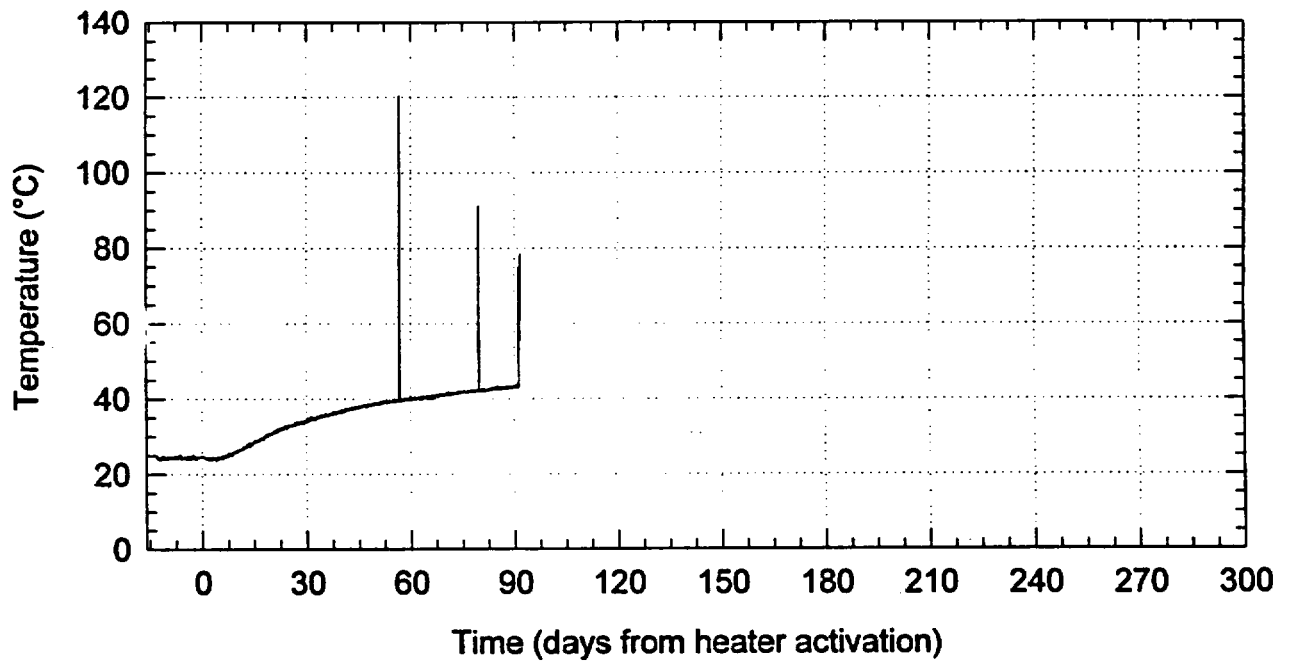


Figure 3-10. Data from gage TMA-BX-3-TC-9.

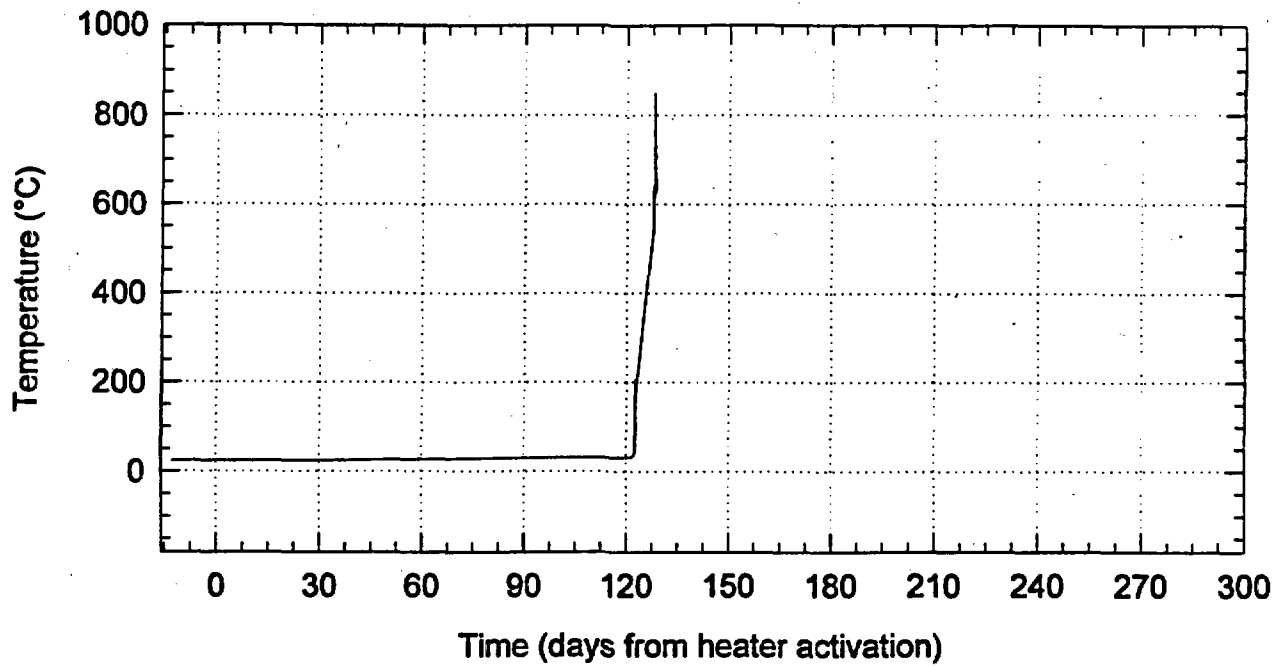


Figure 3-11. Data from gage TMA-BX-4-TC-10.

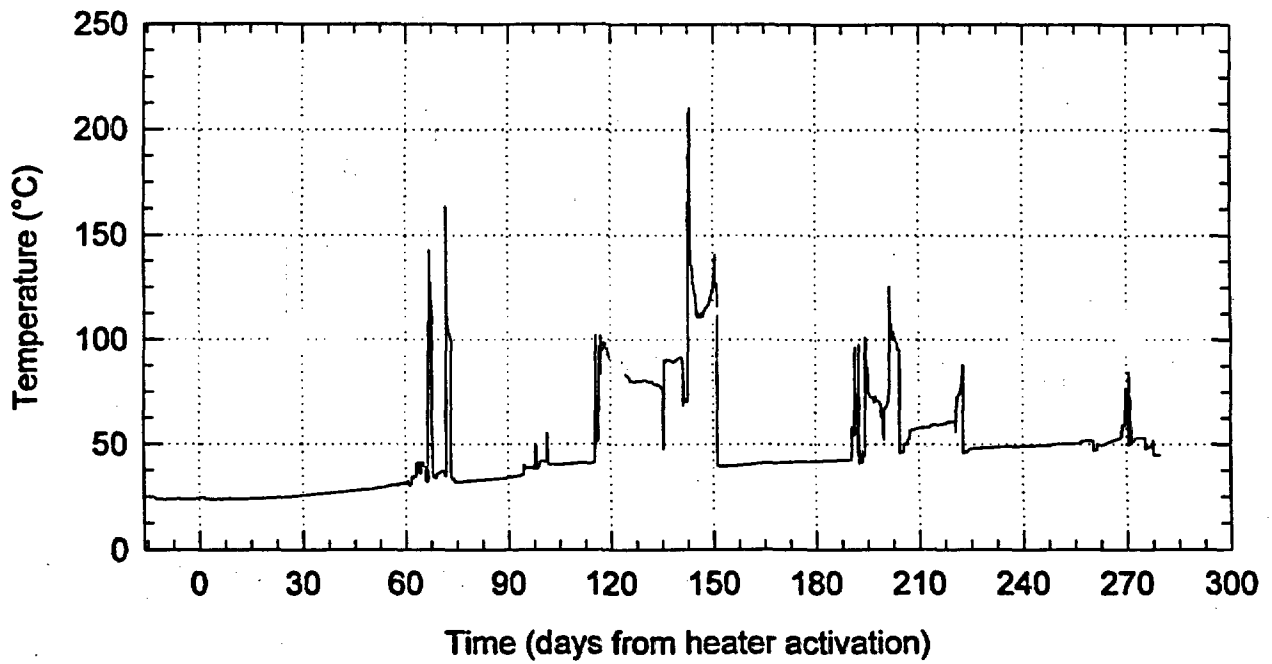


Figure 3-12. Data from gage TMA-RTD-15-20.

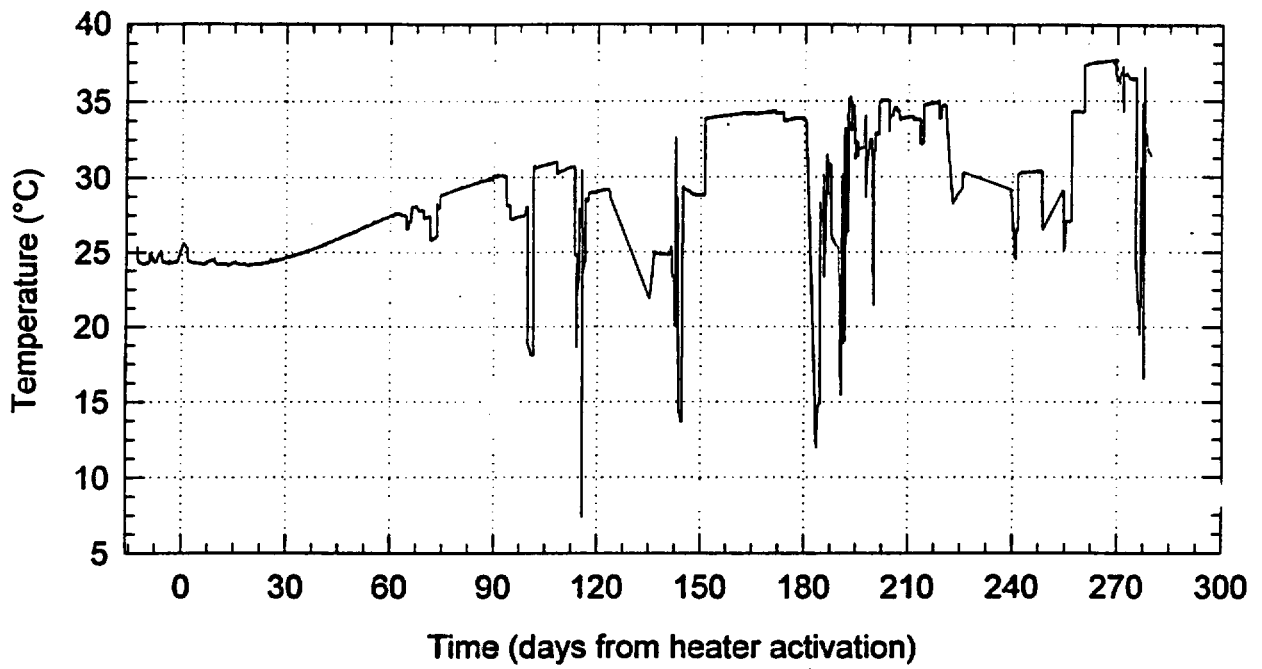


Figure 3-13. Data from gage TMA-RTD-15-23.

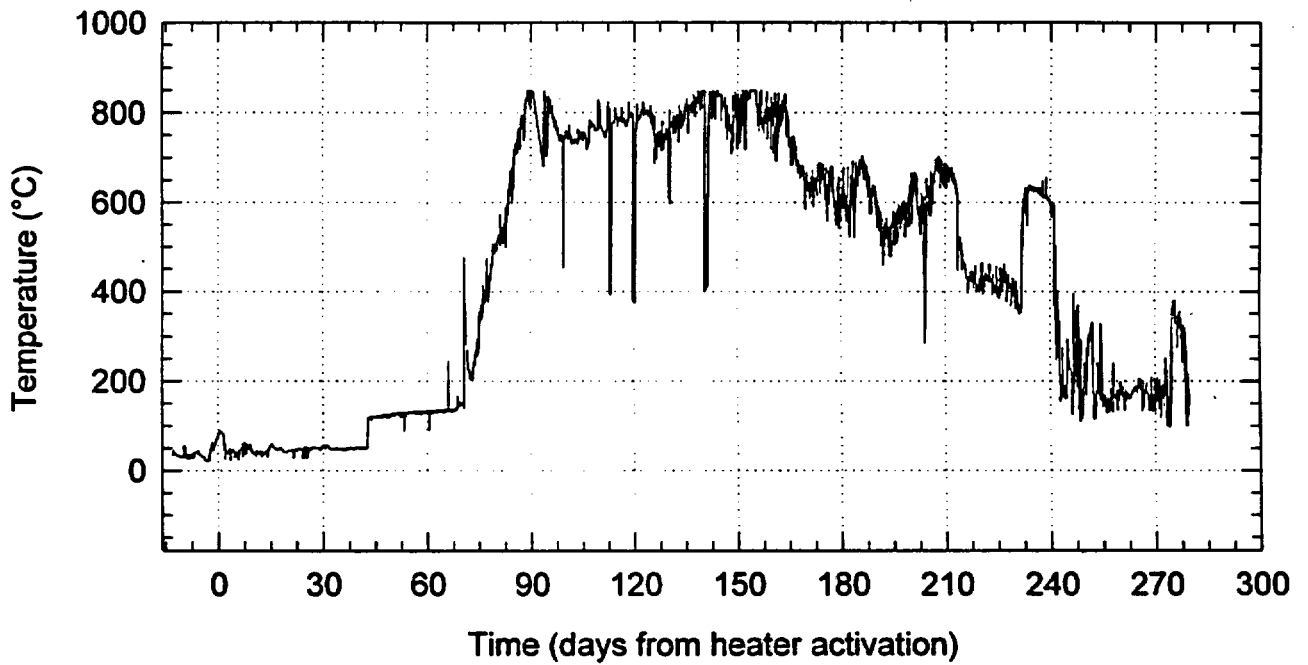


Figure 3-14. Data from gage TMA-RTD-17-26.

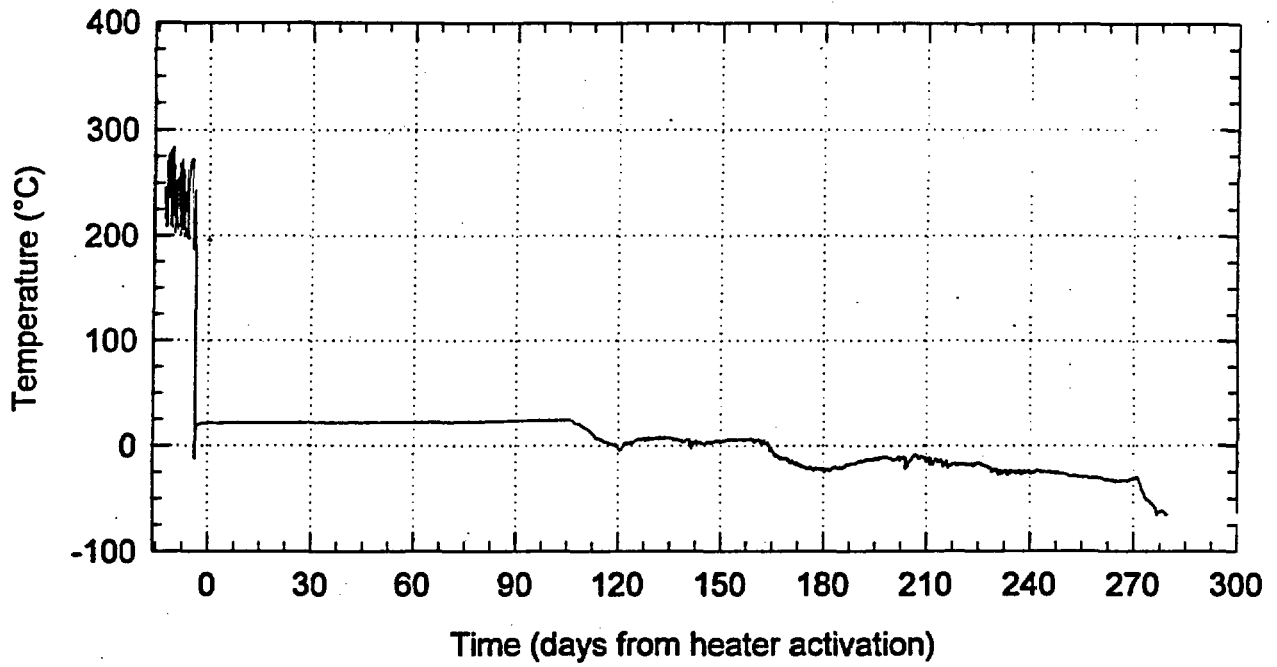


Figure 3-15. Data from gage TMA-RTD-23-19.

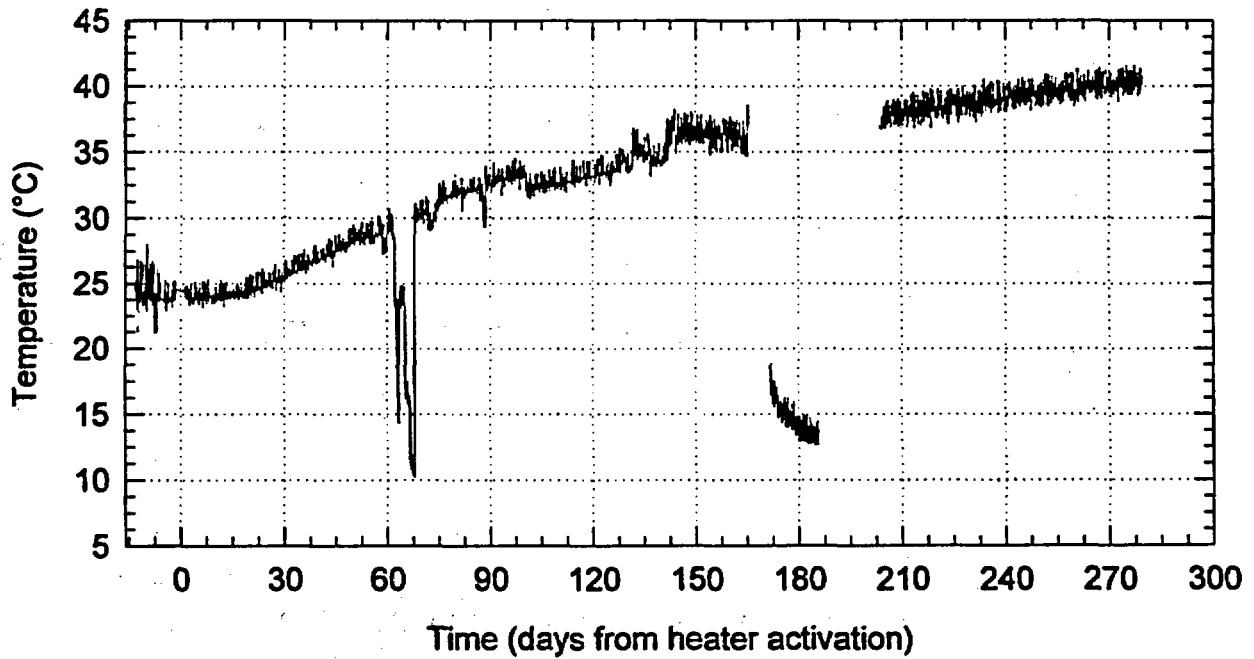


Figure 3-16. Data from gage TMA-RTD-23-11.

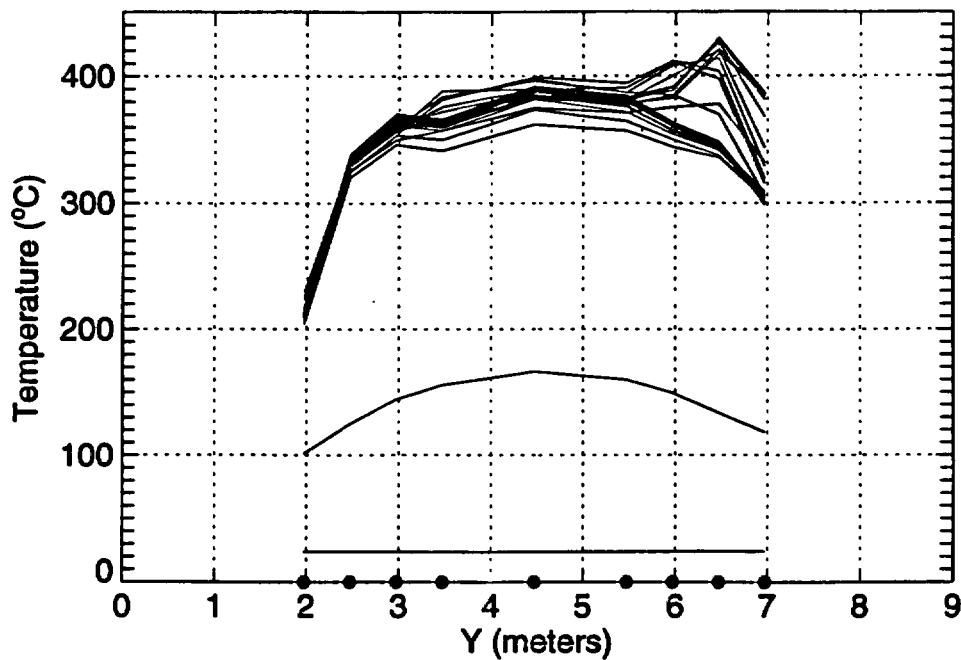


Figure 3-17. Temperature profiles for thermocouple probe TMA-TCT ( $x=-0.005$  m,  $z=0.04$  m) every 10 days since heater activation.

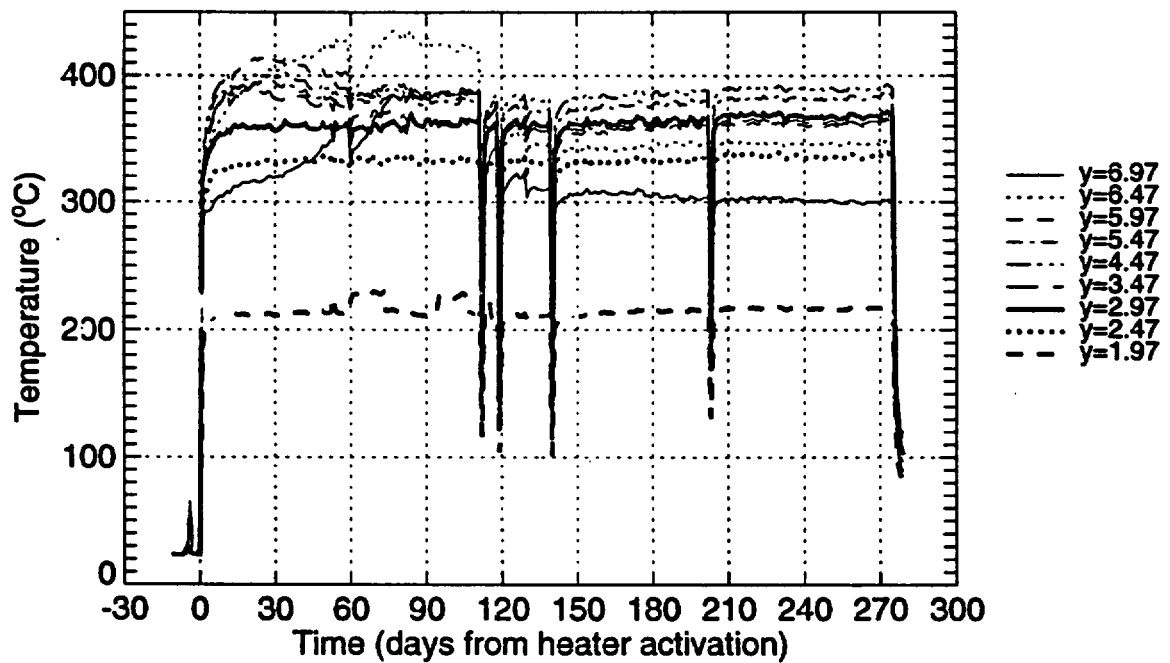


Figure 3-18. Temperature versus time for the temperature gages in probe TMA-TCT.

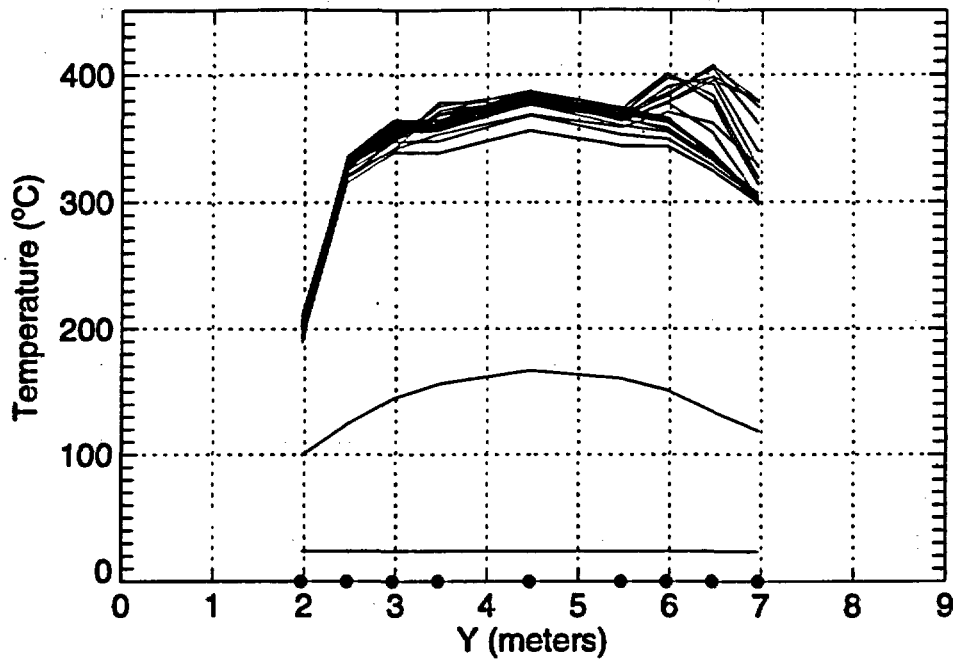


Figure 3-19. Temperature profiles for thermocouple probe TMA-TCS ( $x=-0.038$  m,  $z=-0.006$  m) every 10 days since heater activation.

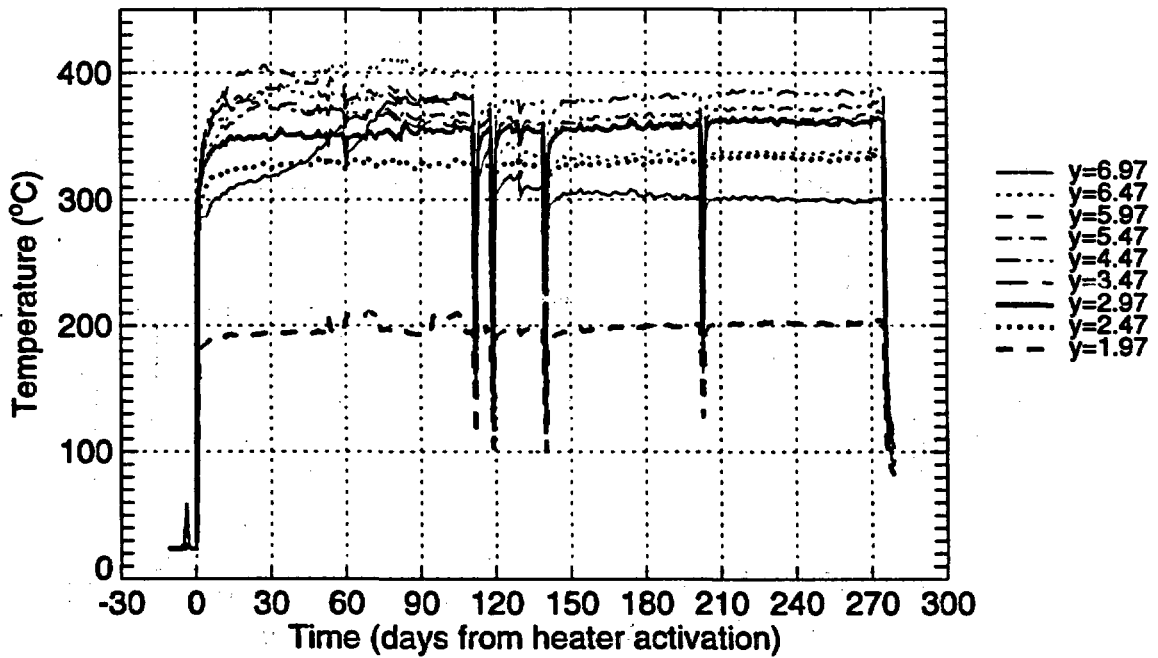


Figure 3-20. Temperature versus time for the temperature gages in probe TMA-TCS.

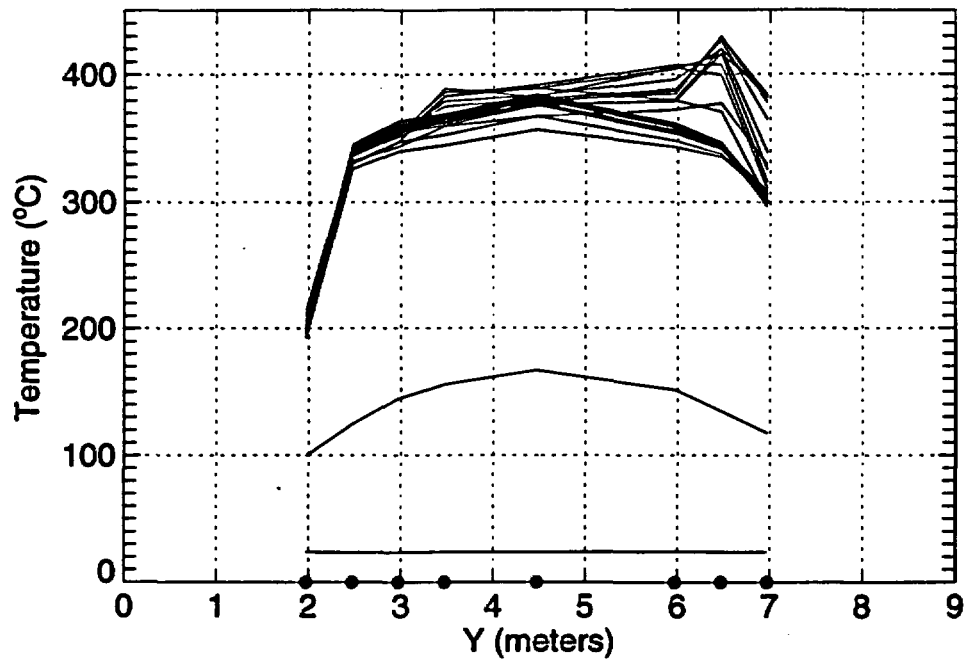


Figure 3-21. Temperature profiles for thermocouple probe TMA-TCB ( $x=-0.005$  m,  $z=-0.027$  m) every 10 days since heater activation.

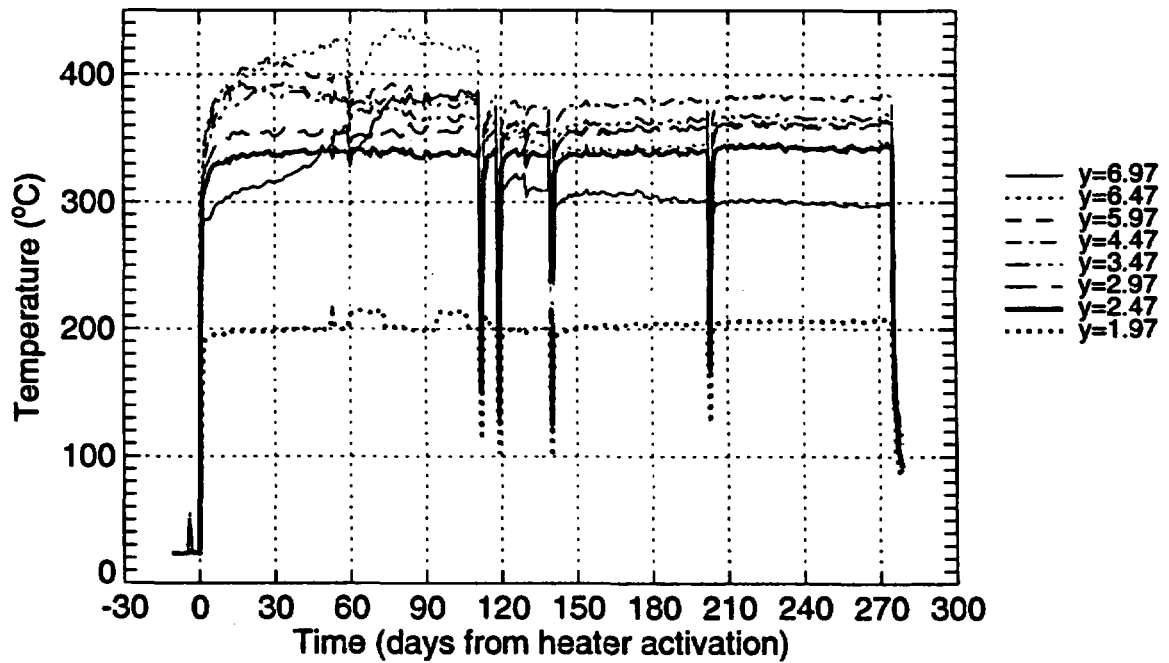


Figure 3-22. Temperature versus time for the temperature gages in probe TMA-TCB.

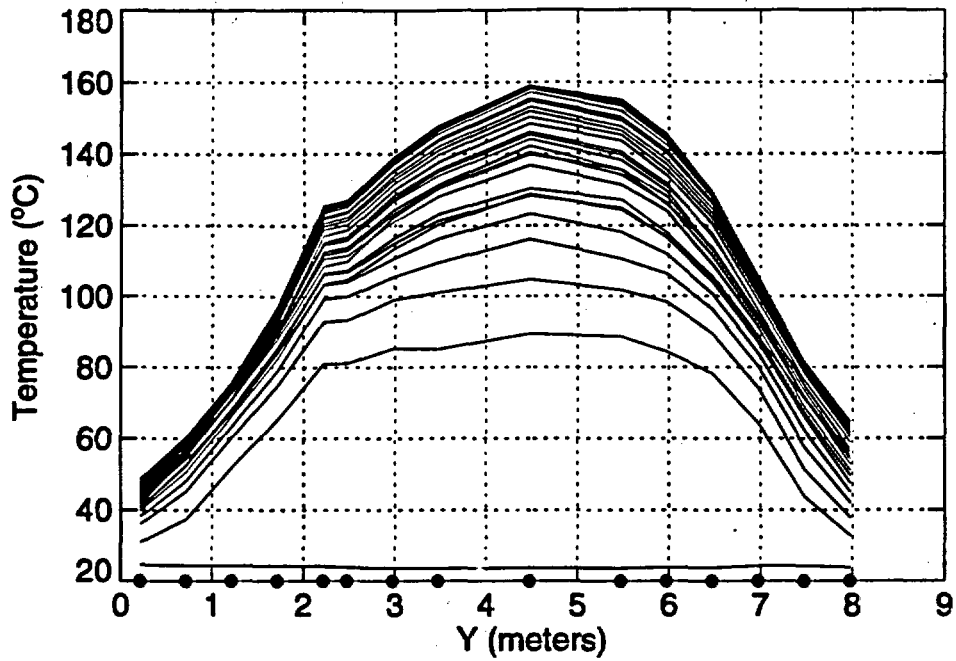


Figure 3-23. Temperature profiles for thermocouple probe TMA-TC-1 ( $x=-0.237$  m,  $z=0.342$  m) every 10 days since heater activation.

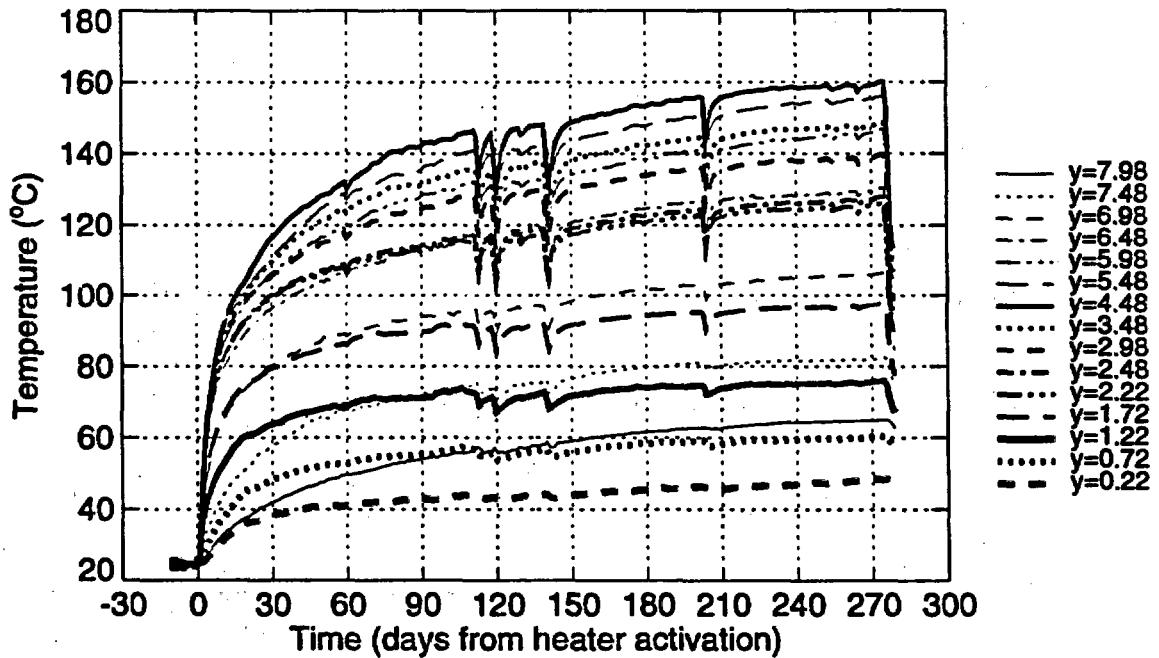


Figure 3-24. Temperature versus time for the temperature gages in probe TMA-TC-1.

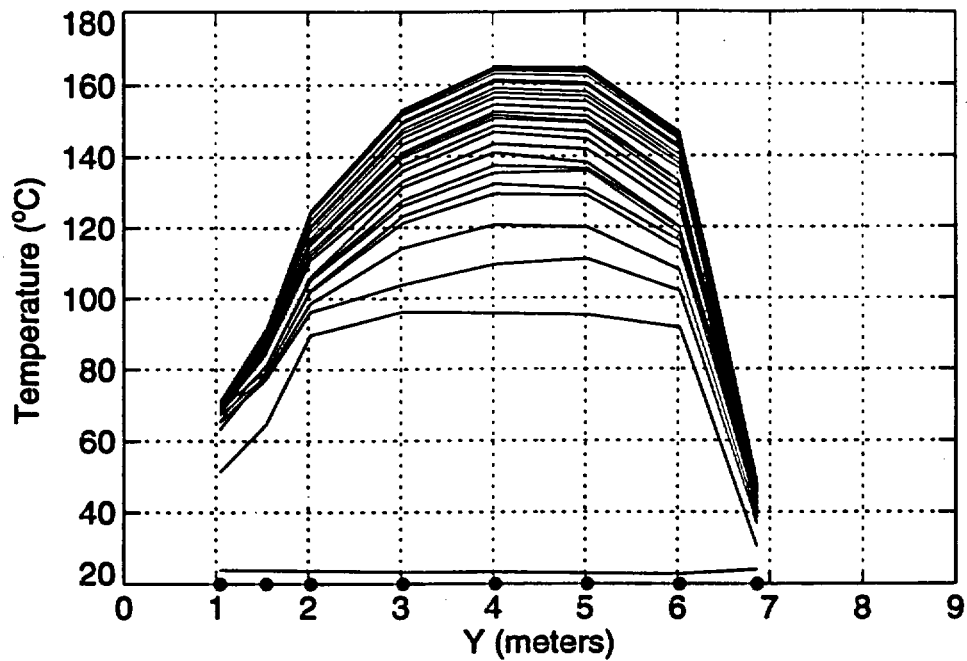


Figure 3-25. Temperature profiles for thermocouple probe TMA-BX-1 ( $x=0.148$  m,  $z=0.306$  m) every 10 days since heater activation.

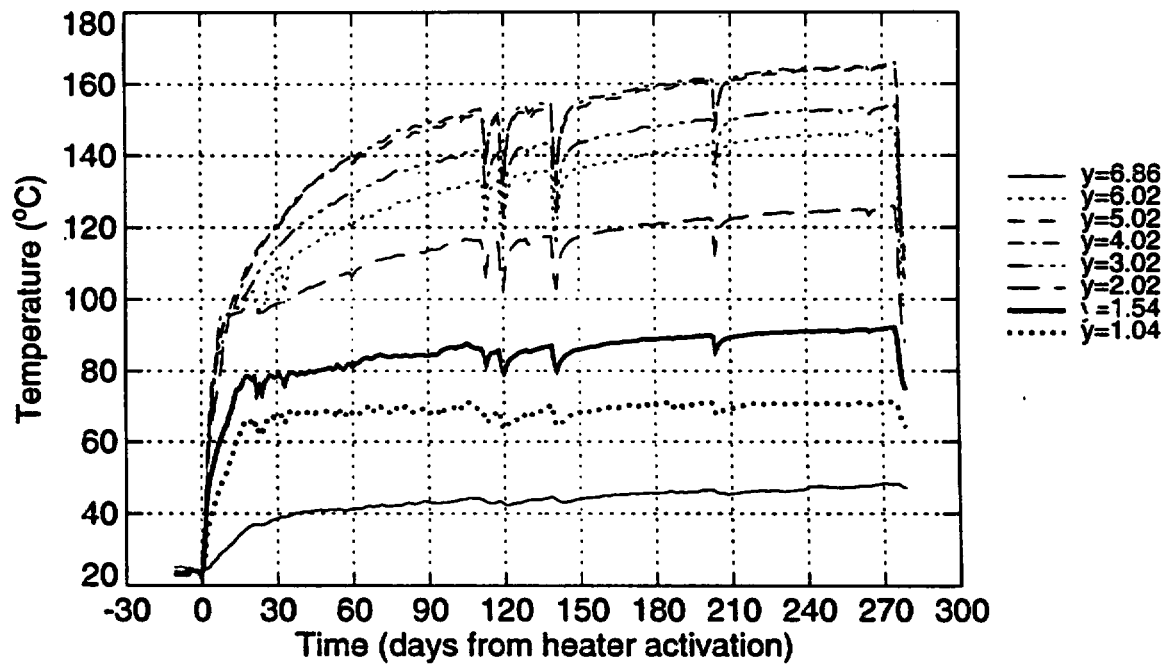


Figure 3-26. Temperature versus time for the temperature gages in probe TMA-BX-1.

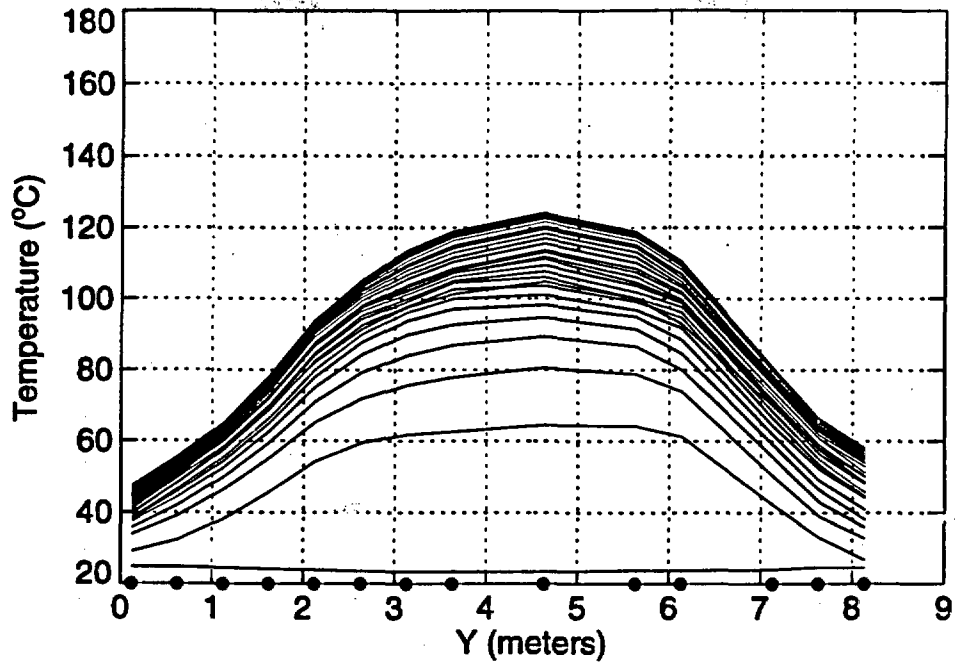


Figure 3-27. Temperature profiles for thermocouple probe TMA-TC-2 ( $x=0.613$  m,  $z=0.263$  m) every 10 days since heater activation.

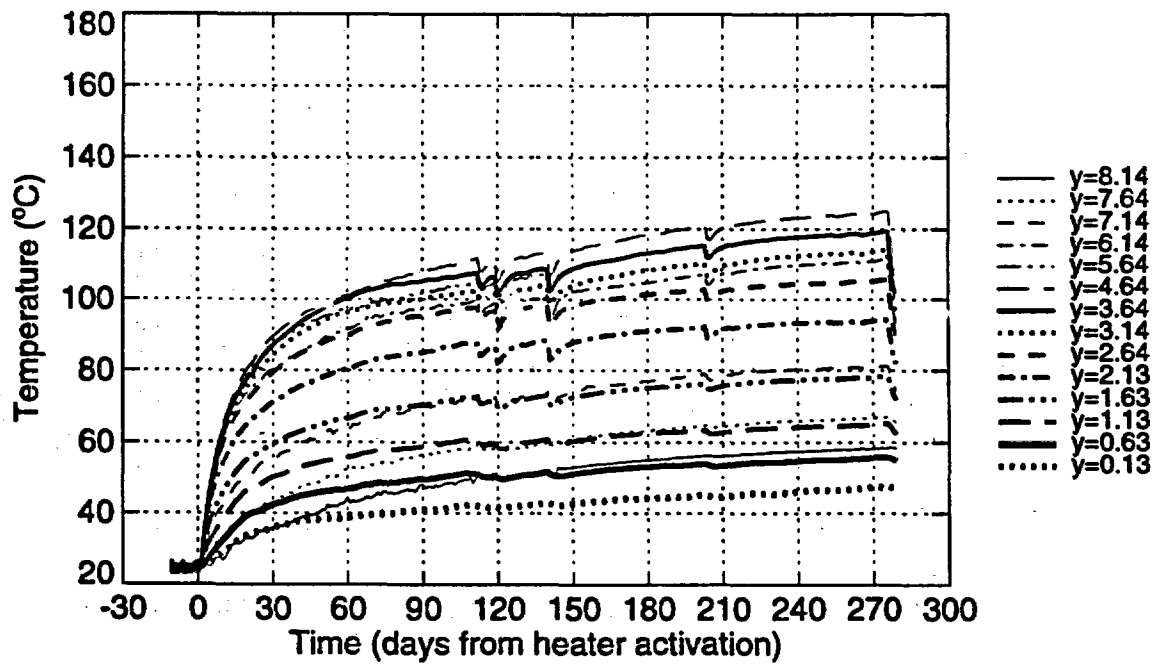


Figure 3-28. Temperature versus time for the temperature gages in probe TMA-TC-2.

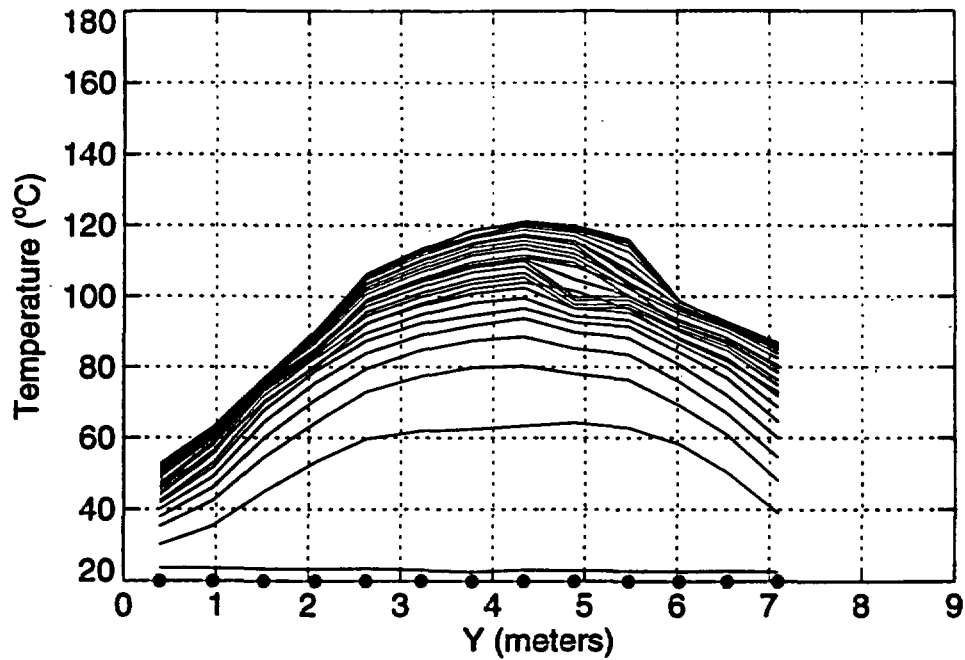


Figure 3-29. Temperature profiles for thermocouple probe TMA-BX-2 ( $x=-0.628$  m,  $z=0.263$  m) every 10 days since heater activation.

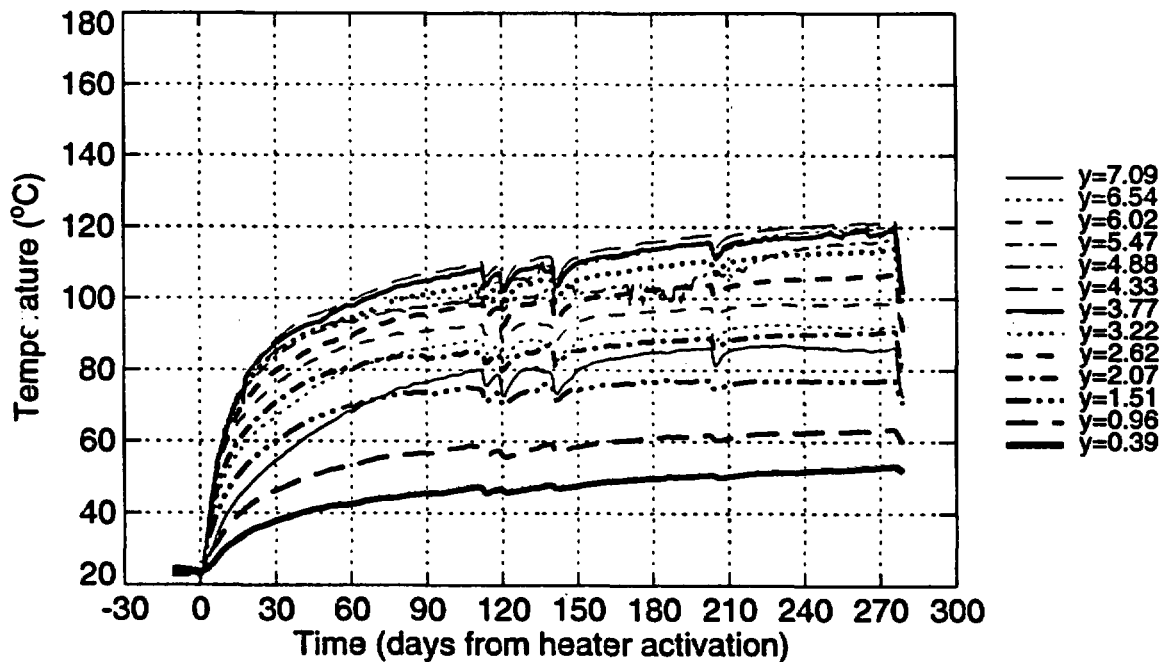


Figure 3-30. Temperature versus time for the temperature gages in probe TMA-BX-2.

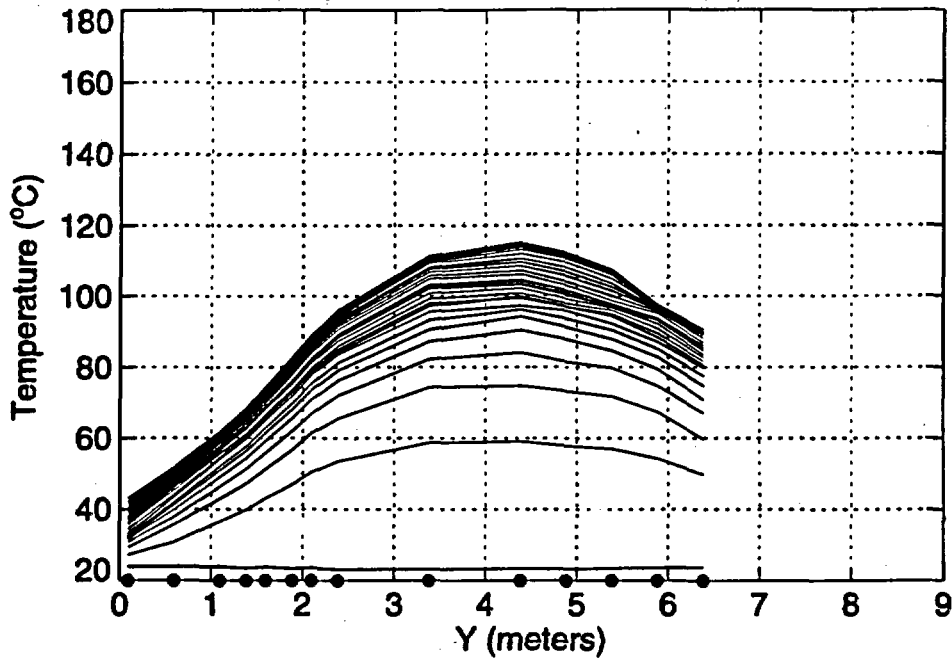


Figure 3-31. Temperature profiles for thermocouple probe TMA-TC-4 ( $x=-0.083$  m,  $z=-0.724$  m) every 10 days since heater activation.

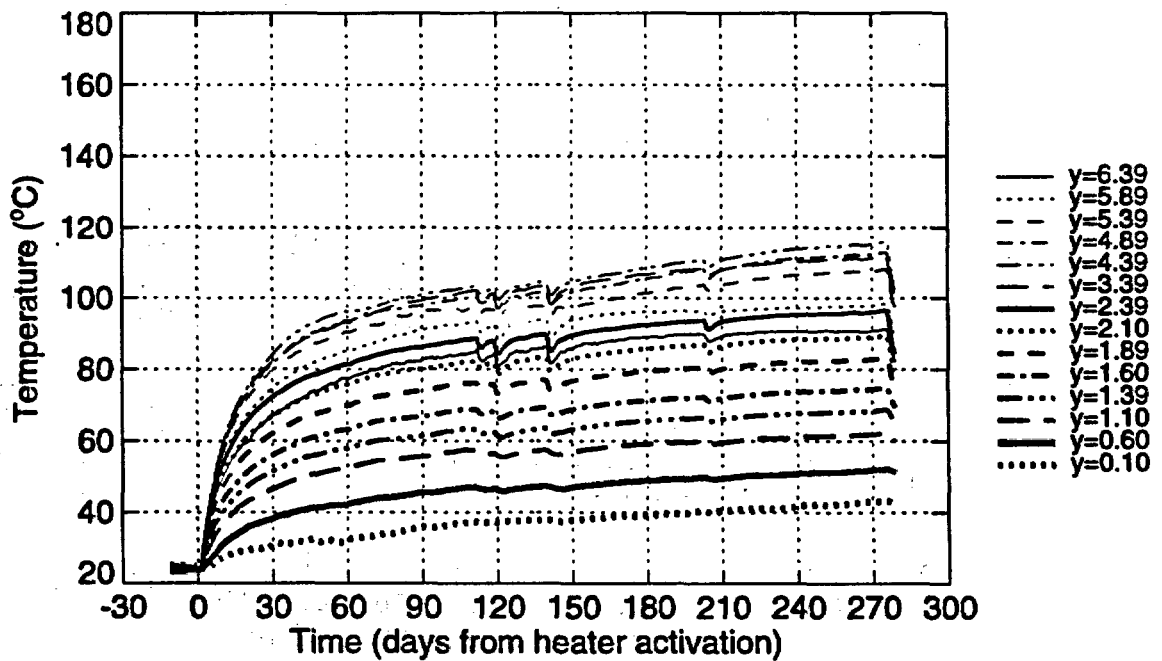


Figure 3-32. Temperature versus time for the temperature gages in probe TMA-TC-4.

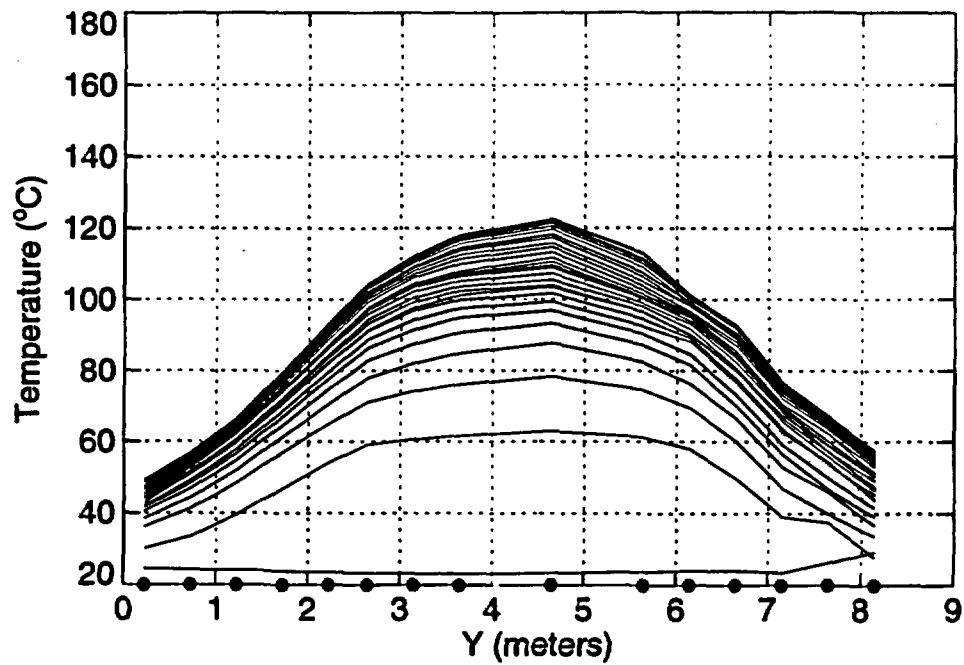


Figure 3-33. Temperature profiles for thermocouple probe TMA-TC-5 ( $x=-0.038$  m,  $z=0.699$  m) every 10 days since heater activation.

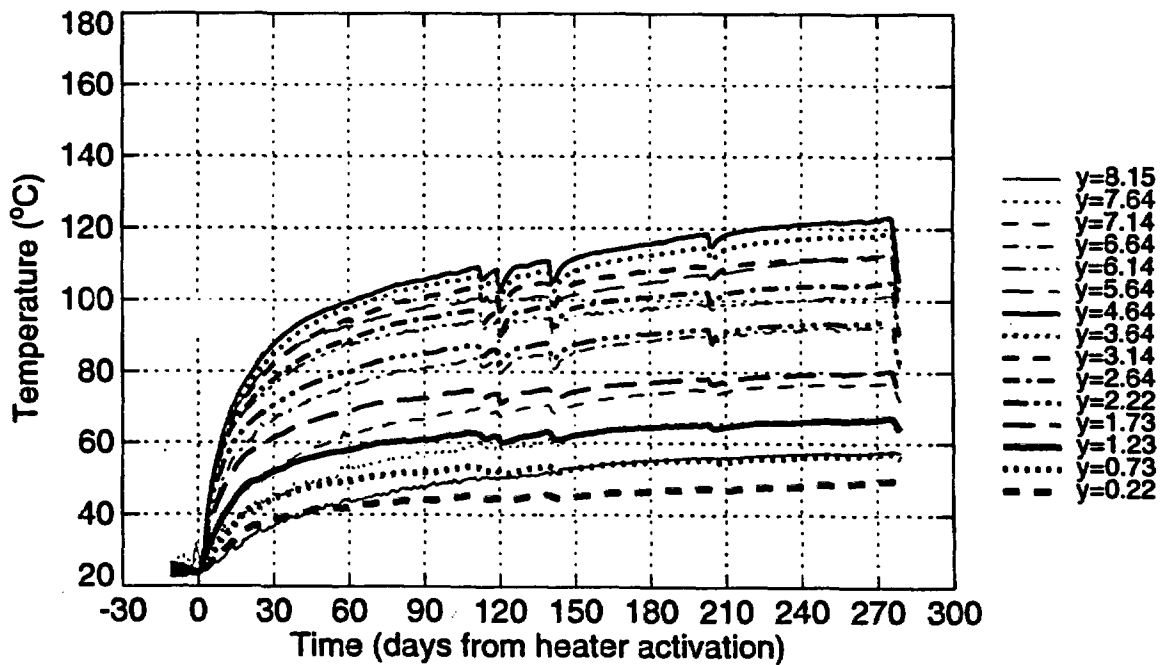


Figure 3-34. Temperature versus time for the temperature gages in probe TMA-TC-5.

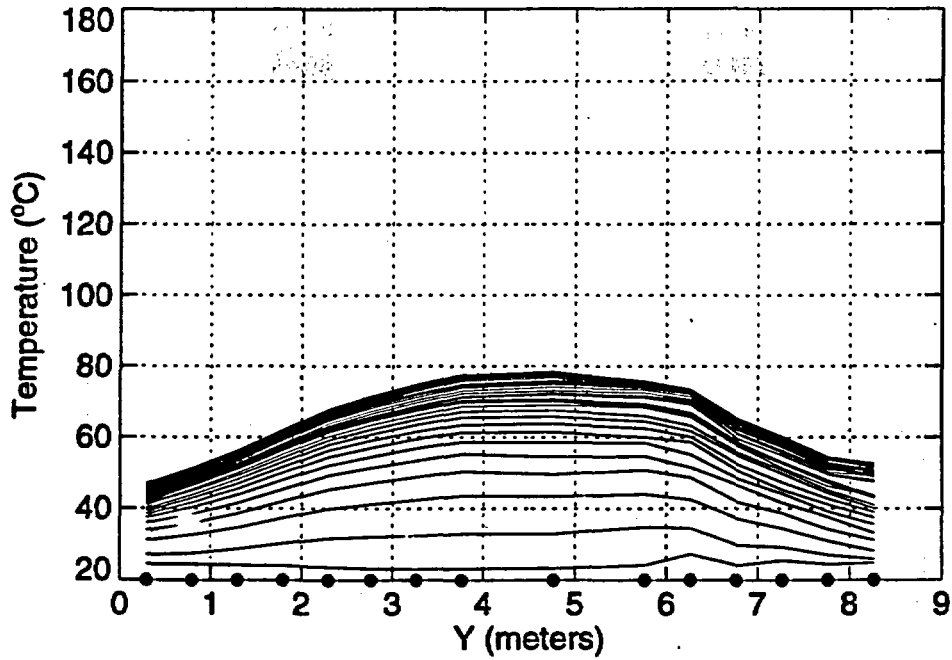


Figure 3-35. Temperature profiles for thermocouple probe TMA-TC-3 ( $x=-0.734$  m,  $z=1.318$  m) every 10 days since heater activation.

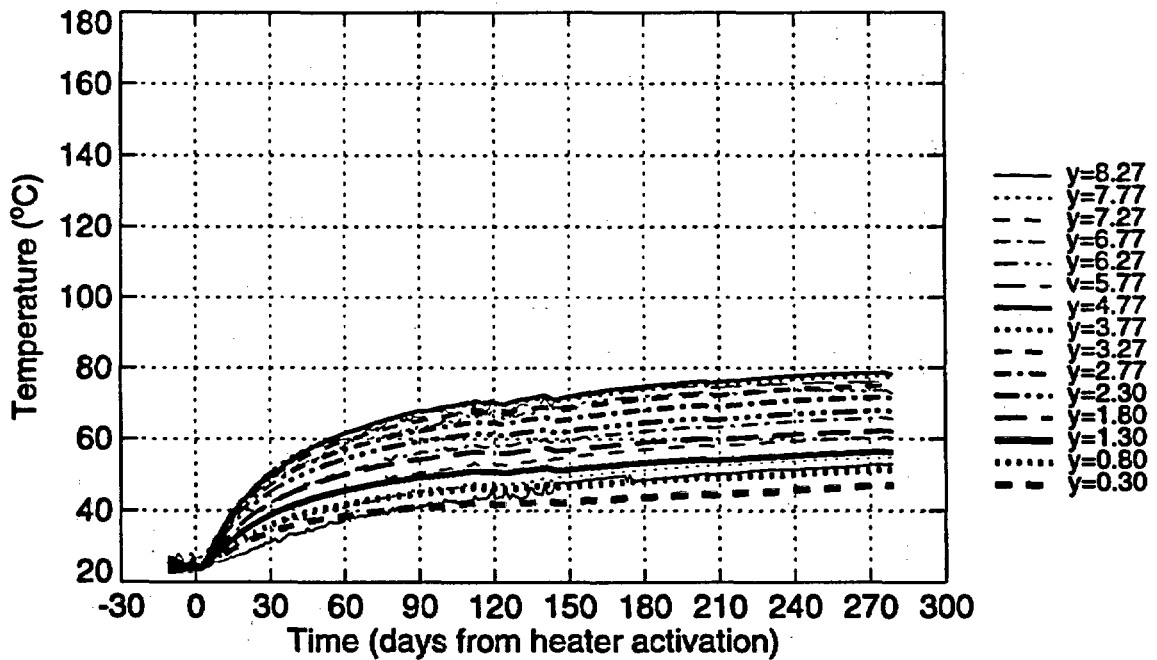


Figure 3-36. Temperature versus time for the temperature gages in probe TMA-TC-3.

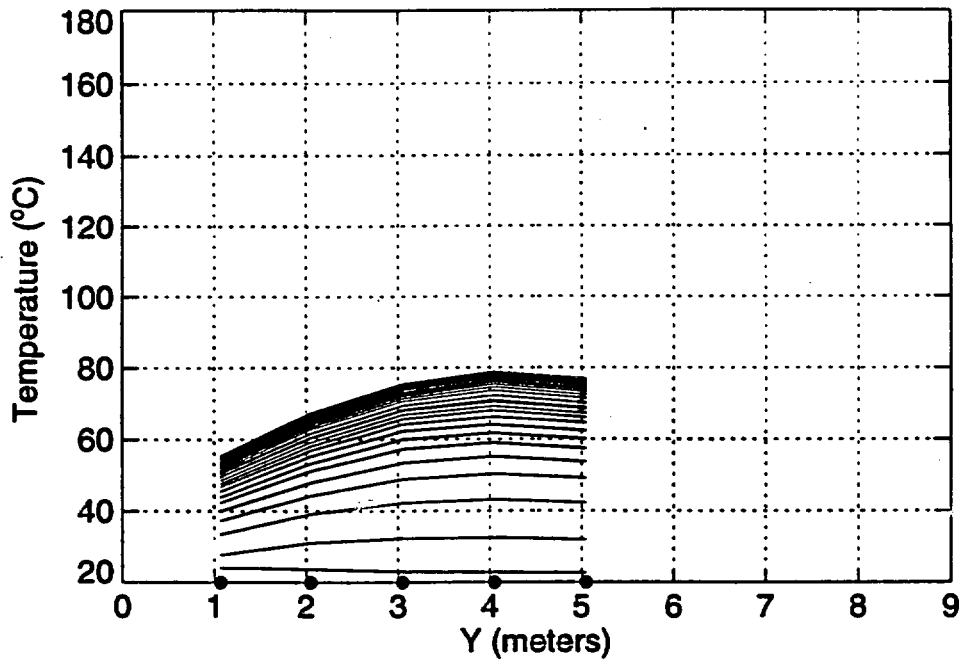


Figure 3-37. Temperature profiles for thermocouple probe TMA-BX-3 ( $x=0.759$  m,  $z=1.295$  m) every 10 days since heater activation.

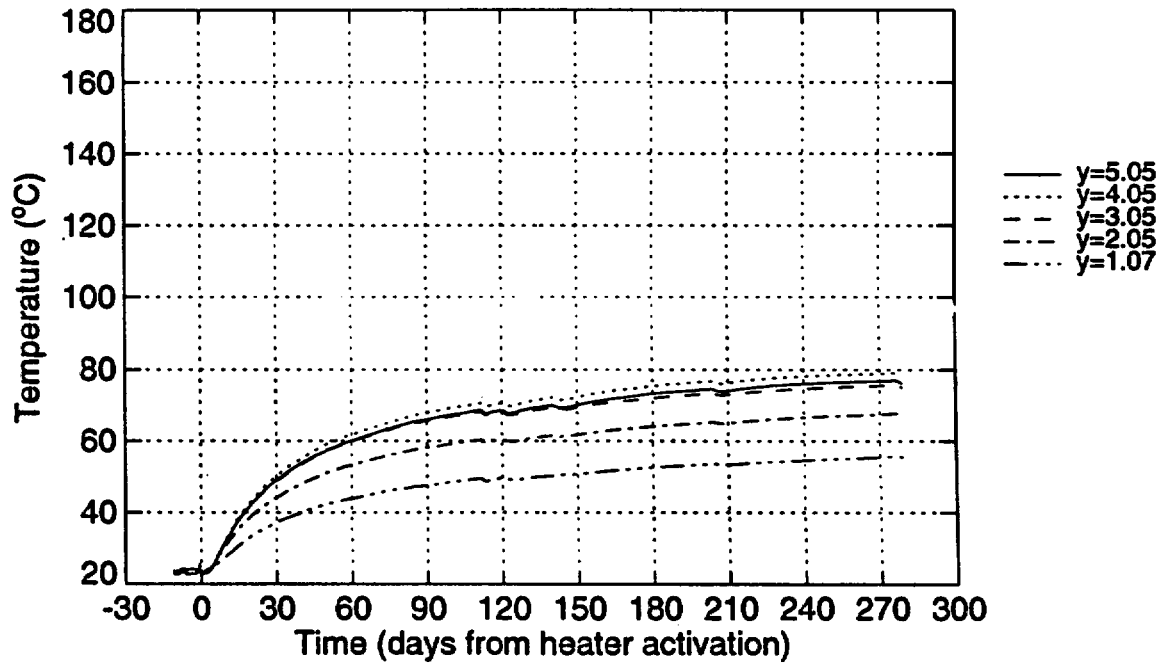


Figure 3-38. Temperature versus time for the temperature gages in probe TMA-BX-3.

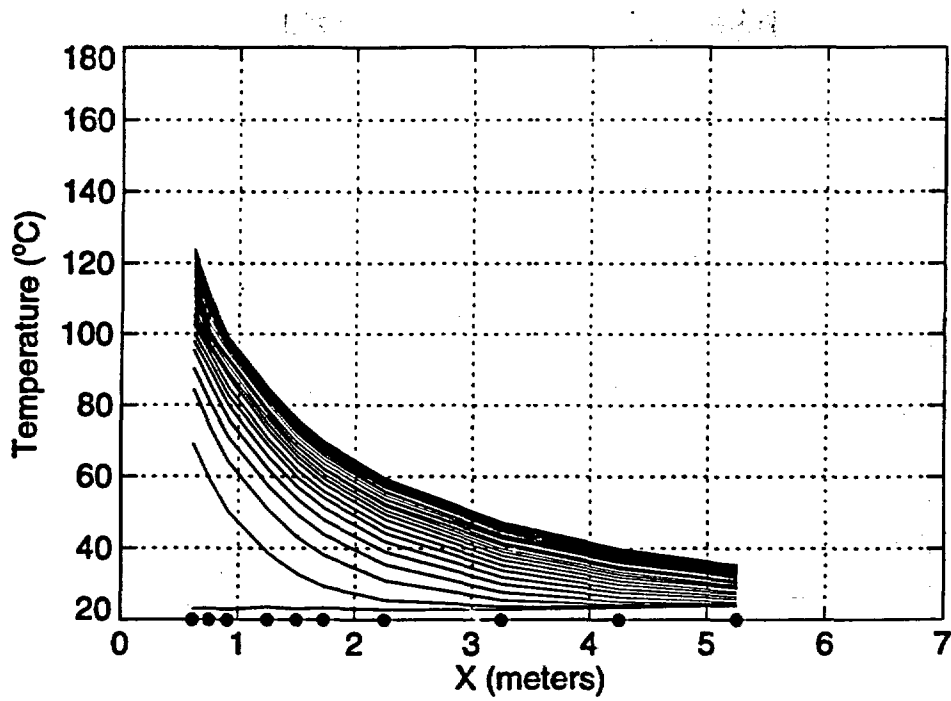


Figure 3-39. Temperature profiles for thermocouple probe TMA-TC-6 ( $y=5.434$  m,  $z=-0.001$  m) every 10 days since heater activation.

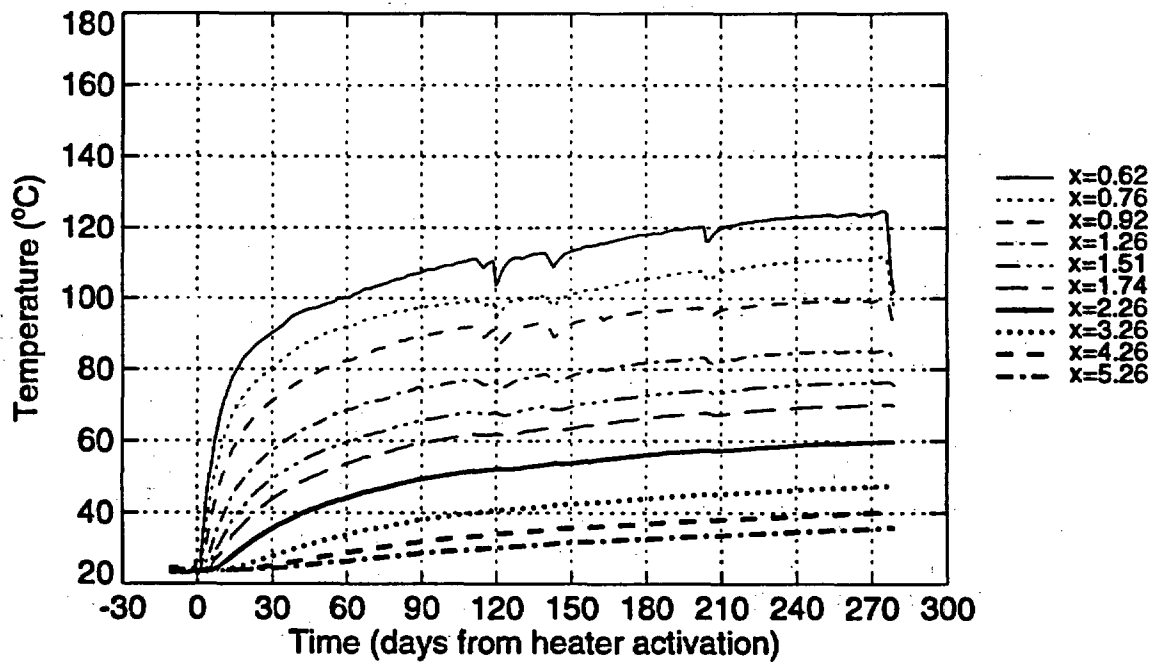


Figure 3-40. Temperature versus time for the temperature gages in probe TMA-TC-6.

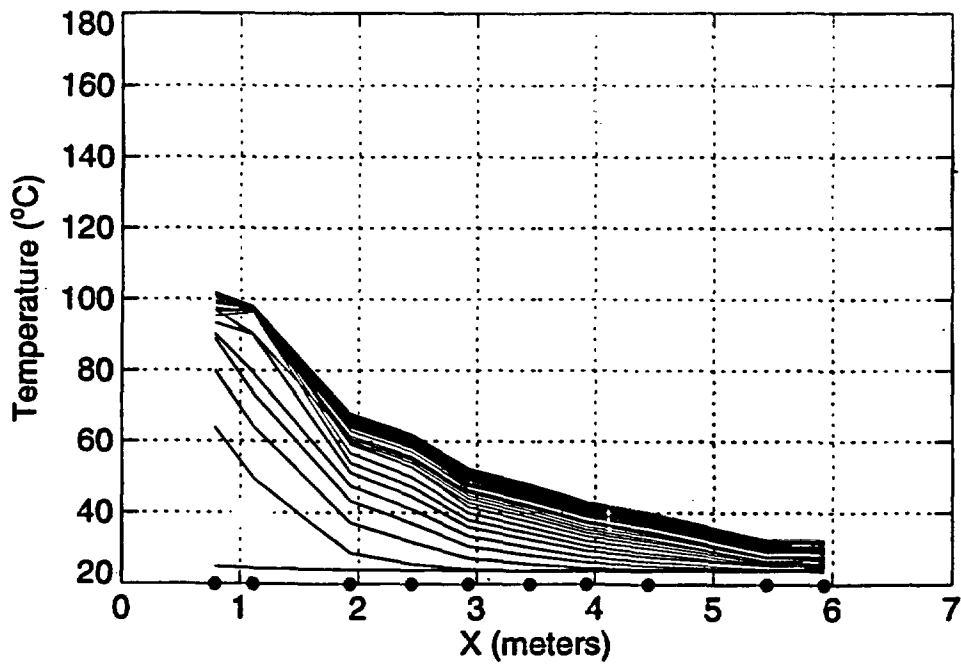


Figure 3-41. Temperature profiles for thermocouple probe TMA-BX-4 ( $y=3.461$  m,  $z=-0.139$  m) every 10 days since heater activation.

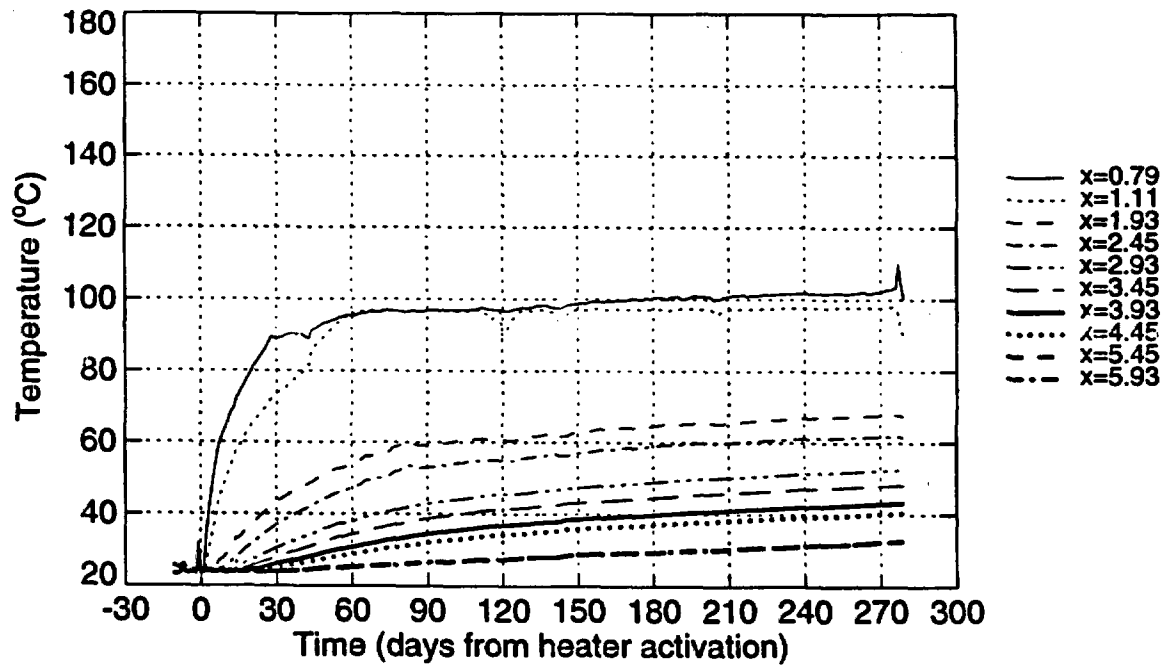


Figure 3-42. Temperature versus time for the temperature gages in probe TMA-BX-4.

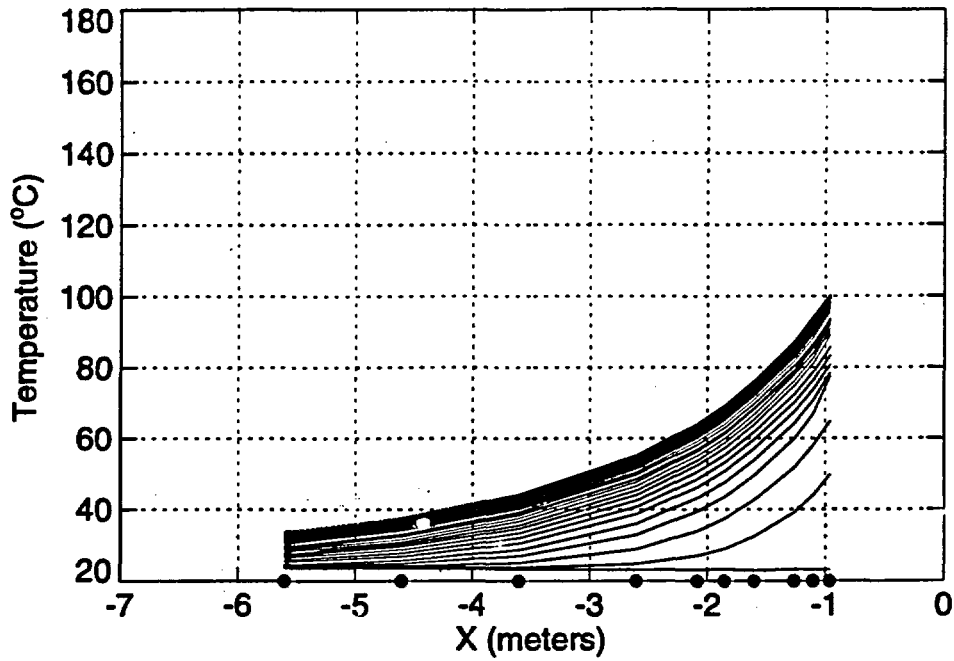


Figure 3-43. Temperature profiles for thermocouple probe TMA-TC-7 ( $y=3.408$  m,  $z=0.011$  m) every 10 days since heater activation.

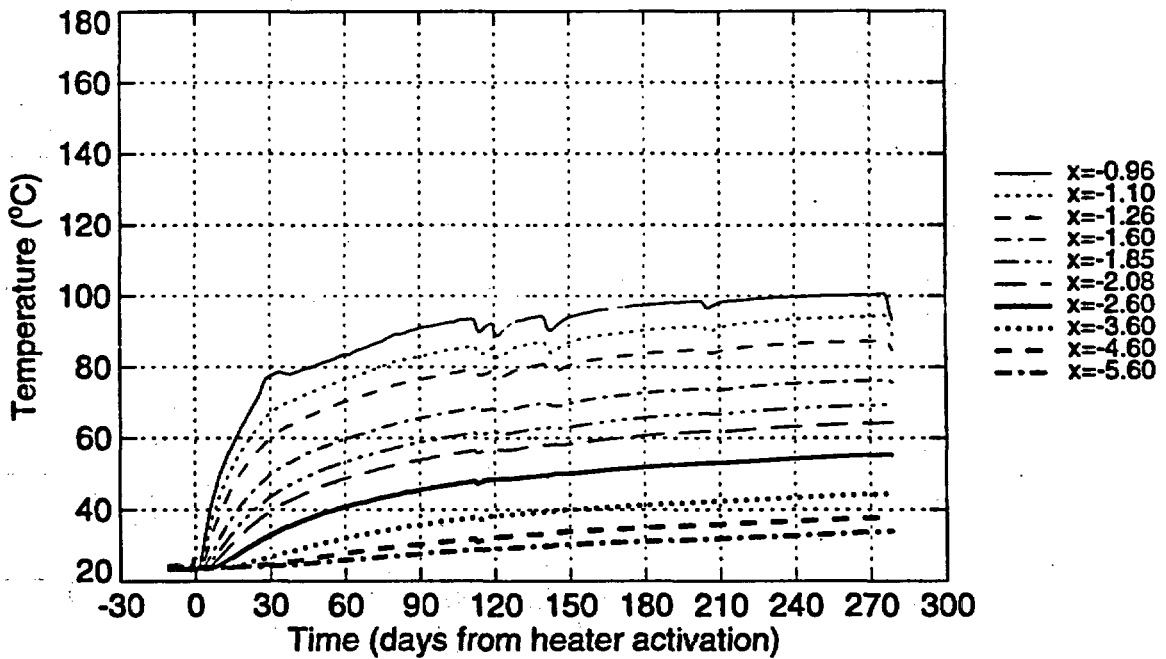


Figure 3-44. Temperature versus time for the temperature gages in probe TMA-TC-7.

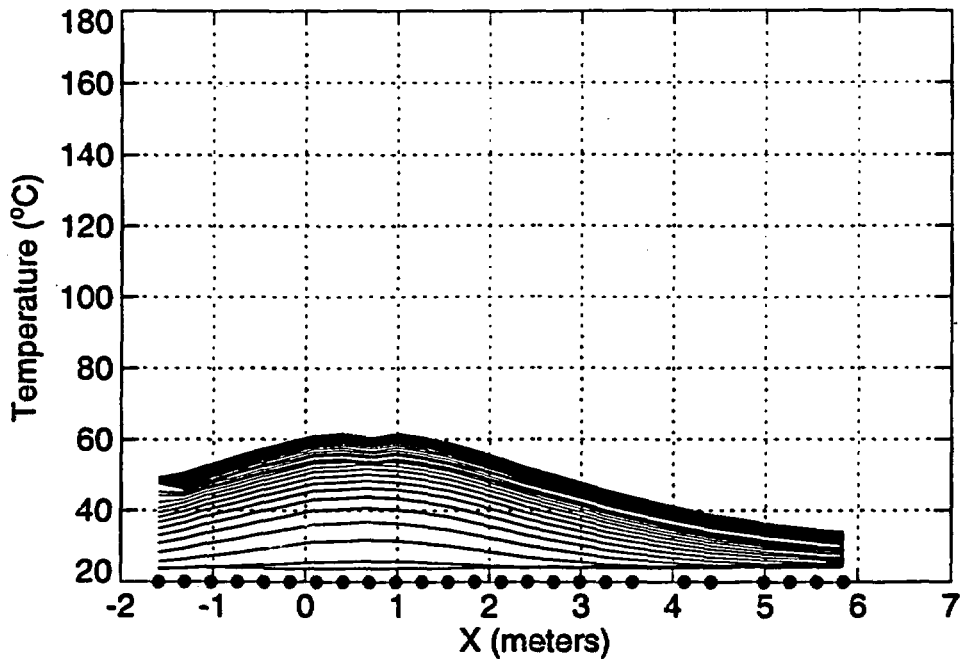


Figure 3-45. Temperature profiles for thermocouple probe TMA-RTD-15 ( $y=4.25$  m) every 10 days since heater activation.

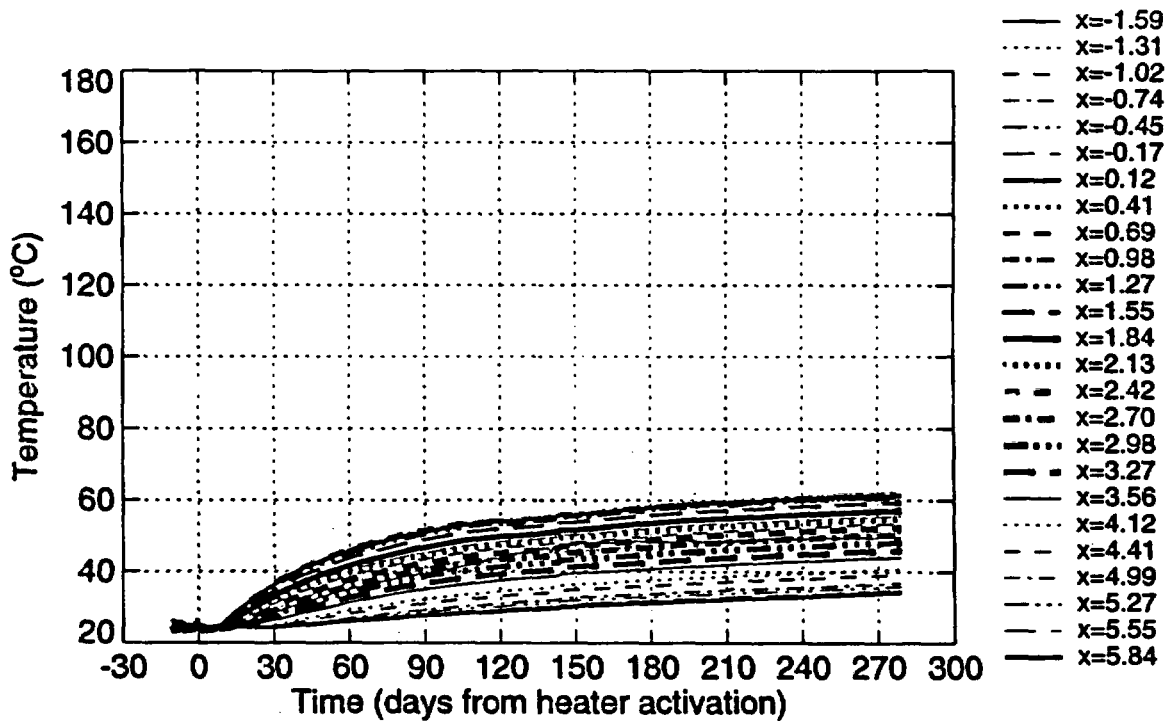


Figure 3-46. Temperature versus time for the temperature gages in probe TMA-RTD-15.

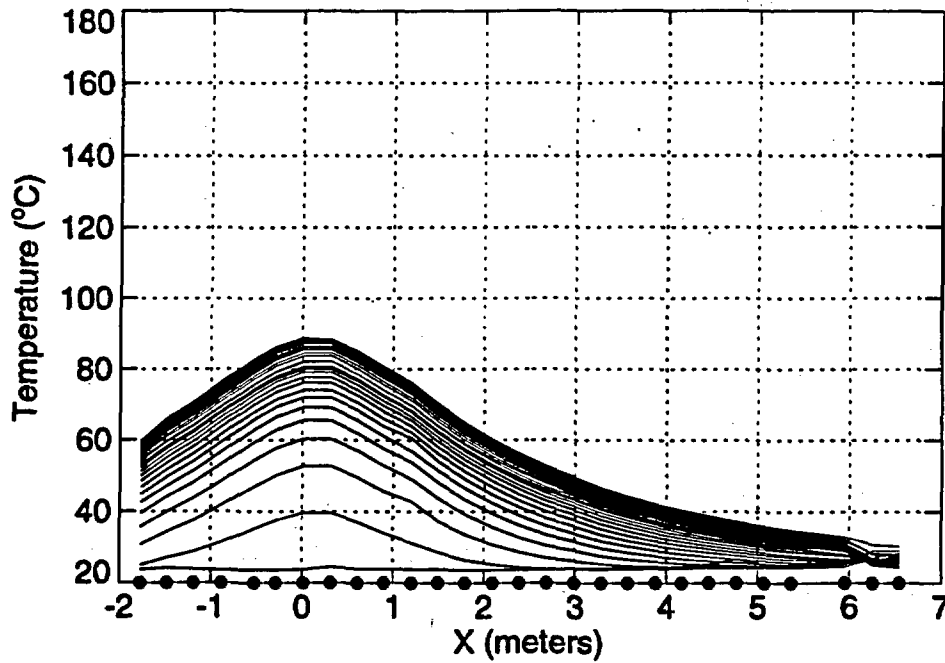


Figure 3-47. Temperature profiles for thermocouple probe TMA-RTD-17 ( $y=4.27$  m) every 10 days since heater activation.

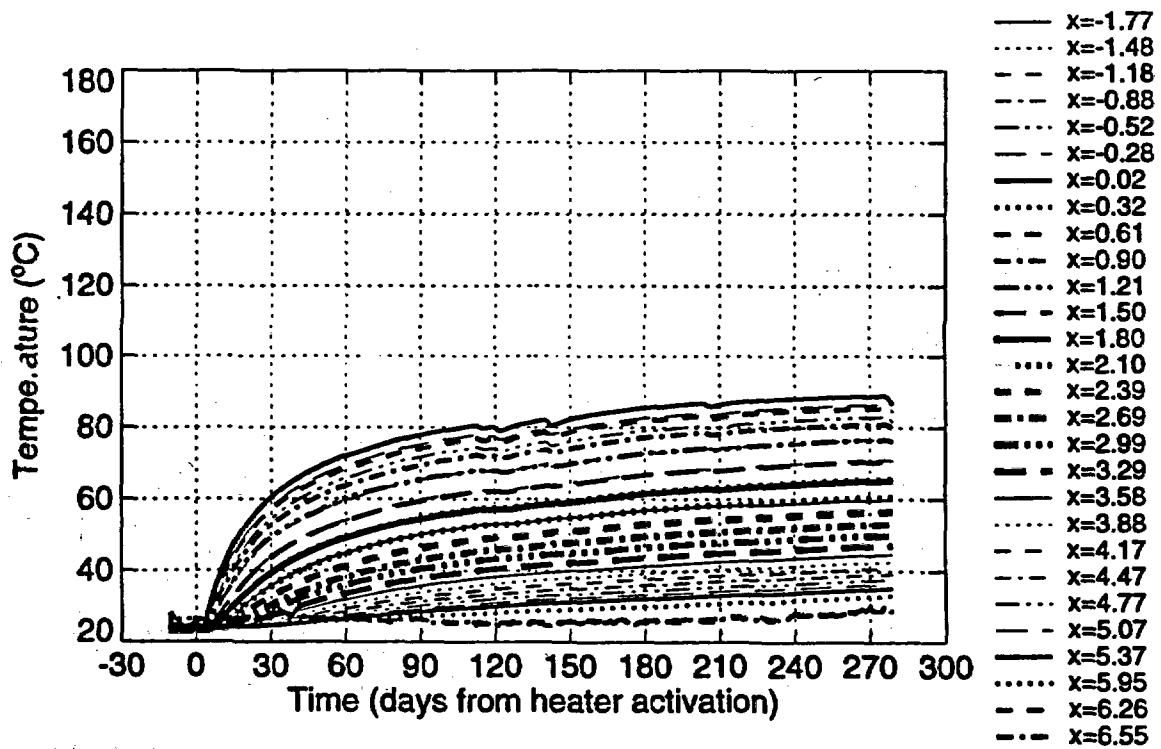


Figure 3-48. Temperature versus time for the temperature gages in probe TMA-RTD-17.

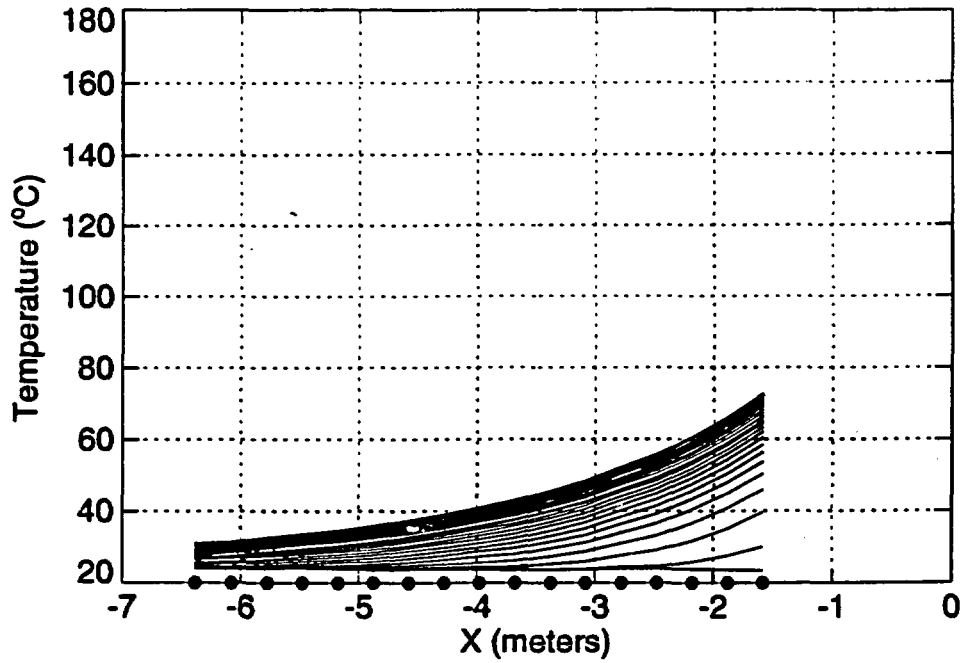


Figure 3-49. Temperature profiles for thermocouple probe TMA-RTD-22 ( $y=4.38$  m,  $z=-0.66$  m) every 10 days since heater activation.

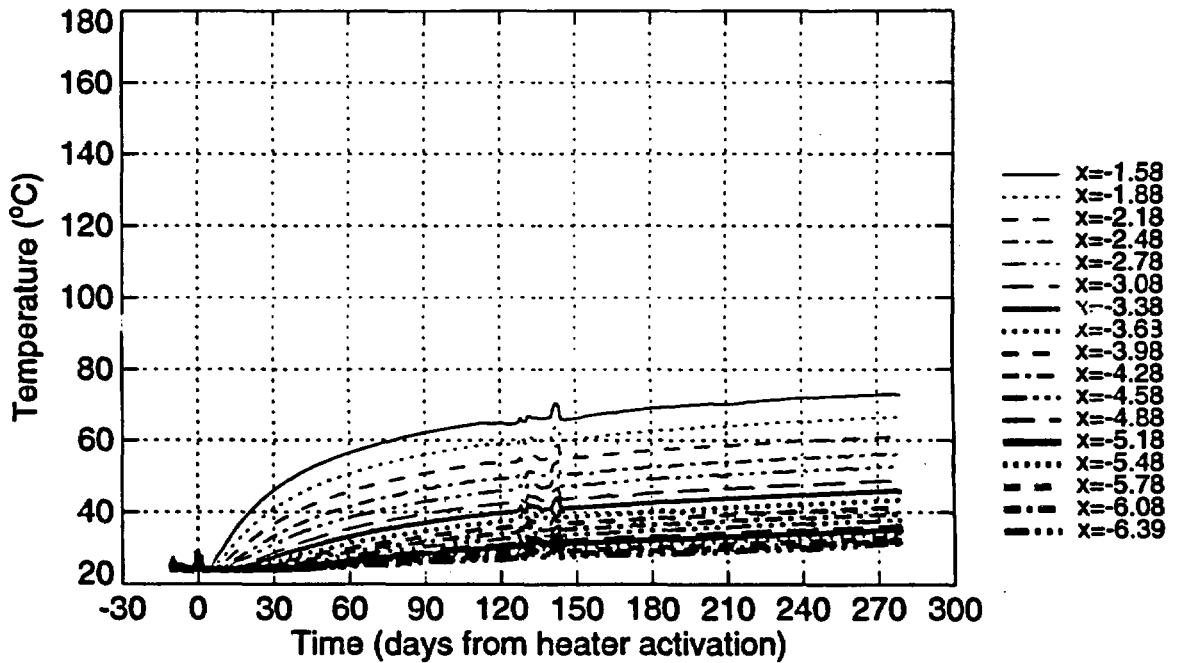


Figure 3-50. Temperature versus time for the temperature gages in probe TMA-RTD-22.

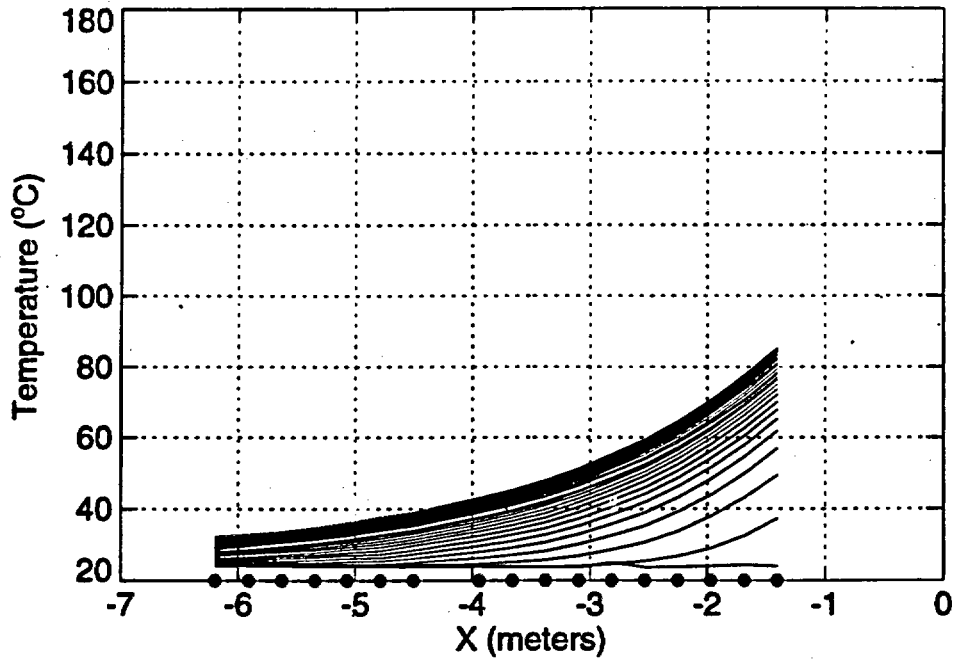


Figure 3-51. Temperature profiles for thermocouple probe TMA-RTD-23 (y=4.39 m) every 10 days since heater activation.

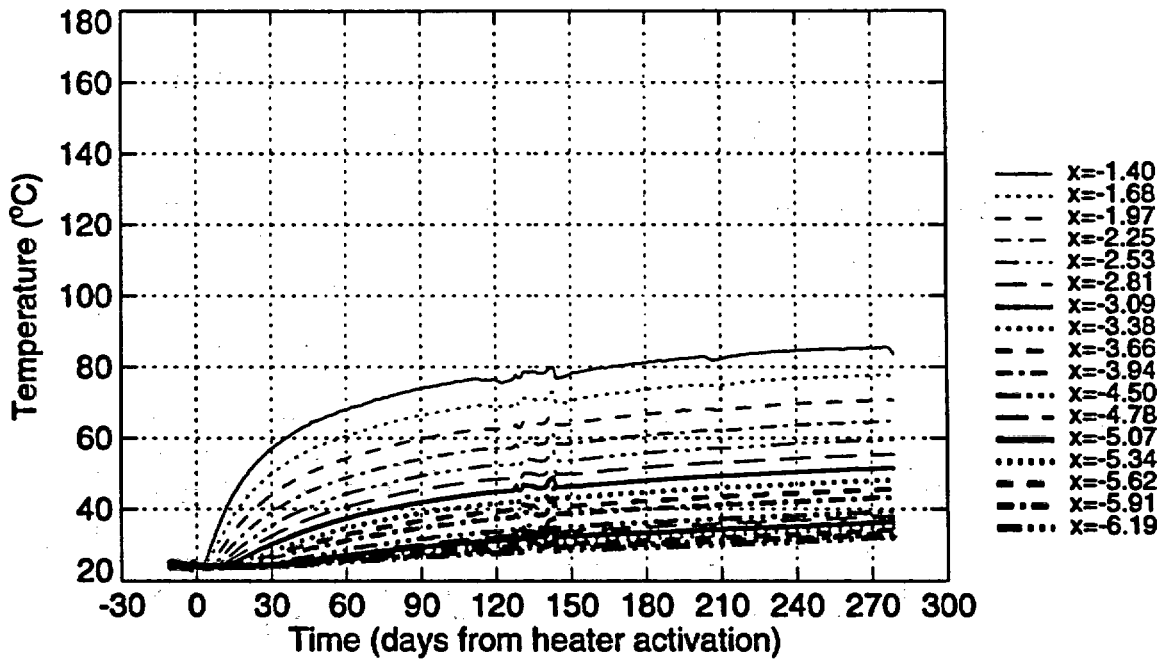


Figure 3-52. Temperature versus time for the temperature gages in probe TMA-RTD-23.

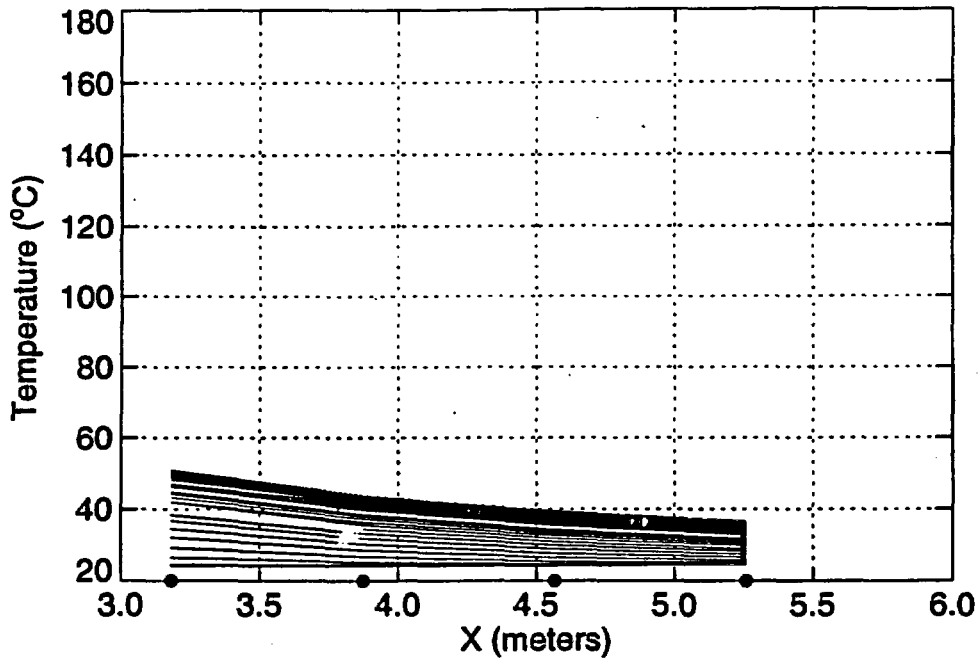


Figure 3-53. Temperature profiles for thermocouple probe TMA-TEMP-16 ( $y=4.275$  m) every 10 days since heater activation.

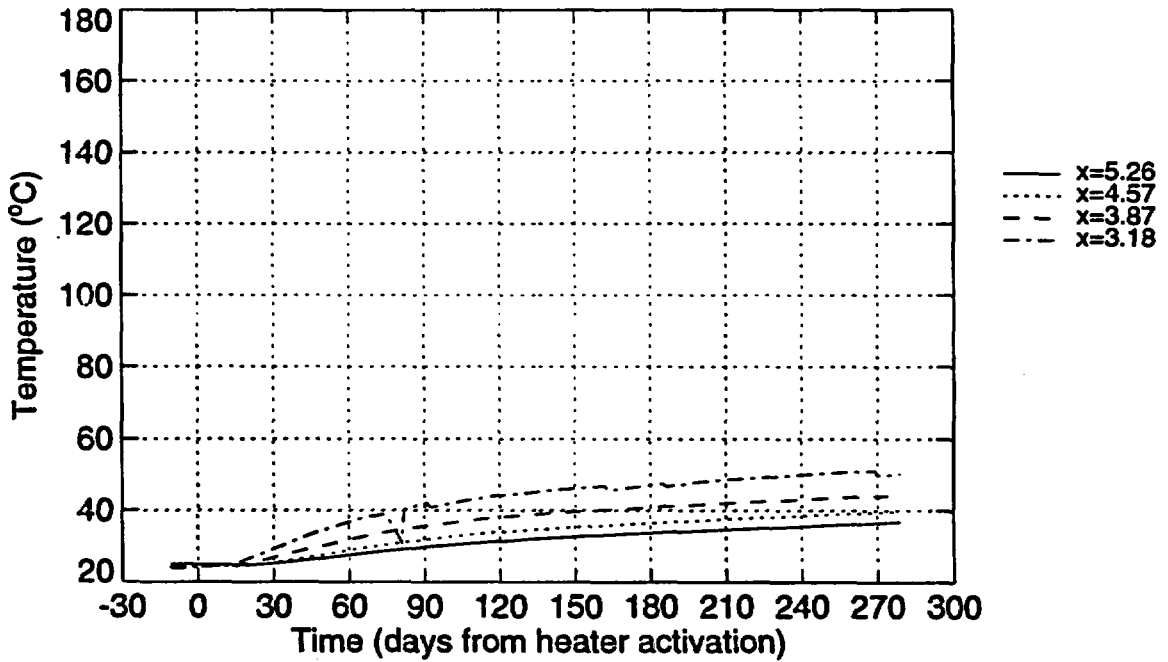


Figure 3-54. Temperature versus time for the temperature gages in probe TMA-TEMP-16.

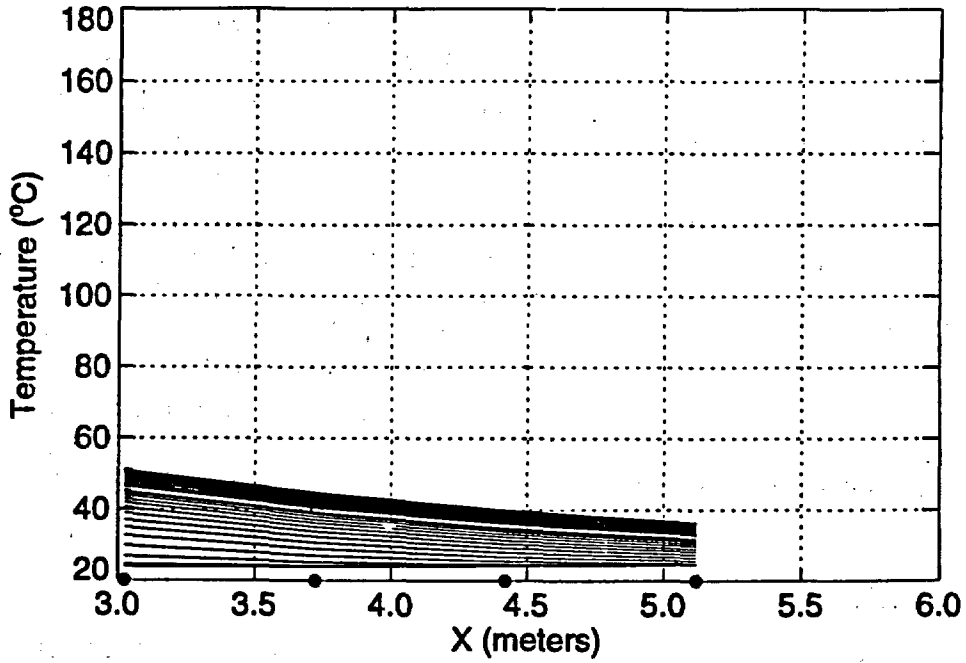


Figure 3-55. Temperature profiles for thermocouple probe TMA-TEMP-18 ( $y=4.25$  m,  $z=-0.22$  m) every 10 days since heater activation.

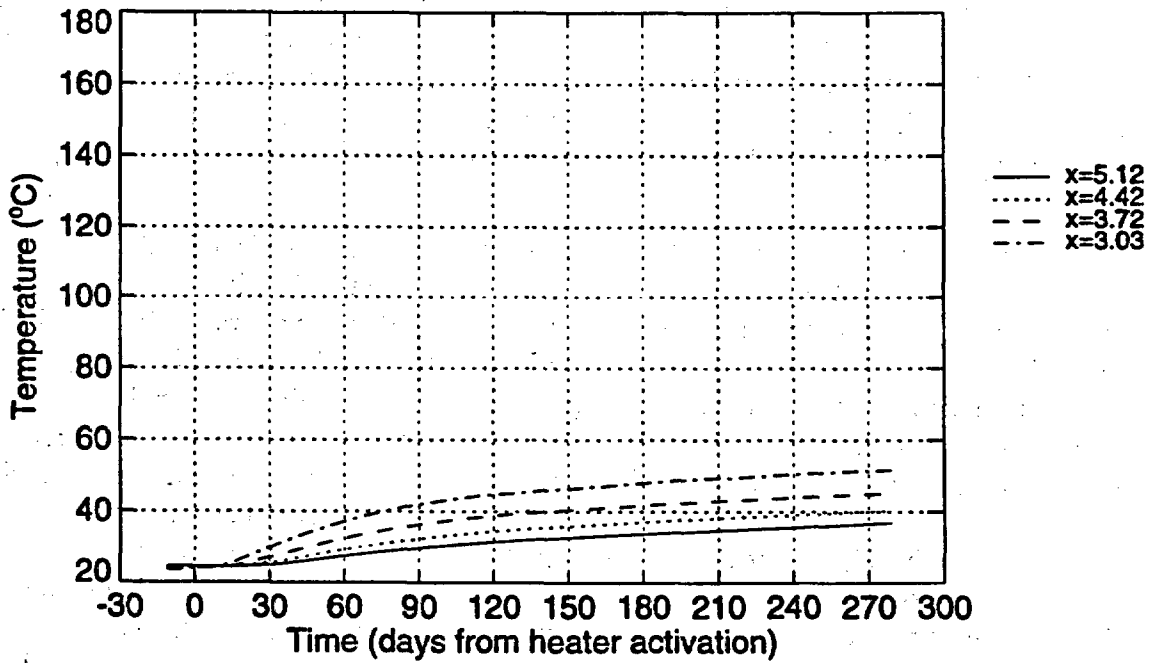


Figure 3-56. Temperature versus time for the temperature gages in probe TMA-TEMP-18.

Figures 3-17 through 3-22 illustrate the temperatures recorded by the three thermocouple probes mounted on the outside of the copper canister in which the heater element is located. They indicate that the temperature of the heater reached 350°C within a day or two of power application to the heater and then increased to around 375°C approximately one week after heater activation. Note that these readings represent the temperatures in the heater borehole and not the temperature of the rock at the surface of the heater borehole. This latter quantity is not accurately determined by these measurements, but the rock temperature is certainly somewhat less than the temperature in the heater borehole. Note that the temperatures recorded in the heater borehole 6 to 6.5 m from the borehole collar are warmer than the rest of the locations in the heater borehole by approximately 50°C. This condition is believed to result from the coincidental juxtaposition of the thermocouples in these locations with one of the centralizers that maintains the heater element in the center of the heater canister, and is not a result of anomalous rock thermal properties. Note also the temperature profiles on the spatial temperature distribution plots, which are at an intermediate temperature of 100 to 170°C. These are the median daily temperature profiles observed on the 140<sup>th</sup> day of heating when the heater power was temporarily interrupted. When the power to the heater was turned off after 275.08 days of heating, the temperatures recorded on the surface of the heater dropped by roughly 100 °C in the first half hour and then dropped to about 100 °C after about 3 days.

Figures 3-23 through 3-26 illustrate the temperatures recorded by probes TMA-TC-1 and TMA-BX-1, which are nominally parallel to the heater and located at radial distances of 42 cm and 34 cm from the heater, respectively. These two probes are located on either side of a presumed plane of symmetry that is vertical and contains the axis of the heater; hence they should respond similarly. The temperature sensors in TMA-TC-1 exhibit relatively smooth temperature increases with time and a spatial temperature distribution that is reasonably symmetric about the position Y=4.5 m, which corresponds to the center of the heater. A minor anomaly exists at Y=2.5 m; its origin is not known as of this writing. There are also significant dips in the temperature data on days 112, 118, 139, and 202 which result from interruptions to the heater power that occurred on those days. The interruptions to heater power were of sufficient duration that the temperature of the rock is probably several degrees centigrade cooler several days after the interruptions than it would have been had the interruptions not occurred.

At early times the response of TMA-BX-1 (Figures 3-25 and 3-26) is quite different from that of TMA-TC-1. The most significant differences occur during the time interval from about day 9 to day 18, during which time the temperatures in the borehole were warming through the boiling point of water (at atmospheric pressure). During this time, and particularly on day 10, the spatial temperature distribution between Y=2 m and Y=6 m was virtually isothermal at about 96°C. It is likely that this results because TMA-BX-1 is installed in an open borehole. As the temperatures in the surrounding rock passed through the boiling point, vapor phase heat transport within the borehole created the observed isothermal conditions, which may not accurately reflect the temperature in the adjacent rock in detail. TMA-TC-1 did not respond in this way because the temperature sensors are grouted in the borehole and there is no open borehole in which vapor phase transport could occur. After the readily accessible water in the rock adjacent to borehole TMA-BX-1 had evaporated, the convective heat transfer in the borehole was reduced in importance and the temperature response returned to a conduction-dominated regime.

Another noteworthy feature about TMA-BX-1 is that the spatial temperature distribution is significantly asymmetric about the center of the heater (Figures 3-57 and 3-58 illustrate the asymmetry for probes oriented parallel to the heater on day 275). Most dramatic for TMA-BX-1 is the gage at  $Y=6.9$  m (2.4 m from the center of the heater), which had only warmed to about  $48^{\circ}\text{C}$  by day 275, whereas the sensor at the other end of the heater ( $Y=2.0$  m; 2.5 m from the center of the heater) had warmed to  $126^{\circ}\text{C}$ . The temperature sensors closer to the center of the heater are asymmetric as well. The two sensors at  $Y=3$  m and 6 m, which are also symmetrically positioned with respect to the center of the heater, differ in temperature by about  $7^{\circ}\text{C}$ .

A third notable feature in TMA-BX-1 is a brief reduction in temperature recorded by the sensors at  $Y=6.0$ , 1.5, 1.0, and 0.6 m during the time intervals from 20 to 24 days and from 31 to 32 days. The fact that these anomalies were observed by several sensors within the borehole makes it unlikely that they result from unreliable sensors. The cause of these anomalies is unknown but likely reflects complex vapor phase heat transport phenomena within the open borehole. Also, no major power fluctuations occurred during that time period. The dips in temperature recorded on days 112, 118, 139, and 202 resulted from heater power outages.

Finally, the warmest temperatures recorded in TMA-TC-1 and TMA-BX-1-TC are about  $160^{\circ}\text{C}$  and  $166^{\circ}\text{C}$  respectively. The fact that TMA-BX-1-TC is somewhat warmer than TMA-TC-1 likely reflects the fact that it is approximately 8 cm closer to the heater than is TMA-TC-1, and the temperature gradient this close to the heater is substantial.

Figures 3-27 through 3-30 illustrate the temperatures recorded by probes TMA-TC-2 and TMA-BX-2-TC, which are located 67 cm and 68 cm from the heater, respectively. By day 275, the central portions of both probes had warmed through the boiling point and reached maximum temperatures of  $125^{\circ}\text{C}$  and  $122^{\circ}\text{C}$ . TMA-TC-2 is grouted into its borehole, while TMA-BX-2-TC is installed in an open hole and is therefore subject to convection effects as it warms through the boiling point. These effects are not as severe as in TMA-BX-1-TC because TMA-BX-2-TC is located twice the distance from the heater as TMA-BX-1-TC, but they are evident nonetheless. The temperature sensor at  $Y=4.9$  m warmed smoothly up to the boiling point but then remained at a temperature near the boiling point for several weeks. As soon as all the liquid water had boiled away from that vicinity, the temperature started to increase again and by day 275 the spatial temperature profile indicates that the anomalously low temperatures observed earlier near  $Y=4.9$  m had disappeared. The dips in temperature on days 112, 118, 139, and 202 result from heater power outages on those days.

TMA-TC-4 and TMA-TC-5 (Figures 3-31 through 3-34) are an important pair of probes because they are located directly below and above the heater, respectively. If convective heat transport through the rock mass is important, TMA-TC-4 should be slightly cooler than TMA-TC-5 because heat from the heater would be carried convectively upward by buoyancy effects. As of day 275, these probes had reached maximum temperatures of  $116^{\circ}\text{C}$  and  $123^{\circ}\text{C}$ , respectively. Note that near  $Y=4.5$  m, TMA-TC-5 was about  $7^{\circ}\text{C}$  warmer than TMA-TC-4 on day 275. It is also located about 3 cm closer to the heater than is TMA-TC-4, so it is not clear that this difference in temperature is an indication of convective heat transfer. Given that the radial temperature gradient at the radial distances of these holes is substantial, the observed difference in temperature can be explained by conduction effects alone.

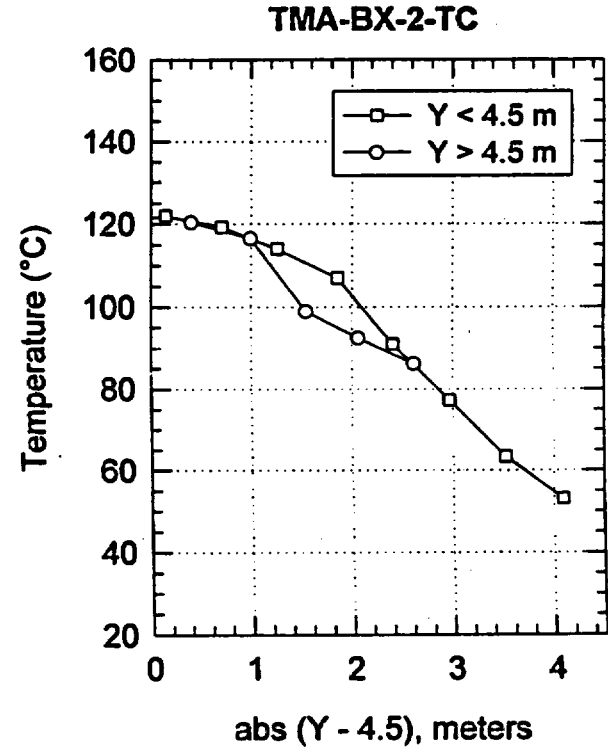
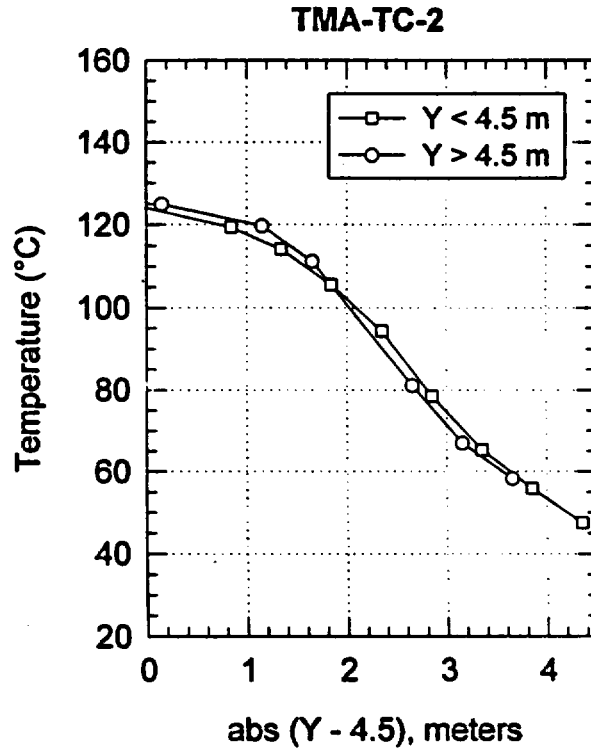
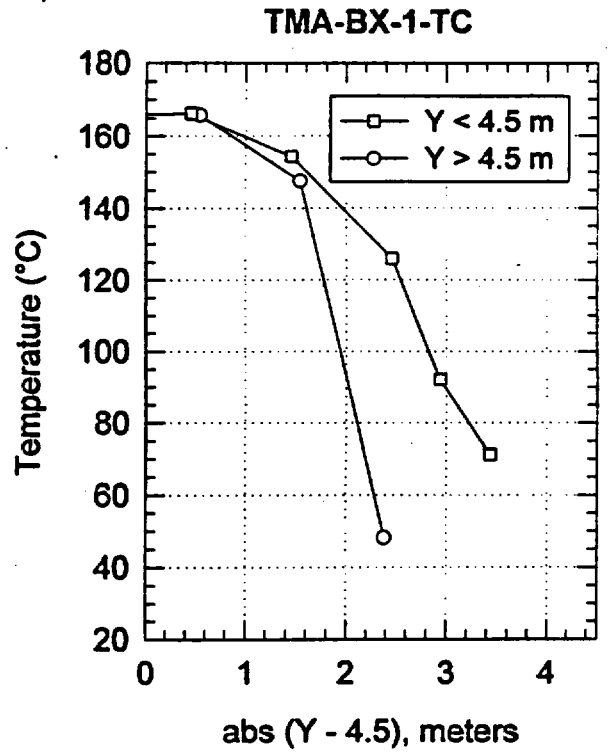
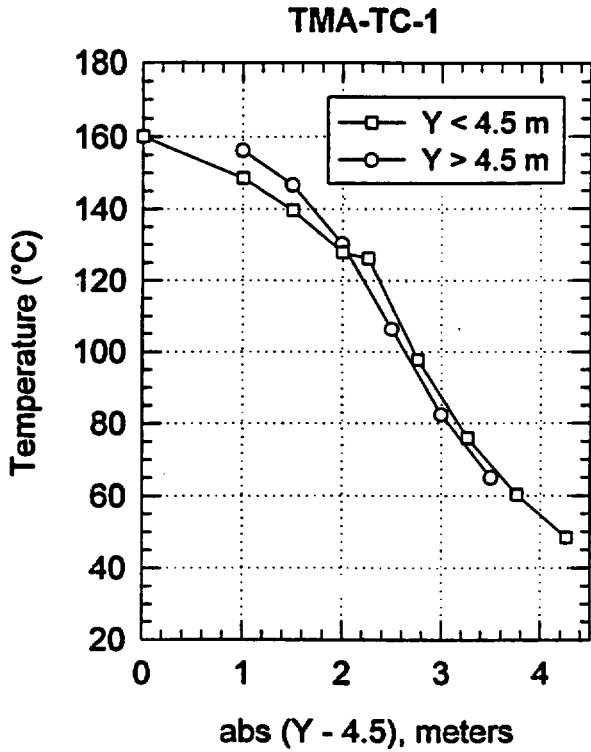


Figure 3-57. Temperature plotted as a function of distance from the center point of the heater.

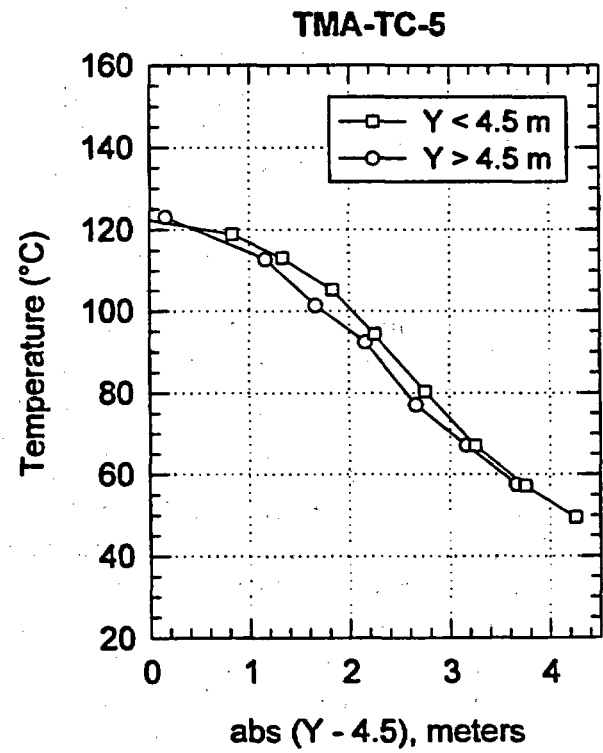
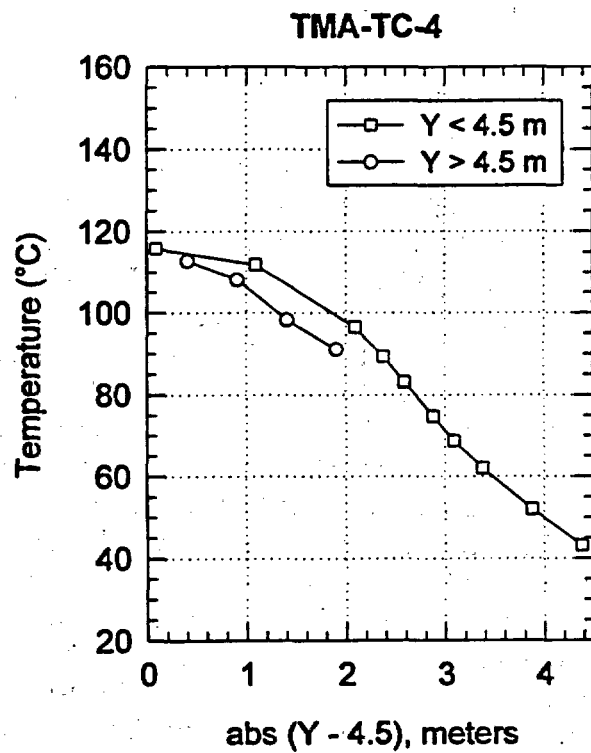
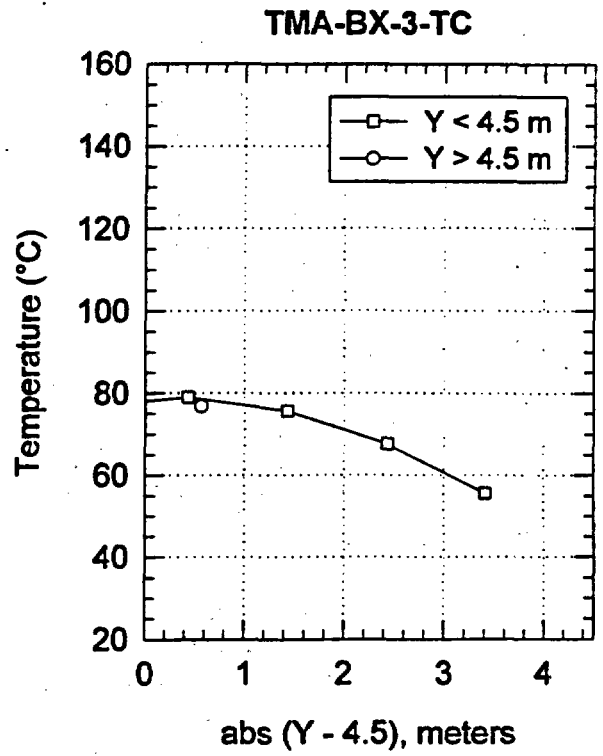
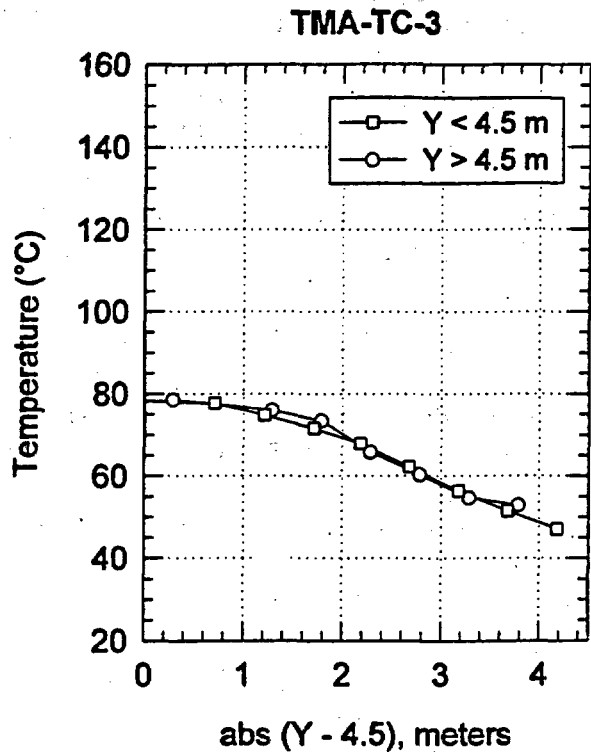


Figure 3-58. Temperature plotted as a function of distance from the center point of the heater.

Probes TMA-TC-3 and TMA-BX-3-TC (Figures 3-35 through 3-38) are located approximately 1.48 m from the heater and hence had only warmed to a maximum of about 79°C by day 275. Some anomalous behavior is evident in TMA-TC-3 in the distal parts of the block. At 5.8 and 6.3 m into the block, the temperatures seem a bit warmer than the trends of other gages would lead one to expect. Because TMA-BX-3-TC, which is an open hole similar to TMA-BX-1-TC and TMA-BX-2-TC, never reached the boiling point, it never exhibited any of the temperature signatures associated with intra-borehole vapor phase heat transport. Four of the thermocouples in TMA-BX-3-TC have failed or have ceased to provide data during the course of the SHT, more than any other borehole. The reasons for this are not clear.

Probes TMA-TC-6 and TMA-BX-4-TC (Figures 3-39 through 3-42) are both oriented parallel to the X direction and hence are perpendicular to the axis of the heater. TMA-TC-6 is located approximately 1 m past the midpoint of the heater in the Y-direction, while TMA-BX-4-TC is located 1 m on the near side of the midpoint of the heater. The data from TMA-TC-6 are very smooth, both in their spatial and temporal distributions. Note in particular that near the boiling point neither the temporal nor the spatial temperature profiles show any evidence of inflections or other anomalies that would indicate significant vapor phase convection. Note also that the temperature drops associated with the heater power outage were observed in the data out to a radial distance from the heater of about 2 m. TMA-BX-4-TC exhibits more erratic behavior because it is deployed in an open borehole. Because the end of the borehole closest to the heater exceeded the boiling point, intra-borehole vapor phase heat transport was significant and was the likely cause of the erratic behavior apparent in the temperature plots. Probe TMA-TC-7 (Figures 3-43 and 3-44) is also parallel to the X-direction but approaches the heater from the opposite side (from the negative X direction). This probe, like all the other TC-series probes, is grouted into its borehole and hence was not subject to the effects of intra-borehole convective heat transport, which accounts for the relatively smooth spatial and temporal temperature distributions obtained from this probe.

Temperature data from TMA-RTD-15 are illustrated in Figures 3-45 and 3-46. As indicated in Figure 3-2, this borehole is parallel to the X direction. It starts from the Thermomechanical Alcove Extension and angles upward, over and beyond the heater. Several notable temperature anomalies are evident in this borehole. In Figure 3-59, data from TMA-RTD-15-1 are compared to data collected from its nearest neighbor, gage TMA-RTD-15-2, about 30 cm away. Up until about day 90, the data from these two gages tracked each other nicely, but after day 90 the temperature of TMA-RTD-15-1 started to increase more rapidly than the temperature of TMA-RTD-15-2. On day 120 the temperature of TMA-RTD-15-1 actually exceeded that of TMA-RTD-15-2, even though TMA-RTD-15-2 is approximately 13 cm closer to the heater. Since day 120 the temperature of TMA-RTD-15-1 has slowly varied relative to the temperature of TMA-RTD-15-2 in an unexpected manner. Also several sudden, brief temperature reductions occur on days when the heater power was interrupted. There are at least two plausible explanations for these observations. The first is that TMA-RTD-15-1 is experiencing some sort of electrical malfunction that renders its behavior erratic and imposes on it an electrical signal that is influenced by the electric power being supplied to the heater. If this were the case, the gage would likely have failed in some more obvious fashion. Another plausible explanation is that a rock fracture exists near the location of gage TMA-RTD-15-1 and that relatively warm fluid is being transported from near the heater into the vicinity of gage TMA-RTD-15-1. The abrupt reductions in temperature observed when the heater power was temporarily interrupted would be consistent with this scenario since during these times the flow of warm fluid in the fracture would also be interrupted.

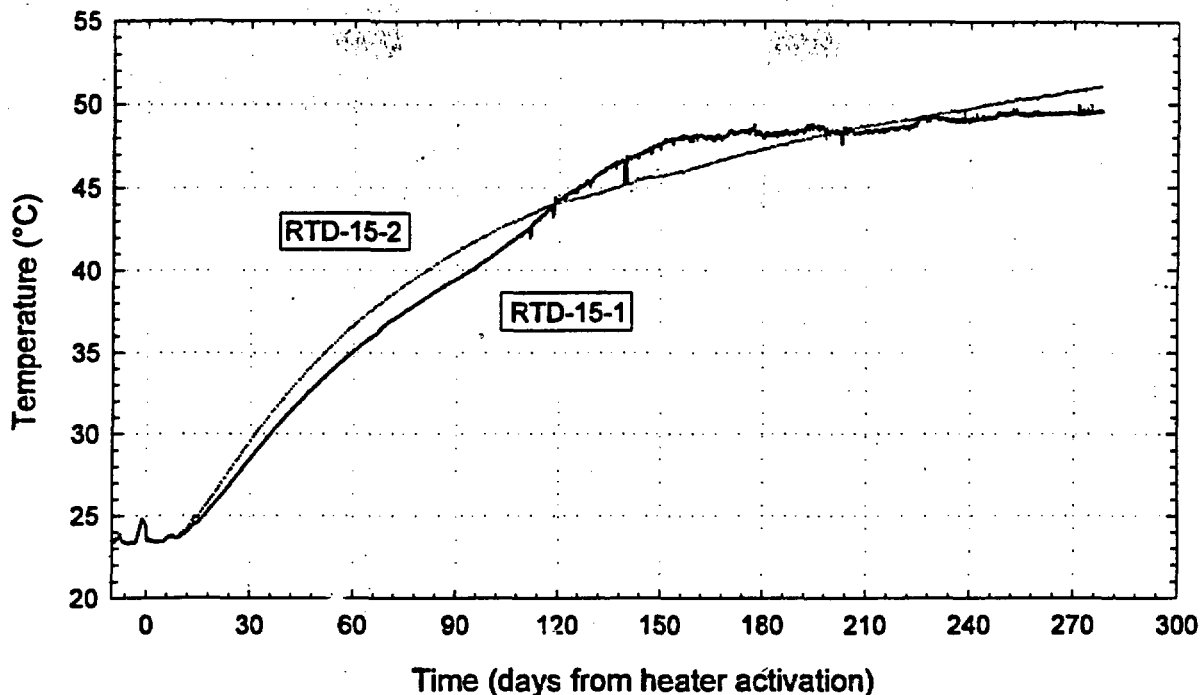


Figure 3-59. Comparison of data from TMA-RTD-15-1 and TMA-RTD-15-2.

Another gage exhibiting anomalous behavior is TMA-RTD-15-9, located approximately 2.17 m from the heater. In Figure 3-60, the temperature data recorded by this gage are compared with the data from TMA-RTD-15-10, its nearest neighbor. The two tracked each other nicely up until about day 103, when TMA-RTD-15-9 experienced a slight inflection. Then between days 112 and 117, TMA-RTD-15-9 experienced an approximately 2°C temperature drop. It may be significant that the timing of this drop coincides with a 15-hour interruption in the heater power. Although TMA-RTD-15-9 had been slightly warmer than TMA-RTD-15-10 before the start of the anomalous behavior, its temperature remained about 1°C cooler than that of TMA-RTD-15-10 up until day 253, at which time it once again started to diverge from TMA-RTD-15-10. Because the data from TMA-RTD-15-10 and from other nearby neighbors of TMA-RTD-15-9 exhibit qualitatively similar but more subdued anomalies at the same time, these data are believed to be valid and not the result of a gage malfunction. This type of behavior is suggestive of fluid flow in a fracture near TMA-RTD-15-9, which is bringing cooler fluid into the vicinity of TMA-RTD-15-9 from greater radial distances from the heater.

The temperature data from TMA-RTD-17 are illustrated in Figures 3-47 and 3-48. Like TMA-RTD-15, this suite of gages starts from the Thermomechanical Alcove Extension but is angled downward so as to pass below and beyond the heater. There are no significant thermal anomalies evident in this hole.

The temperature data from TMA-RTD-22 and TMA-RTD-23 are illustrated in Figures 3-49 through 3-52. The only noticeable anomalies in these holes occurred on days 130 and 140. Because these anomalies are evident on the temporal temperature distribution plots from all the gages, independent of radial distance from the heater, these are likely the result of field personnel working in the wells.

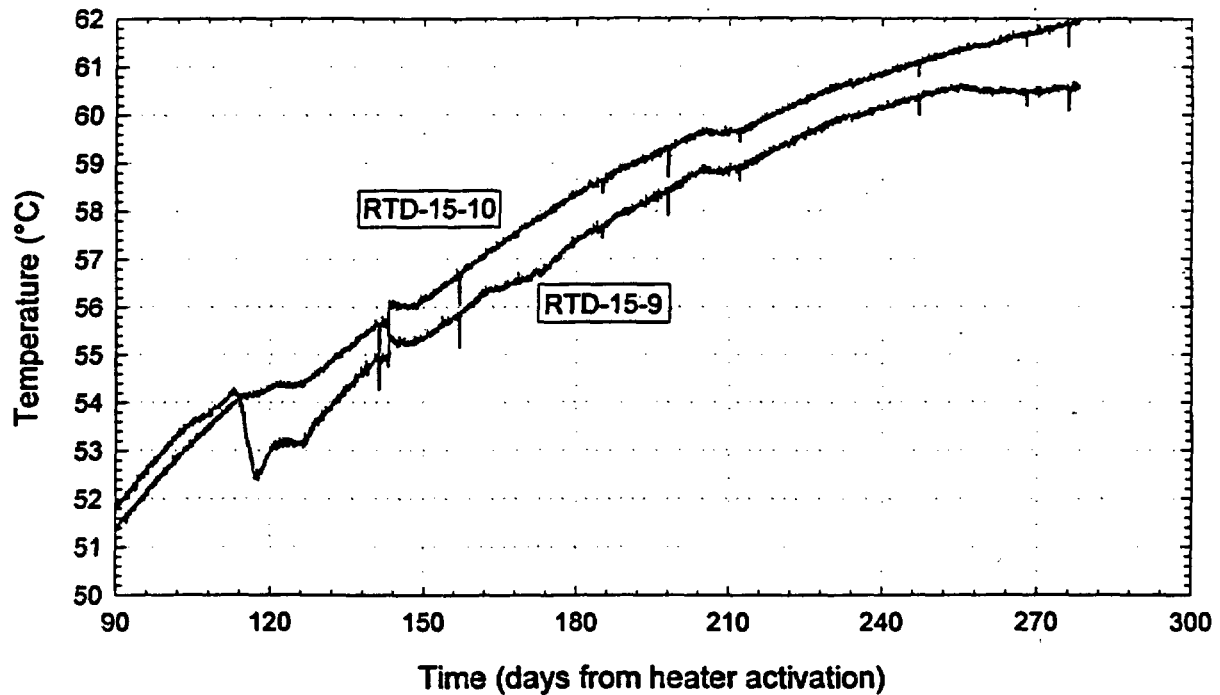


Figure 3-60. Comparison of data from TMA-RTD-15-9 and TMA-RTD-15-10.

Figures 3-53 through 3-56 illustrate the spatial and temporal temperature distributions measured in boreholes TMA-TEMP-16 and TMA-TEMP-18. The temperature gages in these holes are all located at least 3 m from the heater and hence have warmed only slightly during the test. The only anomalous data are from TMA-TEMP-16-4, located about 3.2 m from the heater, which recorded impossible data (less than 30°C) from about day 75 to day 80 as well as negative spikes at several other points in time. Because the rest of the data from this gage appear to be reliable, and because the gage exhibits other interesting behavior, its data have not been omitted from the analysis. Five liters of water have been removed from this hole during the course of the SHT (R. Datta, personal communication), and the unreliable data obtained from TMA-TEMP-16-4 may have resulted from water contacting the temperature gage. Other than the unreliable data, there are several times during the test when temperature drops of a few degrees have been recorded. These may coincide with field operations in the borehole.

The probes that are oriented parallel to the long axis of the heater (the y-axis) lend themselves well to an evaluation of the symmetry of the temperature distribution about a vertical plane perpendicular to the heater and intersecting the heater at its midpoint. In Figures 3-57 and 3-58, the temperature of each gage observed after 275 days of heating is plotted as a function of the distance from the gage to the vertical plane at  $Y=4.5$  m. Caution must be exercised because the boreholes in which the temperature gages are deployed are not perfectly parallel to the axis of the heater (see Figure 3-2). For probes near the heater, where the radial temperature gradient is high, this can impart a significant asymmetry to the borehole spatial temperature profile that does not accurately reflect rock conditions. The data indicate that, in general, the observed temperature distributions are quite symmetric about the vertical plane, which intersects the heater at its midpoint.

The locations of the temperature gages on the three rock faces and in the insulation material are illustrated in Figure 3-61. The temperatures of the thermocouples mounted on the front face of the SHT block are illustrated in Figure 3-62. Several of the thermocouples started warming above ambient only a few days after activation of the heater. By day 275, the temperature gage located 1.25 m vertically above the heater borehole collar had reached a temperature of about 48°C.

Figures 3-63 and 3-64 illustrate the temperatures measured by the thermocouples on the side faces of the SHT block. These faces are parallel to the Y-Z planes at approximately  $X = -6.6$  m and  $X = 6.3$  m, respectively. Several of the thermocouples on the face at  $X = -6.6$  m are relatively constant and are behaving independently of the remaining gages, but these are located near the top of the face near some lights and/or electrical conduits that are warming and thus corrupting the temperature readings. In general, the data indicate that the temperatures of the side faces of the block rose about 8° above their starting point as a result of the SHT. The differences between the two plots may be the result of slight differences in surface distances from the heater.

Figures 3-65 through 3-67 illustrate the temperatures measured by the thermistors deployed in the insulation covering the surface of the SHT block. Although several of the gages on the front face rose as much as 13°C above ambient, those on the sides of the block increased by only about 5°C after 275 days of heating.

Figure 3-68 illustrates the temperatures of the surface and insulation temperature gages on the front face of the SHT block as a function of radial distance from the heater borehole collar after 275 days of heating. These data indicate that, although the temperatures of the surface of the block are generally higher near the heater borehole collar, the correlation between surface temperature and radial distance from the heater borehole collar is far from perfect.

On each of the three insulated surfaces of the SHT block, temperature sensors were installed to estimate the thermal flux. Twelve thermocouples were installed on each of the three rock surfaces, and five thermistors were installed between the layers of insulation. With the exception of two pairs of gages, the locations of the thermocouples and thermistors were coincident. Figure 3-69 illustrates the temperature drop across the insulation at the four locations on the front face of the SHT where the surface and insulation temperature gages are located at similar x-z locations. The data obtained after 275 days of heating are plotted as a function of radial distance from the heater borehole collar. The temperature drop is proportional to the heat flux through the insulation. The measured temperature drops are quite small and, based on only four pairs of data points, do not appear to be strongly correlated with radial distance from the heater borehole collar.

Figures 3-70 through 3-76 illustrate isotherms on seven different planes through the SHT block after 275 days of heating. These temperature contour plots were generated by hand, using good engineering judgment. The isotherms do not violate any of the temperature data from the TMA-TC, TMA-RTD, or TMA-TEMP probes. Some of the data from the TMA-BX probes are violated. This is justified because these probes are deployed in open boreholes and intra-borehole vapor-phase heat transport has influenced the data from the gages so that they do not accurately reflect the rock temperature near the borehole. On slices parallel to the X-Z face (i.e., planes perpendicular to the long axis of the heater), temperature contours are almost perfectly circular and centered on the heater location. There is a slight asymmetry, with the 50 and 75°C contours in the upper left part of the block being bowed out slightly. This is the result of slightly elevated temperatures observed by probe TMA-RTD-23. The contour plot parallel to the Y-Z plane, which is the vertical plane

containing the heater, illustrates the symmetry of the temperature distribution in the Y-direction. The contour plots parallel to the X-Y plane indicate that the temperature distribution is relatively symmetric about the vertical plane through and parallel to the heater.

Figure 3-77 is a plot of temperature as a function of radial distance from the heater for all gages that fall within the range  $4.0 \text{ m} < Y < 5.0 \text{ m}$ . These are the gages located near the vertical plane that intersects the heater near its midpoint. Although all the gages from boreholes TMA-RTD-15, TMA-RTD-17, TMA-RTD-22, TMA-RTD-23, TMA-TEMP-16, and TMA-TEMP-18 are included in Figure 3-74, it should be noted that the locations of these gages have not been reported in a TDIF and hence the data must be considered NQ. Also included in Figure 3-74 are single gages from each of TMA-TC-1, TMA-TC-2, TMA-TC-3, TMA-TC-4, TMA-TC-5, TMA-BX-1-TC, TMA-BX-2-TC, and TMA-BX-3-TC. The data indicate that the temperature distribution around the heater is very radially symmetric. The only exceptions are the temperature data from borehole TMA-RTD-23, which are illustrated by the triangle symbols in Figure 3-77. In the radial distance range from about 1.4 to 2.8 m, they appear to be as much as  $5^\circ\text{C}$  warmer than other gages at similar distances from the heater. Interpretation of this observation is being postponed until the locations of the gages in this hole become Q-level data.

Figure 3-78 illustrates the amount by which the gages used to generate Figure 3-77 increased in temperature during the time interval from 186 to 275 days. For radial distances from the heater greater than 1 m, the amount of warming is well-correlated with radial distance from the heater, ranging from about  $3.5^\circ\text{C}$  at 1 m to about  $2.5^\circ\text{C}$  at 6 m from the heater. The gages located less than 1 m from the heater, however, do not seem to behave in the manner one would predict based on the data at radial distances greater than 1 m. The fact that the temperatures of these gages are all at or above  $100^\circ\text{C}$  suggests that the cause of this disparity is related to a temperature dependent difference in the heat transport mechanism and/or thermal properties of the medium. Note also that gage TMA-RTD-15-1 rose by about  $2^\circ\text{C}$  less than would be indicated by other gages at similar radial distances from the heater. The anomalous data obtained from this gage were discussed in more detail in an earlier section.

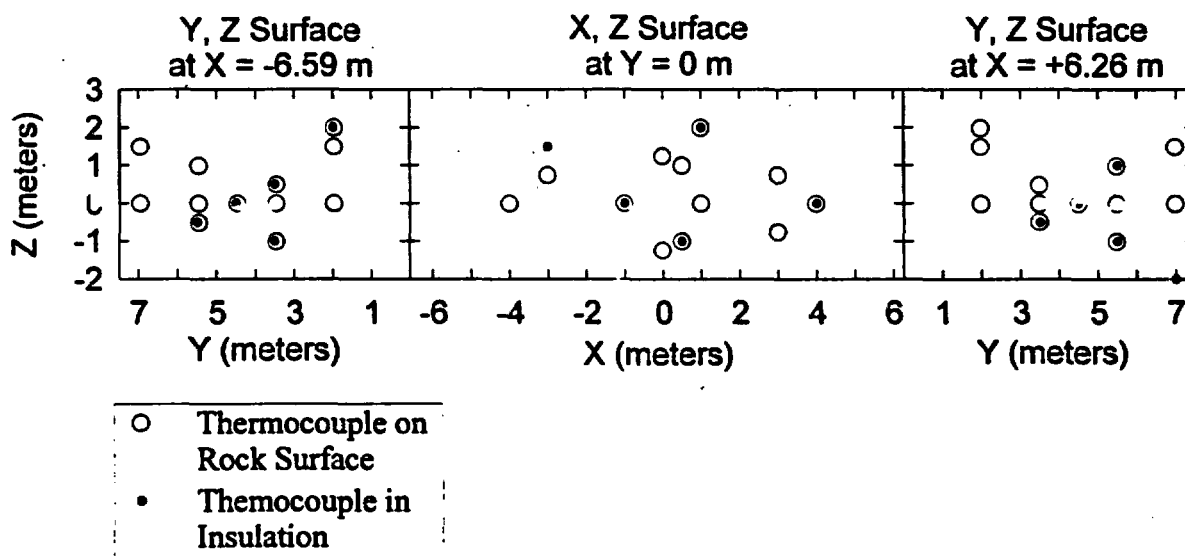
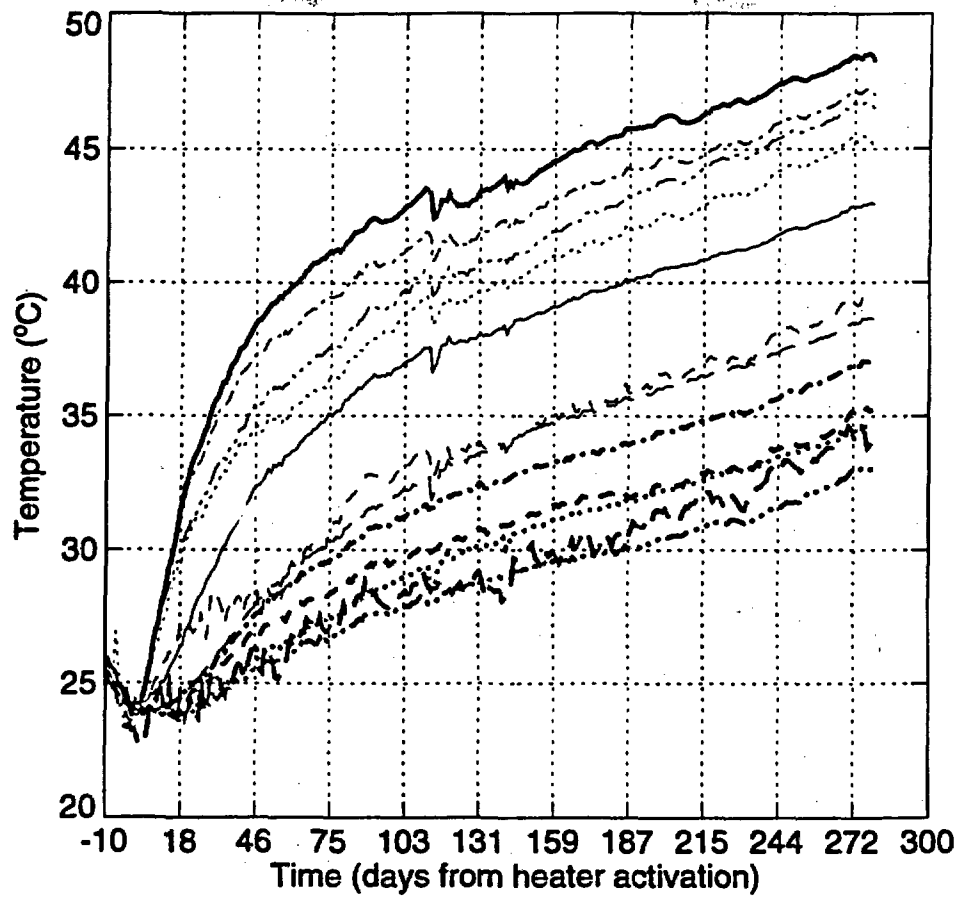
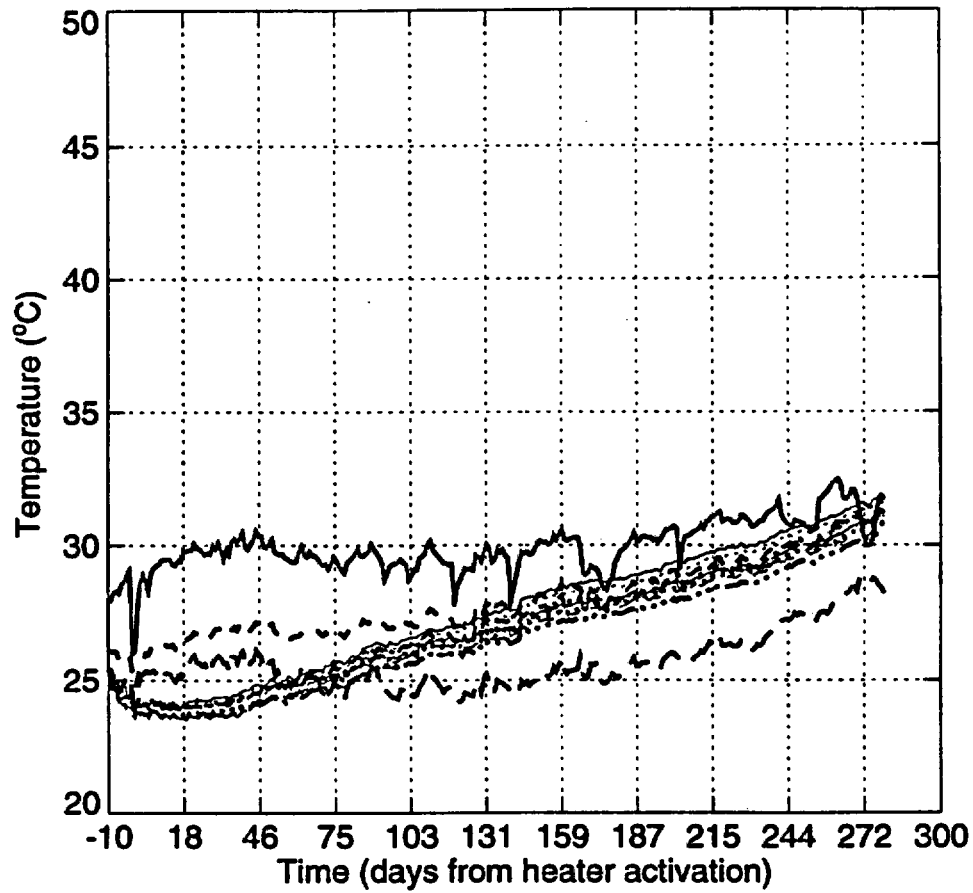


Figure 3-61. Locations of temperature gages on the three rock faces and in the insulation material.



- 1.00, 0.00, 2.00
- ..... 1.00, 0.00, 0.00
- - - 0.50, 0.00, -1.00
- · - · 0.50, 0.00, 1.00
- · - · -1.00, 0.00, 0.00
- - - 3.00, 0.00, 0.75
- 0.00, 0.00, 1.25
- ..... 4.00, 0.00, 0.00
- - - 3.00, 0.00, -0.75
- · - · -3.00, 0.00, 0.75
- · - · -4.00, 0.00, 0.00
- - - 0.00, 0.00, -1.25

Figure 3-62. Temperature versus time for the thermocouples mounted on the Thermomechanical Alcove face of the SHT block.



- -6.59, 3.46, 0.49
- ..... -6.59, 3.46, -0.01
- - - -6.59, 3.46, -1.01
- · - · -6.59, 5.46, 0.99
- · - · -6.59, 5.46, -0.01
- - - -6.59, 5.46, -0.51
- -6.59, 1.96, 1.99
- ..... -6.59, 1.96, -0.01
- - - -6.59, 1.96, 1.49
- · - · -6.59, 4.46, -0.01
- · - · -6.59, 6.96, -0.01
- - - -6.59, 6.96, 1.49

Figure 3-63. Temperature versus time for the thermocouples mounted on the Observation Drift face of the SHT block.

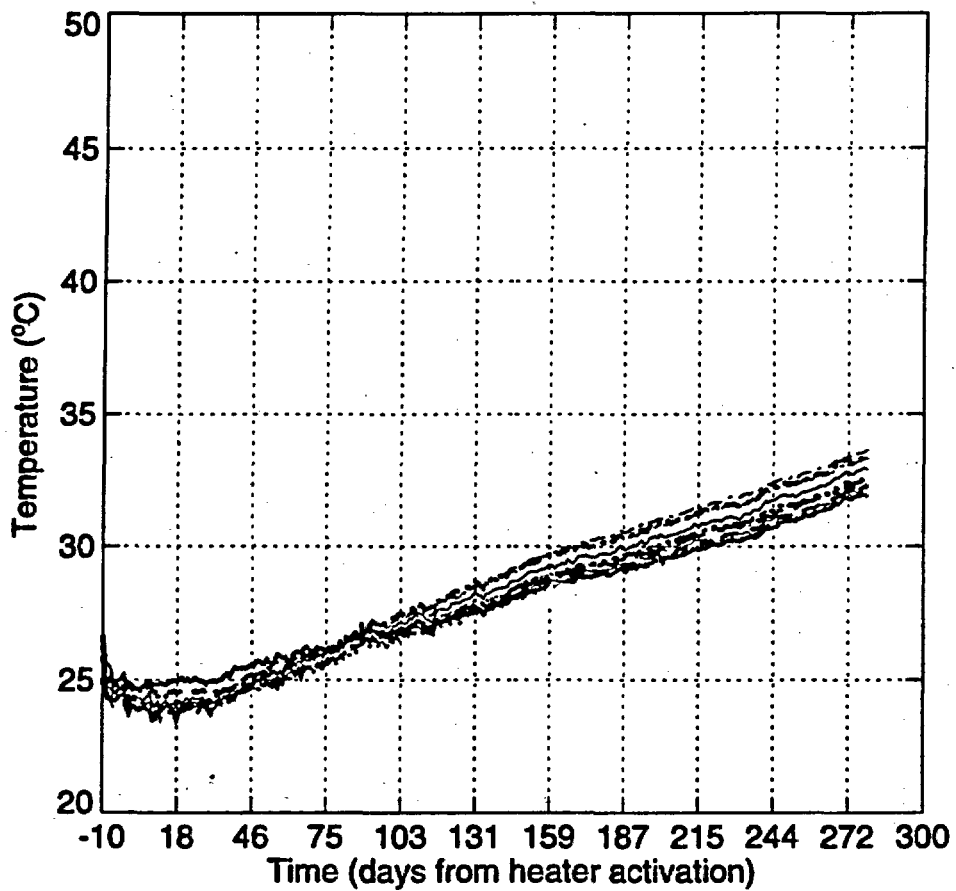
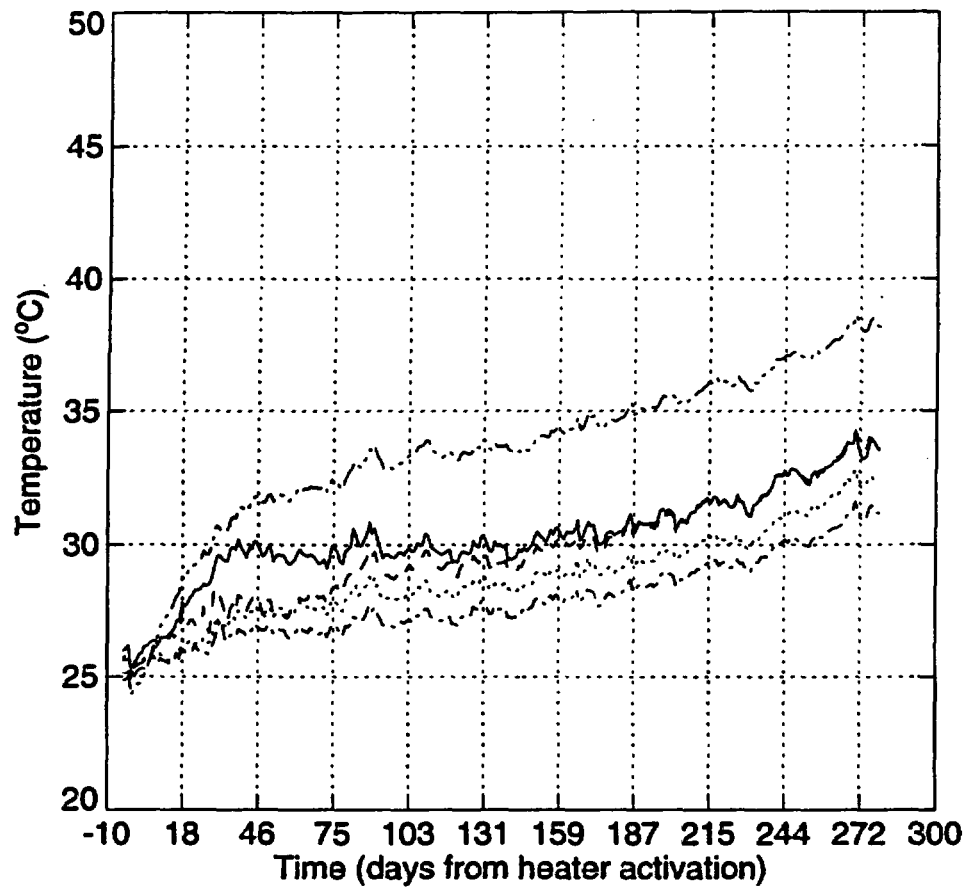
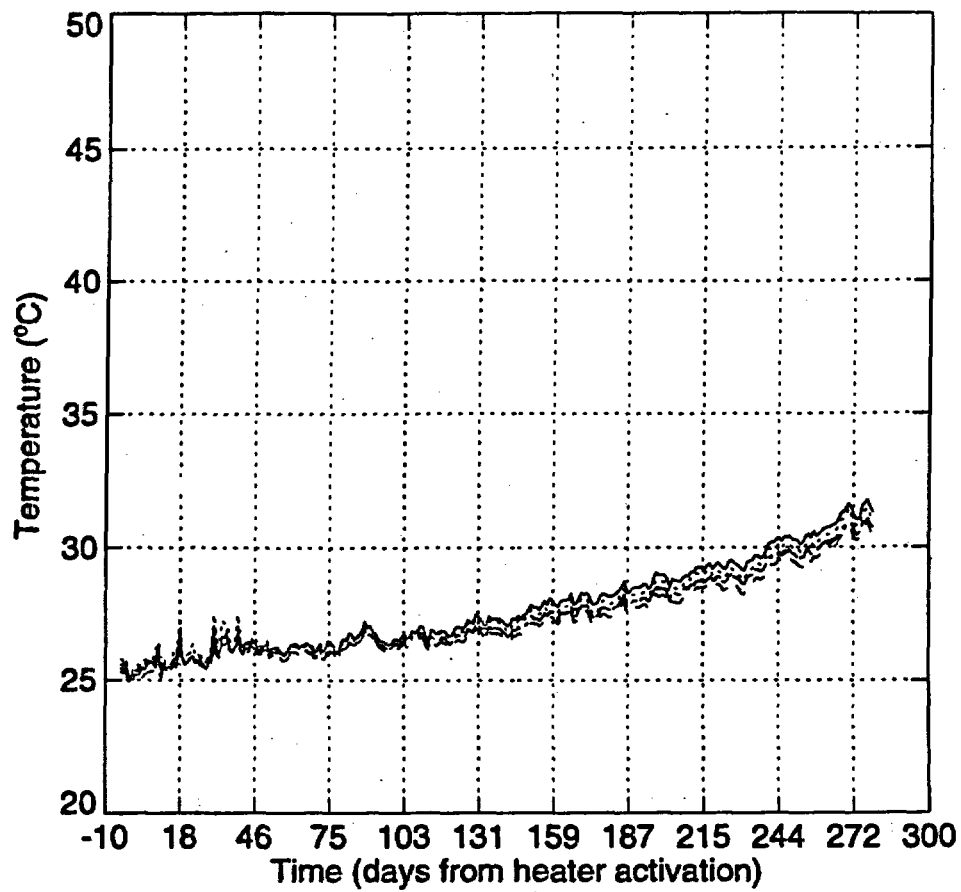


Figure 3-64. Temperature versus time for the thermocouples mounted on the Thermomechanical Alcove Extension face of the SHT block.



— 1.00, -0.08, 2.00  
 ..... -3.00, -0.08, 1.50  
 - - - 0.50, -0.08, -1.00  
 - · - · 4.00, -0.08, 0.00  
 - - - - -1.00, -0.08, 0.00

Figure 3-65. Temperature versus time for the thermistors installed in the insulation covering the Thermomechanical Alcove face of the SHT block.



- 6.34, 5.50, 1.00
- ..... 6.34, 4.50, 0.00
- - - 6.34, 3.50, -0.50
- · - · 6.34, 5.50, -1.00
- - - - 6.34, 7.00, -2.00

Figure 3-67. Temperature versus time for the thermistors installed in the insulation covering the Thermomechanical Alcove Extension face of the SHT block.

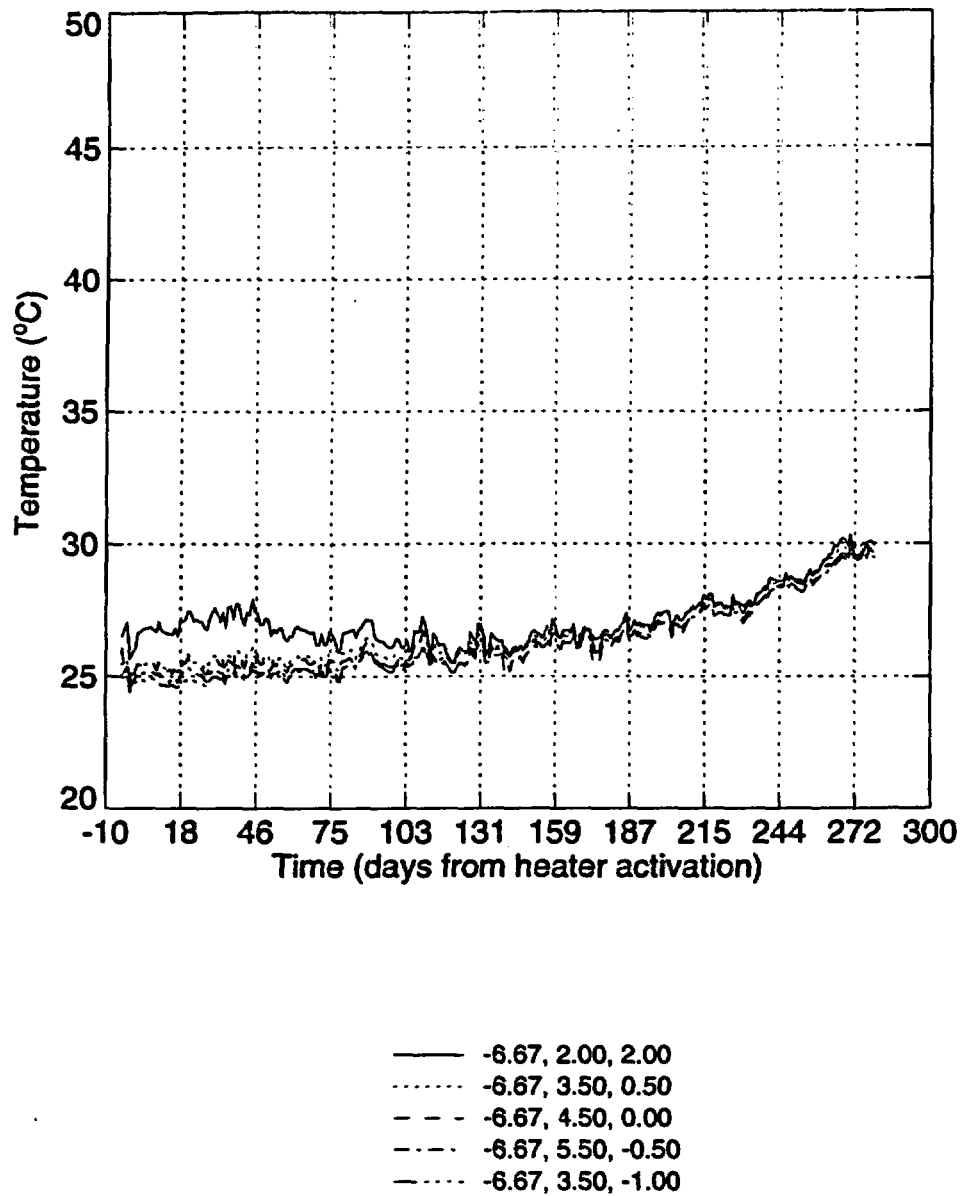


Figure 3-66. Temperature versus time for the thermistors installed in the insulation covering the Observation Drift face of the SHT block.

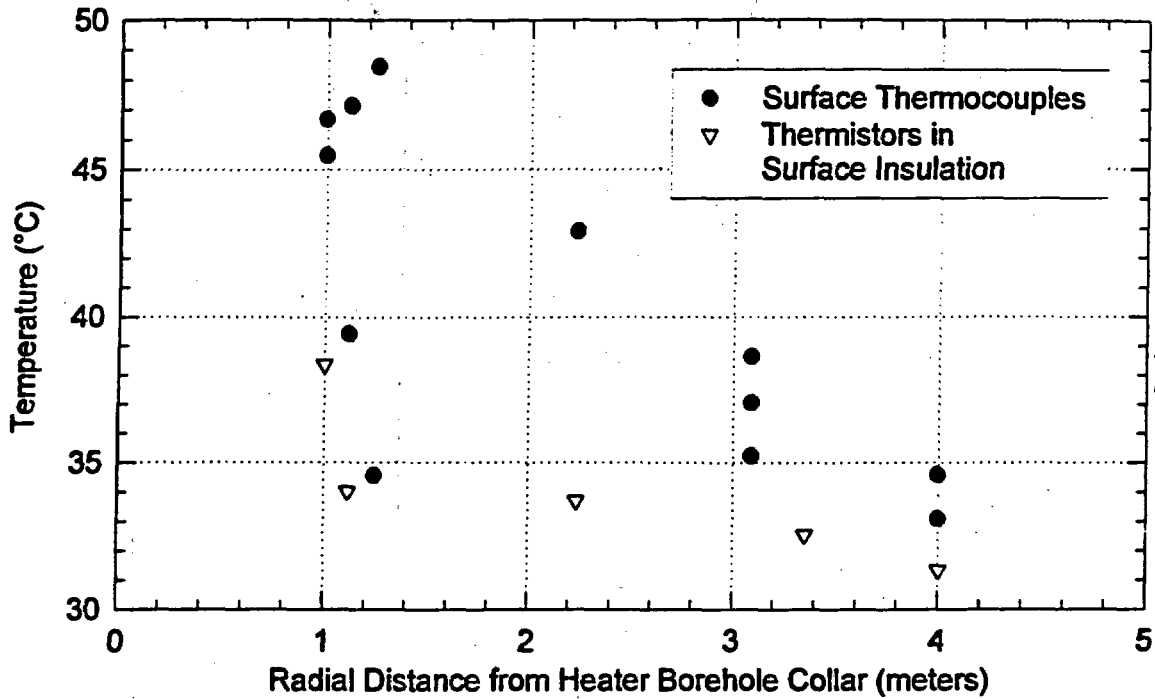


Figure 3-68. Temperature as a function of radial distance from the heater borehole collar for the surface and insulation temperature gages on the front face of the SHT block.

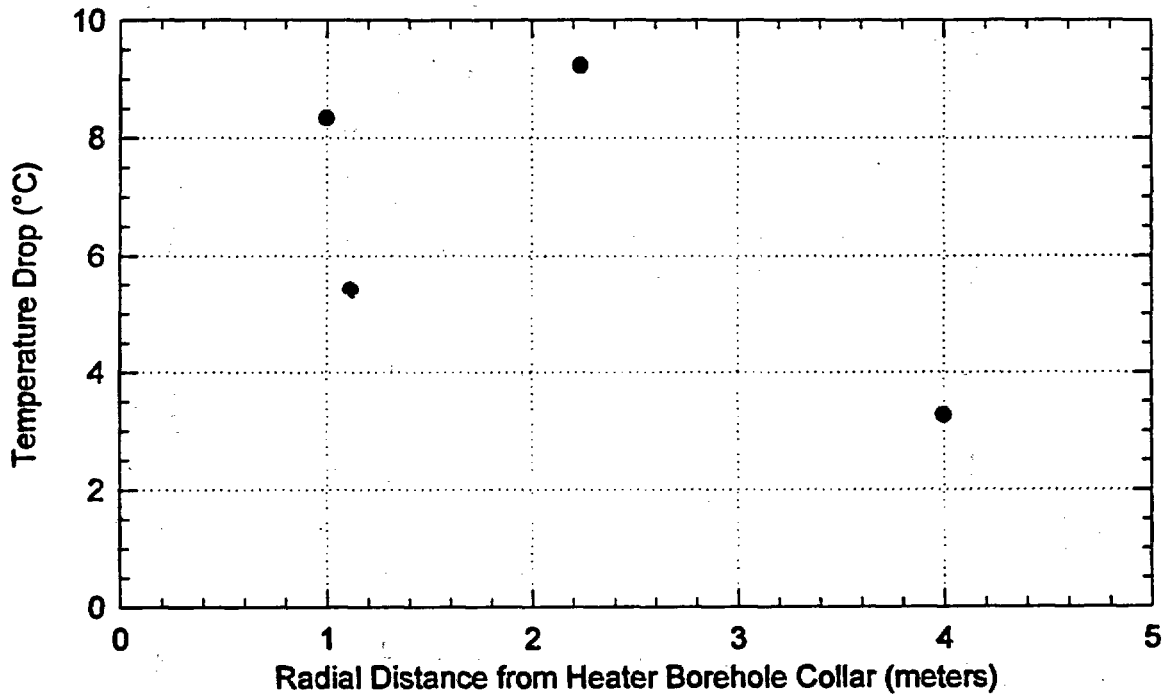
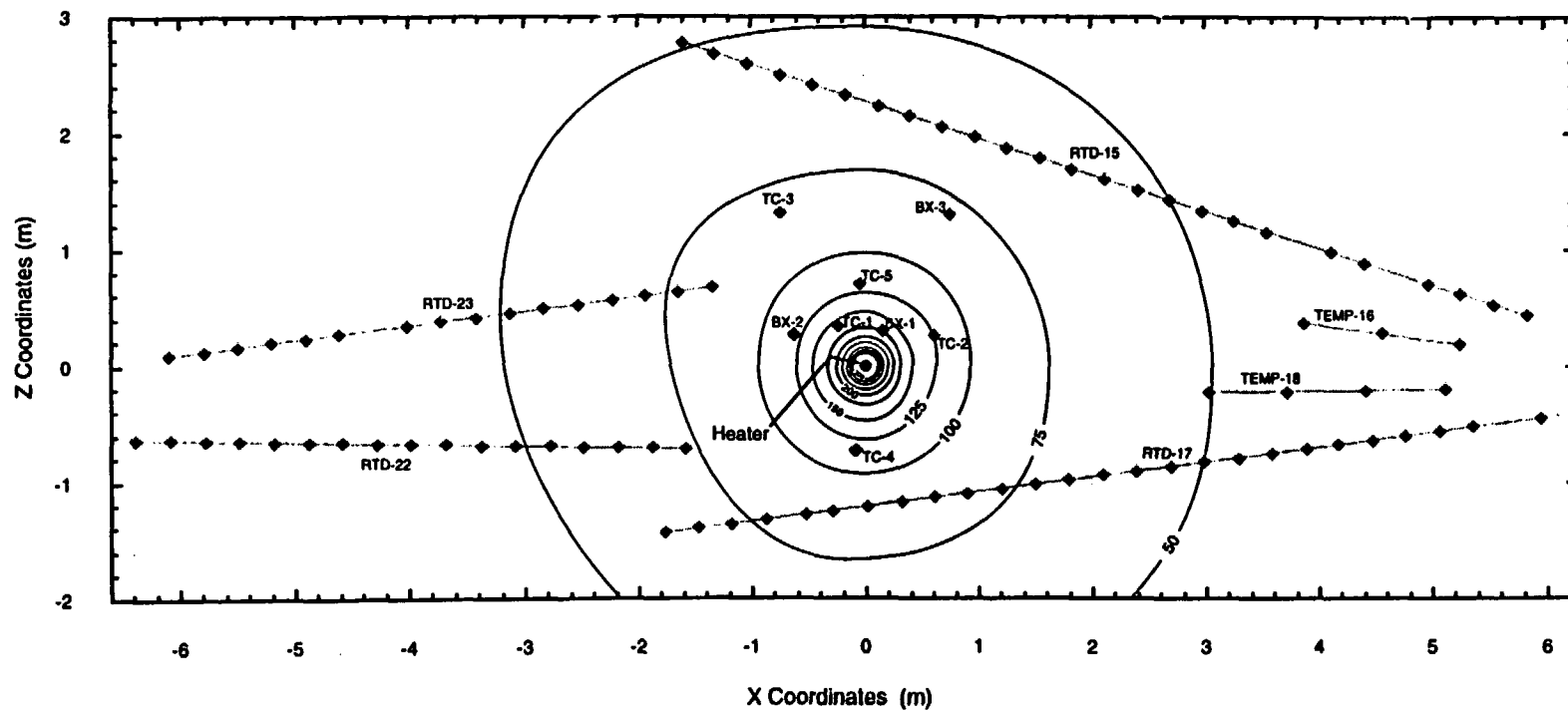
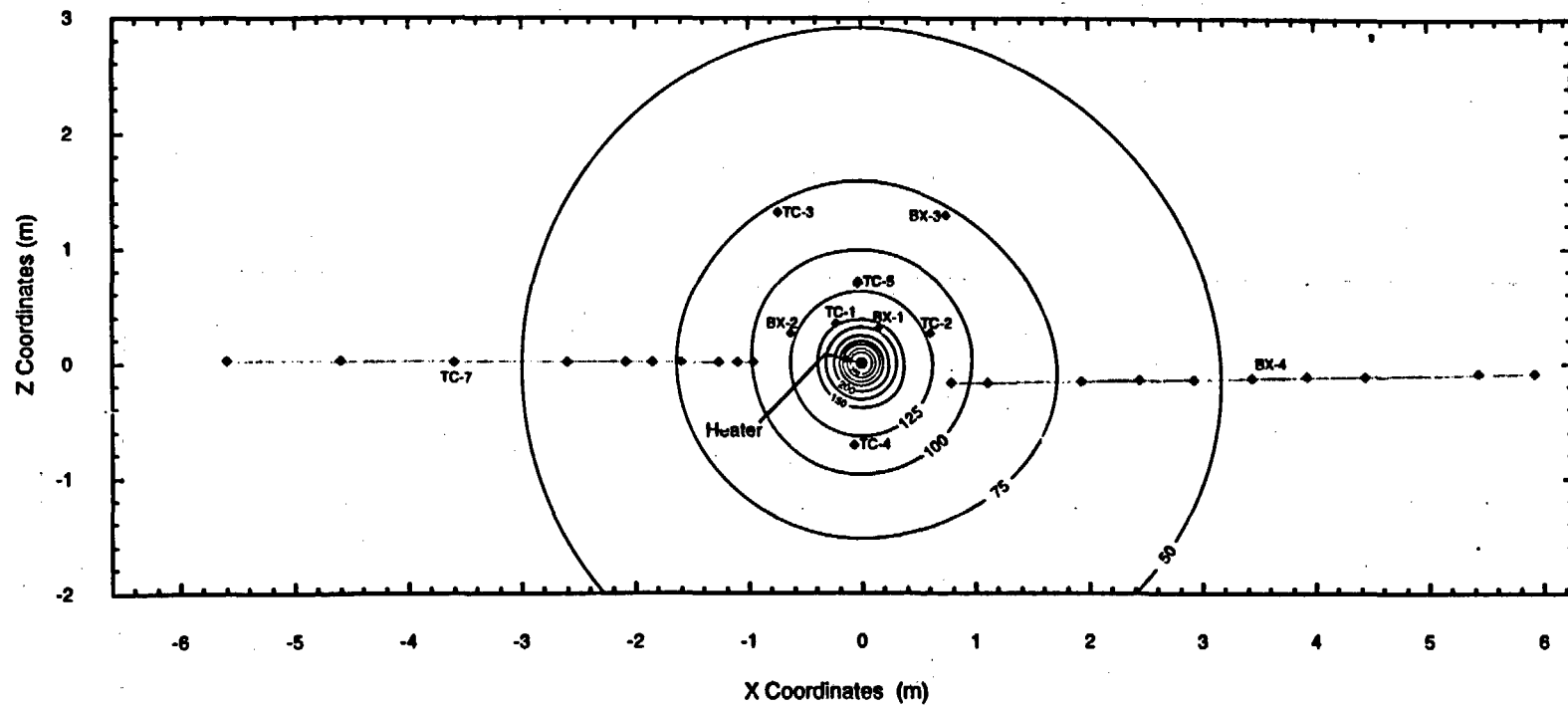


Figure 3-69. Temperature drop across the insulation for surface-insulation temperature gage pairs at four locations on the front face of the SHT, as a function of radial distance from the heater borehole collar.



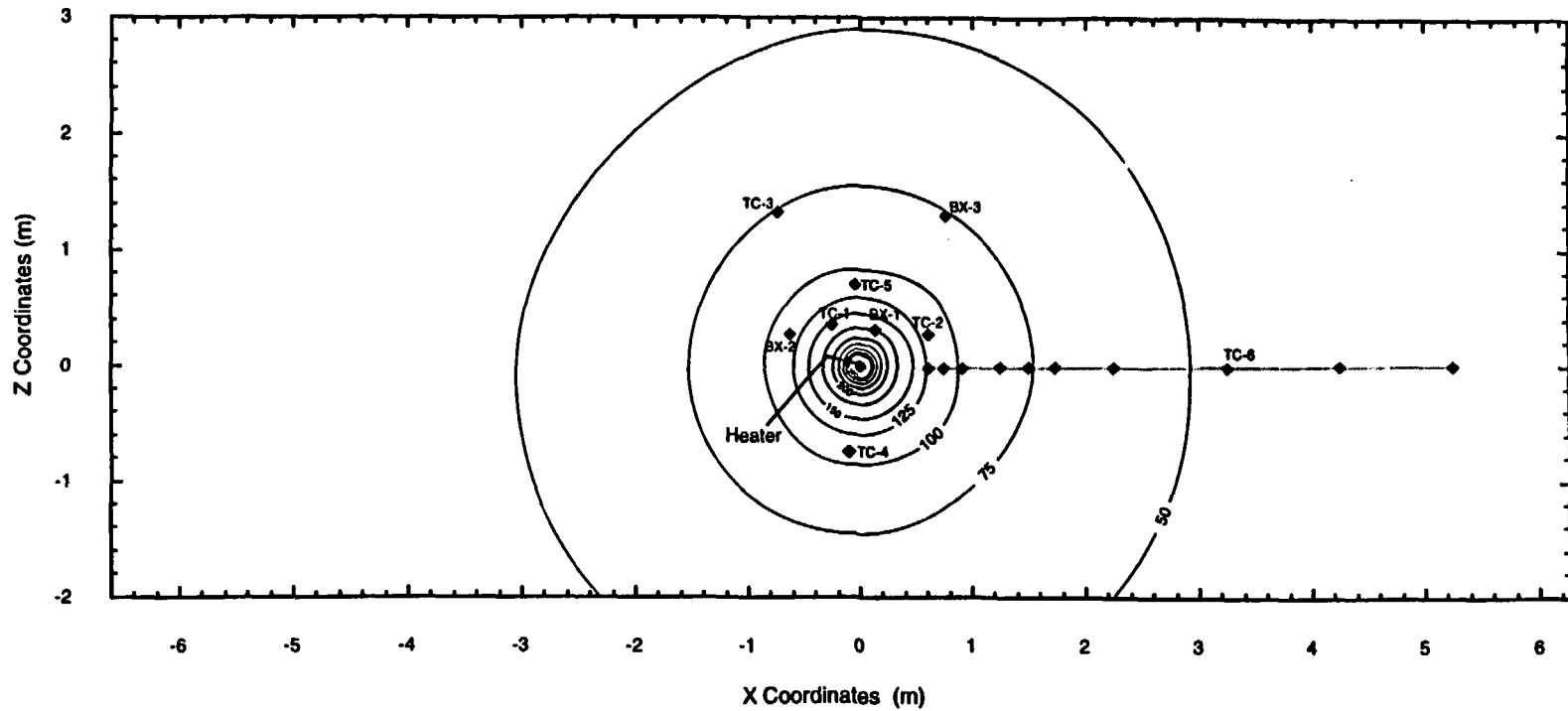
TRI-6117-7-2

Figure 3-70. Vertical slice perpendicular to the heater axis at  $Y=4.5$  m showing temperature contours (interval =  $25^{\circ}\text{C}$ ) after 275 days of heating. Gages in close proximity to the plane of the slice are shown for reference.



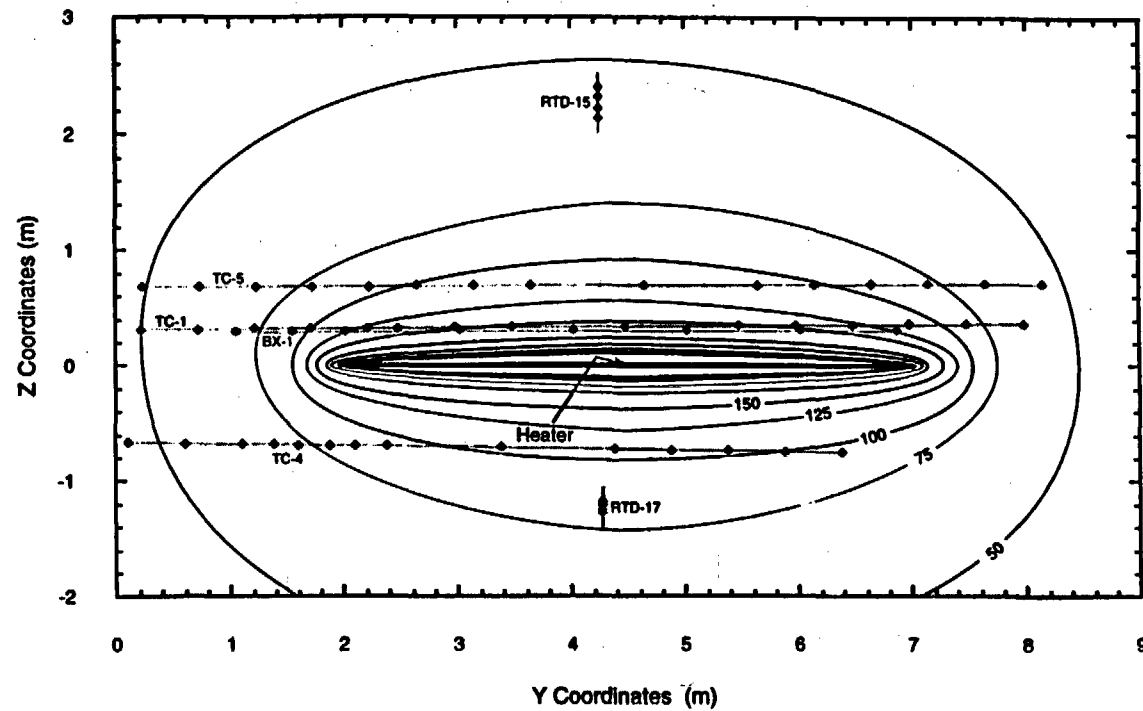
TRR-0117-0-2

Figure 3-71. Vertical slice perpendicular to the heater axis at Y=3.5 m showing temperature contours (interval = 25°C) after 275 days of heating. Gages in close proximity to the plane of the slice are shown for reference.



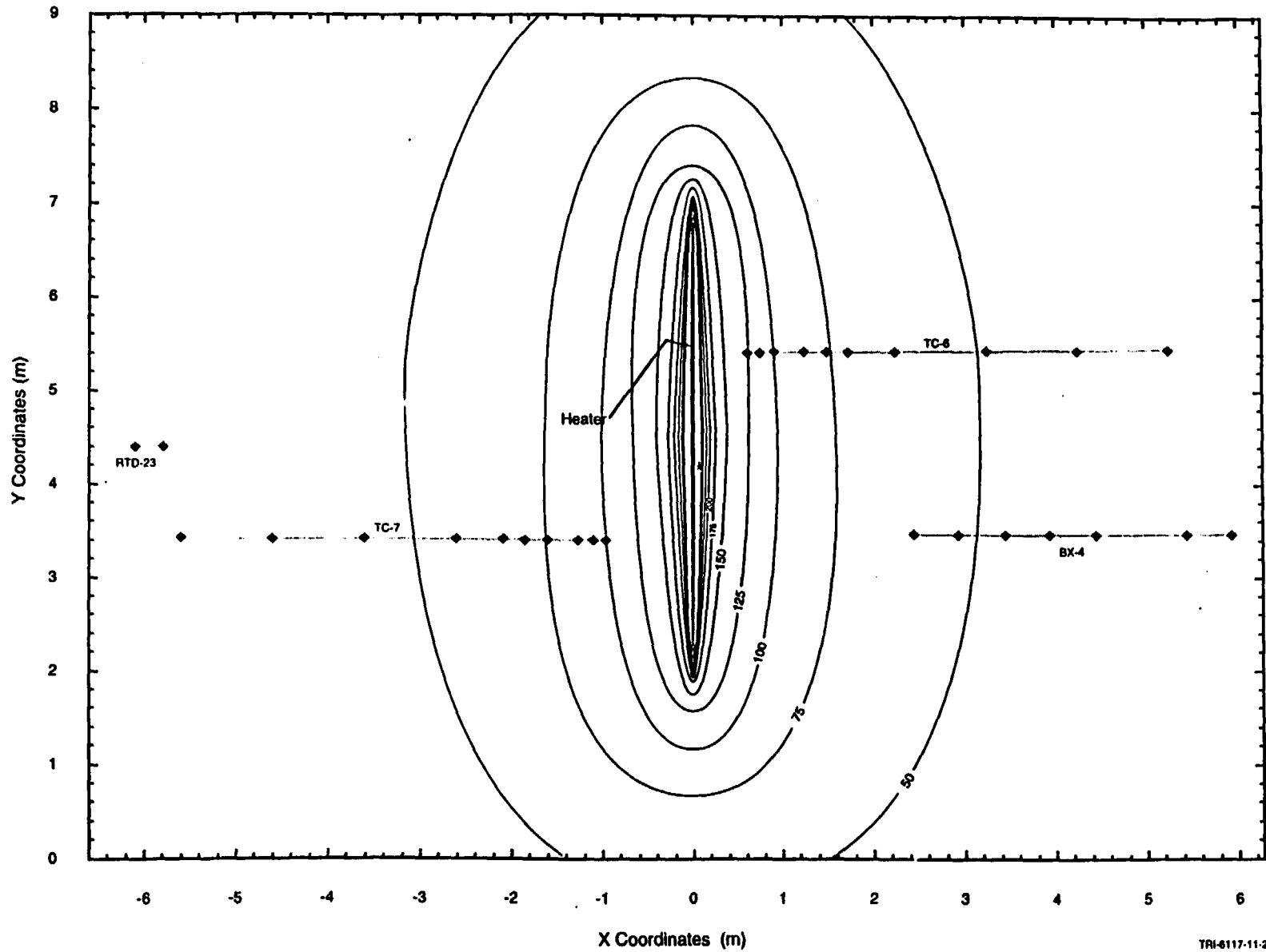
TRI-6117-8-2

Figure 3-72. Vertical slice perpendicular to the heater axis at  $Y=5.5$  m showing temperature contours (interval =  $25^{\circ}\text{C}$ ) after 275 days of heating. Gages in close proximity to the plane of the slice are shown for reference.



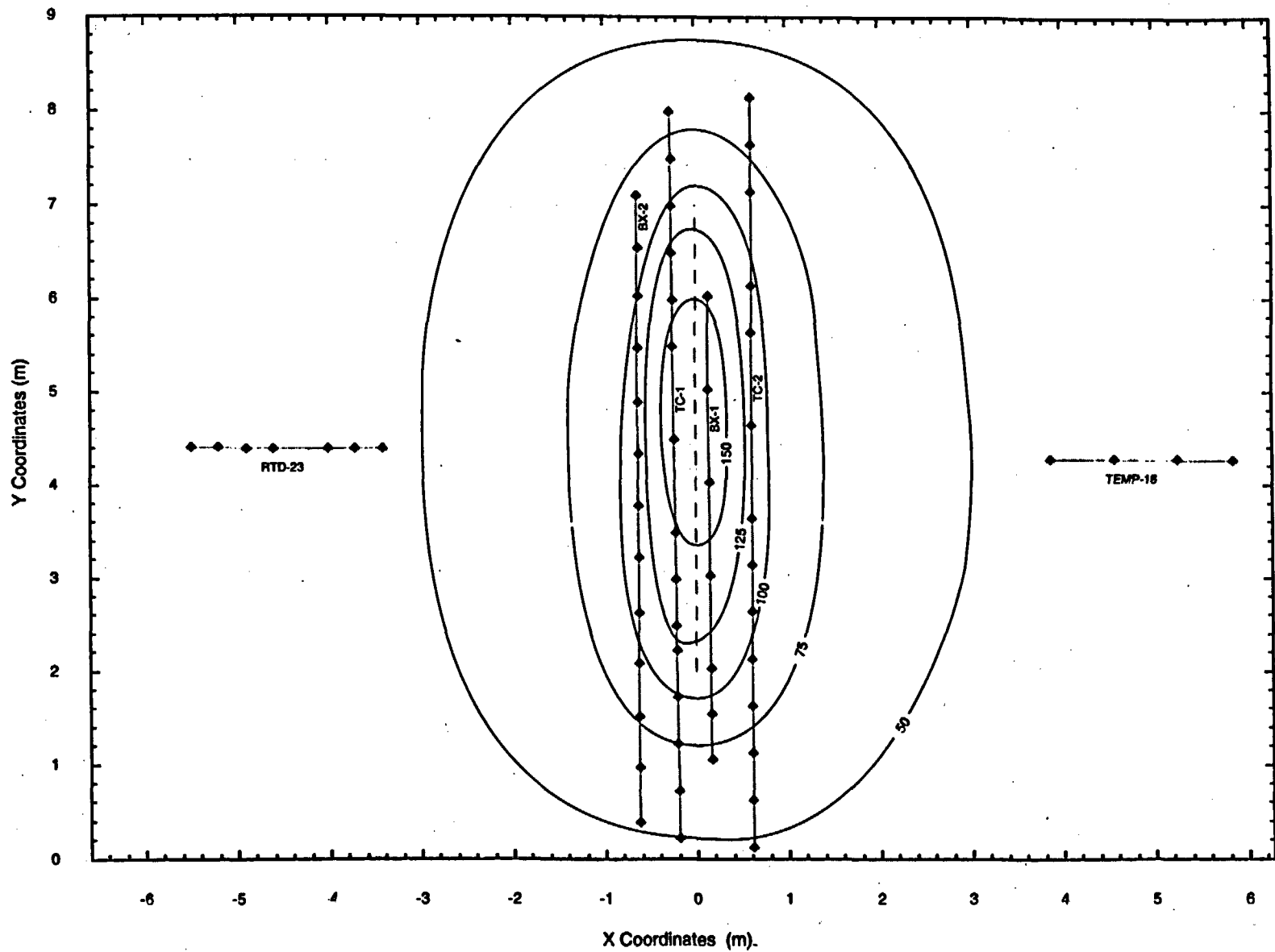
TRI-6117-10-2

Figure 3-73. Vertical slice parallel to the heater axis at X=0 m showing temperature contours (interval = 25°C) after 275 days of heating. Gages in close proximity to the plane of the slice are shown for reference.



TRI-6117-11-2

Figure 3-74. Horizontal slice parallel to the heater axis at  $Z=0$  m showing temperature contours (interval =  $25^{\circ}\text{C}$ ) after 275 days of heating. Gages in close proximity to the plane of the slice are shown for reference.



TRI-6117-12-2

Figure 3-75. Horizontal slice parallel to the heater axis at  $Z=0.3$  m showing temperature contours (interval =  $25^{\circ}\text{C}$ ) after 275 days of heating. Gages in close proximity to the plane of the slice are shown for reference.

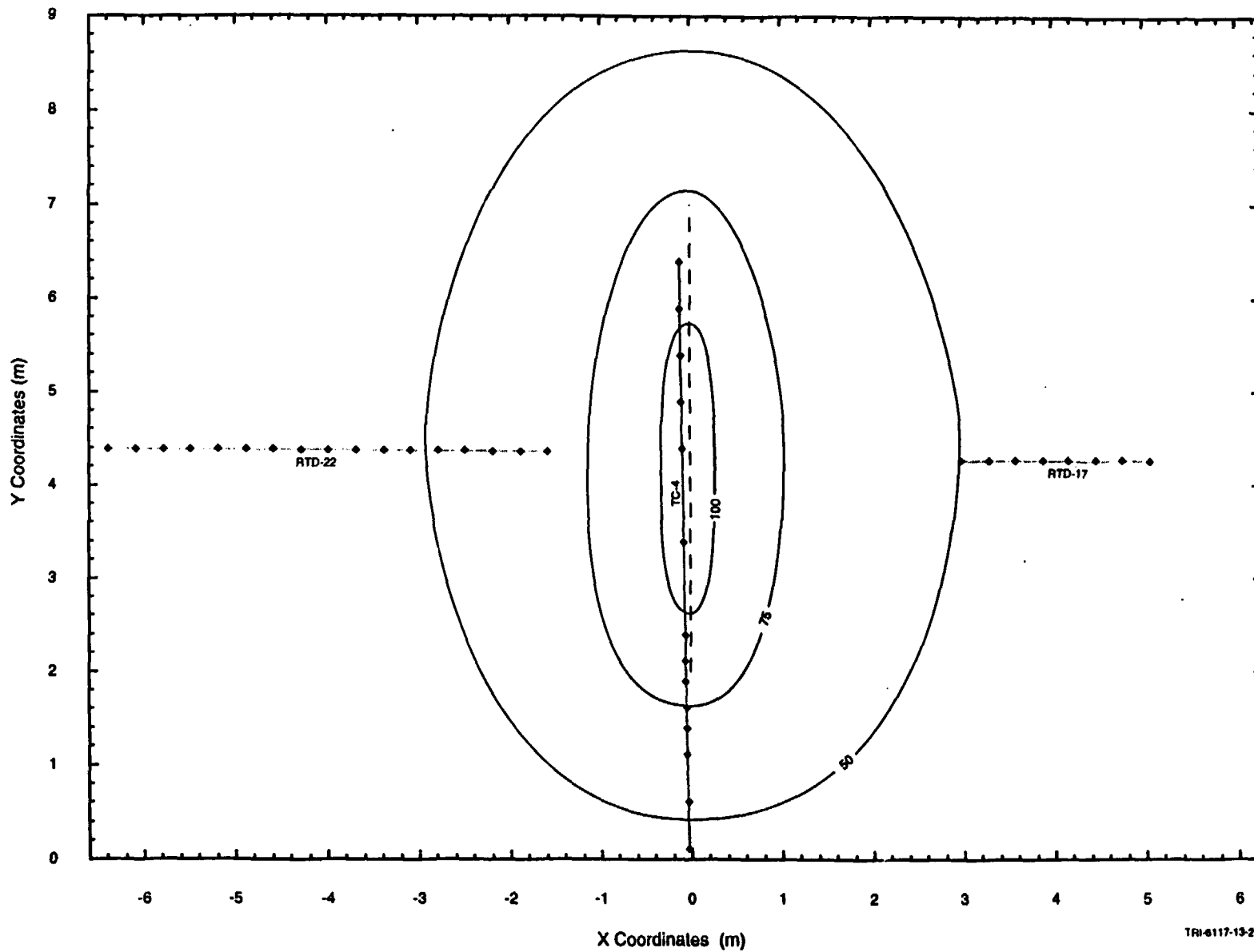


Figure 3-76. Horizontal slice parallel to the heater axis at  $Z=-0.7$  m showing temperature contours (interval =  $25^{\circ}\text{C}$ ) after 275 days of heating. Gages in close proximity to the plane of the slice are shown for reference.

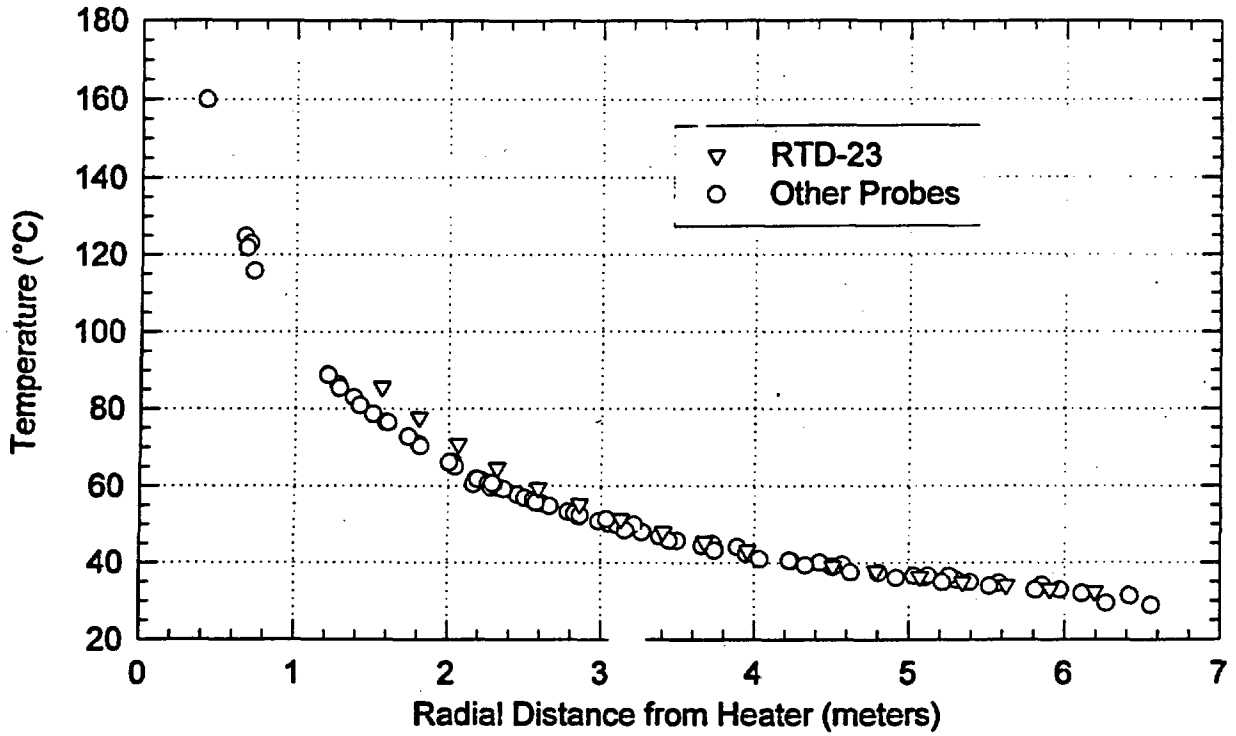


Figure 3-77. Temperature as a function of radial distance from the heater after 275 days of heating.

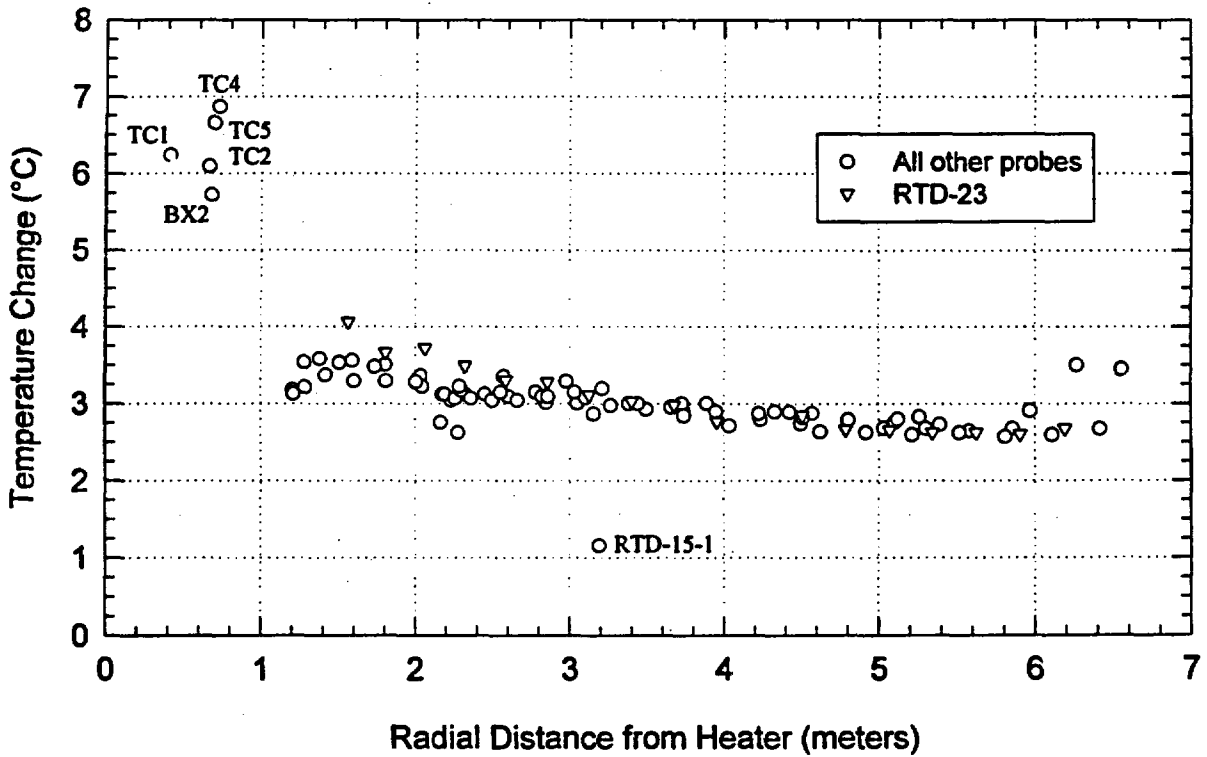


Figure 3-78. Increase in temperature during the time interval from 186 to 275 days.

Page intentionally blank

## 4. Displacement Measurements

This section presents measurements of rock displacement, rock mass modulus, and rock bolt loads. Data collected through 31 May 1997 are presented. A brief description of instruments and equipment is given in Appendix B. Specific details regarding serial numbers, calibration records, etc. can be found in the Scientific Notebook covering this work.

Displacements were measured both within and on the surfaces of the SHT block. These measurements support numerical model evaluations related to T-M-H coupling as well as provide data for determination of rock mass thermal expansion. All displacements reported in this document follow the convention of extension positive.

### 4.1 Extensometers

Four boreholes were instrumented with multiple-point borehole extensometers (MPBXs): three boreholes drilled parallel to the heater axis and one borehole drilled perpendicular to the heater axis. The MPBXs include six or seven anchors spaced along the length of the borehole. Displacements are measured using high temperature linear variable displacement transformers (LVDTs) and vibrating wire displacement transducers. For three of the boreholes, GeoKon C-ring six-anchor MPBXs were used with carbon fiber extension rods transmitting displacements of each of the six anchors to the head, which was fixed and sealed into the borehole collar using cement grout. The displacements measured for each of the anchors is expressed as the relative displacement between the anchor and the borehole collar (head). The other MPBX that was installed was a seven-anchor RocTest BOF-X extensometer that used screw-type mechanical anchors, between each of which a high temperature LVDT was installed. Extension rods between the LVDTs and adjacent anchors were constructed from Invar tubing. The displacements measured for each of the LVDTs represent the discrete displacements between each set of adjacent anchors. Total displacement along the BOF-X borehole is the sum of the displacements measured between each set of adjacent anchors. Temperature measurements were made along the length of each MPBX to provide temperature compensation for rod thermal expansion effects. The locations of the anchors and individual thermocouple junctions were determined from the survey and corrected borehole collar coordinates, from the field notes for installation (e.g., installed depth to various anchors and points on the MPBXs), and from the manufacturers' and SNL specifications for the MPBXs. Information on the MPBX gages is included in Appendix B.

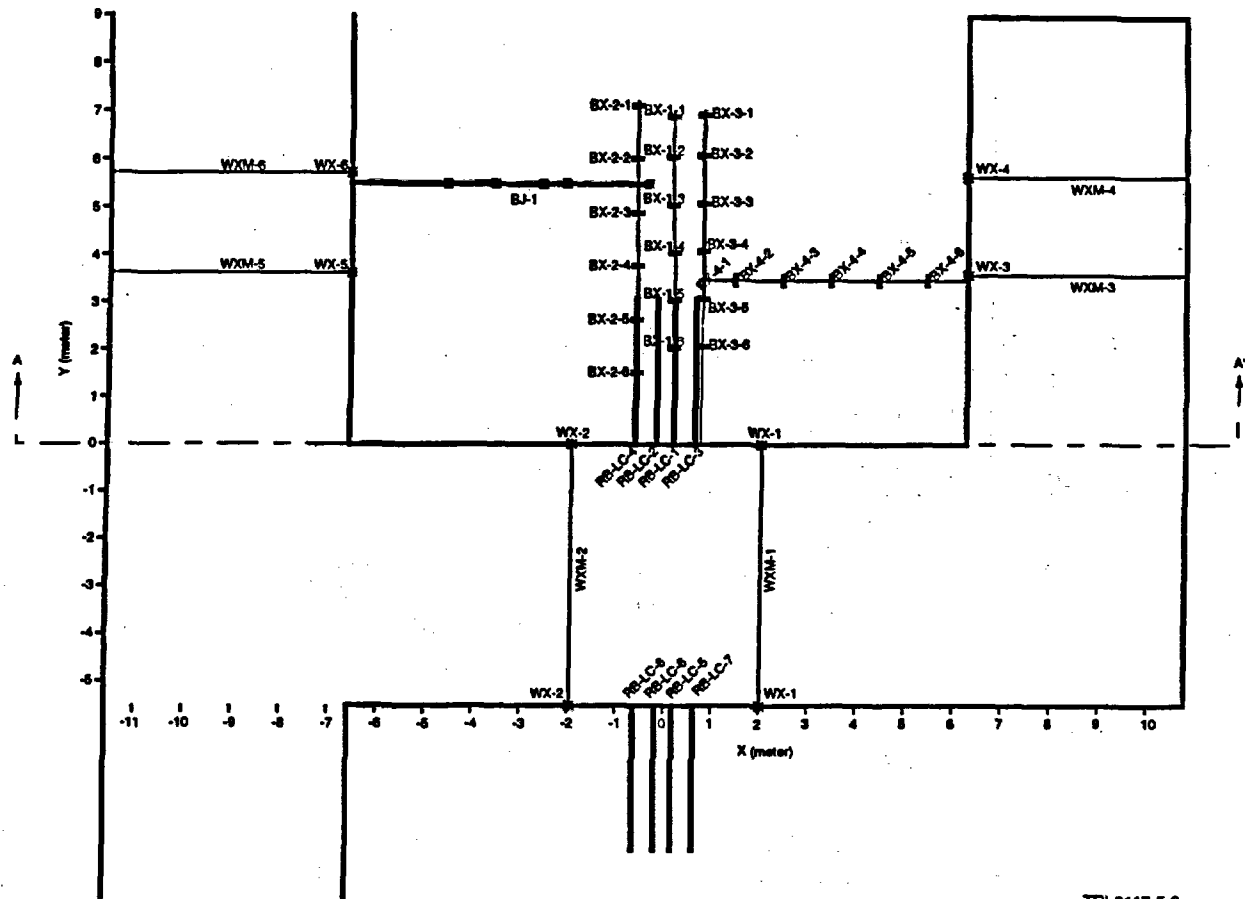
Wire extensometers and tape extensometer pins were installed on the three free surfaces of the SHT block. The wire extensometers consist of spring-loaded linear potentiometers mounted on brackets welded to steel rebar segments. These segments are grouted into the rock near the top of the SHT block at six locations (two on each of the three free surfaces of the SHT block). The wires are then stretched roughly vertically downward to another anchor located near the base of the SHT block. Tape extensometer pins are also located roughly along the midpoints of each of the six vertical lines defined by the wire extensometers. These six tape extensometer stations include six pins on the SHT block and six pins on the opposite ribs. As-built locations for each of these gages were determined from tape and level measurements referenced to known points of reference. Also, the rock surfaces represented by each of the three free surfaces were simplified to be represented by planar surfaces for numerical modeling efforts. Because the pins are

mounted in shallow holes, they can be strongly influenced by movement of discrete blocks near the surface. The data from these measurements should be used only for qualitative purposes.

Figures 4-1 and 4-2 show the locations of the MPBX boreholes and anchor locations. The figures also show wire and tape extensometer pin locations on the SHT block. MPBX-1, MPBX-2, and MPBX-3 are located in boreholes drilled parallel to the heater from the TMA (Figure 4-2, west face of the SHT block). Two wire and tape extensometer stations are located on each of the three free surfaces of the SHT block. On the west face (TMA side), station locations are WX-1, WX-2, WXM-1, and WXM-2 (Figure 4-2). The designator "M" in WXM denotes manual (tape extensometer) pin locations. On the south face of the SHT block (TMA-extension), MPBX-4 is located in a borehole drilled perpendicular to the heater (Figure 4-2). WX-3, WX-4, WXM-3, and WXM-4 wire and tape extensometer stations are located on the south face. Wire and tape extensometer stations WX-5, WX-6, WXM-5, and WXM-6 are located on the north face of the SHT block along the Observation Drift (Figure 4-2).

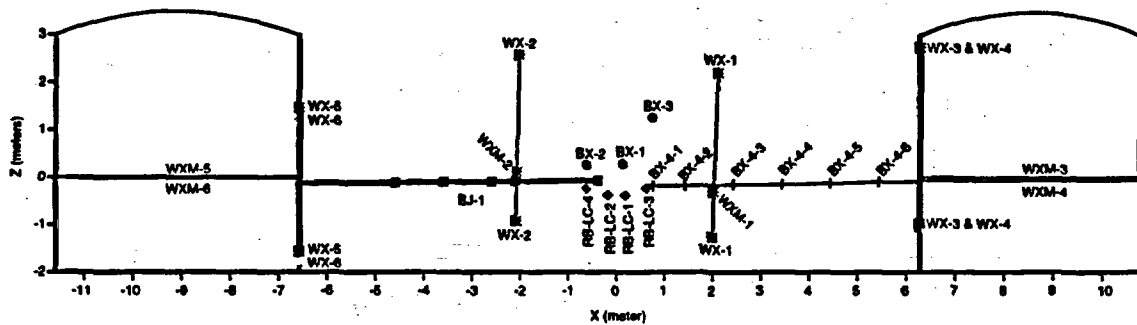
The displacement measurements through 31 May 1997 for the MPBXs are presented in Figures 4-3 through 4-6. The MPBX data are also given in tabular form in Table 4-1. Figure 4-3 shows the displacements measured by TMA-BX-1 (located parallel and approximately 0.33 m from the heater, above and to the south) through 31 May 1997. The anchor locations in x,y,z coordinates for MPBX-1 are given in Appendix C. The displacements given in Figure 4-3 are expressed relative to the borehole collar, with BX-1-1 deepest in the borehole and BX-1-6 nearest the borehole collar. The y-coordinates for each of the TMA-BX-1 anchors are spaced approximately 1 m apart from the bottom of the borehole (anchor BX-1-1 at 6.883 m to anchor BX-1-6 at 2.043 m along the y-coordinate axis).

The data presented in Figure 4-3 are corrected for thermal expansion of the MPBX rods. These rods for MPBX-1 connect each anchor individually with the borehole collar where the vibrating wire displacement transducers are located. The rods are constructed of carbon fiber and have a reported linear thermal expansion coefficient of  $1.48 \times 10^{-6}/^{\circ}\text{C}$  (GeoKon, 1997). The linear thermal expansion of the rods connecting each anchor is calculated from the thermocouples located along their length and integrated for each incremental length between individual thermocouples. The data for MPBX-1 show general extension for all anchor locations through about day 50. After day 50, the displacements for anchors TMA-BX-1-6 and TMA-BX-1-2 change directions and become compressive. Note that only anchor TMA-BX-1-6 is truly compressive; anchor TMA-BX-1-2 merely becomes less extensional. About day 80, anchors TMA-BX-1-4 and TMA-BX-1-5 become less extensional. Anchors TMA-BX-1-1 and TMA-BX-1-3 remain extensional through about day 150 and stabilize at 2 mm of net extension. Anchor TMA-BX-1-1 experienced a slight change in displacement sign about day 90, but thereafter continued in an extensional mode. At about day 210, anchor TMA-BX-1-1 experienced a sudden increase in displacement. This is likely due to discrete fracture movement just on the collar side of the anchor, as none of the other MPBX-1 anchors show such movement. Further discussion of this behavior is given in Section 6 of this report. Anchor TMA-BX-1-4 continues a subtle relative compression from about day 90 through about day 200. Thereafter, anchor TMA-BX-1-4 displacement does not significantly change throughout the third quarter of heating. Several of the MPBX-1 gages appear to have failed as of 31 May 1997. The gage for anchor TMA-BX-1-3 failed around day 140. The gages for anchors TMA-BX-1-2 and TMA-BX-1-6 failed around day 205. The gage for anchor TMA-BX-1-1 failed around day 265. The reason for these apparent failures is unknown at this time. Following the cooldown phase, the MPBX-1 head will be removed and the gages examined. The results of these investigations will be related in future reports.



TRI-8117-5-0

Figure 4-1. Plan view showing locations of boreholes, MPBX anchors, wire extensometers, rock bolt load cells, borehole jack, and tape extensometers in the SHT block.



TRI-8117-6-0

Figure 4-2. Cross-section showing locations of boreholes, MPBX anchors, wire extensometers, rock bolt load cells, borehole jack, and tape extensometers in the SHT block.

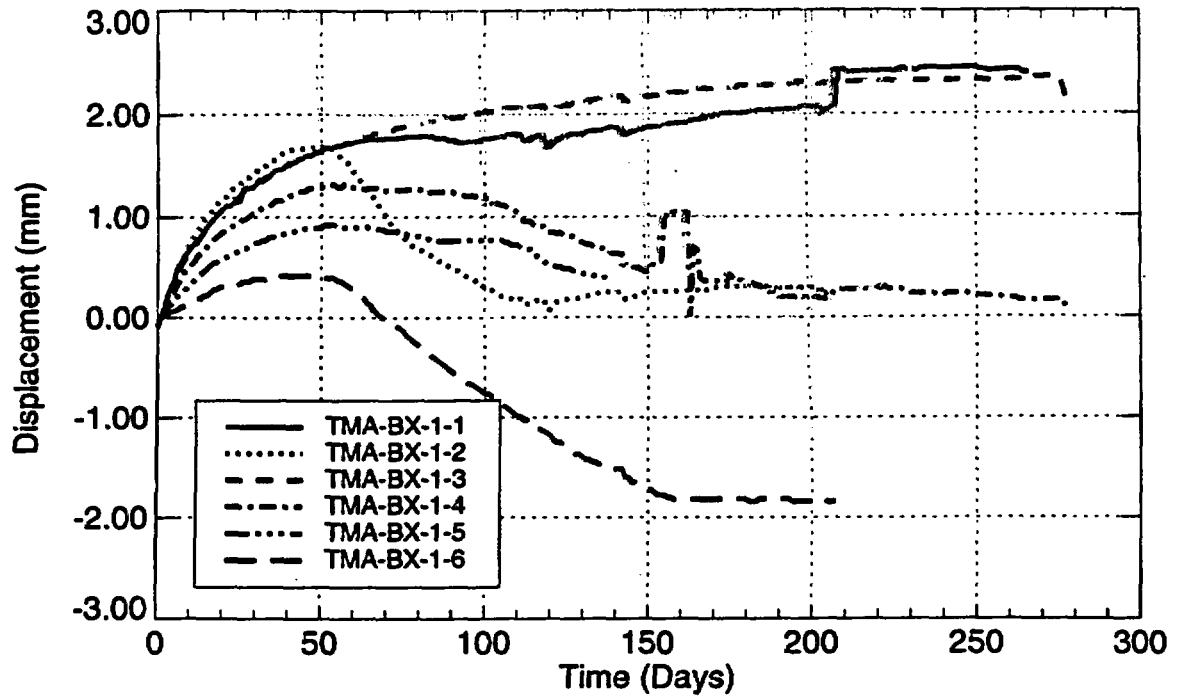


Figure 4-3. Displacement history for ESF-TMA-MPBX-1 (corrected for rod thermal expansion; extension positive).

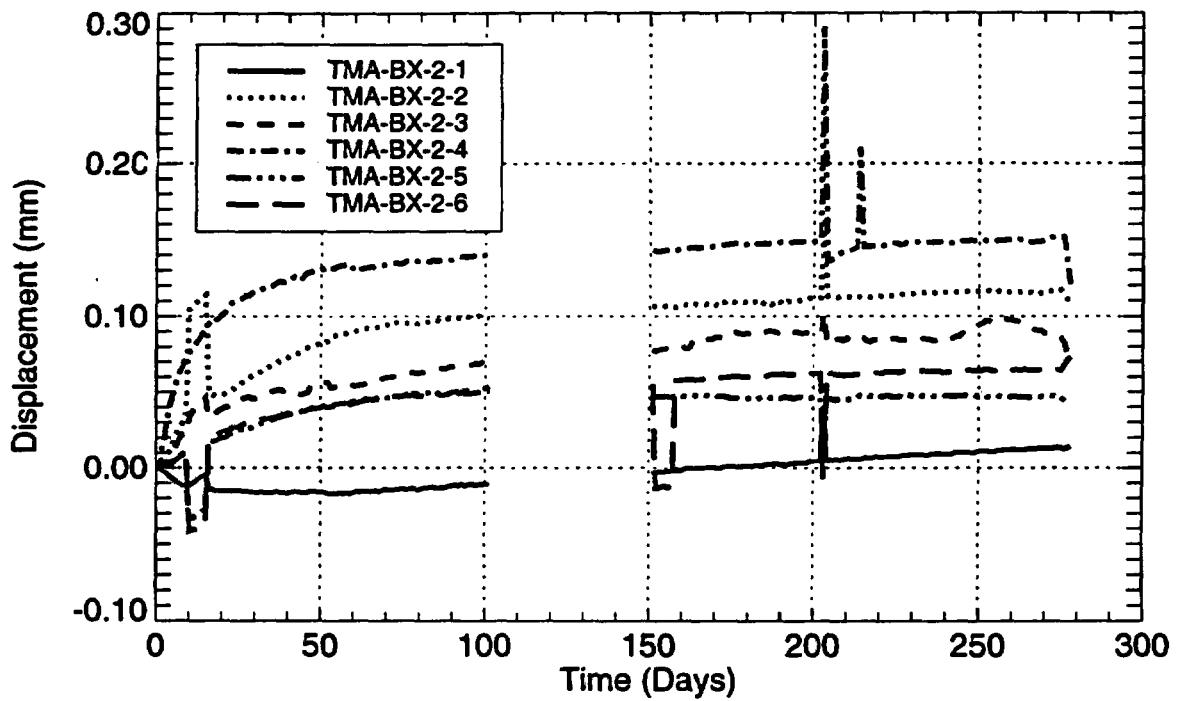


Figure 4-4. Displacement history for ESF-TMA-MPBX-2 (corrected for rod thermal expansion; extension positive). No data collected from about day 100 to about day 150 due to a blown fuse in the signal conditioner for the LVDTs.

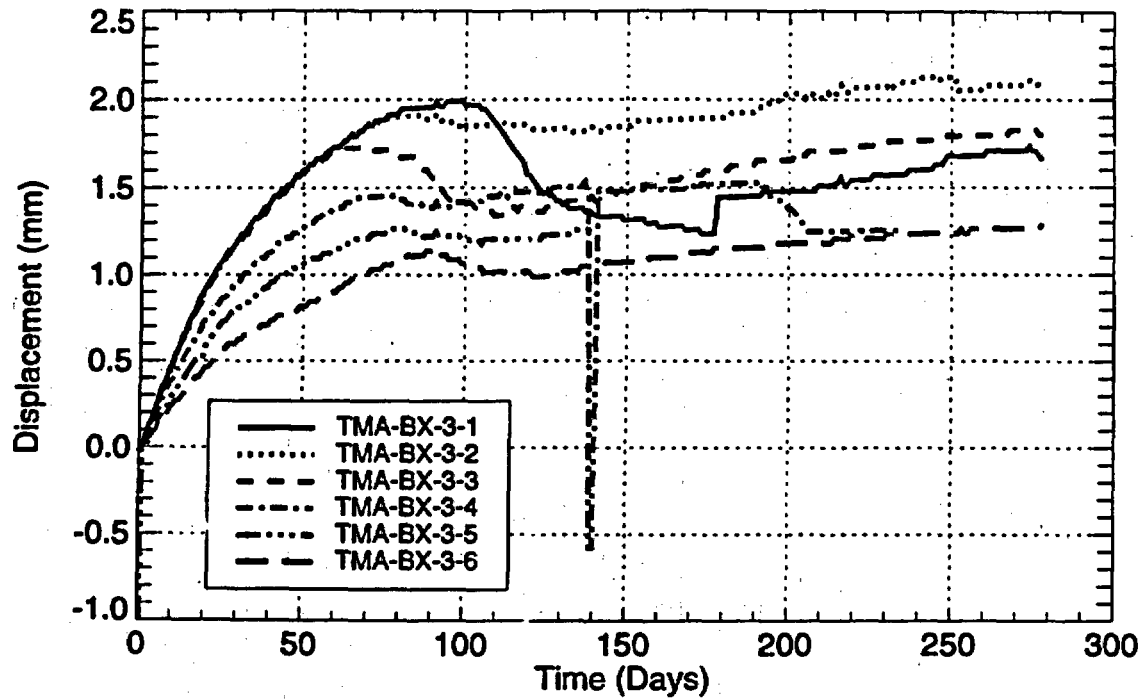


Figure 4-5. Displacement history for ESF-TMA-MPBX-3 (corrected for rod thermal expansion; extension positive).

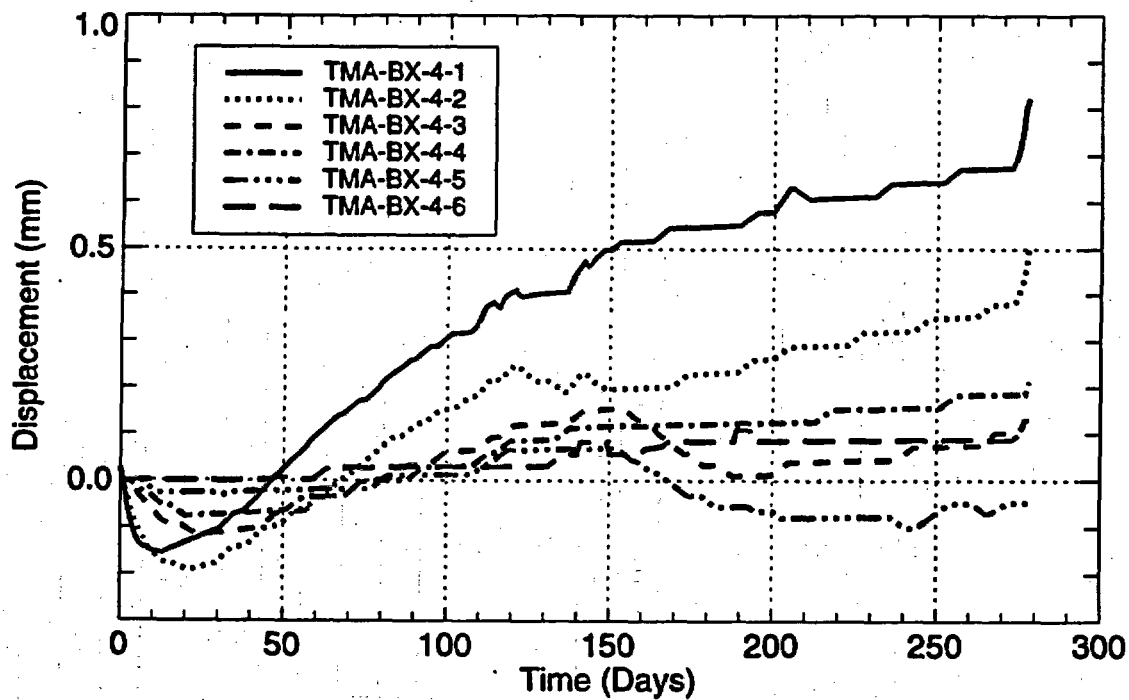


Figure 4-6. Displacement history for ESF-TMA-MPBX-4 (corrected for rod thermal expansion; extension positive).

Table 4-1. MPBX Displacement History (mm) (Corrected for Rod Thermal Expansion; Extension Positive)

Gage	Days after Startup																			
	0	14	28	42	56	70	84	98	112	126	140	154	168	182	196	210	224	238	252	266
TMA-BX-1-1	-0.0903	0.8491	1.2904	1.5386	1.707	1.7723	1.7967	1.7414	1.7478	1.8076	1.8731	1.879	1.9726	2.0128	2.0494	2.4287	2.418	2.4503	2.4292	2.402
TMA-BX-1-2*	-0.0797	0.9609	1.3925	1.6606	1.5712	0.9974	0.6131	0.3272	0.1345	0.1877	0.2518	0.2566	0.2726	0.3112	0.2959	0.2565	NA	NA	NA	NA
TMA-BX-1-3	-0.0808	0.8471	1.3092	1.5377	1.6929	1.8491	1.9417	2.0075	2.0275	2.0914	2.1798	2.1819	2.2459	2.2815	2.2891	2.3125	2.3228	2.3275	2.3392	2.3285
TMA-BX-1-4	-0.0582	0.6777	1.0119	1.2224	1.291	1.2626	1.2471	1.2077	0.9563	0.8047	0.6376	0.5601	0.3681	0.35	0.2027	0.2768	0.2839	0.2111	0.213	0.1613
TMA-BX-1-5*	-0.0373	0.4603	0.7178	0.8613	0.8949	0.8592	0.7615	0.7694	0.6772	0.4892	0.371	NA								
TMA-BX-1-6*	-0.0176	0.2194	0.3621	0.4187	0.369	-0.0035	-0.3849	-0.7106	-1.0241	-1.3237	-1.52	-1.7773	-1.8235	-1.8471	-1.8461	-1.8495	NA	NA	NA	NA
TMA-BX-2-1	-0.0002	-0.0057	-0.0156	-0.0155	-0.0166	0.0141	-0.0125	-0.0112	0.0352			-0.0029	0.0004	0.0015	0.0034	0.0059	0.0076	0.0096	0.0114	0.0129
TMA-BX-2-2	0.0014	0.1126	0.0586	0.0748	0.088	0.0944	0.0975	0.1003	0.1538			0.107	0.1083	0.1095	0.1104	0.1124	0.1134	0.1153	0.1162	0.1184
TMA-BX-2-3	-0.0007	0.0431	0.047	0.0498	0.054	0.0596	0.0648	0.0683	0.0904			0.0781	0.0847	0.0878	0.0886	0.0856	0.0851	0.0852	0.0971	0.092
TMA-BX-2-4	0.0024	0.2343	0.1135	0.126	0.133	0.1339	0.1368	0.1395	0.2827			0.1426	0.2119	0.1468	0.1483	0.143	0.1474	0.1482	0.149	0.1479
TMA-BX-2-5	-0.0012	-0.0283	0.0258	0.0363	0.0423	0.0461	0.0513	0.0497	0.0075			0.0471	0.0479	0.046	0.0467	0.0451	0.0467	0.0474	0.0497	0.0465
TMA-BX-2-6	0.0006	-0.0384	0.03	0.0371	0.0417	0.047	0.0485	0.0518	-0.0116			-0.0122	0.0593	0.0602	0.0616	0.0611	0.0634	0.0638	0.0692	0.0644
TMA-BX-3-1	0.0006	0.6725	1.1419	1.4522	1.6686	1.8499	1.9501	1.9921	1.8026	1.4568	1.3378	1.2199	1.2558	1.4447	1.478	1.5079	1.5446	1.6006	1.6811	1.7097
TMA-BX-3-2	-0.0248	0.6602	1.1455	1.4494	1.6866	1.8644	1.9107	1.8489	1.8607	1.8332	1.8212	1.8784	1.8889	1.9232	1.9805	2.0079	2.07	2.1006	2.0541	2.0828
TMA-BX-3-3	-0.025	0.6663	1.1372	1.4323	1.6633	1.7348	1.6754	1.4331	1.392	1.3902	1.4264	1.5078	1.567	1.6246	1.6552	1.7065	1.7386	1.7682	1.7872	1.7999
TMA-BX-3-4	-0.025	0.543	0.9215	1.1811	1.3545	1.4465	1.4083	1.4171	1.4754	1.4742	-0.5758	1.4864	1.4926	1.5231	1.4255	1.2483	1.2533	1.256	1.256	1.256
TMA-BX-3-5*	-2.4889	0.4198	0.7824	0.9812	1.1223	1.2094	1.2433	1.224	1.2039	1.2286	1.2589	NA								
TMA-BX-3-6	-0.0252	0.3247	0.5973	0.7617	0.8715	1.0047	1.1112	1.0895	1.0166	0.9909	1.0447	1.0724	1.1258	1.1534	1.1805	1.181	1.2084	1.2352	1.2368	1.2434
TMA-BX-4-1	0.0256	-0.1472	-0.1107	-0.0329	0.0727	0.1417	0.2313	0.2881	0.3986	0.4	0.5081	0.5141	0.5447	0.5489	0.5788	0.6067	0.6197	0.6399	0.6433	0.6718
TMA-BX-4-2	0.0006	-0.1772	-0.1796	-0.1073	-0.0613	0.0049	0.0936	0.1503	0.2092	0.2111	0.2425	0.197	0.2017	0.2309	0.2605	0.2885	0.292	0.3209	0.3495	0.378
TMA-BX-4-3	0.0259	-0.0965	-0.1139	-0.1017	-0.0655	-0.03	0.0041	0.0607	0.0924	0.1202	0.1495	0.1544	0.0816	0.0337	0.0117	0.0397	0.0423	0.0452	0.0733	0.1015
TMA-BX-4-4	0.0005	-0.0499	-0.0734	-0.0675	-0.0364	-0.0306	-0.0001	0.0293	0.0589	0.086	0.1138	0.1175	0.1196	0.1214	0.1237	0.1258	0.153	0.155	0.1571	0.1847
TMA-BX-4-5	0.0004	-0.0252	-0.0255	-0.0231	-0.0207	-0.0178	0.0102	0.0121	0.0399	0.066	0.0674	0.0696	-0.0055	-0.0553	-0.0792	-0.0779	-0.0767	-0.0755	-0.0487	-0.0725
TMA-BX-4-6	0.0003	0	-0.0004	0.0004	0.0011	0.0274	0.0283	0.0289	0.0299	0.0304	0.0564	0.0574	0.0833	0.0838	0.0844	0.085	0.0856	0.0862	0.087	0.0878

Note: No data available for MPBX-2 on days 126 and 140 due to a blown fuse in the signal conditioner.

NA: Not available.

\* Suspected failed gages.

The data for MPBX-1 presented in Figure 4-3 give a somewhat confusing picture of the displacements along the length of the borehole. Although all anchors but one exhibit net extension through 31 May 1997, the magnitudes and order of anchor displacements differ from the linear elastic predictions presented in Sobolik et al. (1996) after approximately 50 days of heating. These predictions suggested that the deepest anchor (BX-1-1) should exhibit the greatest extension and the shallowest (BX-1-6) the least, with the other anchors between dependent on their locations. Because the rock surrounding the SHT is fractured, and the thermal expansion of the rock blocks is volumetric, it could be expected that some regions surrounding the heater can experience net compression due to closing of fractures.

It should also be noted that the predictions presented in Sobolik et al. (1996) were simplified by evaluating only the  $\Delta Y$  coordinates for the anchors. Therefore, if all anchor coordinates change during heating, the predictions should be expected to differ from the measured values because the measurements include  $\Delta X$  and  $\Delta Z$  components as well as  $\Delta Y$ . It is also interesting to note that anchor BX-1-2 ceases compression about day 110 and exhibits slight extension through day 205, when the gage apparently failed. The trend of BX-1-2 parallels those of BX-1-1 and BX-1-3 for this time period. This type of behavior may be evidence of closing of fractures between anchors BX-1-1 and BX-1-2 from day 50 through about day 110. After day 140, the trends of BX-1-1 and BX-1-2 parallel each other, suggesting that fracture closure in this region has occurred. It is also important to note that the displacement trends for BX-1-4 roughly parallel those of BX-1-1 and BX-1-3 after about day 200. Again, this is suggestive of a mechanically closed fracture system. The temperatures measured along the length of MPBX-1 are presented graphically in Section 3.2 and in tabular form in Appendix C. The maximum temperatures measured on MPBX-1 are about 160°C and occur near the midpoint with significantly lower temperatures near the bottom anchor (BX-1-1). Additional discussion of all MPBX displacements is given in Section 6.0. The response of MPBX-1 will continue to be monitored and will be reevaluated in future data transmittals.

Figure 4-4 and Table 4-1 show the corrected displacements measured through the third quarter (31 May 1997) by TMA-BX-2, which is located approximately 0.69 m from the heater, above and to the left (north). The anchor locations in x,y,z coordinates for MPBX-2 are given in Appendix C. The y-coordinates for each of the TMA-BX-2 anchors are spaced approximately 1 m apart from the bottom of the borehole (anchor BX-2-1 at 7.093 m, anchor BX-2-6 at 2.073 m, and anchor BX-2-7 at 0.39 m along the y-coordinate axis). As previously discussed, TMA-BX-2 differs from the other MPBXs installed in the SHT by having the gages (high temperature LVDTs) installed in the borehole between each pair of anchors connected via Invar extension rods. Therefore, the relative displacement between anchors is measured and plotted in Figure 4-4. As such, the individual measured displacements should be much smaller than those measured from the other MPBX anchors, particularly the deep anchors. Also, because of the discreet nature of the LVDT measurements, it is possible that adjacent sets of anchors can record displacements of opposite sign (extension vs. compression). This is possible because of the variability of fracturing within the SHT block and the possibility of fracture closure resulting from rock matrix thermal expansion.

One of the primary purposes of TMA-BX-2 is to evaluate the reliability of the high temperature LVDTs to severe thermal-hydrologic environments. This type of LVDT is being considered for use in the drift-scale test where similar environments are expected to exist. Figure 4-4 exhibits

small displacements between all sets of adjacent anchors (less than 0.2 mm). The data also show gaps at various time intervals. These gaps result from power outages that blew the fuse in the signal conditioner for the LVDTs. To date none of the high-temperature LVDT gages appears to have failed.

For TMA-BX-2 the temperature distribution along the length of the borehole is given in Section 3.2 and Appendix C. For TMA-BX-2, thirteen temperature measurements were made (BX-2-TC-1 through BX-2-TC-13), one on each of the seven anchors and one on the extension rods between anchors. MPBX-2 temperatures are presented graphically in Figures 3-29 and 3-30, and in tabular form in Appendix C. The temperatures measured along the length of MPBX-2 are similar to those in MPBX-1 in that the maximum temperatures (about 115°C) are located near the midpoint of MPBX-2, with significantly lower temperatures at the end anchors (BX-2-1 and BX-2-7). MPBX-2 exhibits general extension between all pairs of anchors through the third quarter of heating (31 May 1997). Absolute relative displacements are low, with maximum adjacent anchor displacements of about 0.15 mm (for gage TMA-BX-2-4). The absolute relative displacement for gage TMA-BX-2-1 is slightly extensional but near zero through the third quarter of heating after displaying minor compression early in the test. The thermal expansion coefficient for Invar tubing, which is a low-thermal-expansion nickel alloy, is about 1.48 ppm/°C (personal communication, GeoKon, 1997). Additional discussion of all MPBX displacements is given in Section 6. The response of TMA-BX-2 will continue to be monitored closely to determine whether the trends observed through 31 May 1997 continue. The data will be reevaluated in future data transmittals.

Figure 4-5 and Table 4-1 show displacement data for TMA-BX-3, which is located approximately 1.5 m from the heater, above and to the right (south). The anchor locations in x,y,z coordinates for TMA-BX-3 are given in Appendix C. The y-coordinates for each of the anchors are spaced approximately 1 m apart from the bottom of the borehole (anchor BX-3-1 at 6.887 m to anchor BX-3-6 at 2.047 m along the y-coordinate axis). The data from TMA-BX-3 exhibit results consistent with those of MPBX-1. The data presented in Figure 4-5 show an increase in gage length (extension) for all anchor positions through about the first 70 days. From 70 to about 100 days, all anchors exhibit a gradual decrease in gage length. After about 100 days, all anchors except BX-3-1 reverse trend and increase extension through the second quarter of heating. Anchor BX-3-1 continues the relative compression from day 100 through about day 180, when it experiences a sudden extensional jump followed by continued extension throughout the third quarter of heating. The extensional jump at about day 180 is seen only in anchor BX-3-1; therefore it is likely that it results from discrete movement along a fracture or system of fractures located between anchors BX-3-2 and BX-3-1. This region corresponds with similar presumed behavior near anchor BX-1-1 (MPBX-1) near day 210. Also, pretest characterization suggested that a fracture zone extends through this region (TRW, 1996b). The change in slope of most of the anchor responses after about 70 days may be the result of matrix thermal expansion closing existing fractures, thus limiting additional thermally driven displacements until a greater volume of rock is heated. Thus, three-dimensional confinement effects may influence the response of some anchors. This possibility is discussed further in Section 6.

For TMA-BX-3 the temperature distribution along the length of the borehole is given graphically in Figures 3-37 and 3-38, and in tabular form in Appendix C. MPBX-3 temperatures are similar to those measured in MPBX-1 and MPBX-2 in that the maximum temperatures of about 75°C are

located near the center of the borehole, with lower temperatures at the end anchors (BX-3-1 and BX-3-6).

As stated, the general trends presented for MPBX-3 in Figure 4-5 are somewhat consistent with data for MPBX-1. Figure 4-5 suggests that volumetric expansion of the rock mass may have resulted in mechanically closing fractures beginning after about 60 days for anchor BX-3-3 through about 125 days. It is of interest to note that all anchors except BX-3-1 and BX-3-4 exhibit roughly parallel displacement histories after day 100 and including BX-3-1 after day 180. Additional discussion of all MPBX displacements is given in Section 6.0. For TMA-BX-3, originally nine temperature measurements were made, one on each of the six anchors (BX-3-TC-1 through BX-3-TC-6) and three on the extension rods near the collar (BX-3-TC-7 through BX-3-TC-9). The thermal expansion coefficient for carbon fiber is 1.48 ppm/°C (personal communication, GeoKon, 1997). For each anchor, the thermal expansion of the extension rod is determined by integrating the measured temperatures from the anchor to the collar. Naturally, the largest thermal correction is for anchor BX-3-1 because it includes the greatest length of extension rod.

Figure 4-6 and Table 4-1 show displacement data for TMA-BX-4 (relative to the borehole collar), which is located in a borehole drilled roughly horizontal and perpendicular to the heater. TMA-BX-4 is about 3.5 m from the heater collar in the y-coordinate direction (about 1.5 m from the collar end of the heater). The anchor locations in x,y,z coordinates for MPBX-4 are given in Appendix C. The x-coordinates for each of the MPBX-4 anchors are spaced at the bottom of the borehole (BX-4-1 at 0.768 m and BX-4-2 at about 1.428 m) and then at 1-m intervals to BX-4-6 at X=5.427 m. The data from TMA-BX-4 exhibit fairly consistent response, with the deepest anchor (BX-4-1) displacing the most. The data presented in Figure 4-6 show an almost uniform decrease in gage length (compression) for all anchor positions through about the first 30 days. After 30 days the anchors reverse the sign of the displacement and become extensional. Total corrected displacements for all anchors are small, less than 1.0 mm. It should be expected that anchor BX-4-1 would exhibit the greatest displacement over any time period because it represents the longest gage length.

The change in slope of most of the anchor responses after about 30 days is likely the result of rock mass thermal expansion. The anchors, particularly those nearest the heater, are directly affected by near-heater thermal expansion, whereas at distances farther from the heater no such expansion has yet occurred. Interestingly, anchors BX-4-3 and BX-4-5 exhibit a change in sign after about 150 days. The net result of this displacement change in sign resulted in a relative measured compression for BX-4-3 and BX-4-5 through about day 240, after which extensional trends are reestablished. As with the other MPBXs, it is possible or likely that the fractured nature of the rock mass is strongly influencing the MPBX displacements. Because the thermal expansion of the rock is volumetric, it is possible that as larger volumes of rock are heated, different fractures will be compressed at different times. It is possible that preexisting fractures closed at these anchor locations due to volumetric thermal expansion of the rock near the heater. This would explain the minor compression exhibited during early time. After a larger volume of rock is heated, the overall SHT block displacements overcome the near-field effects.

For TMA-BX-4 the temperature distribution along the length of the borehole is given in Figures 3-41 and 3-42, and in tabular form in Appendix C. For TMA-BX-4, twelve temperature

measurements originally were made (BX-4-TC-1 through BX-4-TC-12), one on each of the six anchors and at intermediate points on the extension rods. The thermal expansion coefficient for carbon fiber is 1.48 ppm/°C (personal communication, GeoKon, 1997). For each anchor, the thermal expansion for the extension rod is determined by integrating the thermal expansion for the measured temperatures and rod lengths from the collar to the anchor. Naturally, the maximum thermal correction is for anchor BX-4-1 because it includes the greatest length of extension rod as well as the highest temperatures. Additional discussion of MPBX displacements is given in Section 6.0. The response of TMA-BX-4 will continue to be monitored closely to determine whether the trends observed through 31 May 1997 continue. The data will be reevaluated in future data transmittals.

The data from the MPBXs show interesting trends that will be further discussed in Section 6.0. Many of the presented MPBX data exhibit observable closures in displacement at the end of the third quarter (31 May 1997). These changes are likely the result of the heater turn-off on 28 May 1997. Displacement trends shown in the MPBX data through 31 May 1997 suggest that closing of fractures may be occurring. Because of this behavior, additional modeling using discrete block models such as UDEC, DDA, or CJM may be required.

Wire and tape extensometer pins were placed on the three free surfaces of the SHT block (see Figures 4-1 and 4-2). These surface displacements are intended to augment the displacement data collected from the MPBXs and to provide qualitative "control" of the SHT free surfaces to support future modeling efforts. Because the measurements are made from short pins installed near the rock surface, they can be influenced by discrete block movement. The data from the wire extensometers are provided in tabular form in Table 4-2 and shown graphically in Figures 4-7 through 4-12.

Table 4-2. Wire Extensometer Data (mm) (Extension Positive)

Gage	Days after Startup										
	0	14	28	42	56	70	84	98	112	126	
TMA-WX-1	0	-0.1	0.08	0.02	0.03	0.27	0.2	0.33	0.49	0.47	
TMA-WX-2	0	-0.14	-0.15	-0.12	3.16	3.21	3.26	3.27	3.29	3.27	
TMA-WX-3	0	-0.03	-0.09	0.01	0.01	0.2	0.25	0.31	0.33	0.41	
TMA-WX-4	0	-0.83	-0.78	-0.78	-0.78	-0.58	-0.49	-0.66	-0.63	-0.51	
TMA-WX-5	0	-0.61	-0.66	-0.58	-0.52	-0.5	-0.44	-0.67	-0.4	-0.58	
TMA-WX-6	0	-2.45	-2.46	-1.98	-1.88	-1.89	-1.83	-2.95	-2.97	-2.97	
Gage	Days after Startup										
	140	154	168	182	196	210	224	238	252	266	
TMA-WX-1	0.39	0.66	0.66	0.55	0.55	0.55	0.55	0.55	0.44	0.59	
TMA-WX-2	3.17	3.52	3.51	3.51	3.51	3.5	3.5	3.5	3.41	3.38	
TMA-WX-3	0.28	0.69	-23.92	-23.92	-23.84	-23.99	-24.08	-24.08	-24	-24.03	
TMA-WX-4	-0.59	-0.2	-0.21	-0.04	-0.04	-0.09	-0.09	-0.1	-0.1	-0.12	
TMA-WX-5	-0.89	-0.48	-0.59	-0.65	-0.78	-0.82	-0.82	-0.83	-0.81	-0.82	
TMA-WX-6	-3.21	-2.75	-2.91	-2.74	-2.74	-3.06	-3.06	-3.06	-2.96	-2.92	

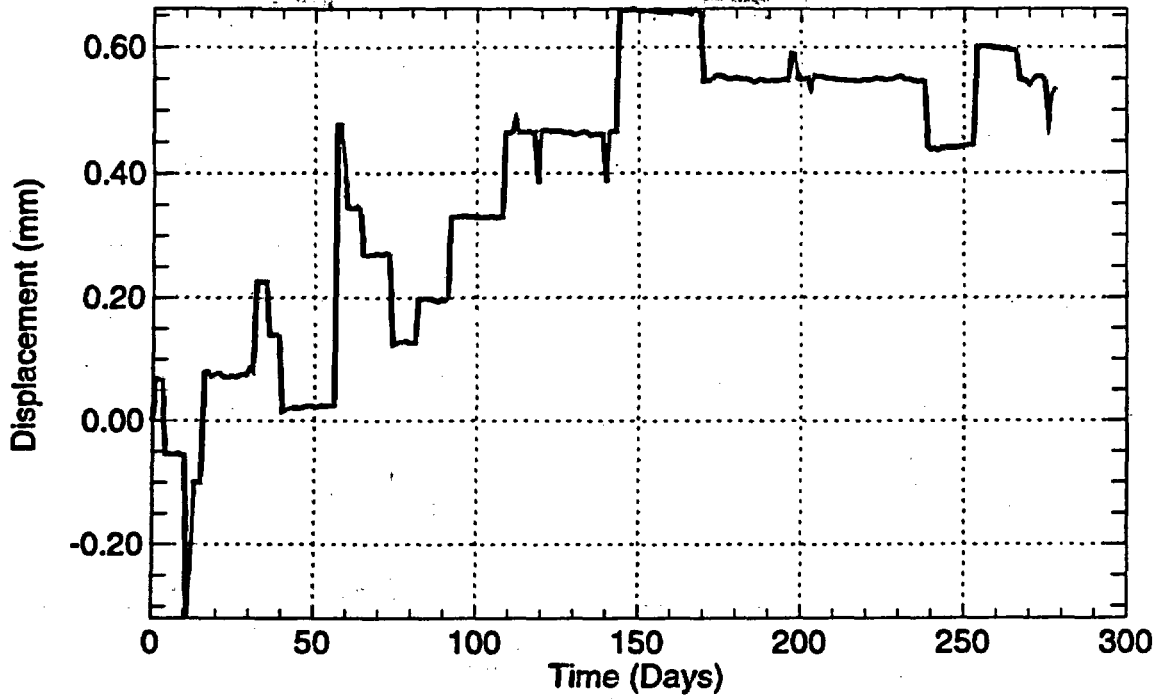


Figure 4-7. Displacement history for wire extensometer ESF-TMA-WX-1 (extension positive).

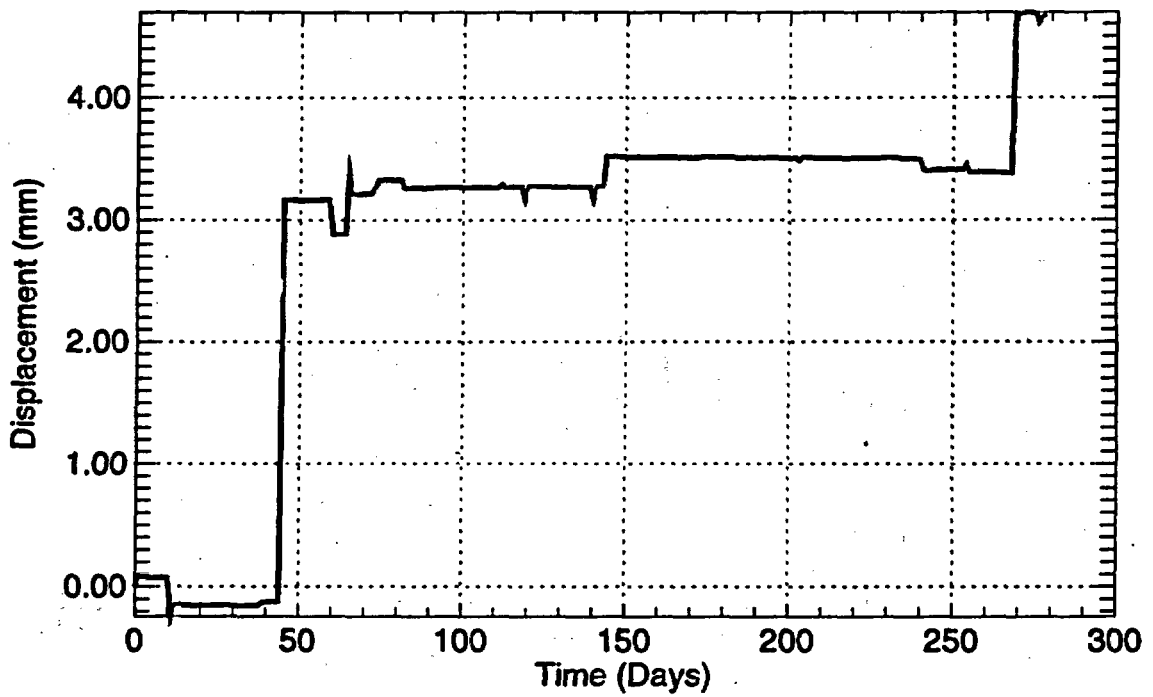


Figure 4-8. Displacement history for wire extensometer ESF-TMA-WX-2 (extension positive).

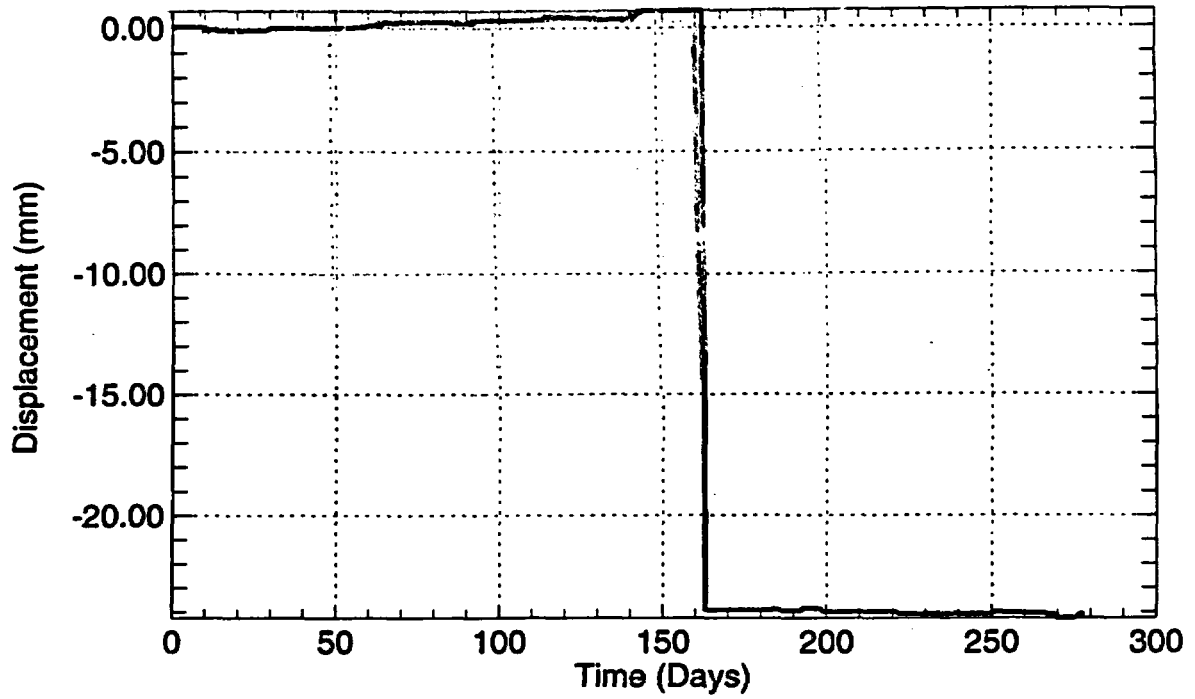


Figure 4-9. Displacement history for wire extensometer ESF-TMA-WX-3 (extension positive).

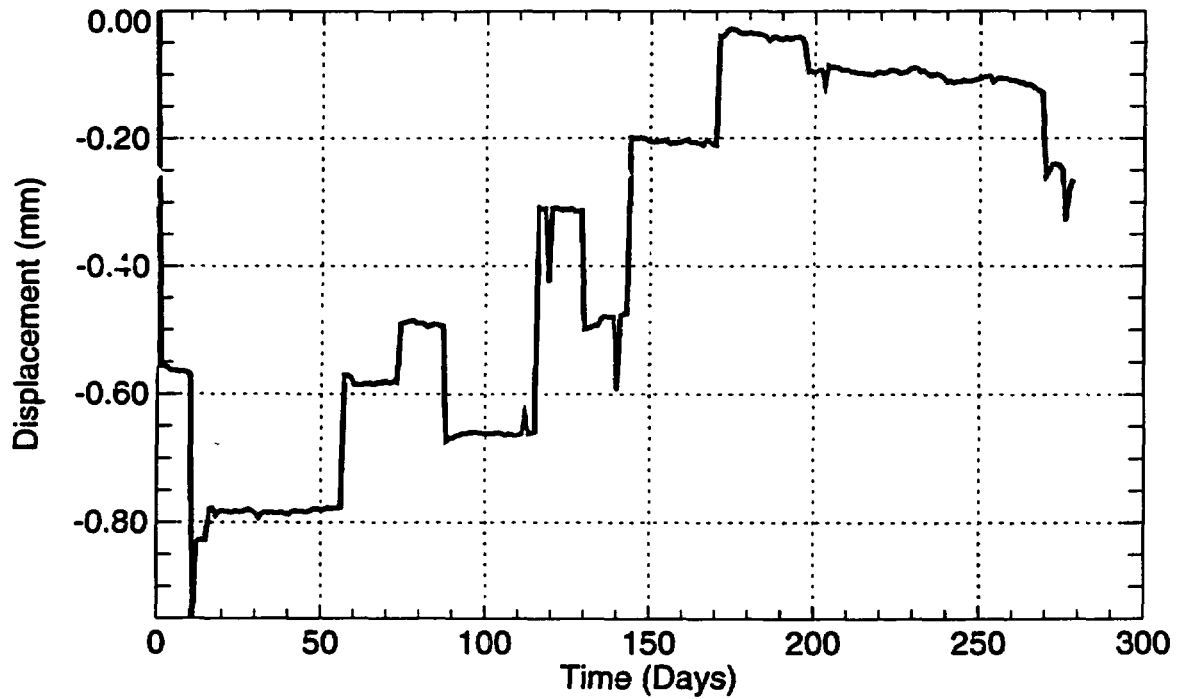


Figure 4-10. Displacement history for wire extensometer ESF-TMA-WX-4 (extension positive).

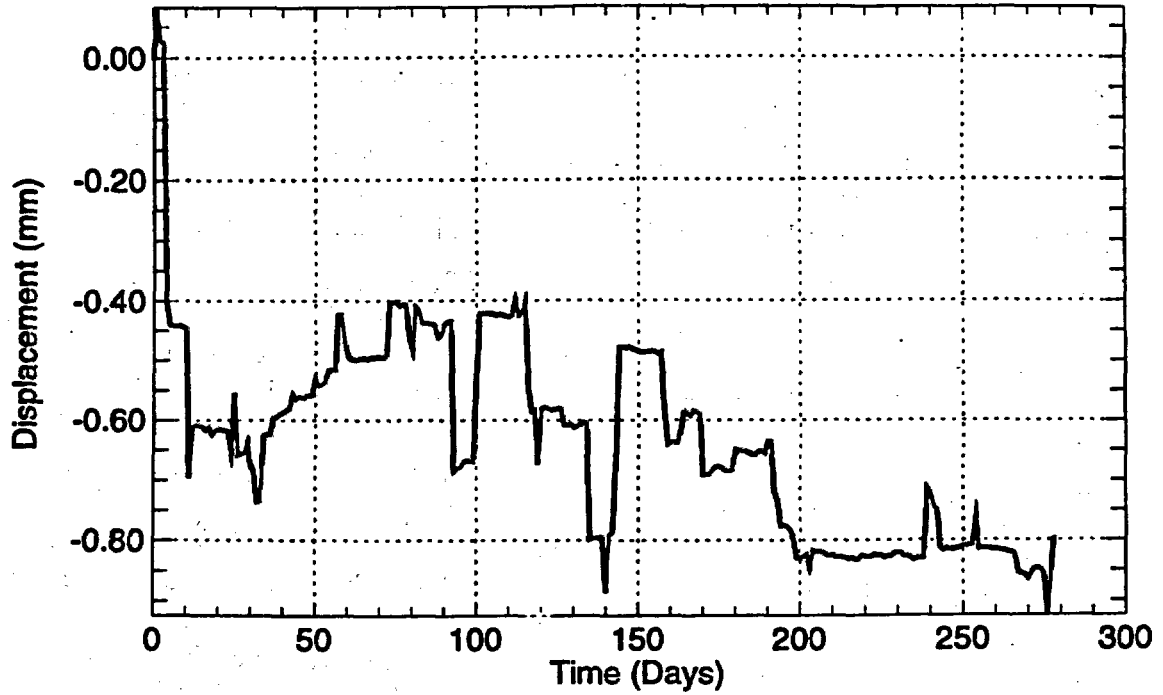


Figure 4-11. Displacement history for wire extensometer ESF-TMA-WX-5 (extension positive).

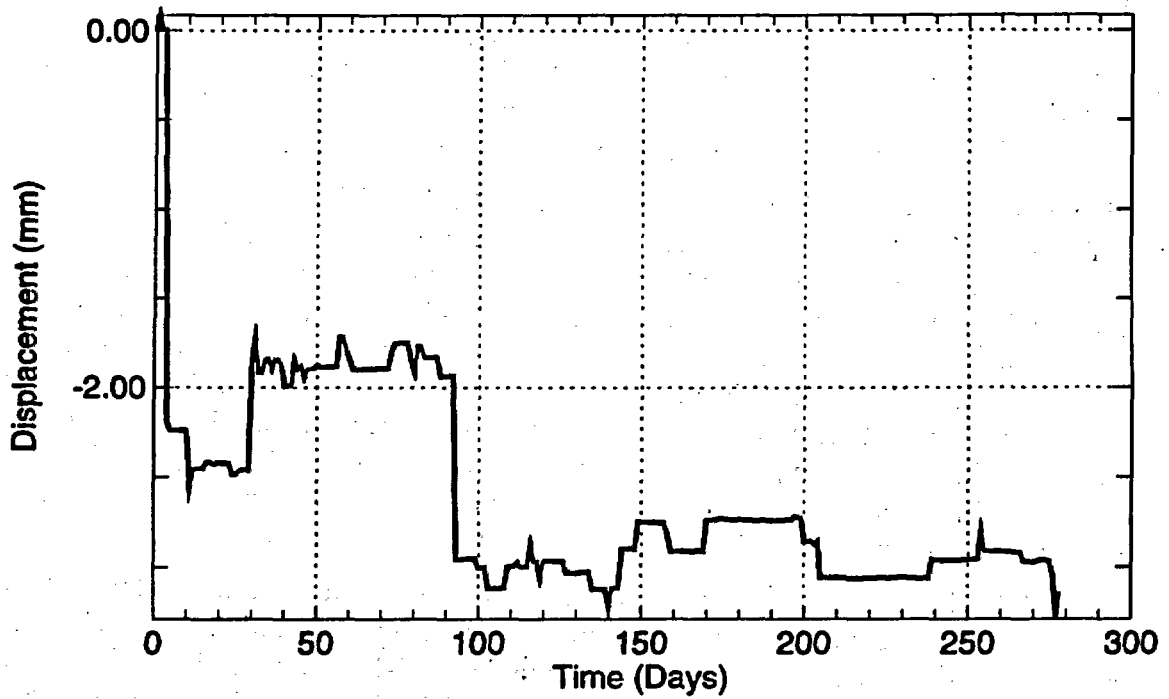


Figure 4-12. Displacement history for wire extensometer ESF-TMA-WX-6 (extension positive).

Figure 4-7 shows data from wire extensometer WX-1, which is located on the west face of the SHT block, about 2 m to the right of the heater. The exact pin locations are given in Appendix C. The data in Figure 4-7 show general extension of about 0.5 mm through 31 May 1997, although the displacements are relatively erratic, with maximum extensions of over 0.6 mm over the time period. This type of behavior can be expected from shallow-mounted surface pins. The response of WX-1 will continue to be monitored closely to determine whether the trends observed through 31 May 1997 continue. The data will be reevaluated in future data transmittals.

Figure 4-8 shows data from wire extensometer WX-2, which is located on the west face of the SHT block, about 2 m to the left of the heater. The exact pin locations are given in Appendix C. The data in Figure 4-8 show general extension of about 5.0 mm through 31 May 1997. The response of WX-2 shows little displacement through day 45, then jumps to about 3.5 mm through about day 270, then jumps to 4.5 mm at about day 270. This type of behavior can be expected from shallow-mounted surface pins. It is likely that the jumps at day 45 and day 270 are caused by a block loosening either at the top pin or the bottom pin, causing pin translation or rotation. Another possible explanation is that the pins located on the TMA side of the block should give extensional results, because the block is being heated near that free surface and the resulting thermal expansion of the rock would likely result in extension along both WX-2 and WX-1. The response of WX-2 will continue to be monitored closely to determine whether the trends observed through 31 May 1997 continue. The data will be reevaluated in future data transmittals.

Figure 4-9 shows data from wire extensometer WX-3, which is located on the south face of the SHT block, about 3.6 m east of the Thermomechanical Alcove. The exact pin locations are given in Appendix C. The data in Figure 4-9 show minor extension of about 0.6 mm through about day 160, then show a sudden drop to -25 mm thereafter. This type of behavior can be expected from shallow-mounted surface pins. It is likely that the jump at day 160 is caused by a block loosening either at the top pin or the bottom pin, causing pin translation or rotation. The response of WX-3 will continue to be monitored closely to determine whether the trends observed through 31 May 1997 continue. The data will be reevaluated in future data transmittals.

Figure 4-10 shows data from wire extensometer WX-4, which is located on the south face of the SHT block, about 5.6 m from the Thermomechanical Alcove toward the east. The exact pin locations are given in Appendix C. The data in Figure 4-10 show general extension of about 0.1 mm through 31 May 1997. The response of WX-4 shows erratic behavior, initially showing 0.8 mm of compression, then reversing at about day 55 and slowly extending throughout the second quarter of heating. This type of behavior can be expected from shallow-mounted surface pins. It is likely that the jumps initially and throughout the time period are caused by a block loosening either at the top pin or the bottom pin, causing pin translation or rotation. The response of WX-4 will continue to be monitored closely to determine whether the trends observed through 31 May 1997 continue. The data will be reevaluated in future data transmittals.

Figure 4-11 shows data from wire extensometer WX-5, which is located on the north face of the SHT block, about 3.7 m from the Thermomechanical Alcove toward the east. The exact pin locations are given in Appendix C. The data in Figure 4-11 show general compression of about 0.6 mm through 31 May 1997. The response of WX-5 exhibits erratic behavior, with frequent reversals of displacement. This type of behavior can be expected from shallow-mounted surface pins. The response of WX-5 will continue to be monitored closely to determine whether the

trends observed through 31 May 1997 continue. The data will be reevaluated in future data transmittals.

Figure 4-12 shows data from wire extensometer WX-6, which is located on the north face of the SHT block, about 5.7 m from the Thermomechanical Alcove toward the east. The exact pin locations are given in Appendix C. The data in Figure 4-12 show uniform compression of about 2.5 mm through 31 May 1997. The response of WX-6 exhibits somewhat erratic behavior, with frequent reversals of displacement. This type of behavior can be expected from shallow-mounted surface pins. Also note that WX-6 shows larger compression than WX-5, which is also expected and can be explained because WX-5 is located nearer the front free surface of the SHT, while WX-6 is located near the "pinned" backside of the SHT. The response of WX-5 will continue to be monitored closely to determine whether the trends observed through 31 May 1997 continue. The data will be reevaluated in future data transmittals.

Tape extensometer pins for measuring the roughly horizontal displacements of the SHT block are associated with each of the six wire extensometer stations. The x,y,z coordinate locations of the tape extensometer pins (denoted by WXM) on the SHT block are given in Appendix C. Tape extensometer measurements were made periodically through 31 May 1997. Tape extensometer WXM-1 is located near the WX-1 station about 0.5 m below the heater borehole collar level. A mating pin is located on the ambient side across the Thermomechanical Alcove. Tape extensometer WXM-2 is located near the WX-2 station about 0.1 m above the level of the heater borehole collar. A mating pin is located on the ambient side across the Thermomechanical Alcove. Tape extensometer WXM-3 is located near the WX-3 station just above the level of the heater borehole collar. A mating pin is located on the ambient side across the Thermomechanical Alcove Extension. Tape extensometer WXM-4 is located near the WX-4 station just below the level of the heater borehole collar. A mating pin is located on the ambient side across the Thermomechanical Alcove Extension. Tape extensometer WXM-5 is located near the WX-5 station just above the level of the heater borehole collar. A mating pin is located on the ambient side across the Observation Drift. Tape extensometer WXM-6 is located near the WX-6 station just below the level of the heater borehole collar. A mating pin is located on the ambient side across the Observation Drift.

The data from the manual tape extensometer measurements are given in Table 4-3. The data show that the horizontal cross-drift measurements are largest for WXM-1, WXM-2, and WXM-3, with all measurements compressive (i.e., shortening of the gage length). In other words, the surface pins are moving away from the SHT block in all cases. These displacements are consistent with the gross displacements measured using the MPBXs. In addition, the tape extensometer results for WXM-2 are consistent with the large displacements measured by the wire extensometer station WX-2. This is suggestive of gross surface displacements near the surface of the SHT block to the left of the heater. It is likely that either or both of the WXW-2 pins are located in a loose block of rock, which appears to have loosened almost immediately during the SHT. The subsequent data suggest that the block(s) stabilized somewhat with only minor additional displacement after 24 September 1996.

It should be noted, however, that the tape extensometer measurements represent contributions from both sides of each drift, although the contribution from the heated side is expected to be larger. The response of the tape extensometer pins will continue to be monitored closely to

determine whether the trends observed through 31 May 1997 continue. The data will be reevaluated in future data transmittals.

Table 4-3. Tape Extensometer Measurements for the SHT (Extension Positive)

TE Gage No.	Initial Reading (m)	$\Delta$ Displ. 9/24/96 (mm)	$\Delta$ Displ. 10/21/96 (mm)	$\Delta$ Displ. 12/19/96 (mm)	$\Delta$ Displ. 1/7/97 (mm)	$\Delta$ Displ. 2/11/97 (mm)	$\Delta$ Displ. 6/25/97 (mm)
WXM-1	5.40439	-0.58	-0.88	-0.96	-0.86	-1.24	-1.49
WXM-2	5.08575	-3.20	-3.15	-1.14	-3.78	-3.83	-4.29
WXM-3	4.67310	-0.71	-0.38	+24.59*	-0.63	-2.64	-0.89
WXM-4	4.33635	-0.56	-0.31	-0.66	-0.74	-0.94	-1.27
WXM-5	5.87639	-0.14	-0.47	-0.61	-0.69	-0.48	-0.98
WXM-6	5.83158	-0.39	-0.29	-0.08	-0.48	-0.81	-1.25

\*Note: Data for WXM-3 on day 12/19/96 likely erroneous reading.

## 4.2 Borehole Jack

No additional borehole jack tests were performed after the publication of the second quarter SHT report (SNL, 1997) because of mechanical problems with the jack. The discussion presented in the previous report is included here for completeness. Additional discussion about the significance of the borehole jack measurements is given in Section 6. Because the rock mass modulus measured using the borehole jack is directional (perpendicular to the borehole), no estimate of horizontal modulus anisotropy was possible during conduct of the SHT. It is likely that some anisotropy in modulus exists locally due to differences in fracture stiffness for each set of fractures present in the SHT block. Also, it is likely that the rock mass modulus varies across the repository block. Additional sets (orthogonal boreholes) of borehole jack measurements at various locations throughout the repository block would serve to provide critical information on the spatial variability and potential anisotropy of rock mass modulus. These borehole tests could be conducted in conjunction with additional single heater tests to evaluate the thermal dependence of rock mass modulus seen in the SHT testing. Bounding knowledge of the rock mass modulus is critical for interpretation of Exploratory Studies Facility heater tests as well as predictions of long-term stability of repository openings.

A single borehole (ESF-TMA-BJ-1) was drilled roughly horizontal and perpendicular to the SHT heater borehole for operation of the NX borehole jack (Goodman Jack) (see Figures 4-1 and 4-2). This nonpermanent borehole instrument is periodically inserted into the borehole and pressurized at various distances along the hole. Jack pressure and loading platen displacements are monitored, and rock mass modulus is determined from the pressure/displacement curve. For the SHT, borehole jack tests were run before heater startup (26 August 1996), again on 10 October 1996, on 26 November 1996, and on 18 March 1997 (days 0, 45, 92, and 204 from start of heating). Temperatures were measured in the borehole for each set of tests prior to insertion of the jack using a portable Type-K thermocouple probe at various points, and by manually taking temperature readings using a hand-held thermocouple reader. Jacking tests were run along the borehole at depths (from the collar) of 2.0 m, 3.0 m, 4.0 m, 4.51 m, and 6.2 m, although not all locations were tested on each of the dates. All borehole jack testing followed ASTM 4971-89 (Reapproved 1994) (ASTM, 1996) with minor exceptions. These exceptions include performing

multiple loadings on only 50% of the ambient (preheating) runs. No multiple loadings were conducted during the 10 October 1996, the 26 November 1996, or the 18 March 1997 tests to limit thermal effects on the jack.

Borehole ESF-TMA-BJ-1, located about 5.5 m from the front (west) face of the SHT block, is collared in the Observation Drift and is oriented toward the heater. As such, the borehole is expected to exhibit a temperature gradient from the bottom to the collar as the test is conducted. This allows for evaluation of the effect (if any) of increased temperature on the measured rock mass modulus. Figures 4-1 and 4-2 show the general location of borehole ESF-TMA-BJ-1 and its location relative to the heater.

The NX borehole jack consists of two hydraulically activated steel loading platens approximately 20.3 cm long, which apply a unidirectional load to a nominal 7.62-cm diameter borehole wall. The maximum jack pressure is 69 MPa, and the maximum platen displacement is 0.63 cm. The total displacement of both platens is 1.27 cm, with total jack diameter at 8.25 cm. Platen displacement is measured using LVDTs (one for each platen). The platens pressurize 90° of the borehole wall on each side. Jack pressure is applied using an Enerpak hand pump. Typically, the jack is pressurized in 3.44 MPa (500 psi) increments to 55.2 MPa (8000 psi), then back to zero, with LVDT readings recorded during both loading and unloading.

The historical use of the borehole jack has shown that corrections must be taken into consideration for the mismatch between borehole and platen radii, longitudinal bending of the platens, and tensile cracking of the intact rock or opening of existing fractures. The use and interpretation of the borehole jack is discussed at length in several references: ASTM (1996), Heuze and Amadei (1985), and elsewhere. The jack is inserted into the borehole and platens are slowly expanded until the pressure just begins to rise. The resulting LVDT readings represent the initial borehole diameter and are used for calculations of borehole wall displacement under pressure. The jack pressure is increased in increments to the desired maximum pressure and then decreased in similar increments. Because of the necessary data corrections, as described in ASTM D4971-89, the calculated minimum pressure to achieve "full platen contact" based on the approximate borehole diameter (7.57 to 7.90 cm) was about 21 MPa (3000 psi). For the tests conducted on 26 August 1996, the maximum pressure applied to the rock by the jack was limited to about 34.5 MPa. For all subsequent tests, the maximum pressure was limited to about 55.2 MPa. Also, it should be noted that Equation 1 in ASTM D4971-89 is incorrect. Equation 6 from Heuze and Amadei (1985) was used to determine the calculated modulus.

The initial tests conducted on 26 August 1996 included one test in which the load cycle was repeated. For subsequent testing, each location in the borehole was tested only once to minimize the effects of elevated temperature on the jack. The locations within the borehole were retested to evaluate potential changes in the rock mass modulus resulting from thermal expansion of the surrounding rock mass.

The data from the borehole jack testing conducted on 26 August 1996, 10 October 1996, 26 November 1996, and 18 March 1997 are presented graphically in Appendix D. The data shown in the figures have been analyzed using the procedure outlined in ASTM D4971-89. Only the data above a jack pressure of about 21 MPa were used to calculate the rock mass modulus. For most of the pressure/displacement curves, this also corresponds to the most linear portions of

each loading curve. The calculated rock mass moduli are given in Table 4-4 along with the rock temperature at the time of the test.

Table 4-4. Estimated Rock Mass Modulus in Borehole ESF-TMA-BJ-1 Using the Borehole Jack

Date	Distance from Collar				
	2.0 m	3.0 m	4.0 m	4.51 m	6.2 m
Rock Mass Modulus GPa (Temp °C)					
8/26/96	6.9 (25)	3.71 (25)	No test	No test	No test
10/10/96	10.3 (27.5)	10.3 (27.7)	8.3 (30.2)	6.0 (34)	No test
11/26/96	<i>Results discarded (31.1)</i>	10.2 (35.9)	<i>5.71 (46.4)</i>	<i>5.01 (55.4)</i>	8.4 (141.8)
3/18/97	<i>Results discarded (35)</i>	6.3 (41)	<i>10.3 (52)</i>	<i>5.7 (58.7)</i>	22.8 (143.1)

Note: Italicized calculated moduli are based on field data in which the difference between the two borehole jack LVDT readings slightly exceeded the limits set in ASTM D4971-89. The fractured nature of the rock made setting the jack difficult. Discarded results were for data that far exceeded ASTM D4971-89 limits.

The results from the borehole jack testing show that the measured rock mass modulus ranges from about 3 to 23 GPa. The highest value is for the deepest measurement location in the borehole (~6.2 m from the collar). This location corresponds to roughly 0.33 m from the heater borehole located about 1.5 m from the end of the heater. The previous measurement at this location on 26 November 1996 showed a modulus of only 8.46 GPa. The large increase in modulus may be consistent with the closing of fractures due to thermal expansion in this region. The data are also consistent with some of the MPBX data, which may suggest fracture closure as well. All the other borehole jack data are relatively low, less than about 10 GPa. These values are considerably less than the intact modulus of about 32.4 GPa measured on intact samples of the Topopah Spring Welded Tuff and from the rock mass value estimated using the Rock Mass Rating (RMR) technique outlined in Serafim and Periera (1983). It is not known what impact these lower moduli have on the overall SHT block performance; however, the potential impact will be evaluated in upcoming evaluations. The data presented in Table 4-4 include italicized results in which the two LVDT readings (far and near) differ by slightly greater than 0.02 in. at the maximum test pressure. According to ASTM D4971-89, these data should be discarded because of uneven loading. The fractured nature of the rock surrounding the borehole made it difficult in some cases to "set" the borehole jack at those locations. However, the data presented represent only slight deviation from the ASTM D4971-89 criteria and are presented to qualitatively assess modulus difference along borehole BJ-1. The italicized data should not be used in calculations requiring rock mass modulus.

The rock mass modulus information presented in Table 4-4 and Appendix D does not exhibit identifiable trends either spatially, temporally, or thermally, with the exception of the bottom hole measurements. The reported low values of modulus could be the result of the relatively small volume of rock energized (~0.15 m<sup>3</sup>) and as such could be overly influenced by nearby fractures. Additional tests may be conducted along the length of borehole BJ-1 during cooldown. The data will be evaluated to determine if the change in temperature influences rock mass modulus. Measurements will continue to be made on a periodic basis and will be presented in future data evaluations.

### 4.3 Rock Bolt Load Cells

Eight rock bolt load cells were installed on Williams B7X Hollow Core rock bolts as part of the SHT. The objective is to evaluate qualitatively the effects of elevated temperature on bolt performance by (1) monitoring load changes during the test, (2) post-test evaluations of the bolt/grout/rock interface, and (3) pull testing selected bolts to failure after heating and subsequent cooling. Each rock bolt included one vibrating wire load cell (load washer) that was installed between cover plates and adjustable angled washers. This entire assembly was bolted to the Williams bolt on the cold side of the insulation.

Four of the rock bolts were installed on the heated side of the Thermomechanical Alcove below the level of the heater. Another four rock bolts were installed on the opposite cold side of the Thermomechanical Alcove. The rock bolts and load cells were installed during July 1996. Initial readings were taken using a hand-held GeoKon readout box, prior to connection to the DAS. The load cells each contain three strain gages, and the total load acting on the cell is calculated by averaging the measurements from all three.

The locations of the rock bolts instrumented with rock bolt load cells (RBLCs) are shown in Figures 4-1 and 4-2. Four RBLCs were installed on the heated side of the west face of the SHT block (RB-1, RB-2, RB-3, and RB-4), and four were installed on the opposite ambient side of the Thermomechanical Alcove (RB-5, RB-6, RB-7, and RB-8). The gage locations for rock bolts are given in Appendix C. The RBLC data are presented in Figures 4-13 through 4-20. The data are presented as load (lb.) versus time from the start of heating (day zero). The data are also given in tabular form in Table 4-5.

Table 4-5. Rock Bolt Load Cells, Load Versus Time

TMA RLBC Gage	Days after Startup									
	0	14	28	42	56	70	84	98	112	126
	Average Load (lb.)									
RB-LC-1-AVG	22662	22262.8	22158	21732.3	21537.1	21444.1	21407.5	21380.8	21340.3	21308.5
RB-LC-2-AVG	14859.4	14739.7	14708.6	14680.1	14643.7	14597	14559.8	14522.5	14496.5	14449.6
RB-LC-3-AVG	22428	22402.2	22378.7	22348.4	22317.5	22281	22262.3	22243.2	22231	22224.1
RB-LC-4-AVG	16663.9	16602.8	16580.3	16558.8	16522.1	16496.6	16467.4	16446.3	16424.2	16407.5
RB-LC-5-AVG	25971.9	25928.5	25887	25856.6	25829.3	25802.6	25783.4	25765.5	25748.7	25738.1
RB-LC-6-AVG	14642.7	14633.2	14632.7	14627.3	14619.4	14609.5	14601.2	14595.9	14589.2	14573.7
RB-LC-7-AVG	4932.6	4921.1	4919.7	4911.8	4904.3	4893.6	4890.9	4883.8	4877.5	4873
RB-LC-8-AVG	16862.8	16818.5	16783.6	16758.7	16738.7	16605	16592.7	16575.4	16566	16561.5
TMA RLBC Gage	Days after Startup									
	140	154	168	182	196	210	224	238	252	266
	Average Load (lb.)									
RB-LC-1-AVG	21279.7	21254.3	21206.3	21176.9	21161.2	21145.9	21127.1	21112.2	21100.9	21102.1
RB-LC-2-AVG	14422.7	14405.6	14389.9	14378.6	14369.9	14365.5	14353.4	14349	14342	14341.1
RB-LC-3-AVG	22214.2	22206.8	22201.1	22194.3	22189.6	22183.4	22176.4	22171.7	22165.3	22158.4
RB-LC-4-AVG	16394.3	16377.4	16361.5	16350.8	16340.4	16331	16320.2	16316.8	16312.1	16310.9
RB-LC-5-AVG	25728.1	25722.2	25714.1	25705.1	25698.3	25692.7	25683.1	25676	25665.6	25652
RB-LC-6-AVG	14567.1	14563.5	14562.3	14557.4	14553.9	14551.2	14549.3	14543.8	14543.4	14538.9
RB-LC-7-AVG	4866.9	4866.7	4867.2	4866.6	4868.2	4865.2	4863.2	4863.9	4864.1	4867.1
RB-LC-8-AVG	16552.8	16544.8	16538	16533.3	16528.6	16522.3	16516.4	16514	16503.2	16501.5

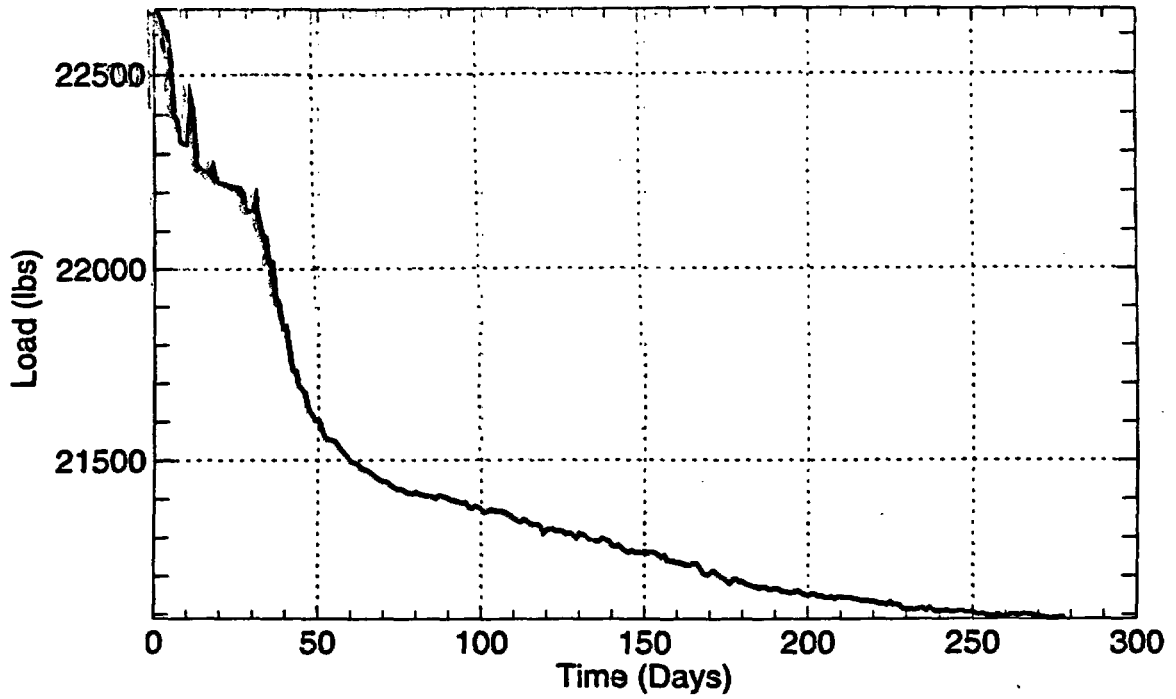


Figure 4-13. Rock bolt load history for TMA-RB-LC-1 (average).

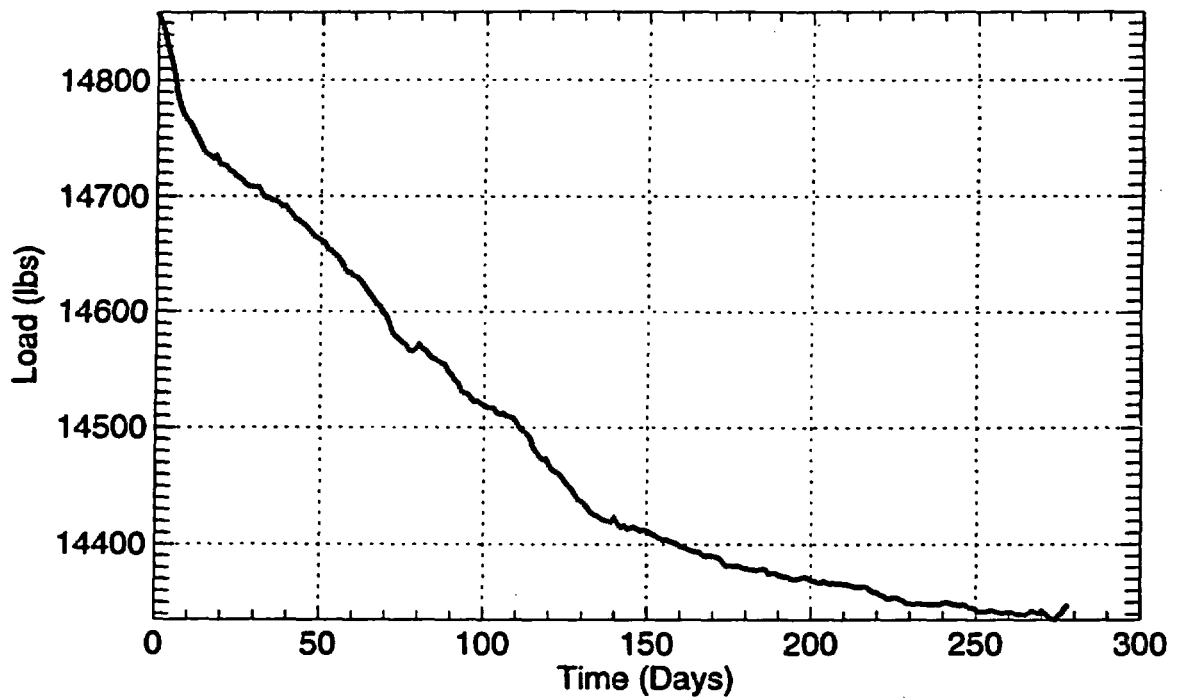


Figure 4-14. Rock bolt load history for TMA-RB-LC-2 (average).

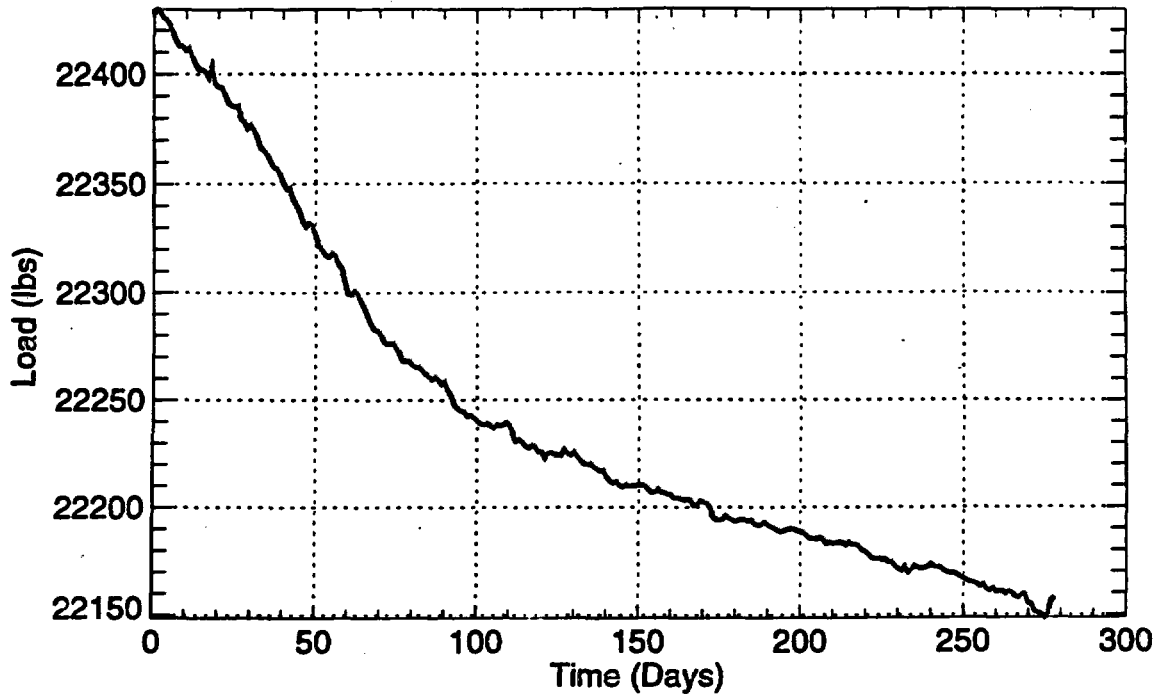


Figure 4-15. Rock bolt load history for TMA-RB-LC-3 (average).

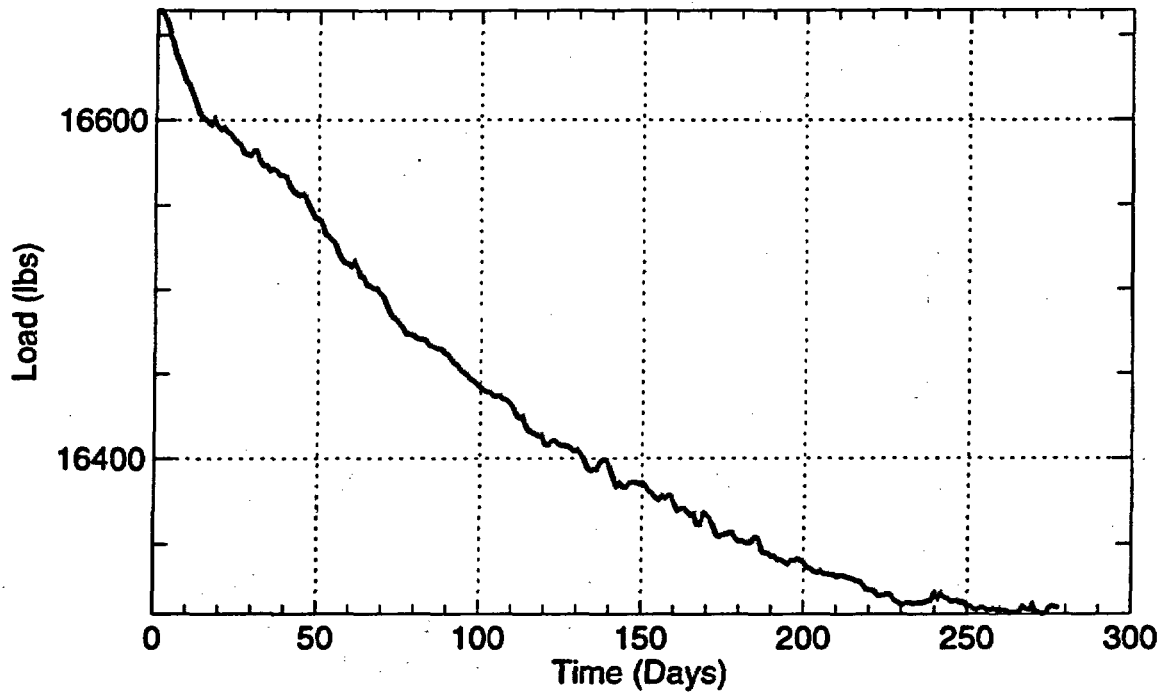


Figure 4-16. Rock bolt load history for TMA-RB-LC-4 (average).

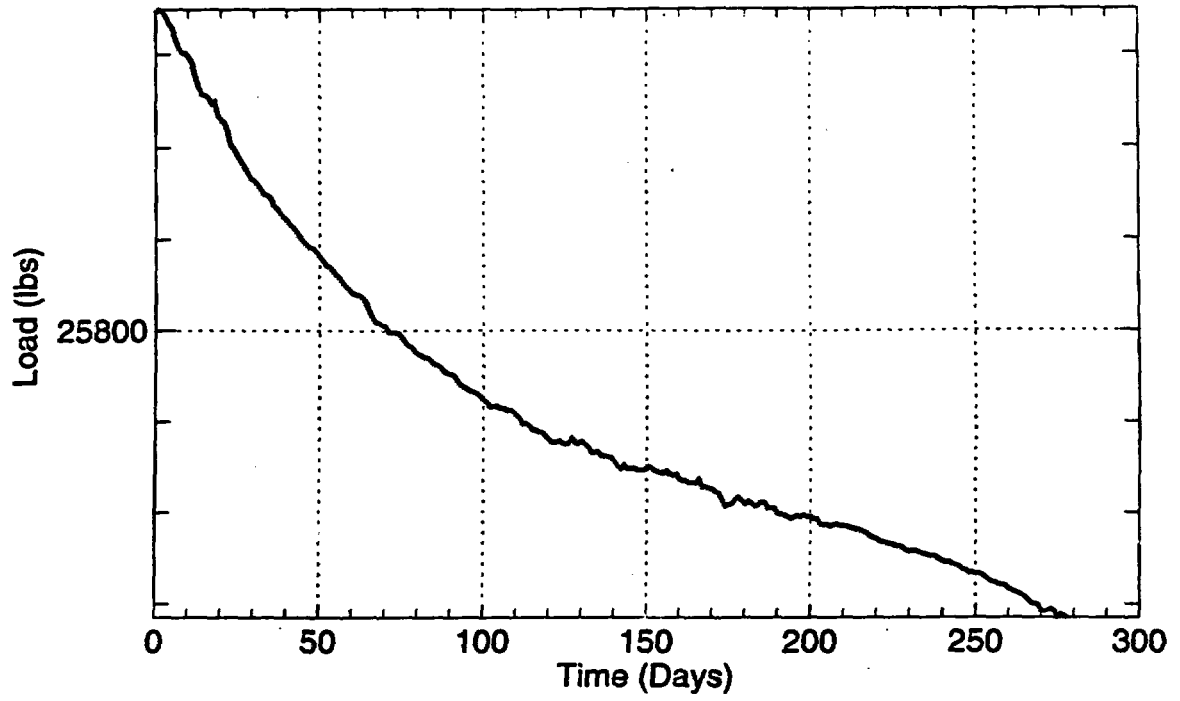


Figure 4-17. Rock bolt load history for TMA-RB-LC-5 (average).

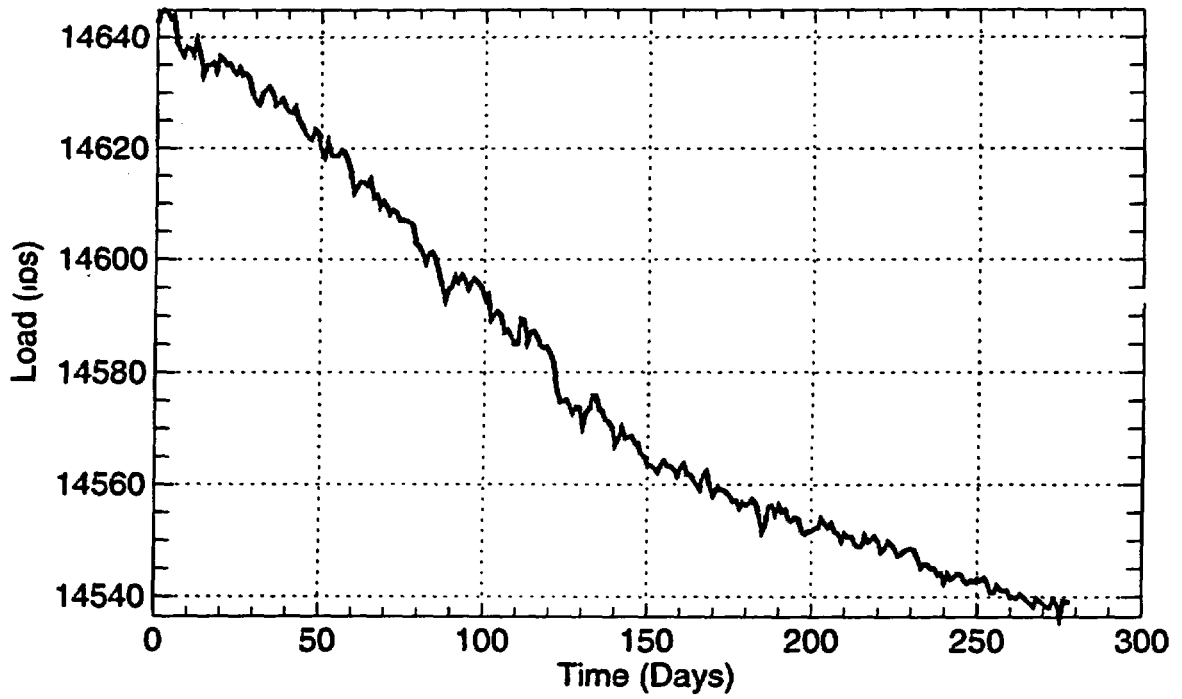


Figure 4-18. Rock bolt load history for TMA-RB-LC-6 (average).

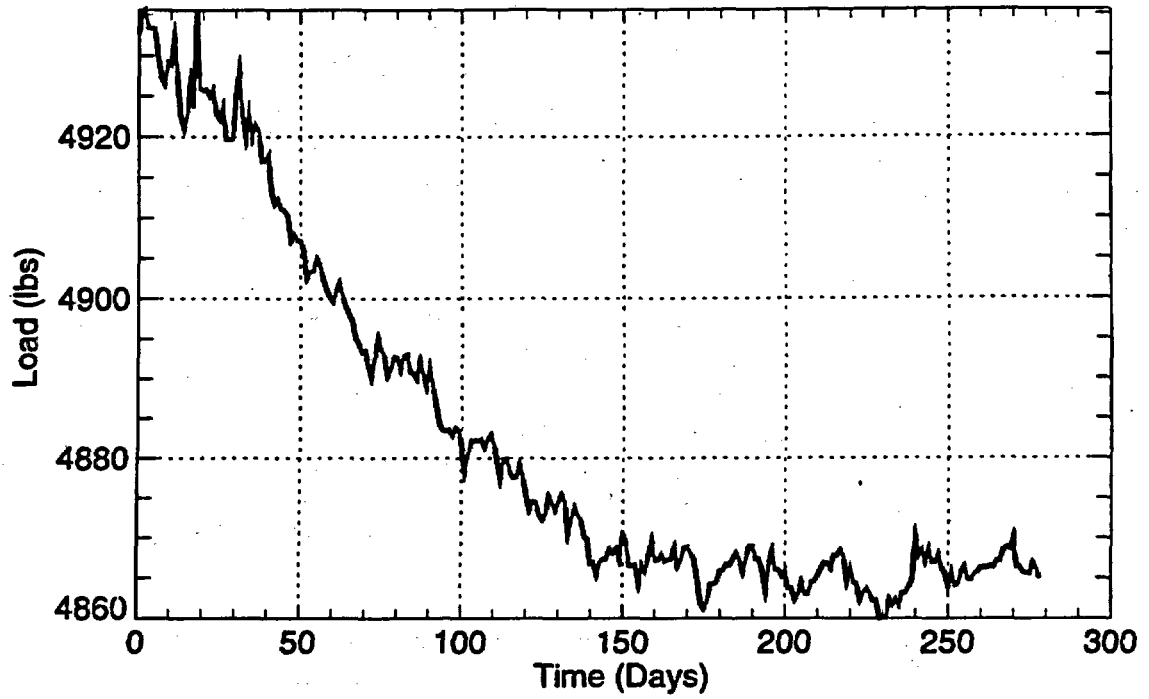


Figure 4-19. Rock bolt load history for TMA-RB-LC-7 (average).

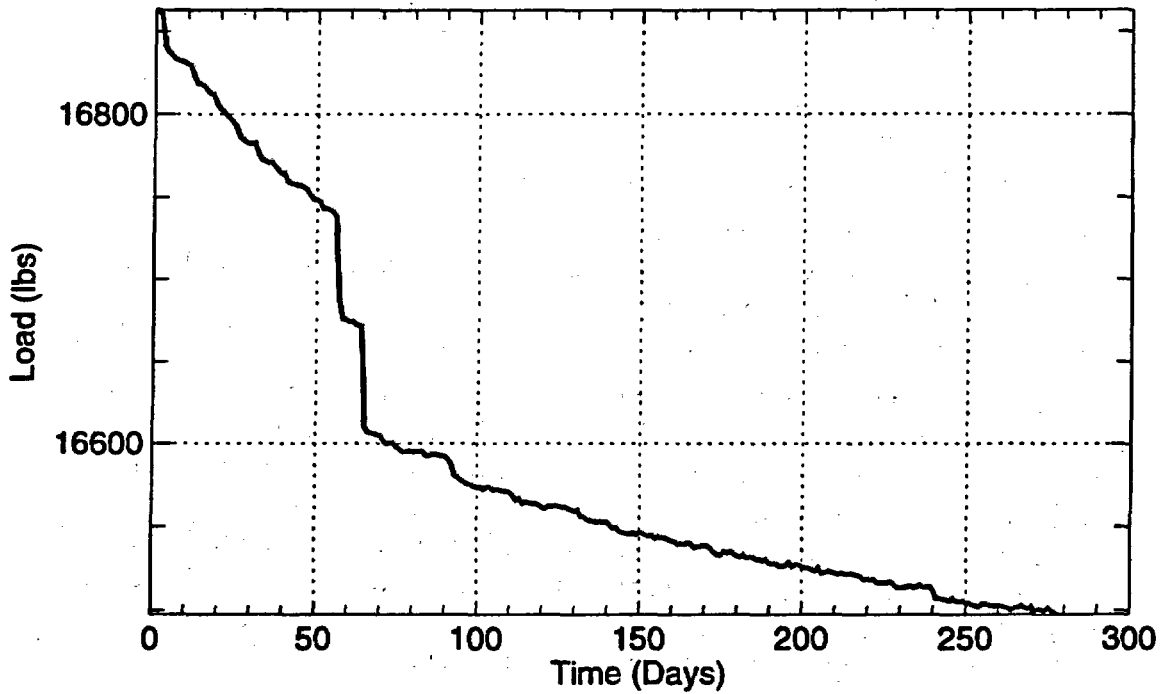


Figure 4-20. Rock bolt load history for TMA-RB-LC-8 (average).

The load cells are actually washers that fit over the rock bolts and are held in place by flat steel plates on either end and loaded with a nut. Each wedge washer includes three strain gages whose outputs must be averaged. Each RBLC was torqued to an initial load. Also, each of the three strain gages in each RBLC was monitored during torquing to maintain relatively uniform loading. If the loading was nonuniform, the wedge washers were adjusted and the nut retorqued. The important consideration in evaluating the rock bolt performance is the change in load from day zero, as well as the difference between the response of the heated versus the ambient rock bolts.

The data shown in Figures 4-13 through 4-20 show a general decline in load measured in all the RBLCs. Table 4-6 presents the RBLC data expressed as a percent change from day zero (heater startup). Although measurable, the decreases are all less than 7% of the initial load. Interestingly, the average percent decrease for the ambient RBLCs is 1.37%, whereas the average decrease for the heated RBLCs is 3.45%, although this decrease is most influenced by the decrease observed in RB-LC-1. Also, the two largest decreases are seen in the RBLCs that are nearest the heater (RB-1 and RB-2) and are therefore the hottest. It is too early in the testing to draw solid conclusions; however, the RBLCs will continue to be monitored, particularly the heated side. The data will be evaluated in future data transmittals.

Table 4-6. Change in Rock Bolt Load Cell Readings (8/26/96 – 5/31/97)

Gage	RBLC-1	RBLC-2	RBLC-3	RBLC-4	RBLC-5	RBLC-6	RBLC-7	RBLC-8
Percent Change	6.89	3.49	1.24	2.18	1.24	0.70	1.38	2.15
Location	Hot side	Hot side	Hot side	Hot side	Ambient side	Ambient side	Ambient side	Ambient side
	Average % change = 3.45				Average % change = 1.37			

#### 4.4 Miscellaneous Instrumentation

Miscellaneous instrumentation and equipment include

- power, current, and voltage monitors;
- air temperature (ambient) monitors in the Thermomechanical Alcove Extension, Thermomechanical Alcove, and Observation Drift; and
- insulation and vapor barrier installed on the three free surfaces of the SHT block.

Power, current, and voltage (EMF) were monitored continuously using a Magtrol power monitor. The temperatures of the ambient air within the testing facility were measured using Type-K thermocouples. The ambient temperatures, heater power, heater current, and heater voltage were recorded on the DAS. In addition, two 7.6-cm thick layers of insulation were installed on the three vertical surfaces of the SHT block. This insulation is aluminum foil-backed fiberglass insulation on the inner layer (which serves as the vapor barrier), and vinyl-backed fiberglass insulation for the outer layer. The insulation was attached to the rock surface using short copper "nails" at approximately regular intervals using high-temperature adhesive.

## 5. Performance of Measuring Systems

An important consideration for long-term thermal testing at Yucca Mountain is the reliability of the installed measurement systems. It is likely that some gages will fail or produce unreliable data during large-scale, long-duration thermal tests. Identification of unreliable measurement systems is necessary for evaluation of data and for planning future tests. Data and measurement systems for the SHT were presented in Section 3.0 of this document, as well as a discussion of likely failed, unreliable, or suspect gages. Table 5-1 presents failed, unreliable, and suspect thermomechanical gages installed in the SHT based on data collected through 31 May 1997.

Table 5-1. Failed, Unreliable, and Suspect Thermomechanical Gages Installed in the SHT

Gage	Reason for Omission
TMA-H-1-TCB-4	No data after heater activation
TMA-TC-2A-4	Erratic temperature readings
TMA-TC-4A-1	Erratic temperature readings
TMA-BX-1-TC-9	Erratic or missing temperature readings starting on day 210
TMA-BX-3-TC-1	Erratic temperature readings starting on approximately day 210
TMA-BX-3-TC-2	Erratic temperature readings starting on approximately day 210
TMA-BX-3-TC-7	Erratic temperature readings starting on day 140
TMA-BX-3-TC-9	Erratic temperature readings; no data after day 90
TMA-BX-4-TC-3	TC extension wire broken during installation
TMA-BX-4-TC-10	Missing data after day 120
TMA-RTD-15-20	Erratic temperature readings
TMA-RTD-15-23	Erratic temperature readings
TMA-RTD-17-26	Erratic temperature readings
TMA-RTD-23-11	Erratic temperature readings
TMA-RTD-23-19	Erratic temperature readings
TMA-BX-1-5	Broken vibrating wire in gage
TMA-BX-1-1	Suspected failed gage
TMA-BX-1-2	Suspected failed gage
TMA-BX-1-6	Suspected failed gage
TMA-BX-3-4	Suspected failed gage
TMA-BX-3-5	Suspected failed gage

The total number of failed, unreliable, and suspect thermomechanical measurement systems (20 gages) identified in the SHT through 31 May 1997 represent about 5% of the measurement systems installed. This represents quite a small percentage for such an experiment. The measurement systems will continue to be monitored, and the reliability will be evaluated in future reports.

### Measurement Uncertainty

There are several potential sources for error in the measurements presented in Sections 3 and 4 of this report. These errors originate either in the instrumentation itself or in the physical location of the gages in the SHT block. The gage accuracy, range, and precision of SNL-installed

instrumentation are presented in Appendix B. The location error is important for analyses of the reported data, particularly thermal data. For instance, the thermocouple probes installed and grouted in boreholes in the SHT (TMA-TC-1, TMA-TC-2, TMA-TC-3, TMA-TC-4, TMA-TC-5, TMA-TC-6, TMA-TC-7) were installed in EQ and BQ sized boreholes (4.8 cm to 6.0 cm diameter). The gage as-builts assume that the probes (nominally 0.6 cm diameter) are located along the centerline of the borehole. Naturally, the potential error in this location is equal to one borehole radius. Therefore the location uncertainty is about 2.4 cm to 3.0 cm. This location uncertainty is particularly important for thermocouples located in high thermal gradient areas such as are found near the heater. The location uncertainty is not nearly as important for displacement measurements because of the extremely small displacement gradients associated with the SHT.

The planned post mortem evaluations of the SHT block will include evaluations of instrumentation, including post-test calibrations (where possible). These evaluations can assist in quantification of some of the uncertainties in the SHT data.

## 6. Discussion

This section presents a brief discussion of the thermal and thermomechanical data from the SHT. The discussion will center on (1) comparisons between data and models for the temperature data through 31 May 1997 and (2) conceptual discussions of the thermomechanical data through 31 May 1997.

### 6.1 Thermal Data Discussion

In this section temperatures measured in the SHT block are compared to the latest available numerical models. Two of the models to which the data are compared are derived from the pretest low and high permeability models described in Sobolik et al. (1996). These models use bulk permeabilities of  $5.0 \times 10^{-15}$  and  $5.2 \times 10^{-12}$  m<sup>2</sup>, respectively. The original pretest models were based on a uniform thermal conductivity of 1.67 W/m/K for both wet and dry rocks. In the models compared to the data in this report, the rocks have a thermal conductivity that is a function of liquid saturation. For fully saturated rocks the thermal conductivity is 2.1 W/m/K, while the thermal conductivity of rocks from which all the liquid water has evaporated is 1.67 W/m/K. In addition to the low and high permeability models, the data are also compared to a new numerical simulation, which is referred to as the matrix permeability model. This model differs from the low and high permeability models in that fluid flow occurs only in the matrix, which is assigned a permeability of  $4 \times 10^{-18}$  m<sup>2</sup>. The fracture domain has been removed from the model and the system behaves as an unfractured porous medium with the properties of the matrix.

Figure 6-1 illustrates the measured and predicted temperatures as a function of time at the location of gage TMA-TC-1A-7, which is located about 41 cm away from the heater. Note the behavior of the model temperatures as the rock warms through the boiling point of water (96°C at the SHT elevation). In the high permeability model, the rock near this gage location remains at the boiling point for several weeks. As the water in the rock pores boils, all the thermal energy entering the rock near this gage location is devoted to boiling water rather than raising the rock temperature. After all the water has boiled off, the rock temperature begins to rise once again.

The low permeability model exhibits an inflection in the temperature profile near the boiling point, but not an isothermal period as did the high permeability model. When the rock near the location of gage TMA-TC-1A-7 reaches 96°C in the low permeability model, the water in the pores begins to boil, but the water vapor is somewhat inhibited from escaping from the pores of the rock, so the pore pressure begins to build. This increase in pressure causes the boiling point of water to rise. The result is that not all of the thermal energy entering the rock is consumed by the process of boiling water; a portion is devoted to raising the temperature of the rock.

In the matrix permeability model, the temperature at the location of gage TMA-TC-1A-7 rises smoothly through 96°C without the flat spots or inflections observed in the other two models. As the temperature in the model rises, minute amounts of liquid water vaporize but cannot escape from the pore space, so the pore pressure rises dramatically. This pressure increase very effectively inhibits evaporation of the pore water, and the liquid saturation remains near ambient levels, even up to temperatures of 160°C. Very little thermal energy is being devoted to boiling water, and most of the heat being input to the rock is going to raising the temperature. Because there is very little liquid or vapor flow in the system, heat is transferred in the rock almost entirely by conduction; convection is a relatively insignificant process.

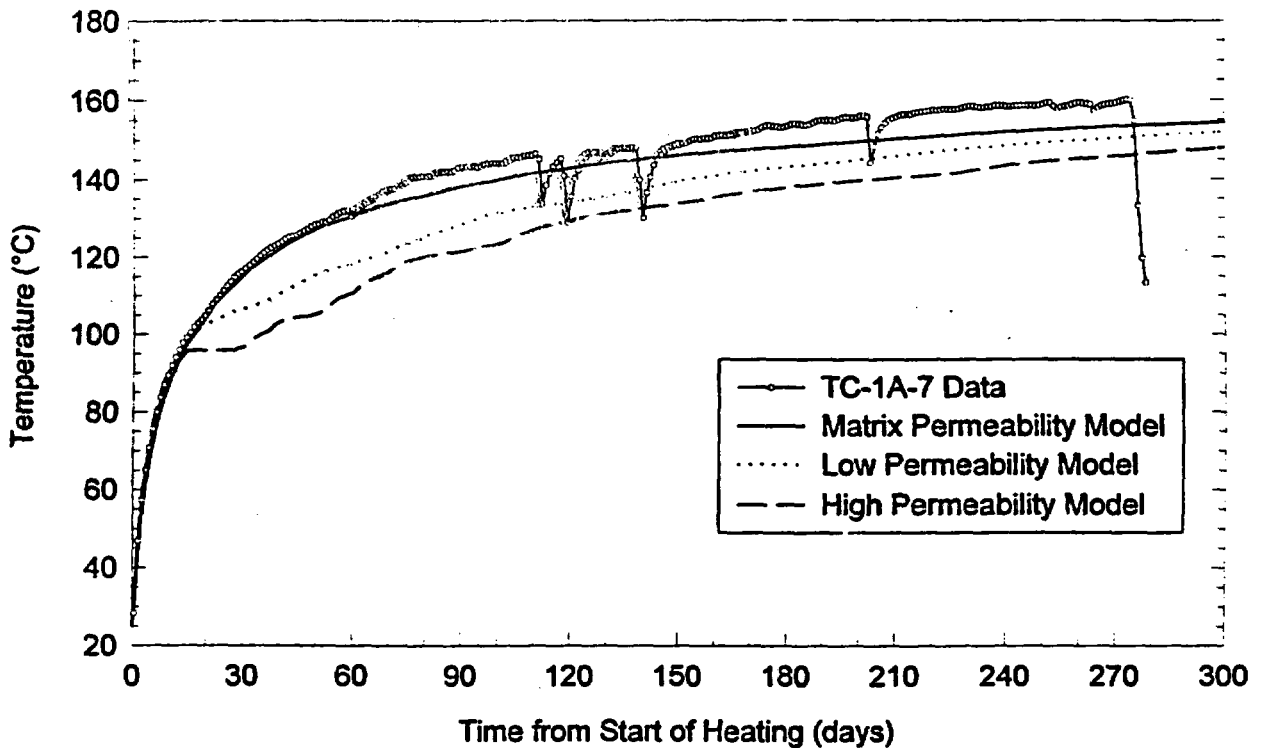


Figure 6-1. Temperature-time history at the heater mid-plane for gage TMA-TC-1A-7.

Note that the temperatures measured by TMA-TC-1A-7 exhibited a very smooth temperature profile as they warmed through the boiling point. Of the three numerical simulations, the matrix permeability model most closely matches the data recorded from this temperature gage.

In Figure 6-2 the temperatures measured by temperature gage TMA-TC-5A-7, located about 70 cm directly above the center point of the heater, are compared to the results of the three numerical predictions at the same location. As was the case for TMA-TC-1A-7, the measured and predicted temperatures agree very well up to about 96°C. In the vicinity of 96°C, however, the temperatures measured by TMA-TC-5A-7 deviate from the matrix permeability model and are somewhat closer to the temperatures predicted by the low permeability model. This response implies that some degree of convective heat transfer is occurring in the rock.

In Figure 6-3, the temperatures measured by temperature gage TMA-TC-4A-6, located 73 cm immediately below the center point of the heater, are compared to the numerically simulated temperatures at the same location. In this case there is a noticeable "flat spot" in the measured temperature profile at 96°C. This indication of thermal convection only persists for a few days, and then the measured temperatures begin to rise again. From day 70 onward, the measured temperatures rise somewhat more rapidly than predicted by the models, ultimately achieving a temperature intermediate between the low permeability and the matrix permeability models.

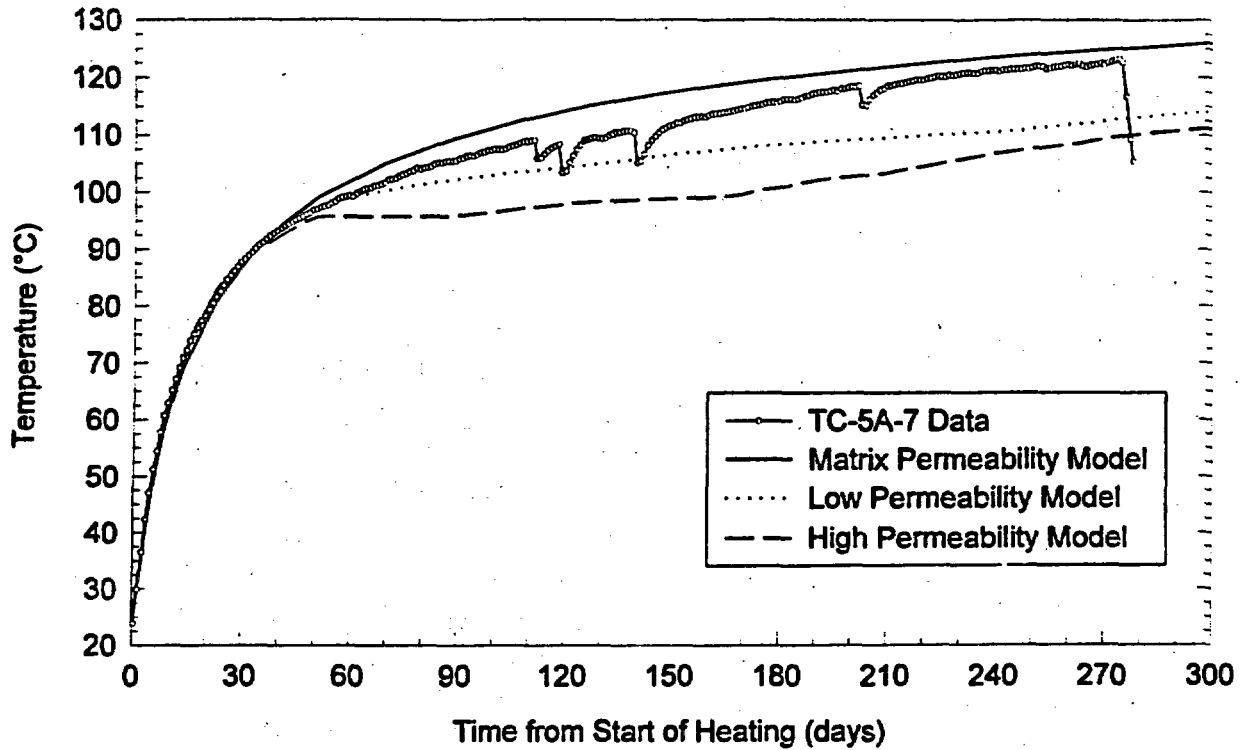


Figure 6-2. Temperature-time history at the heater mid-plane for gage TMA-TC-5A-7.

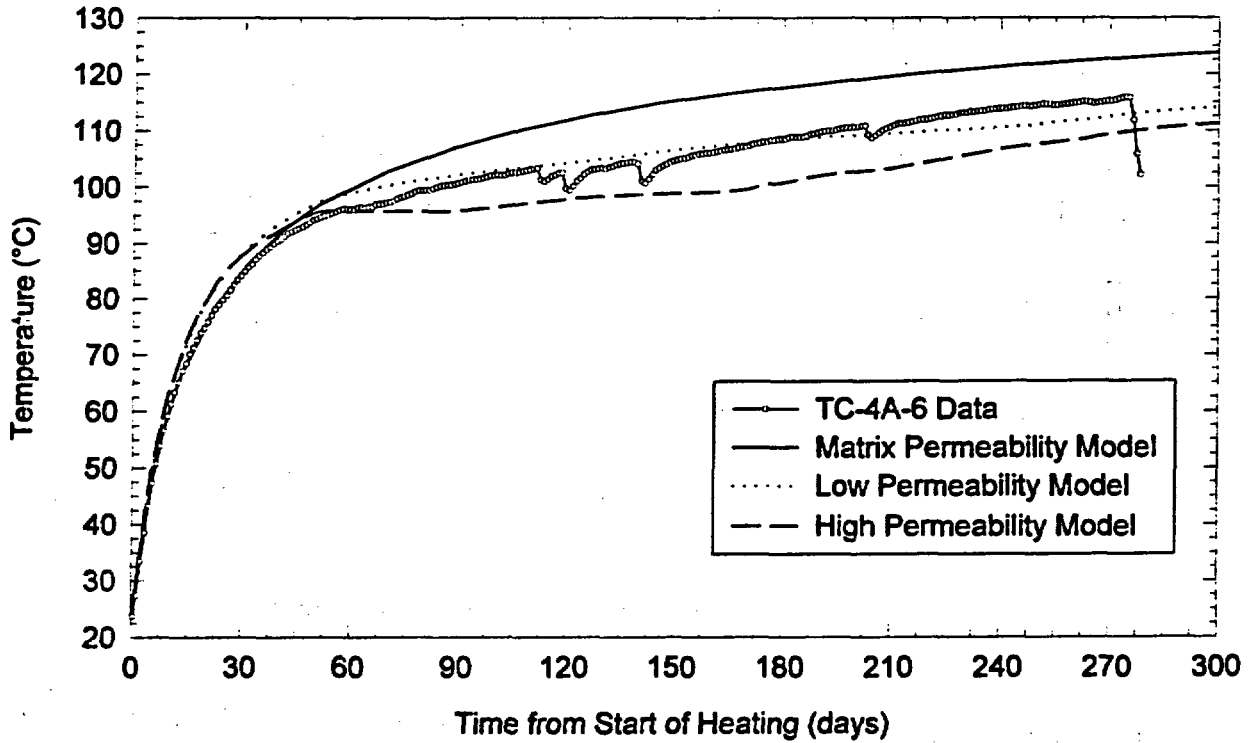


Figure 6-3. Temperature-time history at the heater mid-plane for gage TMA-TC-4A-6.

The measured and modeled temperatures after 275 days of heating, as a function of radial distance from the heater, are compared in Figure 6-4. At radial distances greater than about 1.2 m, where the measured temperatures are less than 96°C, all three models yield essentially the same results, indicating that conduction is the primary mechanism for heat transfer predicted in this region. Also in this region the models overpredict the measured temperature by as much as about 5°C. This overprediction could be easily corrected by increasing the wet thermal conductivity of the rock in the simulations, which would cool the predicted rock temperatures. At radial distances from the heater less than 1 m, the three models exhibit very different thermal behaviors. The high permeability model has a “flat spot” where the temperature is at about 96°C over a radial distance range from about 1 m out to 1.2 m. In this region, liquid water and steam coexist in the pores of the rock. The permeability is sufficiently high to allow the water vapor to readily escape so that the pore pressure does not rise significantly above atmospheric pressure. Because the pore pressure remains near atmospheric, the boiling point of water—and hence the temperature in the annular region where liquid water and water vapor coexist—remains constant at 96°C.

The low permeability model exhibits a significant inflection in this region. As with the high permeability model, water and steam coexist in the pores of the rock, but in this case the permeability is sufficiently low that the water vapor cannot readily escape from the pores of the rock, resulting in an increase in the pore pressure and hence in the boiling point of water. This results in an inflection in the temperature profile but not in an isothermal annular region, as was the case with the high permeability model.

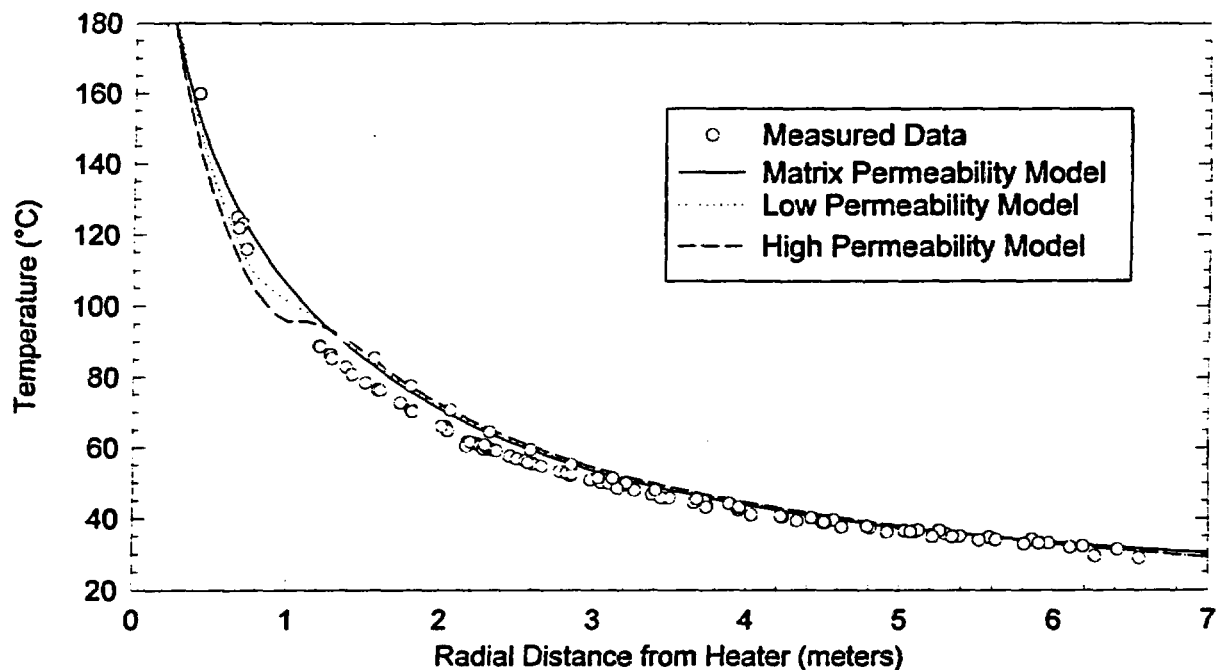


Figure 6-4. Radial temperature distribution in the vertical plane that intersects the heater at its midpoint, after 275 days of heating.

In the matrix permeability model, the permeability is so low that very little water vapor can escape from the pore spaces and the pore pressure rises dramatically, thereby essentially precluding evaporation of water. In this model, the liquid saturation of the rock remains essentially unchanged from ambient conditions until the rock reaches temperatures in excess of 160°C, the maximum achieved at TMA-TC-1A-7. Because water vapor cannot readily move about in the rock, convection is not important and the dominant mode of heat transfer is by conduction. This results in a very smooth radial temperature profile with no isothermal regions or significant inflections.

The data exhibit a very smooth temperature profile as a function of radial distance. Even though data are scarce in the annular region 1 m from the heater, where inflections in the temperature profile would be anticipated, the available data do not indicate that any such inflections exist.

To compare the models and data from a more global perspective, the model temperatures after 266 days of heating were interpolated at most gage locations in the interior of the SHT block, and then the temperatures measured at the those locations after the same amount of heating were subtracted from them. The result is the amount by which the model overpredicts the data after 266 days of heating. This quantity is plotted as a function of the measured temperature in Figure 6-5 for each of the three models. Note that the data from temperature gages located past the ends of the heater have been omitted from the analysis. In Figure 6-5 the models and data agree very well at temperatures less than about 50°C, which is not surprising because the temperatures are not elevated very significantly above ambient. In the range from 50 to 85°C the models for the most part overpredict the measurements by up to 6 or 7°C. As noted earlier, these discrepancies could be easily corrected by increasing the wet thermal conductivities in the models slightly.

Above about 90°C the discrepancies between the models and the data are different for the three models. The high permeability model yields the poorest match between the measured and predicted temperature, with the model underpredicting the measurements by a substantial amount. Underprediction indicates that the model is allowing too much heat to escape from regions where the temperature exceeds 90°C. The low permeability model provides a better match, but the measured temperatures above 100°C are still systematically underpredicted by the model. As with the high permeability model, this indicates that too much heat is escaping from regions where the temperature exceeds 96°C. These discrepancies between the models and the data may be explained in part by the value of dry thermal conductivity used in the models: a lower value would allow less heat to escape. Alternatively, the discrepancies may indicate that the models overpredict the amount of convective heat transfer occurring in the rock. The matrix permeability model does not systematically violate the data at temperatures exceeding 100°C and therefore does the best job of matching the measured temperature data.

The comparisons between the measured data and the numerical predictions presented so far suggest that the matrix permeability model yields the best match between measured and modeled temperatures. For one observation, however, this is not true. In Figure 6-6a the amount by which the temperature of the gages in the interior of the SHT block increased between days 186 and 266 is plotted as a function of the temperature measured on day 186. The temperatures recorded by gages whose temperature on day 186 was less than 100°C increased by about 2.5 to 3.5°C, while the temperature of gages whose temperature on day 186 exceeded 100°C rose by 6 to 7°C. This can be taken as evidence for the formation of a dry-out zone around the heater. As the water in the rock evaporated, two thermal properties of the rock changed. Drying the rock reduced its heat

capacity, with the result that after drying the same rate of heat input to the rock resulted in faster warming of the rock. Evaporation of the water in the rock also reduced its thermal conductivity. As the drying front propagated radially outward, the temperature of the relatively low thermal conductivity rocks in the dry-out zone increased more rapidly than the temperature of rocks outside the dry-out zone. The data in Figure 6-6a suggest that by the end of the SHT heating phase, the dry-out zone extended out to the 100°C isotherm, located about 1 m from the heater.

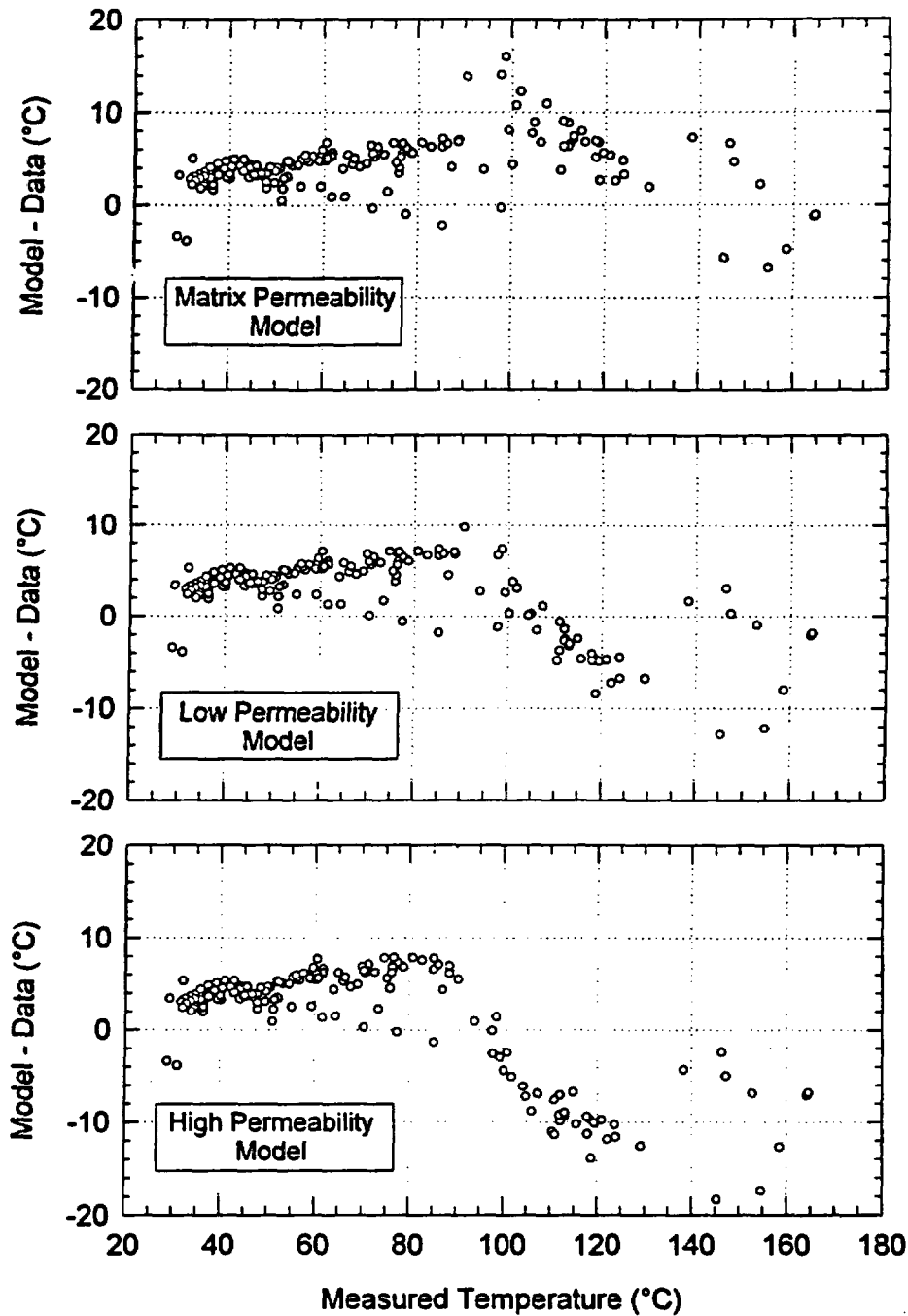


Figure 6-5. Comparison of measured data and numerical models, after 266 days of heating.

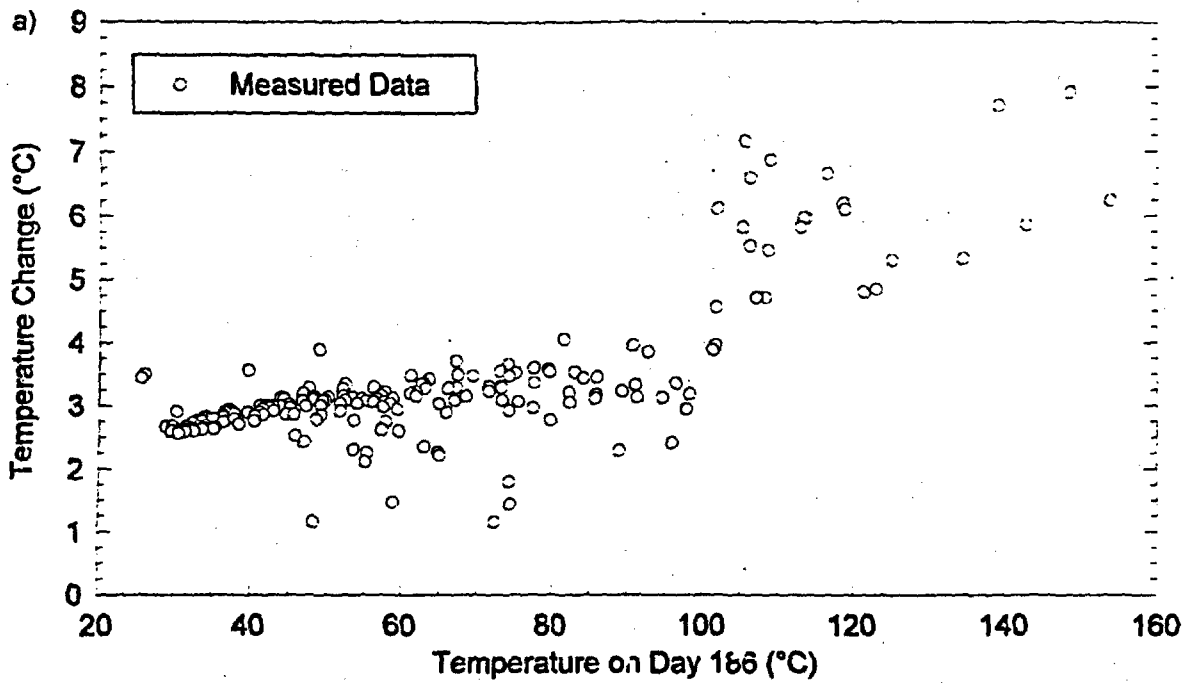


Figure 6-6a. Amount by which the temperature increased between day 186 and day 266 as a function of the temperature measured on day 186; data only.

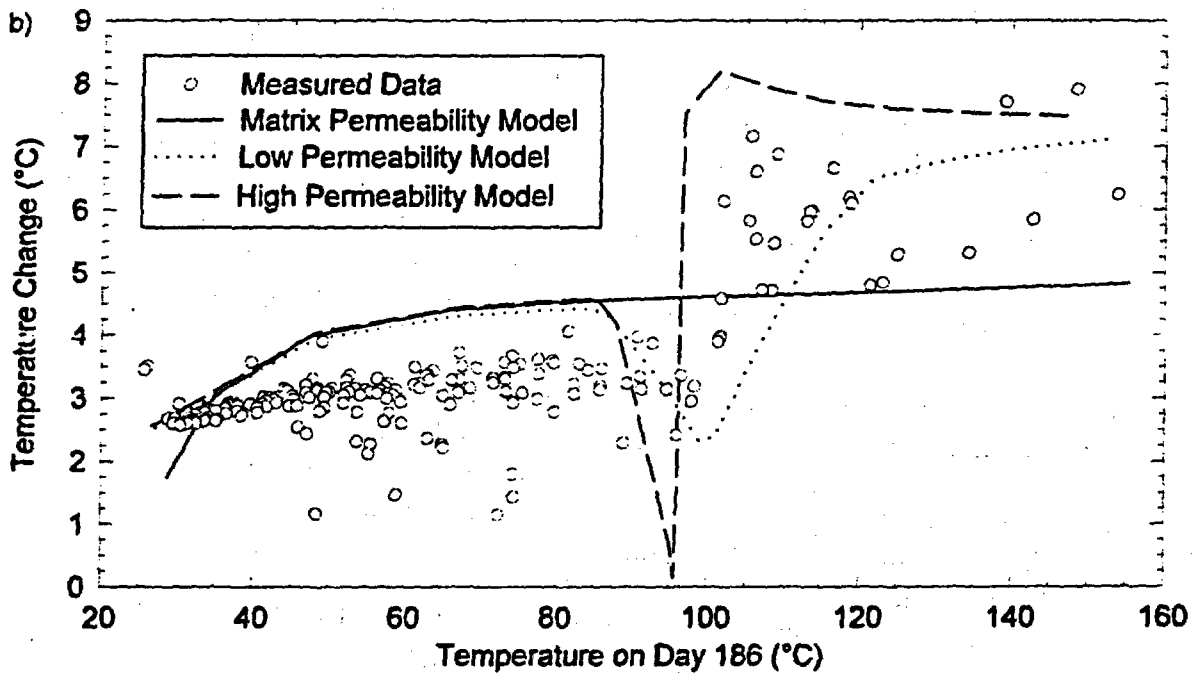


Figure 6-6b. Amount by which the temperature increased between day 186 and day 266 as a function of the temperature measured on day 186; data and model predictions.

Dry-out zone formation can similarly be deduced from the temperature increases predicted by the models, which are plotted along with the measured values in Figure 6-6b. The matrix permeability model exhibits enhanced temperature increases only at temperatures well in excess of temperatures actually observed during the SHT, suggesting only a very small dry-out zone within about 15 cm of the heater. The low permeability and high permeability models exhibit enhanced temperature increases extending to considerably lower temperatures (i.e., greater radial distances from the heater), and are therefore more consistent with the data. In addition to regions with enhanced temperature increases, the low and high permeability models also have regions right near the boiling point where the temperature increases are lower than those observed at cooler temperatures. These correspond to annular regions where liquid water and steam coexist in the pores of the rock and thermal energy is being devoted to evaporating water instead of raising the temperature of the rock. Although the measured data show a very slight decline in the temperature increases in this temperature range, the effect is much less pronounced than predicted by the low and high permeability models.

### Conceptual Models of Coupled Thermal-Hydrologic Processes

In this section, our mental conceptual model of how the thermal and hydrologic processes are coupled will be described. Then the conceptual model that is the basis of the numerical simulations which have been run to date, and which have been compared to the measured data in this report, will be described. Finally, the two conceptual models will be contrasted.

From a thermal perspective, there are two heat transport mechanisms at work in the SHT: conduction and convection. Although both contribute to the overall heat transfer, convection will be inhibited by the limited permeability of the rock, and hence conduction is likely the predominant heat transfer mechanism. The other important thermal effect operative in the SHT is the change in thermal properties of the rock, which occurs as its liquid saturation is decreased as a result of boiling. Drier rock will have lower thermal conductivity and heat capacity compared to rock with a higher liquid saturation. Because a substantial amount of heat is being transferred conductively through the rock, lowering the thermal conductivity of the rock will increase the temperature gradient within it. A higher gradient will result in higher temperatures in the dry-out zone. Lower heat capacity, and lower thermal conductivity coupled with a radially propagating drying front, will cause temperatures within the dry-out zone to rise more rapidly than temperatures outside the dry-out zone.

From a hydrologic perspective, the rocks where the SHT is being conducted consist of a low permeability matrix intersected by numerous fractures that have a much higher permeability. The rock is also intersected by several open boreholes, which could be significant conduits for fluid flow. There are two fluid phases of concern in the SHT: liquid water and water vapor. The permeability of the matrix is such that liquid water residing in the matrix can be considered essentially immobile at the time scale of the SHT. Water vapor, on the other hand, can flow at a significant rate through the matrix because of its much lower viscosity. Liquid water and water vapor can both move easily through the fractures and along the boreholes.

At ambient conditions, the matrix is partially saturated, with about 92% of the pore space occupied by liquid water. The fractures are probably fairly dry because, if they contained significant water, that water would drain due to gravity. The liquid water in the matrix is held in place by capillary suction.

During the SHT, as the rock is heated to temperatures exceeding the boiling point of water, liquid phase buoyant convection is probably of fairly minor significance due to the limited permeability of the matrix. Once the water begins to boil, however, the resulting water vapor flows readily. Because boiling will occur close to the heater first, a substantial pore pressure gradient will develop, which will cause the vapor to flow in a net direction that is radially away from the heater. Because the fractures have a much higher permeability than the matrix, the vapor will tend to first flow from the matrix into the nearest fracture or borehole and then along the fracture or borehole in a direction away from the heater.

As the vapor flows away from the heater, it will eventually encounter the boiling point isotherm, where it will condense back to a liquid. Because the vapor had been preferentially flowing along fractures and boreholes, the liquid saturation of the fractures on the cool side of the boiling point isotherm will increase substantially. As a result of capillary suction, some of the liquid water will be imbibed into the matrix and some will be drawn back into the dry-out zone and reevaporized. Much of the water, however, may flow downward in the fractures and boreholes due to gravity, ultimately leaving the region of influence of the SHT. From a broad spatial perspective, then, the heating process can be viewed as a mechanism for moving liquid water from the matrix, where it is relatively immobile due to capillary suction and the relatively low permeability of the matrix, to the fractures, where it can flow more easily due to the higher permeability of the fractures.

The numerical simulations that have been run to date, which have been compared to the measured data in this report, are based on the Equivalent Continuum Model (ECM). To achieve computational efficiency, the ECM assumes that the matrix and the fractures are in thermodynamic equilibrium. With this assumption, the thermal and hydrologic properties of the matrix and the fractures can be combined into single, bulk values. The effects of boreholes are ignored completely. The model then computes the temperature, pressure, and saturation that would exist in a single medium with those bulk properties. In the implementation used for the SHT, the bulk permeability and bulk capillary suction more closely resemble those of the matrix until such time as the liquid saturation approaches unity. This means that it is very difficult for liquid water to flow in the model until near total saturation is achieved. In the SHT models, when the rock temperature exceeds the boiling point of water, vapor forms and flows radially away from the heater in response to the pore pressure gradient. When the water vapor flows past the boiling point isotherm it condenses, but then the resulting liquid water cannot readily flow anymore because complete saturation is only rarely achieved in the SHT models. As the boiling point isotherm progressively moves radially outward away from heater in response to the continued addition of heat, the liquid water is boiled once again and moves radially outward where it recondenses. This process is called refluxing because the water is continually vaporized, transported radially away from the heater, condenses when it crosses the boiling point isotherm, and then is later reevaporized, ad infinitum.

The key difference between our mental conceptual model and the ECM is that the ECM almost never allows liquid water to leave the system whereas, in reality, this probably occurs. This means that in the ECM there is more liquid water filling the pores of the rock near the boiling point isotherm than there likely is in reality. Consider a cylindrical surface 40 cm in radius whose axis coincides with the axis of the heater. In the ECM, when the temperature of this surface reaches the boiling point, all the water that originally filled the pores of the cylindrical volume of now-dry rock enclosed by the cylindrical surface is filling the pores in close proximity

to the surface of the cylinder. Throughout the time period required to vaporize all of this liquid water, virtually all the thermal energy entering the rock is consumed by the vaporization process, and very little is devoted to raising the temperature of the rock. This leads to the development of the substantial predicted isothermal time periods and isothermal annular regions described earlier in this report. If, once the vapor condensed, it did so in a material with the permeability of the fractures, the resulting condensate could readily drain out of the system under the influence of gravity, thereby reducing the amount of liquid water that would have to be vaporized as the boiling point isotherm expanded. In this case, the isothermal time periods and annular regions would still exist because the water that was originally in the pores still needs to be vaporized, but their magnitudes might be greatly reduced due to the reduction in the amount of water that has to be refluxed.

The implication of this analysis is that the ECM may be significantly overpredicting the magnitude of the isothermal temporal and spatial regions observed in the numerically predicted temperature profiles by retaining condensate water in the system. Because these features were the primary pieces of evidence suggesting that the matrix permeability model fit the measured data better than the low and high permeability models, it is likely inappropriate to draw any conclusion from those comparisons. The observation of a dry-out zone extending out to the 100°C isotherm is compelling evidence that the bulk permeability of the rock is substantially higher than the permeability of the matrix, which was the conceptual model on which the matrix permeability model was based. This conclusion is more robust than conclusions based on the shapes of the spatial and temporal temperature profiles because it is not as dependent on comparisons with the numerical model; it can be gleaned from the measured data alone. The apparent poor fit between the measured data and the low and high permeability models should not be interpreted as evidence that convective heat transfer is not important in the rock. More likely, the poor fit is due to shortcomings of the conceptual model on which the ECM is based.

There are several approaches to improving the numerical models which should be considered. One possibility is that a significant amount of fluid and heat are leaving the system through the open boreholes, which are primarily oriented parallel to the long axis of the heater. Although boreholes are very difficult to model directly, it may be possible to simulate their effect by imparting to the rock an anisotropic permeability that would allow fluids, both liquid and vapor, to flow more easily in a direction parallel to the heater than perpendicular to it.

Another approach would be to implement a Dual Permeability Model (DKM). To relax the assumption of capillary pressure equilibrium between the matrix and the fractures, DKMs have two coupled model domains: one for the matrix and one for the fractures. DKM models are computationally very intensive—so intensive, in fact, that 3-D implementations are impractical. It might be possible, however, to gain insight into the problem from 2-D models.

A third approach would be to modify the ECM so that the bulk permeability would more closely reflect the permeability of the fractures at liquid saturation values lower than unity, perhaps even as low as the ambient saturation. This would promote gravitational draining of liquid water in the model and diminish the importance of the refluxing effect, which is causing the pronounced, unobserved thermal effects in the temperature profiles near the boiling point. This approach should be tried before implementing DKMs due to the vastly superior computational efficiency of ECMs. Other minor improvements in the models which should be implemented would include

adjusting the wet and dry thermal conductivity values and including a temporally variable heater power that more closely matches the actual heater power.

## 6.2 Displacement Data Discussion

The thermomechanical model predictions were described in Sobolik et al. (1996). This discussion will center on comparisons between the model predictions, where appropriate (e.g., displacement measurements), and discussion of the significance of other T-M measurements such as borehole jack rock mass modulus measurements and rock bolt load cell (RLBC) data.

Displacements were measured both within and on the surface of the SHT block. Four boreholes were instrumented with multiple point borehole extensometers (MPBXs), with three boreholes drilled parallel to the heater axis and one borehole drilled perpendicular to the heater axis. The MPBXs include six or seven anchors spaced along the length of the borehole. Wire and tape extensometer pins were installed on each of the three free surfaces of the SHT block. Two wire and tape extensometer "stations" were located on each face. The wire extensometers measured the vertical component of displacement and the tape extensometers measured the horizontal component. A single borehole is used to make borehole jack rock mass modulus measurements. This borehole is oriented perpendicular to the heater axis, and measurements were made at roughly one-month intervals directly before and after heating. Finally, rock bolts are monitored with four RLBCs within the heated region and four RLBCs on the opposite ambient side of the Thermomechanical Alcove.

The thermomechanical code used for predicting the rock mass displacements is JAC3D (Biffle, 1993), which is a finite element nonlinear structural mechanics code developed at SNL. For these preliminary analyses, linear elastic isotropic behavior of the rock mass was assumed. The model domain included the SHT block as well as drifts that bound the block on three sides. Naturally, the fractures were not discretely considered in these analyses. Therefore, some likely discrete block movement, particularly near the free surfaces of the SHT block, will not be predicted by the model. Specific details regarding the T-M modeling can be found in Sobolik et al. (1996).

The displacements measured using the T-M instrumentation are caused by both ambient gravity-driven and thermally driven processes. Because the numerical analyses incorporate both processes, the following discussion will not differentiate between them. In some cases the two processes are additive (e.g., MPBX displacements and tape extensometer displacements); both processes will tend to cause the rock mass to move toward the excavations. In other cases the processes compete with each other (e.g., wire extensometers); the thermal component tends to extend the block vertically, and the gravitational component tends to compress the block.

The vertical displacements measured using the wire extensometers exhibit erratic behavior, as described in Section 4. Naturally, the predicted displacements from Sobolik et al. (1996) exhibit relatively smooth displacements, with all wire extensometers exhibiting net extension and the greatest extension measured by WX-1 and WX-2, which are located on the "front" face of the SHT block. The actual wire extensometer measurements are not nearly so smooth. The measurements are typical of wire extensometer data, with displacement jumps that likely result from discrete block movement near the surface. In fact, three of the six wire extensometers exhibit net compression, which is not shown in the model results. As was stated previously, the wire extensometers are influenced by the competing processes of thermal expansion-driven

extension and gravity-driven compression of the SHT block. Also, the wire extensometers are mounted on shallow pins, which can be highly influenced by block rotation and other surface mechanical processes.

Thermomechanical data obtained during the SHT include preliminary estimates of rock mass thermal expansion, rock mass modulus, and rock bolt load. The rock mass thermal expansion coefficient ( $\alpha$ ) is determined from selected MPBX displacements and temperatures. The rock mass modulus is determined directly from the borehole jack measurements. The rock bolt load is measured directly using RLBCs, and comparisons are made between the thermally perturbed and ambient rock bolts.

Rock mass thermal expansion was estimated for the pretest numerical analyses (see Sobolik, 1996) based on unconstrained laboratory tests on welded tuff samples obtained from the SHT block. These laboratory values ranged from  $7.47 \times 10^{-6}/^{\circ}\text{C}$  for temperatures of  $25^{\circ}\text{C} - 50^{\circ}\text{C}$ , to  $51.7 \times 10^{-6}/^{\circ}\text{C}$  for temperatures of  $275^{\circ}\text{C} - 300^{\circ}\text{C}$ . The very high thermal expansions reported for the intact lab specimens represent the effect of the silica phase transition. It is unlikely that these high temperatures will be detected by any thermomechanical instrumentation installed in the SHT. It is more likely that the maximum temperatures at thermomechanical instrumentation locations will not exceed  $225^{\circ}\text{C}$ . The intact thermal expansion reported for temperatures between  $200^{\circ}\text{C}$  and  $225^{\circ}\text{C}$  is  $15.86 \times 10^{-6}/^{\circ}\text{C}$ . Therefore, realistic bounding values for the intact rock thermal expansion are  $7.47 - 15.86 \times 10^{-6}/^{\circ}\text{C}$ . It is likely that the rock mass thermal expansion calculated from the in situ data would be lower than the laboratory values because of the presence of fractures. The fractures would tend to accommodate some of the thermal expansion in the joint stiffness, particularly during early heating, because the thermal displacement would be insufficient to mechanically close fractures (i.e., low stresses). Also, the three-dimensional effects of heated rock bounded by lower temperature rock would decrease the net effect of thermal expansion by resisting the thermal displacements in adjacent volumes of rock.

Rock mass thermal expansion is calculated from the in situ data, including temperature change for a given axial length from ambient, gage length, and measured thermal displacement over the gage length. The rock mass thermal expansion coefficient was calculated for the SHT using selected data from MPBX-1 and MPBX-3. Only the data from these MPBXs with relatively uniform temperature were used. The calculated values for rock mass thermal expansion are presented in Table 6-1 for data through 30 November 1996. Because the data for MPBX-2 and MPBX-4 become difficult to evaluate after 30 November 1996 due to reversals in displacement direction (extension to compression) these data have not yet been used to evaluate rock mass thermal expansion. These complex behaviors require additional modeling efforts. Simple analytic techniques are inadequate because of the thermal and displacement gradients seen in MPBX-4.

Table 6-1. Calculated Rock Mass Thermal Expansion Coefficient from SHT Data through Day 90

MPBX #	Average $\alpha$ ( $10^{-6}/^{\circ}\text{C}$ )	Average Temperature ( $^{\circ}\text{C}$ )	Maximum Gage Length (m)
TMA-MPBX-1	5.02	118.64	2.0
TMA-MPBX-3	5.27	63.81	3.0

Note: Data in table through 30 November 1996.

The data presented in Table 6-1 are relatively consistent regardless of temperature and gage length. The data are averaged values for each MPBX over the gage lengths shown. For MPBX-1 the values ranged from  $4.26 - 5.73 \times 10^{-6}/^{\circ}\text{C}$ ; for MPBX-3 they ranged from  $3.91 - 6.32 \times 10^{-6}/^{\circ}\text{C}$ . The calculated values for rock mass thermal expansion are, as expected, lower than the values from intact laboratory specimens and less than the values used in the pretest thermomechanical analyses. Also, the values presented in Table 6-1 are for the single orientation parallel to the heater ( $N72^{\circ} W$ ). It is possible that there could be some significant anisotropy in the rock mass thermal expansion coefficient due to differences in fracturing along different orientations. Following the time periods of relative compression seen in the data for MPBX-1 and MPBX-3 (Section 4), the anchor responses again become extensional. It is possible to estimate rock mass linear thermal expansion at the conclusion of the SHT heating period by evaluating the relative differences in displacement and between anchors of a given MPBX. For anchors (gages) that have failed, the displacements for the last reliable data can be used. The thermal expansion at each time is simply the relative displacement difference divided by the respective gage length and the change in temperature from ambient. Using the anchors for MPBX-3 and MPBX-1, an estimate of the rock mass thermal expansion at the end of the heating period (or at gage failure) can be made. Simple analytical calculation of the thermal expansion coefficients for the longest gage lengths available near the end of the heating cycle yield the results presented in Table 6-2.

Table 6-2. Thermal Expansion Coefficients for Longest Available Gage Lengths Near Heating Cycle Culmination

MPBX Number	Anchor Numbers	Average $\alpha$ $10^{-6}/^{\circ}\text{C}$	Average Temperature ( $^{\circ}\text{C}$ )	Gage Length (m)
TMA-MPBX-1	1 to 4	5.88	160.3	2.84
TMA-MPBX-3	2 to 6	4.14	70.07	4

These thermal expansions over the longest gage length available for each MPBX near the end of the SHT heating cycle do not differ significantly from those reported for the first three months of heating. The value for MPBX-1 is about 18% higher than the previous number, and for MPBX-3 the value is 21% lower. The significance of these numbers is not yet known; however, the rock mass thermal expansion values remain much lower than the laboratory values from intact samples. These differences must be attributed to the presence of fractures and 3-dimensional effects. Parametric numerical studies should be performed using a range of thermal expansion coefficients to evaluate the likely rock mass values.

The linear rock mass thermal expansion in its most simple perspective is the relative displacement change between anchors (gage length) for a given measured temperature (temperature change from ambient). Because temperature gradients exist in the SHT, the approach is to use "average" temperatures over a given gage length (between anchors).

The rock mass thermal expansion values presented in Table 6-1 are consistent, though slightly lower than expected values. Previous in situ thermal tests in G-Tunnel (in a welded tuff similar to TSw2, the Grouse Canyon welded tuff) measured thermal expansion coefficients of similar magnitude ( $8.0 \times 10^{-6}/^{\circ}\text{C}$ ), although the intact values reported were lower than the intact values from samples taken from the SHT (Zimmerman and Finley, 1987). The thermal expansion

coefficients from the SHT will continue to be evaluated via sensitivity analyses and will be documented in future reports.

Rock mass modulus was measured in the SHT from a single borehole drilled horizontal and perpendicular to the heater axis. A borehole jack was used to measure the rock mass modulus at various distances from the heater in a horizontal configuration in borehole ESF-TMA-BJ-1. Only horizontal measurements were made because this orientation is of most direct interest to underground opening design and stability. For the pretest analyses, the rock mass modulus was estimated from laboratory tests on intact specimens from the SHT and by estimating the modulus from rock mass quality (RMR) data using the technique described in Serafim and Periera (1983). The rock mass modulus value suggested from these sources (upper bound value of 32.4 GPa) was used in the pretest numerical analyses. The results of the Goodman Jack testing in the SHT suggest rock mass modulus values ranged from about 3 GPa to 23 GPa. The SHT borehole jack testing through 28 February 1997 shows significant change due to heating at the deepest testing location in the borehole (about 6.2 m from the collar or about 0.33 m from the heater). Other testing locations in the borehole do not yet show any thermal effects. The lower modulus values measured throughout ESF-TMA-BJ-1 (with the exception of the recent bottomhole test) would result in the development of significantly lower stresses in the SHT block than the pretest analyses predicted. However, the SHT displacements would not change in the elastic analyses with a reduced modulus. The low ambient measured modulus is certainly not unexpected. It is known from previous in situ experiments conducted in welded tuff in G-Tunnel that the modulus values measured for various in situ tests were about half the intact value of about 23 to 35 GPa (Zimmerman and Finley, 1987). Zimmerman and Finley also report results of Goodman Jack measurements in welded tuff from the G-Tunnel facility. Over forty Goodman Jack tests were conducted, and the recommended rock mass modulus from these tests ranged from 14.7 GPa to 17.6 GPa, roughly half the intact value from laboratory tests. Additional Goodman Jack testing and analyses will be conducted in the SHT to evaluate further the rock mass modulus from ESF-TMA-BJ-1 and its effect on overall SHT performance, particularly whether there is a consistent increase in modulus due to thermal expansion effects.

Loads were measured in rock bolts installed on both the heated side of the SHT Block and on the opposite ambient rib of the Thermomechanical Alcove. The rock bolts were installed to evaluate the longer-term effects of elevated temperature on this type of rock anchorage. Preliminary results show that loads are decreasing in all load cells; however, the decrease is greatest in those rock bolts on the heated side of the SHT. In particular, two bolts predicted to be at the highest temperature experienced the greatest load decreases (up to about 6.6%) from their initial pre-load values. The higher load decreases seen in the higher temperature rock bolts could result from several sources. For instance, the thermal expansion coefficient of carbon steel is about 10 to  $11 \times 10^{-6}/^{\circ}\text{C}$  (Popov, 1976). Thus the thermal expansion of the steel is likely greater than the rock mass expansion surrounding it. Alternatively, there could also be some load loss due to creep of the anchorage, which is composed of the steel bolt and mechanical anchor, the surrounding grout, and the rock itself. Post-test evaluations, including pull tests and post-mortem testing of the bolt/grout/rock interface, will shed light on the most likely explanation for the rock bolt behavior.

The primary concern regarding the thermomechanical measurements reported here is the reliability of the MPBX measurements. As stated in Section 4, the MPBXs employing the long carbon fiber extension rods with vibrating wire displacement transducers in the MPBX head at

the borehole collar exhibit somewhat consistent displacement data, with all three showing changes in displacement for at least some of their anchors. These results are not expected based on the simplistic linear elastic analyses conducted prior to testing (Sobolik et al., 1996). These analyses predicted only extension for MPBX-1 and MPBX-3. The analyses did predict initial compression for MPBX-4 and are consistent with the in situ data presented in this report. The analyses did not predict relative compression between the anchors of MPBX-1 and MPBX-3. However, those analyses only evaluated the relative change in the Y-coordinate of nodes nearest the MPBX anchors and did not include changes in the X and Z coordinates. It is likely that the truly three-dimensional nature of the thermal perturbation will require inclusion of the X and Z coordinates to describe the MPBX responses.

One possible explanation for the MPBX response is that there is a catastrophic failure of some part of these MPBX components. For these MPBXs, the possible contributors to this behavior include gage failure, rod failure, anchor failure, or actual rock mass response. Although one of the vibrating wire gages is known to have failed, it is unlikely that these gages are not responding properly because the vibrating wire and activator are sealed against the effects of moisture and the temperatures at the head are within the operating range of these instruments. The instantaneous "jumps" seen in the bottom anchors for both MPBX-1 and MPBX-3 also support the validity of the data. These type of gages have been used throughout the ESF without gage failure and are used extensively in the mining industry, often in harsh moisture environments. As a check of the vibrating wire response, SNL checked several of the gage counts using a portable readout box and found the vibration frequency consistent with the DAS output. To assure that the vibrating wire gage response from these MPBXs is correct, the gages should be recalibrated after cooldown of the SHT to provide assurance that they remained in calibration.

It is also unlikely that the MPBX anchors have slipped. These are C-ring anchors that are relatively heavy (about 1 to 2 pounds). If the C-ring has failed, there is little impetus to "slip," particularly in horizontal holes. Finally, the carbon fiber extension rods are connected using stainless steel male/female screw end pieces. SNL conducted some simple heated tension tests to evaluate the possibility that these rods could slip themselves. The tests showed no evidence of slipping or failing at temperatures up to 200°C. Therefore, without additional information suggesting MPBX component failure, the data presented in this report must be considered valid.

### **Conceptual Model of Thermomechanical Behavior**

The mechanical behavior of the SHT block resulting from heating is complex, due largely to the presence of the fractures. An intact block of rock would likely behave as predicted by the pretest elastic modeling. The fractures, however, create localized areas of lower stiffness, which are able to accommodate somewhat the thermally activated expansion of the intact rock blocks. The fracture stiffnesses are also nonlinear, being dependent on the initial (ambient) apertures and mating conditions. The presence of multiple fracture sets contributes anisotropy to the uncertain fracture stiffness matrix. The net outcome of these inhomogeneities results in the MPBX displacements presented in Section 4 of this report. A descriptive conceptual model of the thermomechanical behavior is presented using the displacement results of MPBX-3 as an example. This conceptual model should be considered in future thermomechanical analyses of the SHT block, and the results should also be considered when modeling the larger DST and repository openings.

The SHT consists of a block of rock about 13 m wide by about 10 m long and 5 m high. The back of the SHT block is constrained by the surrounding cooler rock mass. The other sides of the SHT block are not completely free surfaces, as the floor and roof act to pin the block at these locations. The SHT block is therefore free to displace, based on the thermal expansion characteristics of the rock mass, restricted by these boundary conditions. In addition, there exists a zone of higher air permeability (TRW, 1996b) that is roughly sub-perpendicular to the heater axis near the end of the heater. This presumed fracture zone can, and has, contributed to the measured thermomechanical behavior of the SHT block. Because the heater is emplaced within this partially constrained heterogeneous rock mass, the thermomechanical response should be expected to also be nonuniform.

Consider the behavior of a single hypothetical MPBX borehole drilled parallel and near a heater similar to the one used in the SHT, as shown in Figure 6-7. The borehole extends to about the same depth as the heater, and anchors are located similar to those in the SHT. The MPBX borehole is bounded on one side by the free surface where the borehole collar is located and on the other side by an infinite rock mass. Also assume no influence on measured displacements from gravitational effects. The initial state of stress in the region is dominated by gravitational loading with relatively low horizontal stresses. Remember that MPBXs by their nature are intended to provide displacement data parallel to their axis only. Initially, the MPBX borehole is parallel to the heater axis. Likewise, the MPBX anchors are all aligned along the axis of the MPBX. The MPBX shows no relative displacement between the collar and anchors. Shortly after the heater is energized, the high-temperature pulse has yet to reach the MPBX borehole; however, the effects of the near-heater rock mass thermal expansion can be measured by the MPBX. Because the rock mass thermal expansion is volumetric, the rock surrounding the heater expands in proportion to the shape and volume of the temperature field. This results in a slight "bending" of the MPBX borehole as shown in Figure 6-8. Naturally, the MPBX gages located at the collar record a relatively uniform elongation of the borehole, which is partially due to the bending of the MPBX extension rods that connect the anchors with the gages themselves. Some of the measured displacements during this early time period are caused by net elongation along the MPBX axis as the rock mass expands toward the free surface. The stresses very near the heater have changed so that locally  $\sigma_H > \sigma_V$ , with the horizontal stresses parallel to the heater axis greater than those perpendicular to it. These stresses originate from a very small volume of rock so that the net effect is relatively confined to the very near field around the heater. Therefore, the stress change has little effect on fracture closure and the net signature of the MPBX response is consistent with the linear thermoelastic predictions, which show monotonically increasing displacements for all anchor locations.

At later times the thermal pulse has surrounded the MPBX, as shown in Figure 6-9. Note also that large thermal gradients exist near the ends of the heater so that the MPBX anchors on either end are in a lower temperature regime and influenced by a smaller volume of heated rock, in the axial direction. The volume of rock influenced by the thermal pulse has expanded to sufficient size to create a larger region of stress perturbation in which  $\sigma_H > \sigma_V$ , with the horizontal stresses parallel to the heater axis greater than those perpendicular to it. In this case, the increased horizontal stresses encompass a sufficient volume of rock to influence the fractures, resulting in fracture closure. The net result in the MPBX response appears complicated, with reversals in displacement direction; some adjacent anchors appear to experience relative compression for the time period.

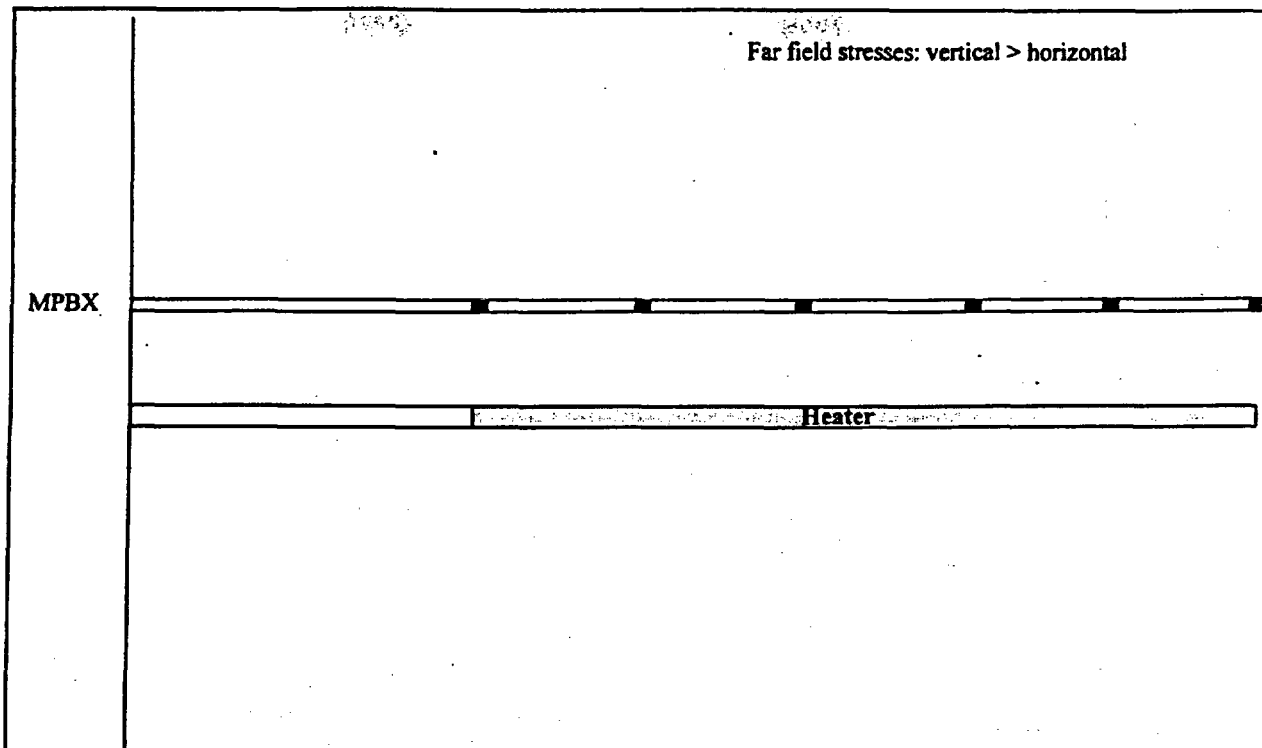


Figure 6-7. Initial pre-heating condition and layout for descriptive thermomechanical conceptual model.

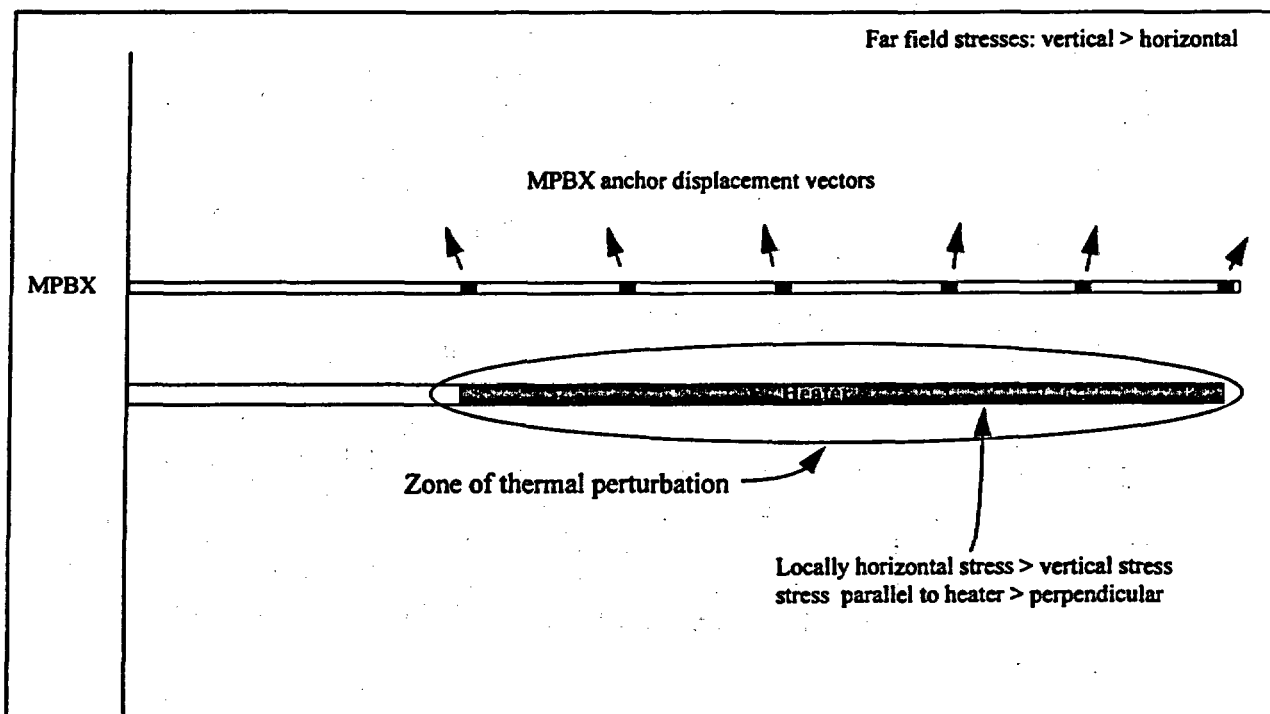


Figure 6-8. Descriptive conceptual model of MPBX behavior shortly after heater startup.

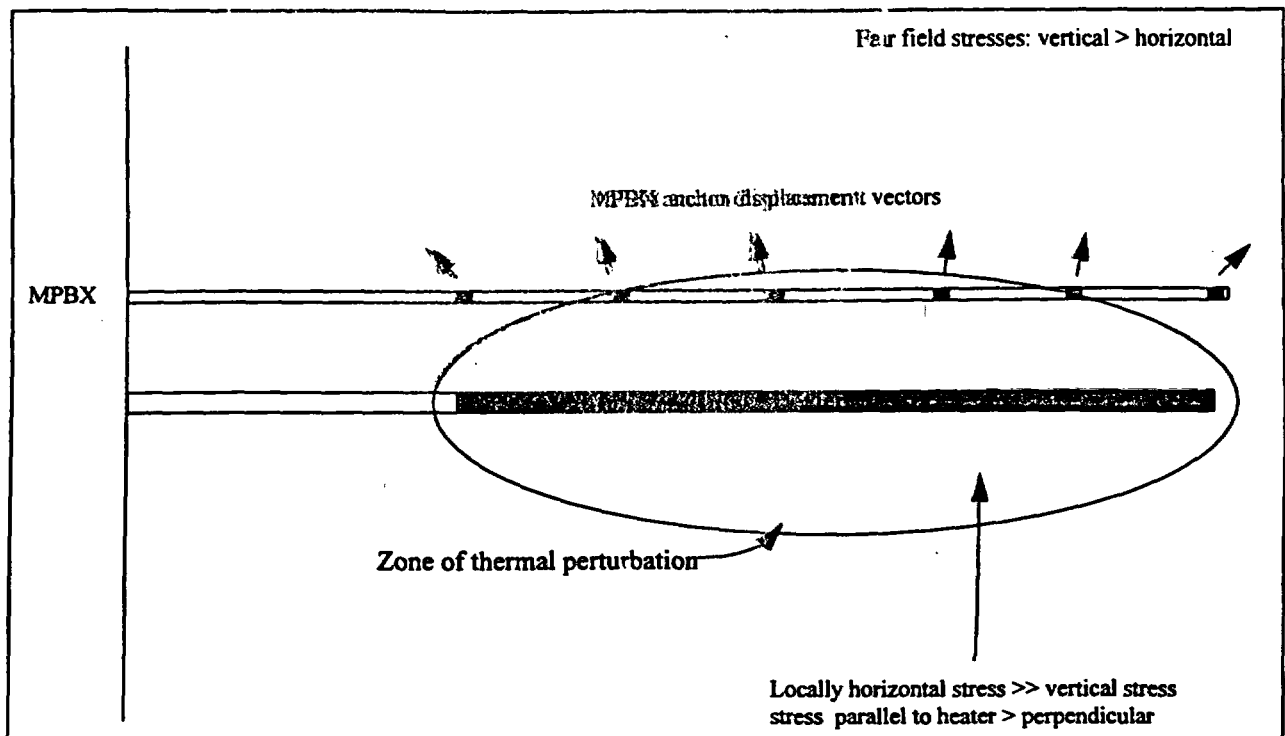


Figure 6-9. Descriptive conceptual model of MPBX behavior midway through heating.

The behavior is further complicated by the presence of more highly fractured zones, which likely have a significantly lower stiffness. Also, the relative locations of the anchors can contribute to the measured response. For instance, the bottom MPBX anchor is influenced by the cool outer boundary on one side and a growing thermally expanding region on the other. The net effect of this, depending on fracturing, etc., is that this bottom anchor can, under these circumstances, move away from the borehole collar due to thermal expansion from the heated rock on the collar side. Again, depending on fracturing extent and thermal gradients, the anchors can move during this time period in opposite directions.

At late stages of heating, the MPBX borehole is completely engulfed by the thermal pulse, as shown in Figure 6-10. The stress condition in the region surrounding the MPBX borehole is one in which  $\sigma_H > \sigma_V$ , with the horizontal stresses parallel to the heater axis predominating. Because the heater is surrounded by the thermally expanding rock mass, the predominant thermally induced displacements are again parallel to the MPBX axis, which is consistent with the MPBX design. The existing fractures have mechanically closed due to the stress increase, and the MPBX anchor response is again more uniform. The anchor response is roughly parallel, with continued monotonically increasing displacements. Naturally, additional fracture effects can influence the MPBX response; however, the MPBX is again in a region of rock that appears to behave as a continuum.

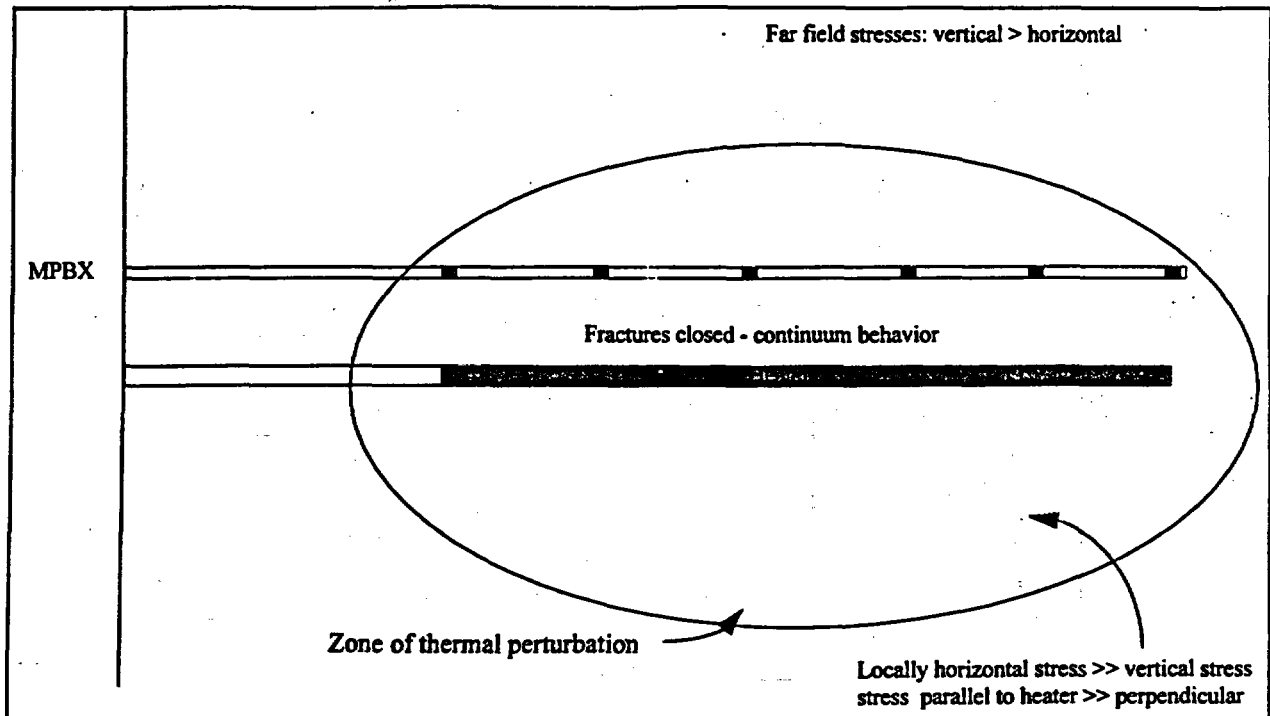
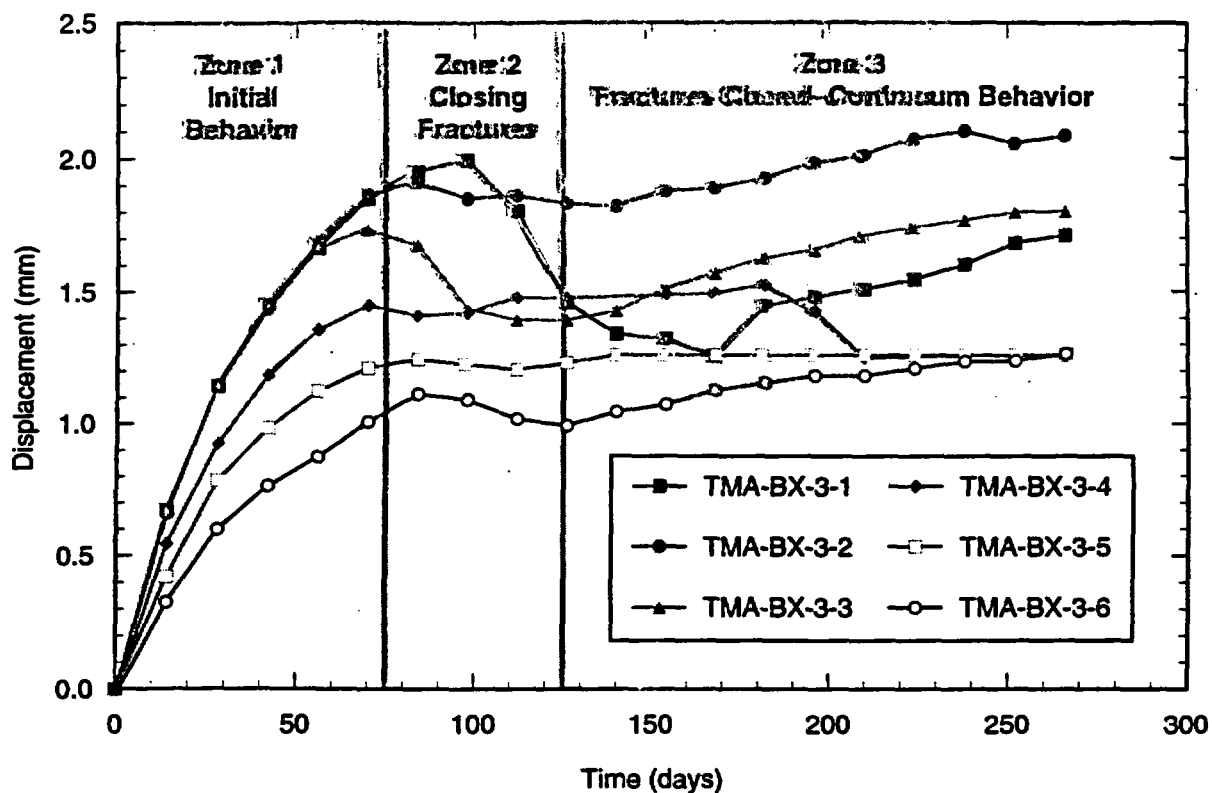


Figure 6-10. Descriptive conceptual model of MPBX behavior near the end of heating.

As a direct example for the SHT, consider the MPBX-3 displacements presented in Section 4 and shown in Figure 6-11. The figure delineates the three thermomechanical behavioral zones described above. Through about day 70 of heating, the MPBX response is reasonably consistent with the pretest thermoelastic predictions. From day 70 through about day 130, the behavior is quite complex, with reversals of displacement sign. Note that the largest reversal in displacement sign occurs for MPBX-3-1, which is located at the bottom of the borehole and is likely most affected by the fracture zone identified in that region. After about day 130, the displacements become consistent again, monotonically increasing. There are also obvious “jumps” in the data, which are likely due to discrete movement along the fracture zone near the end of the heater, as discussed in Section 4 of this report.

The behavior of the other two SHT MPBXs can also be explained using the descriptive conceptual model described above. For MPBX-1, located parallel and closest to the heater, the anchor response is similar to MPBX-3, but the displacement reversals are of a larger magnitude, as should be expected. MPBX-1 also experiences the three thermomechanical behavior zones at an earlier time than MPBX-3. The initial zone extends through about day 50, the second zone (fractures closing) extends from day 50 through about days 130–150, and the third zone extends through the rest of the heating phase. For MPBX-4 the thermomechanical behavior zones are somewhat different because it is oriented perpendicular to the heater axis and therefore extends through only a limited heated zone. MPBX-4 does, however, show some effects of the thermomechanical behavior zones, particularly after about day 150, when some minor reversal in displacement trends occur. After about day 200, the displacement trends again change sign,



TRI-8117-47-0

Figure 6-11. Descriptive conceptual thermomechanical model applied to MPBX-3 behavior.

suggesting that the third thermomechanical behavior zone has been reached for these anchor locations. Again, because of the limited volume of rock heated along this orientation, a longer time period would likely be needed to energize a volume of rock sufficient to create horizontal stresses necessary to close fractures.

The descriptive conceptual model of thermomechanical behavior presented here is intended to provide a means to describe the likely rock mass response to the heating phase of the SHT. Because of the complexities seen in the MPBX responses and the differences between the measurements and the predicted response (using linear elastic continuum models) it is strongly recommended that future post-test thermomechanical analyses modeling the SHT employ discrete block techniques. This method would allow realistic incorporation of the effects of fracture closing due to increased horizontal stresses. Alternatively, planes of lower stiffness could be added to the finite-element mesh between MPBX anchor locations, particularly between anchors 1 and 2 of the MPBXs parallel to the heater axis. These planes would simulate the gross effect of fracture zones, although the behavior of individual fractures would not, of course, be captured.

Adequately modeling the thermomechanical behavior of the SHT is important for several reasons, the most important of which is to provide some direction to the thermomechanical modeling requirements for the DST and repository. It is possible that the larger tests and repository openings can only be modeled using continuum approaches, which essentially "smear" the effects of the fractures throughout the volume modeled. In order to adequately perform this smearing, an

understanding of how best to conceptualize the smearing is necessary. The SHT data present an excellent opportunity to develop the theoretical framework to complete this effort. For instance, it is common practice to "degrade" intact properties such as modulus to account for the presence of the fractures. Likewise, the thermal expansion coefficient can be degraded to account for the presence of the fractures. It is also likely that some anisotropy can be incorporated into the 3-D finite element codes by employing this degrading approach. It is possible that true 3-D modeling of the drift-scale test and repository openings using discrete block models will prove too numerically complex to apply realistically to either the DST or repository openings. Currently available numerical models (e.g., JAC3D, UDEC) require mathematical functions to model the interaction between contact surfaces, such as friction as a function of stress or temperature, slip functions, degree of contact based on aperture width, etc.

The data collected during the SHT provide the first opportunity to evaluate the coupled thermal-mechanical-hydrologic-chemical processes that are likely to occur as a result of waste emplacement at the proposed Yucca Mountain repository. These couplings will be further studied in the Large Block Test, Drift-Scale Test, and laboratory and numerical studies. The most significant uncertainties lie in the thermal-hydrologic (T-H) coupling, related to movement of the water due to heating the rock mass surrounding the repository openings. The other couplings are also of significant interest on their own and in their influence on the hydrologic behavior through alteration of the flow system. A thorough discussion of coupled processes and their relationship with nuclear waste repositories can be found in Tsang (1987).

The thermal-mechanical (T-M) coupling is of importance to predictions of the structural behavior of repository openings. The T-M coupling can also influence T-H behavior by changing fracture apertures as a direct result of stress changes caused by rock matrix thermal expansion. Another minor effect (which cannot be addressed by the SHT) is the potential change to pore size/geometry in the matrix due to stress changes. The mechanical coupling in turn can influence the net effect of the chemical coupling by reducing the amount of thermochemical infilling (deposition) necessary to close-off or divert conductive fractures. The T-M coupling directly influences the stresses around the underground openings through the rock mass modulus and thermal expansion terms.

The T-M coupling is directly evidenced in the SHT in the temperature, MPBX, and borehole jack measurements. These data show evidence of fracture closure due to the rock matrix thermal expansion. The MPBX displacement data give a lower rock mass thermal expansion value than that obtained from laboratory tests of intact rock samples. The borehole jack data show an increased rock mass modulus at elevated temperature, likely caused by thermally driven fracture closure. These data are discussed in greater detail in Section 4 of this report. These data can be used directly in structural analyses of repository opening T-M behavior.

Typically, analyses incorporate only one way T-M coupling; that is, the rock thermal expansion is driven by the temperature change. However, no backwards link is usually employed to alter the thermal processes as a result of the mechanical changes. As stated previously, these changes are largely the result of fracture aperture changes, although in regions of high temperatures or high thermal gradients, thermally driven cracking or fracturing of the intact rock matrix can occur. As a result, the T-H response of the rock mass may incorrectly predict temperatures and water movement in a rock mass whose fracture porosity is changing both spatially and temporally. This in turn will likely influence to some degree the chemical coupling in a manner as previously

discussed. Because the predominant influence of the mechanical coupling is in closing and opening fractures, the obvious link is through the stress term predicted from numerical models of the rock mass behavior in heated regions. The T-H models used to predict behavior incorporate the fracture apertures typically using the so-called "cubic law," which states that the flow through a conductive fracture is a function of the cube of the aperture. Naturally, closing the fractures will have a marked influence on the ability of the fracture to conduct fluids. Laboratory experiments measuring fluid flow have been performed and reported on single and multiple natural- and artificial-rock fractures (Olsson and Brown, 1993; Olsson, 1992; Billaux and Gentier, 1990; Gale, 1990; Hakami and Barton, 1990; Piggott and Elsworth, 1990; Pyrak-Nolte et al., 1990; Brown, 1987; Schrauf and Evans, 1986; Barton et al., 1985). These laboratory studies have shown that the flow of fluid through fractures is markedly influenced by the stress acting on the fracture. Obviously, the stress normal to the fracture will act to mechanically close the aperture. It is important to note that the mechanical closure of the fracture aperture as evidenced in increasing the rock mass stiffness to values approaching the intact laboratory-derived values does not directly correspond to hydraulic closure of the fracture aperture. Ambient temperature laboratory tests on natural and artificial fractures conducted at SNL have shown the following:

- The cubic law is not obeyed.
- Fluid conductivity decreases with increasing normal stress.
- Flow rates are up to two orders of magnitude greater for uncorrelated surfaces (fracture surfaces unmated).
- Normal stress influences fracture transmissivity by a factor of two to three.
- Flow rates are insensitive to shear stress up to peak stress (onset of shear).
- Fracture dilation during sliding (shear) can cause an order of magnitude increase in fracture transmissivity.

Incorporation of the reverse coupling of fracture closure/opening can most logically be made through the stress term predicted from the T-M models. Naturally, these models must be "calibrated" from the in situ testing program and the fracture normal and shear stiffnesses must be known or estimated. Also, the appropriate flow rule (cubic law) must be determined or estimated. In this way, the T-M effects can be applied to the T-H temperature and hydrologic predictions for each of the numerical time-steps. These fracture changes can then also be incorporated into the chemical analyses.

Perhaps one of the most difficult aspects of the T-M-H-C coupling is the limitation of the numerical tools used in the predictions. For small-scale tests such as the SHT, true 3-D dual-porosity T-H and discrete fracture T-M models can be employed. It is likely that the scale of the DST and the repository itself will limit the numerical models to equivalent continuum models that tend to "smear" the effects of the fractures and inhomogeneities. Therefore, it is possible that the use of alternative continuum approaches must be used, such as degradation of the rock mass modulus and rock mass thermal expansion coefficient in the T-M modeling to account for the presence of fractures. In this way potential anisotropy can be accounted for in a numerically efficient manner. The coupled effect of stress on flow is included in numerous geomechanical numerical codes (e.g. UDEC, FLAC); however, whether these codes accurately represent the correct phenomenology unique to the Yucca Mountain tuffs is uncertain. The two-way coupling between the T-H and T-M codes must certainly be evaluated and developed in a numerically efficient manner.

## **7. Summary and Recommendations**

The SHT heating phase of nine months of heater power was completed on 28 May 1997. One of the SHT tasks is to evaluate and/or propose conceptual models that can best describe the observed response from the SHT data. The standard approach for evaluating experimental results is to initially employ simplified conceptual models and progress to more complex models if the data warrant such complexity. The SHT analyses performed by SNL have followed this logical engineering approach. For initial analyses, the SHT block was assumed to behave as an isotropic linear elastic and Darcian continuum. In reality, the presence of the fractures likely creates a mechanically and hydrologically anisotropic discontinuum. Because of the complexity associated with the presence of the fractures, the SHT will likely require additional modeling efforts to adequately simulate the acquired data. The numerical tools (conceptual models and codes) needed to adequately describe the expected coupled behavior around the larger Drift-Scale Test and repository openings should also be capable of describing the behavior of the smaller, shorter duration, and simpler SHT, regardless of the predominant mode of heat transfer. The logic here is that there likely will be little confidence in the project's ability to describe the complex coupled behavior around the large-scale tests and repository drifts if it cannot be demonstrated that the SHT can be adequately modeled. Because of the expected complexity, and code limitations, it may be necessary to develop "equivalent" approaches that account for the fracture effects by using equivalent properties in continuum models.

The SHT post-mortem evaluations should be performed following completion of the cooldown period. These evaluations are planned to include rock bolt testing including: pull-tests, overcoring of selected bolts, and geochemical evaluations of the visible anchorages. The post-mortem should also include additional rock sampling and laboratory testing, post-test air permeability characterization of the SHT block, and possible removal, recalibration, and examination of instrumentation and equipment.

It is also important that actual measurements of the rock mass saturation be used to compare to numerical simulations describing the SHT behavior. The electrical resistance tomography and neutron logging instrumentation should be calibrated over the range of temperatures experienced in the SHT so that absolute values of saturation are available for analysis. Relative measures of changes in saturation, although important, are not sufficient for comparisons to model results.

**Page intentionally blank**

- Piggot, A.R., and D. Elsworth. 1990. "Laboratory Studies of Transport Within a Single Rock Fracture," *Rock Joints*, Loen Norway, June 4-6, 1990, Eds. N. Barton and O. Stephansson. Rotterdam, Netherlands: A.A. Balkema, 397-404.
- Popov, E.P. *Mechanics of Materials*, 2nd edition. Prentice Hall, Englewood Cliffs, NJ.
- Pyrak-Nolte, L.J., D.D. Nolte, L.R. Myer, and N.G.W. Cook. 1990. "Fluid Flow Through Single Fractures," *Rock Joints*, Loen Norway, June 4-6, 1990, Eds. N. Barton and O. Stephansson. Rotterdam, Netherlands: A.A. Balkema, 405-412.
- Serafim, J.L. and J.P. Periera. 1983. "Consideration of the Geomechanical Classification of Bieniawski," *Proceedings of the International Symposium on Engineering Geology and Underground Construction*. pp. 1133-1144.
- Sandia National Laboratories (SNL). 1995. "Single Heater Test: Test Installation," Work Agreement WA-0310, Albuquerque, NM.
- Sandia National Laboratories (SNL). 1996. "Conducting the Single Heater Test in the ESF," Work Agreement WA-0334, Albuquerque, NM.
- Sandia National Laboratories (SNL). 1997. "Evaluation of Single Heater Test Thermal and Thermomechanical Data: Second Quarter Results (8/26/96 through 2/28/97)." Albuquerque, NM.
- Schrauf, T.W., and D.D. Evans. 1986. "Laboratory Studies of Gas Flow Through a Single Natural Fracture," *Water Resources Research*, Vol. 22, no. 7, 1038-1050.
- Sobolik, S.R., N.D. Francis, and R.E. Finley. 1996. "Pre-Experiment Thermal-Hydrological-Mechanical Analyses for the ESF Single Heater Test - Phase 2." Sandia National Laboratories Letter Report, SLTR96-0005, Albuquerque, NM.
- Tsang, C.F. 1987. *Coupled Processes Associated with Nuclear Waste Repositories*, Lawrence Berkeley Laboratory, Berkeley, Ca., Academic Press, Orlando, Fla.
- TRW. 1996a. "Test Design, Plans, and Layout for the ESF Thermal Test." BAB000000-01717-4600-00025, Rev 01, Sept. 20, 1996. TRW Environmental Safety Systems, Las Vegas, NV.
- TRW. 1996b. "Characterization of the ESF Thermal Test Area." B00000000-01717-5705-00047, Rev 1, Sept 25, 1996. TRW Environmental Safety Systems, Las Vegas, NV.
- Zimmerman, R.M. and R.E. Finley. 1986. *Summary of Geomechanical Measurements Taken In and Around the G-Tunnel Underground Facility, NTS*. Sandia National Laboratories Report, SAND86-1015, Albuquerque, NM.

## 8. References

- ASTM. 1996. "Standard Test Method for Determining the In Situ Modulus of Deformation of Rock Using the Diametrically Loaded 76-mm (3-in.) Borehole Jack." ASTM D4971-89, American Society for Testing and Materials, West Conshohocken, PA.
- Barton, N., S. Bandis, and K. Bakhtar. 1985. "Strength, Deformation, and Conductivity of Rock Joints," *International Journal of Rock Mechanics and Mining Sciences & Geomechanics Abstracts*, Vol. 22, no. 3, 121-140.
- Biffle, J.H. 1993. *JAC3D - A Three-Dimensional Finite Element Computer Program for the Nonlinear Quasi-static Response of Solids with the Conjugate Gradient Method*. Sandia National Laboratories Report, SAND87-1305, Albuquerque, NM.
- Billaux, D., and S. Gentier. 1990. "Numerical and Laboratory Studies of Flow in a Fracture," *Rock Joints*, Loen Norway, June 4-6, 1990, Eds. N. Barton and O. Stephansson. Rotterdam, Netherlands: A.A. Balkema, 369-373.
- Brown, S.R. 1987. "Fluid Flow Through Rock Joints: The Effect of Surface Roughness," *Journal of Geophysical Research*, Vol. 73, No. B2, 1337-1347.
- CRC. 1994. *CRC Handbook of Chemistry and Physics*. CRC Press, Boca Raton, FL.
- DOE (U.S. Department of Energy). 1988. "Site Characterization Plan, Yucca Mountain Site, Nevada Research and Development Area, Nevada." DOE/RW-0199.
- Data Tracking Number (DTN) SNF35110695001.001. Technical Data Information Form (TDIF) No. 305721 (Single Heater Test: As-Built Gage Layouts [Thermocouples, Thermistors, MPBXs]).
- Elsworth, D., and R.E. Goodman. 1986. "Characterization of Rock Fissure Hydraulic Conductivity Using Idealized Wall Roughness Profiles," *International Journal of Rock Mechanics and Mining Sciences & Geomechanics Abstracts*, Vol. 23, no. 3, 233-243.
- Gale, J. 1990, "Hydraulic Behavior of Rock Joints," *Rock Joints*, Loen Norway, June 4-6, 1990, Eds. N. Barton and O. Stephansson. Rotterdam, Netherlands: A.A. Balkema, 351-362.
- GeoKon. 1997. "Thermal Expansion Coefficients for Carbon Fiber and Invar Extension Rods," personal communication.
- Hakami, E., and N. Barton. 1990. "Aperture Measurements and Flow Experiments Using Transparent Replicas of Rock Joints," *Rock Joints*, Loen Norway, June 4-6, 1990, Eds. N. Barton and O. Stephansson. Rotterdam, Netherlands: A.A. Balkema, 383-390.
- Heuze, F.E. and B. Amadei. 1985. "The NX-Borehole Jack: A Lesson In Trials and Errors," *International Journal of Rock Mechanics, Mineral Sciences, and Geomechanics Abstracts*. Vol. 22, no. 2, pp. 105-112.
- Olsson, W.A. 1992. "The Effect of Slip on the Flow of Fluid Through a Fracture," *Geophysical Research Letters*, Vol. 19, no. 6, 541-543.
- Olsson, W.A., and S.R. Brown. 1993. "Hydromechanical Response of a Fracture Undergoing Compression and Shear," *International Journal of Rock Mechanics and Mining Sciences & Geomechanics Abstracts*, Vol. 30, 845-851.

**Appendix A**  
**Available DAS-Acquired Data for the SHT**  
**(through 31 May 1997)**

CD-ROMs with all data were submitted to the records as part of this TDIF. A copy may be obtained from Fred Homuth, LANL/TCO, at (702) 794-2351.

Page intentionally blank

## Appendix B

### Thermomechanical Gage Specifications for the SHT

#### Summary of SNL-installed Measurement System Specifications

Measurement System	Manufacturer	Gage Accuracy, Range & Precision	Comments
Type-K Thermocouples	STI (probes) Omega	$\pm 2.2^{\circ}\text{C}$ max 1280 $^{\circ}\text{C}$	Chromel-Alumel
Vibrating Wire Displacement Transducers	GeoKon	1 in. full range Resolution: .02%	
High-Temp LVDT	RDP	$\pm 0.5\%$ of full range = $\pm 19$ mm @200 $^{\circ}\text{C}$	
Wire Extensometer	Houston Scientific, Inc.	0.1% resolution 2-in. range	
Vibrating Wire Load Cell	GeoKon	60,000 lb max $\pm 0.5\%$ full range	
Tape Extensometer	GeoKon	$\pm 0.127$ mm	
Goodman Jack -Readout Box -Near LVDT -Far LVDT -Pressure Gage -Enerpak Pump	Sinco	0-10,000 psi -0.25 to +0.25 in. displacement	
Power Monitor	Magtrol	Volts (0.2% of reading +0.2% of range) 0-600 volts Amps (0.22% of reading +0.25% of range) 0-50 amps watts (0.2% of reading +0.3% of range)	
Thermistor.	Omega	$\pm 0.2^{\circ}\text{C}$ 100 $^{\circ}\text{C}$ range	

Note: Additional gage information can be found in the SNL Scientific Notebook covering this work.

**Page intentionally blank**

## **Appendix C**

### **As-built Gage Locations**

**Tabulated Heater Power Data**

**Tabulated Temperature Gage Data**

**Tabulated Mechanical Gage Data**

The gage locations presented in this appendix are identified by a unique designation based on borehole (if used), gage type, and gage location along the hole. In all cases the gage identification for the SHT begins with TMA, which stands for Thermo Mechanical Alcove (the location of the SHT). This is followed by the borehole ID and number as follows:

H-1	=	Heater borehole
TC-1 through TC-7	=	Thermocouple borehole
BX-1 through BX-4	=	MPBX borehole
WX-1 through WX-6	=	Wire extensometer station pins
WXM-1 through WXM-6	=	Wire extensometer manual pins (tape extensometer)
RBLC-1 through RBLC-8	=	Rock bolt boreholes
STC	=	Surface Thermocouple (on rock surface)
IN-THRM	=	Insulation Thermistor
TEMP	=	Temperature data from hydrology boreholes in which RTDs were used to measure temperature
TCT	=	Thermocouple top (of heater)
TCS	=	Thermocouple side (of heater)
TCB	=	Thermocouple bottom (of heater)
RTD	=	Resistance Temperature Device

The gage numbers follow at the end of the designation. Exceptions are the RTD and Temp gages in which the gage type precedes the LANL-TCO borehole number and are of the form TMA-RTD-15-1, where RTD is the gage type, 15 is the borehole number, and 1 is the unique gage number.

The "as-built" gage locations (x,y,z coordinates) for all gages presented in Appendix C have been submitted as QA records in TDIF#305721 (DTN#SNF35110695001.001) *with the exception of RTD and TEMP gages*. RTD and TEMP gage locations are the responsibility of Lawrence Livermore National Laboratory.

Table C-1 Power Data Obtained from the Heater Power Gage

Gage	Location (m)				Days after Startup								
					0	14	28	42	56	70	84	98	112
	x	y	z	r	(W)								
TMA-HEATER-POW	0	0	0	0	16.81	3911.4	3869.4	3856.3	3831.6	3899.9	3881.8	3831.1	1367.8

Table C-2 Thermal Data Obtained from the SHT Block

Gage	Location (m)				Days after Startup								
					0	14	28	42	56	70	84	98	112
	x	y	z	r	°C								
TMA-H-1-TCT-1	-0.008	6.97	0.048	0.049	24.11	312.48	320.14	331.89	358.86	367.79	388.13	385.4	147.04
TMA-H-1-TCT-2	-0.007	6.47	0.046	0.047	24.33	388.51	404.76	415.87	425.83	426.18	435.97	423.47	164.7
TMA-H-1-TCT-3	-0.007	5.97	0.045	0.046	23.94	402.59	416.72	407.92	401.27	391.74	395.02	387.2	184.48
TMA-H-1-TCT-4	-0.006	5.47	0.043	0.043	23.66	382.87	400.17	388.86	383.79	383.1	384.55	379.69	196.8
TMA-H-1-TCT-5	-0.005	4.47	0.04	0.04	23.64	384.43	400.17	396.21	389.98	388.08	390.1	383.79	207.01
TMA-H-1-TCT-6	-0.004	3.47	0.037	0.037	23.56	391.36	386.75	383.93	376.19	372.14	368.88	363.93	189.65
TMA-H-1-TCT-7	-0.003	2.97	0.035	0.035	23.66	360.71	360.31	361.95	359.14	361.48	368.6	361.81	177.59
TMA-H-1-TCT-8	-0.003	2.47	0.033	0.033	23.74	329.81	333.06	334.04	332.44	334.45	335.29	333.21	151.69
TMA-H-1-TCT-9	-0.002	1.97	0.032	0.032	23.79	212.7	212.8	213.82	212.88	229.83	214.4	227.2	116.46
TMA-H-1-TCS-1	-0.041	6.97	0.002	0.041	23.34	309.71	318.87	329.69	353.33	361.64	381.37	379	148.13
TMA-H-1-TCS-2	-0.04	6.47	0	0.04	23.76	370.26	385.26	394.43	404.03	404.34	413.1	401.25	165.63
TMA-H-1-TCS-3	-0.04	5.97	-0.001	0.04	23.86	393.21	405.88	397.46	392.81	385.73	388.79	381.73	186.26
TMA-H-1-TCS-4	-0.039	5.47	-0.003	0.039	23.79	360.79	378.33	371.79	370.43	369.74	371.05	366.98	196.82
TMA-H-1-TCS-5	-0.038	4.47	-0.006	0.038	23.66	372.19	388.93	386.45	382.32	381.99	383.34	377.48	207.34
TMA-H-1-TCS-6	-0.037	3.47	-0.009	0.038	23.79	380.88	377.02	375.98	371.12	367.93	365.5	361.02	190.05
TMA-H-1-TCS-7	-0.036	2.97	-0.011	0.038	23.76	349.35	350.67	352.36	350.43	352.88	360.31	354.43	177.66
TMA-H-1-TCS-8	-0.036	2.47	-0.013	0.038	23.71	324.74	328.61	329.76	329.23	330.79	330.72	328.59	151.22
TMA-H-1-TCS-9	-0.035	1.97	-0.014	0.038	23.79	193.32	194.02	195.1	194.75	210.15	196	207.93	112.82
TMA-H-1-TCB-1	-0.008	6.97	-0.019	0.021	23.76	307.84	316.54	328.37	355.12	364.71	385.14	382.68	147.59
TMA-H-1-TCB-2	-0.007	6.47	-0.021	0.022	23.84	389.27	409.31	417.76	425.97	426.35	435.49	423.14	165.13
TMA-H-1-TCB-3	-0.007	5.97	-0.022	0.023	24.28	397.44	412.18	404.17	397.8	388.39	391.36	383.27	185.48
TMA-H-1-TCB-4*	-0.006	5.47	-0.024	0.025	24.11	NA	NA	NA	NA	NA	NA	NA	NA
TMA-H-1-TCB-5	-0.005	4.47	-0.027	0.027	23.56	376.76	392.74	389.88	381.64	380.99	382.49	376.69	207.11
TMA-H-1-TCB-6	-0.004	3.47	-0.03	0.03	23.76	391.95	388.39	386.49	379.9	375.12	371.55	366.83	189.82
TMA-H-1-TCB-7	-0.003	2.97	-0.032	0.032	23.54	355.05	355.62	356.21	353.69	355.45	362.12	356.07	177.24
TMA-H-1-TCB-8	-0.003	2.47	-0.034	0.034	23.54	335.93	339.67	340.81	339.28	341.01	340.72	338.68	150.8
TMA-H-1-TCB-9	-0.002	1.97	-0.035	0.035	23.76	198.4	198.95	200.23	199.7	215.37	200.8	213.25	113.01
TMA-TC-1A-1	-0.275	7.977	0.367	0.459	23.81	34.88	41.31	45.68	48.61	51.09	53.77	55.17	57.39
TMA-TC-1A-2	-0.269	7.477	0.364	0.453	24.26	47.71	56.59	63.12	67.25	68.89	71.39	72.62	75.7
TMA-TC-1A-3	-0.264	6.977	0.36	0.446	24.26	69.2	79.81	84.83	88.44	91.23	92.87	94.35	96.14
TMA-TC-1A-4	-0.259	6.477	0.356	0.44	23.76	83.65	95.65	101.4	105.85	109.03	112.26	114.13	116.63
TMA-TC-1A-5	-0.253	5.978	0.353	0.434	23.91	91.28	105.17	113.3	118.24	124.07	127.14	129.65	131.67
TMA-TC-1A-6	-0.248	5.478	0.349	0.428	23.64	95.43	108.79	120.15	127.71	131.42	134.83	138.22	140.32
TMA-TC-1A-7	-0.237	4.478	0.342	0.416	23.74	97.73	114.64	124.63	130.66	136.93	141.48	143.82	145.1
TMA-TC-1A-8	-0.226	3.478	0.335	0.404	23.51	93.67	108.35	117.58	123.71	128.2	131.18	133.65	134.71
TMA-TC-1A-9	-0.221	2.978	0.331	0.398	23.64	92.73	104.47	111.75	116.88	121.02	124.19	126.33	127.09
TMA-TC-1A-10	-0.215	2.478	0.328	0.392	23.84	87.19	99.15	105	108.28	111.55	113.79	115.51	114.85
TMA-TC-1B-1	-0.213	2.218	0.326	0.389	24.11	86.68	98.36	104.15	107.48	110.68	112.35	114.37	113.15
TMA-TC-1B-2	-0.207	1.718	0.322	0.383	24.23	70.58	78.61	83.04	85.84	89.18	89.45	91.5	90.22
TMA-TC-1B-3	-0.202	1.218	0.319	0.378	24.31	56.38	63.16	66.76	68.65	71.08	71.06	72.79	72.02
TMA-TC-1B-4	-0.196	0.718	0.315	0.371	24.36	41.04	47.68	51.01	52.73	54.64	54.98	56.18	56.59
TMA-TC-1B-5	-0.191	0.218	0.312	0.366	24.58	33.31	37.55	39.97	40.97	41.85	42.55	42.86	43.54
TMA-TC-2A-1	0.609	8.136	0.283	0.672	24.58	31.03	35.54	38.95	41.85	44.54	46.76	48.07	51.23
TMA-TC-2A-2	0.61	7.636	0.28	0.671	24.63	35.98	42.52	47.39	50.53	53.5	55.56	57.29	59.95
TMA-TC-2A-3	0.61	7.136	0.277	0.67	24.03	46.63	55	60.05	63.5	66.35	69.11	70.29	73.17
TMA-TC-2A-4*	0.611	6.636	0.274	0.67	24.08	60.05	-89.66	-119.36	-5.33	46.02	66.62	75.14	79.98
TMA-TC-2A-5	0.611	6.136	0.272	0.669	23.76	67.8	79.4	85.34	90.63	94.76	96.84	97.97	100.07

NA: Not available.

\* Suspected failed gages.

Table C-1. Power Data Obtained from the Heater Power Gage

Gage	Days after Startup											
	126	140	154	168	182	196	210	224	238	252	266	275
	(W)											
TMA-HEATER-POW	3870.6	3788.2	3824.2	3718.2	3798.5	3790.3	3779.1	3791.9	3751.2	3758.9	3752.7	3725.8

Table C-2 Thermal Data Obtained from the SHT Block

Gage	Days after Startup											
	126	140	154	168	182	196	210	224	238	252	266	275
	°C											
TMA-H-1-TCT-1	322.43	118.29	310.6	308.01	306.95	303.68	300.94	304.54	301.51	300.72	299.98	299.98
TMA-H-1-TCT-2	356.74	133.63	345.69	343.13	347.01	347.15	345.45	347.92	345.81	346.41	345.93	346.7
TMA-H-1-TCT-3	364.05	149.68	358.07	357.98	360.6	361.14	360.1	363.76	360.95	360.95	362.31	362.93
TMA-H-1-TCT-4	376.98	160.07	375.88	376.88	379.24	380.47	380.69	384.15	382.06	382.01	383.17	384.53
TMA-H-1-TCT-5	385.19	166.68	386.56	385.45	387.8	388.51	388.17	392.21	389.53	389.36	389.67	390.64
TMA-H-1-TCT-6	361.29	155.72	361.69	360.55	362.79	363.21	363.17	366.43	363.95	363.81	363.6	364.79
TMA-H-1-TCT-7	364.83	144.34	365.67	364.24	366.05	366.21	367.38	370.5	367.57	367.48	367.93	368.71
TMA-H-1-TCT-8	334.74	124.73	334.62	333.42	334.59	334.59	335.84	338.52	336.03	335.81	335.81	336.41
TMA-H-1-TCT-9	212.65	101.28	213.27	214.77	215.47	216.04	216.14	217.74	216.82	216.79	217.21	217.56
TMA-H-1-TCS-1	319.59	118.54	308.49	305.96	304.95	303.24	299.93	303.2	300.24	300.1	298.72	299.01
TMA-H-1-TCS-2	345.91	134.07	336.48	333.99	338.09	338.47	336.46	339.23	336.87	336.89	337.63	338.18
TMA-H-1-TCS-3	363.67	151.02	359.17	360.36	362.14	362.86	362.86	365.93	364.17	364.12	366.9	367.1
TMA-H-1-TCS-4	365.38	160.18	364.69	365.86	368.1	369.12	370.1	373.57	371.64	371.76	373.76	375.17
TMA-H-1-TCS-5	380.14	166.68	381.61	380.21	382.54	383.15	383.32	387.18	384.83	384.1	384.27	385.36
TMA-H-1-TCS-6	359.48	155.82	360.05	358.76	360.57	361.05	361.6	365.07	362.52	362.43	362	363
TMA-H-1-TCS-7	358.21	144.63	359.12	357.74	359.48	359.64	361.05	364.24	361.31	361.07	361.1	361.98
TMA-H-1-TCS-8	330.79	124.44	331.32	329.9	331.24	331.32	332.87	335.62	332.89	332.63	332.66	333.09
TMA-H-1-TCS-9	197.5	99.64	197.48	199.05	199.82	200.58	200.9	202.46	201.83	201.88	202.46	203.17
TMA-H-1-TCB-1	322.09	117.51	309.74	307.79	305.43	302.31	300	302.52	299.95	299.13	297.42	297.75
TMA-H-1-TCB-2	356.52	134.34	344.98	342.54	345.65	345.5	343.99	346.29	344.45	344.31	344.14	345.07
TMA-H-1-TCB-3	362.62	151.44	357.29	356.83	359.24	359.52	358.6	361.74	359.5	359.12	360.83	361.36
TMA-H-1-TCB-4*	NA	NA	NA	NA	NA	NA	NA	NA	NA	NA	NA	NA
TMA-H-1-TCB-5	379	166.75	379.48	378.43	380.59	381.18	380.88	384.6	382.23	381.71	381.54	382.56
TMA-H-1-TCB-6	364.24	155.52	364.43	363.52	365.31	365.83	365.95	369.1	366.5	366.67	366.19	367.31
TMA-H-1-TCB-7	358.29	144.19	358.83	357.6	359.17	359.76	360.6	363.95	361.1	360.98	361.24	362.07
TMA-H-1-TCB-8	340.77	124.19	340.89	339.64	340.62	340.81	342.61	345.57	342.63	342.46	342.56	343.04
TMA-H-1-TCB-9	200.88	99.57	201.91	203.49	204.27	204.93	205.32	206.91	206.17	205.99	206.67	207.19
TMA-TC-1A-1	56.59	58.89	59.44	60.8	61.72	62.63	62.71	63.7	64.28	64.52	64.69	65
TMA-TC-1A-2	73.75	76.27	77.19	78.82	79.66	80.7	80.14	81.18	81.52	81.76	81.57	82.49
TMA-TC-1A-3	95.97	94.52	99.18	100.68	101.74	102.92	103.09	104.35	104.9	105.51	105.58	106.36
TMA-TC-1A-4	118.24	114.05	121.27	123.29	125.07	126.55	126.72	127.61	128.4	129.11	128.84	130.39
TMA-TC-1A-5	131.94	125.96	134.83	136.91	138.94	140.64	141.11	142.93	144.29	145.17	144.7	146.82
TMA-TC-1A-6	141.06	135.59	144.38	146.52	148.26	150.12	150.4	152.54	153.93	154.93	154.15	156.37
TMA-TC-1A-7	146.39	139.9	149.63	151.82	153.78	155.42	155.35	157.59	158.63	159.15	158.11	160.07
TMA-TC-1A-8	135.84	130.32	138.81	140.89	142.61	144.11	143.94	145.99	146.91	147.39	146.82	148.66
TMA-TC-1A-9	128.3	122.32	130.78	132.57	134.26	135.59	135.42	137.33	138.07	138.54	137.87	139.73
TMA-TC-1A-10	117.32	110	119.68	121.44	122.98	124.15	124.02	125.67	126.38	126.75	126.33	127.91
TMA-TC-1B-1	115.46	108.59	118.07	119.93	121.39	122.51	122.32	123.93	124.61	125.03	124.51	126.23
TMA-TC-1B-2	90.39	88.05	92.17	93.53	94.47	95.07	94.83	96.09	96.47	96.81	96.64	97.71
TMA-TC-1B-3	70.34	70.79	72.28	73.51	74.16	74.3	73.77	74.9	75.07	75.26	75.14	75.91
TMA-TC-1B-4	54.85	56.62	56.69	57.83	58.41	58.67	58.14	59.25	59.4	59.73	59.81	60.31
TMA-TC-1B-5	42.96	44.1	44.2	44.95	45.37	45.76	45.56	46.32	46.83	47.24	48.12	48.39
TMA-TC-2A-1	50.29	51.28	53.36	54.28	55.1	55.82	56.16	56.93	57.42	57.95	58.26	58.36
TMA-TC-2A-2	58.53	60.77	61.26	62.63	63.53	64.23	64.47	65.53	65.87	66.35	66.67	67.03
TMA-TC-2A-3	71.88	74.01	74.74	76.11	77.26	78.32	78.46	79.71	80.29	80.6	80.63	81.16
TMA-TC-2A-4*	82.42	85.24	88.22	89.76	91.35	91.93	92.05	96.45	97.15	98.31	97	97.49
TMA-TC-2A-5	98.77	101.16	102.46	103.74	104.95	106.36	107.09	108.64	109.49	110.24	110.29	111.24

NA: Not available.

\* Suspected failed gages.

Table C-2 Thermal Data Obtained from the SHT Block

Gage	Location (m)				Days after Startup								
					0	14	28	42	56	70	84	98	112
	x	y	z	r	°C								
TMA-TC-2A-6	0.612	5.636	0.269	0.669	23.84	71.61	85.53	92.46	96.5	99.23	101.21	102.71	105.73
TMA-TC-2A-7	0.613	4.636	0.263	0.667	23.42	72.5	88.13	95.63	100	103.7	106.8	109	111.6
TMA-TC-2A-8	0.614	3.636	0.257	0.666	23.47	70.46	85.53	93.82	99.18	102.71	104.66	105.97	107.33
TMA-TC-2A-9	0.615	3.136	0.254	0.665	23.42	68.74	82.78	90.77	95.68	98.02	99.57	101.11	102.37
TMA-TC-2A-10	0.615	2.636	0.251	0.664	23.61	65.39	78.05	85.02	89.42	92.54	94.83	96.3	97.63
TMA-TC-2B-1	0.616	2.126	0.248	0.664	23.99	59.95	70.1	75.82	79.61	82.75	84.54	86.42	87.48
TMA-TC-2B-2	0.616	1.626	0.245	0.663	24.21	50.51	58.87	63.28	66.18	68.72	69.95	71.56	72.36
TMA-TC-2B-3	0.617	1.126	0.242	0.663	24.56	42.09	49.49	53.19	55.41	57.44	58.36	59.71	60.44
TMA-TC-2B-4	0.617	0.626	0.239	0.662	24.73	35.37	41.51	44.88	46.58	48.19	49.17	50.19	51.06
TMA-TC-2B-5	0.618	0.126	0.237	0.662	24.83	31.15	35.32	37.67	38.55	39.58	40.51	41.12	41.99
TMA-TC-3A-1	-0.719	8.268	1.342	1.522	24.8	27.12	31.08	33.87	36.52	38.87	40.36	42.01	44.15
TMA-TC-3A-2	-0.721	7.768	1.338	1.52	24.45	28.97	33.28	37.84	40.58	42.67	44.39	46.51	47.81
TMA-TC-3A-3	-0.723	7.268	1.335	1.518	25.47	31.76	37.3	41.87	44.64	47.24	50.07	51.18	53.5
TMA-TC-3A-4	-0.725	6.768	1.332	1.517	24.13	33.31	41.17	46.39	49.54	52.54	54.98	56.76	58.43
TMA-TC-3A-5	-0.728	6.268	1.328	1.514	27.27	38.36	47.37	52.75	57.87	60.15	62.01	64.01	68.62
TMA-TC-3A-6	-0.73	5.768	1.325	1.513	24.23	39.14	49.76	56.06	59.54	62.58	64.95	67.97	69.88
TMA-TC-3A-7	-0.734	4.768	1.318	1.509	23.29	38.06	48.24	55.65	60.36	63.82	66.74	68.57	70.53
TMA-TC-3A-8	-0.738	3.768	1.312	1.505	23.22	37.87	49.12	55.99	60.39	63.53	66.38	68.36	70
TMA-TC-3A-9	-0.741	3.268	1.308	1.503	23.07	37.06	47.58	54.15	58.5	61.62	64.25	66.06	67.58
TMA-TC-3A-10	-0.743	2.768	1.305	1.502	23.22	36.4	46	52.05	56.11	59.13	61.52	63.14	64.66
TMA-TC-3B-1	-0.745	2.298	1.302	1.5	23.64	35.34	44.25	49.81	53.58	56.3	58.5	60.05	61.5
TMA-TC-3B-2	-0.747	1.798	1.299	1.498	24.06	33.33	41.12	45.98	49.32	51.69	53.7	55.02	56.33
TMA-TC-3B-3	-0.749	1.298	1.295	1.496	24.23	31.32	37.87	42.06	44.85	46.95	48.63	49.76	50.99
TMA-TC-3B-4	-0.751	0.798	1.292	1.494	24.48	29.61	35.24	38.85	41.19	42.91	44.32	45.22	46.37
TMA-TC-3B-5	-0.754	0.298	1.289	1.493	24.5	28.74	33.24	36.28	37.97	39.34	40.53	41.04	42.01
TMA-TC-4A-1*	-0.117	6.888	-0.759	0.768	23.07	46.07	55.02	60.29	10.98	51.96	70.19	59.03	58.96
TMA-TC-4A-2	-0.111	6.388	-0.752	0.76	23.69	55.56	65.77	71.85	76.32	79.81	82.1	83.19	85.53
TMA-TC-4A-3	-0.104	5.888	-0.745	0.752	23.64	61.21	73.34	80.17	84.28	87.09	89.88	91.86	93.41
TMA-TC-4A-4	-0.097	5.388	-0.738	0.744	23.44	64.37	78.22	85.39	89.23	92.2	94.78	96.74	97.71
TMA-TC-4A-5	-0.09	4.888	-0.731	0.737	23.24	65.72	80	88.53	92.61	95.77	97.39	98.94	100.65
TMA-TC-4A-6	-0.083	4.388	-0.724	0.729	23.37	67.13	82.44	91.28	95.6	97.22	99.98	101.81	103.36
TMA-TC-4A-7	-0.07	3.888	-0.709	0.712	23.17	66.43	80.8	88.1	92.22	95.48	98.36	100.39	102.17
TMA-TC-4A-8	-0.056	2.389	-0.695	0.697	23.14	59.4	71.01	77.07	80.68	83.6	85.63	87.16	88.49
TMA-TC-4B-1	-0.052	2.099	-0.691	0.693	23.61	55.65	65.97	71.51	75.1	77.89	79.61	81.04	82.2
TMA-TC-4A-9	-0.05	1.889	-0.688	0.69	23.34	51.93	61.11	66.28	69.35	71.97	73.41	75	76.03
TMA-TC-4B-2	-0.046	1.599	-0.684	0.686	23.81	47.29	55.22	59.95	62.8	65.14	66.3	67.83	68.74
TMA-TC-4A-10	-0.043	1.38	-0.681	0.682	23.44	43.64	50.87	54.95	57.68	59.85	60.89	62.34	63.16
TMA-TC-4B-3	-0.039	1.099	-0.677	0.678	23.94	39.76	45.83	49.73	52.15	54.13	55.17	56.5	57.39
TMA-TC-4B-4	-0.032	0.599	-0.67	0.671	23.91	33.14	37.7	40.41	41.97	43.57	44.81	45.9	47
TMA-TC-4B-5	-0.025	0.099	-0.662	0.662	23.94	28.57	29.73	31.47	31.5	33.24	35.03	35.86	37.13
TMA-TC-5A-1	-0.059	8.145	0.712	0.714	29.24	30.78	36.37	40.15	42.74	45.15	47.15	48.83	49.66
TMA-TC-5A-2	-0.056	7.645	0.71	0.712	26.28	37.79	43.74	48.24	52.05	53.72	55.8	58.33	61.57
TMA-TC-5A-3	-0.053	7.145	0.708	0.71	23.49	43.54	51.98	57.37	60.51	63.87	66.23	67.97	69.95
TMA-TC-5A-4	-0.05	6.645	0.706	0.708	24.06	55.46	65.39	71.15	74.83	77.74	80.31	81.62	83.84
TMA-TC-5A-5	-0.047	6.145	0.705	0.707	24.03	64.18	75.26	82.17	86.54	89.14	91.28	92.8	95.05
TMA-TC-5A-6	-0.044	5.645	0.703	0.704	23.71	68.26	81.06	88.05	91.79	94.52	96.81	98.74	100.58
TMA-TC-5A-7	-0.038	4.645	0.699	0.7	23.34	70.86	86.13	94.11	98.38	101.67	104.83	106.97	109.1
TMA-TC-5A-8	-0.032	3.645	0.696	0.697	23.09	68.96	83.41	91.84	96.76	99.9	102.92	104.93	106.77
TMA-TC-5A-9	-0.029	3.145	0.694	0.695	23.19	67.44	80.58	88.41	93.38	96.86	99.71	101.84	103.7
TMA-TC-5A-10	-0.025	2.645	0.692	0.692	23.27	65.1	76.71	83.79	88.1	91.38	93.89	95.65	97.15
TMA-TC-5B-1	-0.023	2.225	0.691	0.691	23.59	59.95	69.83	75.5	79.28	82.37	84.4	86.15	87.11
TMA-TC-5B-2	-0.02	1.725	0.689	0.689	23.79	51.86	60.6	65.19	68.16	70.84	72.11	73.61	74.45
TMA-TC-5B-3	-0.017	1.225	0.687	0.687	24.16	43.57	51.4	55.24	57.54	59.59	60.51	61.76	62.46
TMA-TC-5B-4	-0.014	0.725	0.685	0.685	24.18	36.59	43.71	47.1	48.95	50.6	51.4	52.25	53.02

NA: Not available.

\* Suspected failed gages.

Table C-2 Thermal Data Obtained from the SHT Block

Gage	Days after Startup											
	126	140	154	168	182	196	210	224	238	252	266	275
	°C											
TMA-TC-2A-6	104.95	107.5	109.2	111.29	113.32	115.05	114.88	116.73	117.76	118.54	118.51	119.76
TMA-TC-2A-7	110.9	112.99	114.47	116.66	118.61	120.19	120.18	122.05	123.1	123.81	123.73	125.03
TMA-TC-2A-8	106.5	107.99	109.42	111.33	113.25	114.71	114.71	116.73	117.73	118.37	118.32	119.44
TMA-TC-2A-9	101.88	103.45	104.69	106.65	108.5	109.56	109.25	111.17	112.21	112.79	112.84	114.15
TMA-TC-2A-10	96.79	97.92	98.86	100.31	101.5	102.39	102.13	103.7	104.35	104.76	104.61	105.63
TMA-TC-2B-1	86.3	87.96	88.56	90.14	91.06	91.78	91.5	92.78	93.31	93.65	93.45	94.37
TMA-TC-2B-2	71.18	72.86	73.08	74.4	75.24	75.89	75.72	76.88	77.26	77.74	77.79	78.53
TMA-TC-2B-3	59.08	60.77	60.8	61.93	62.63	62.99	62.83	63.84	64.13	64.57	64.73	65.29
TMA-TC-2B-4	50.07	51.64	51.67	52.63	53.21	53.55	53.38	54.35	54.56	55.1	55.41	55.89
TMA-TC-2B-5	41.72	42.91	42.99	43.74	44.22	44.59	44.71	45.44	45.85	46.44	47.07	47.49
TMA-TC-3A-1	43.33	47.37	48.15	49.51	48.76	49.63	50.34	51.18	51.4	51.98	52.44	52.9
TMA-TC-3A-2	47.63	49.34	49.71	50.77	51.5	52.08	52.61	53.19	53.67	54.15	54.32	54.69
TMA-TC-3A-3	53.02	54.78	55.29	56.33	57.2	57.9	58.09	58.84	59.32	59.73	60.22	60.41
TMA-TC-3A-4	57.99	59.95	60.17	61.42	62.29	63.14	63.33	64.2	64.81	65.29	65.63	65.92
TMA-TC-3A-5	55.63	70.07	69.98	71.25	72.16	72.72	72.45	73.25	73.56	73.63	73.46	73.51
TMA-TC-3A-6	68.26	71.61	71.8	73.17	74.14	74.57	74.4	75.17	75.5	75.82	75.94	76.06
TMA-TC-3A-7	70.1	72.28	72.45	73.92	74.98	75.67	75.94	76.97	77.6	78.1	78.46	78.65
TMA-TC-3A-8	69.69	71.44	71.59	72.86	73.92	74.83	74.98	75.99	76.64	77.16	77.52	77.74
TMA-TC-3A-9	67.29	68.82	68.99	70.29	71.39	72.19	72.24	73.27	73.89	74.4	74.71	74.88
TMA-TC-3A-10	64.37	65.87	66.06	67.25	68.29	69.03	69.03	70.07	70.7	71.13	71.49	71.66
TMA-TC-3B-1	61.13	62.63	62.58	63.72	64.71	65.41	65.41	66.33	66.93	67.39	67.71	67.95
TMA-TC-3B-2	55.99	57.29	57.27	58.26	59.08	59.71	59.81	60.65	61.16	61.59	61.98	62.27
TMA-TC-3B-3	50.65	51.76	51.74	52.61	53.41	53.96	54.01	54.76	55.19	55.7	56.01	56.33
TMA-TC-3B-4	46.07	47	46.93	47.66	48.42	48.95	49.12	49.73	50.1	50.72	51.16	51.42
TMA-TC-3B-5	41.82	42.6	42.62	43.15	43.69	44.27	44.49	45.1	45.54	46.1	46.73	47.07
TMA-TC-4A-1*	48.15	64.64	66.64	68.99	75.53	77.16	76.42	77.96	78.13	78.63	78.08	79.06
TMA-TC-4A-2	84.37	86.11	86.83	88.13	89.04	89.83	89.18	90.39	90.53	90.87	90.41	91.18
TMA-TC-4A-3	92.54	93.74	94.35	95.56	96.06	96.43	96.09	96.91	97.17	97.54	97.68	98.33
TMA-TC-4A-4	96.79	97.8	98.02	99.9	101.55	103.14	103.5	105.41	106.38	107.16	107.31	108.18
TMA-TC-4A-5	100.02	101.57	102.25	103.86	105.75	107.57	107.99	110.02	111.12	111.8	111.99	112.91
TMA-TC-4A-6	102.68	104.13	105.32	106.99	108.74	110.32	110.65	112.5	113.76	114.68	114.83	115.9
TMA-TC-4A-7	101.33	102.95	103.96	105.49	106.87	108.01	107.86	109.49	110.29	110.87	110.92	111.85
TMA-TC-4A-8	87.84	89.16	90.05	91.33	92.46	93.36	93.24	94.57	95.27	95.65	95.68	96.55
TMA-TC-4B-1	81.67	82.85	83.48	84.76	85.84	86.54	86.37	87.62	88.22	88.68	88.63	89.4
TMA-TC-4A-9	75.34	76.66	77.26	78.56	79.5	80.22	80.14	81.23	81.88	82.42	82.58	83.21
TMA-TC-4B-2	67.71	69.06	69.3	70.55	71.35	72.02	71.85	72.98	73.56	74.01	74.25	74.81
TMA-TC-4A-10	61.93	63.45	63.72	64.83	65.63	66.16	66.04	67.05	67.54	67.97	68.21	68.77
TMA-TC-4B-3	56.11	57.37	57.46	58.5	59.25	59.71	59.52	60.56	60.87	61.38	61.67	62.13
TMA-TC-4B-4	46.32	47.29	47.37	48.29	48.88	49.42	49.49	50.39	50.65	51.23	51.69	52.08
TMA-TC-4B-5	37.38	37.82	38.04	38.7	39.24	39.78	40.39	40.9	41.43	41.99	42.79	43.2
TMA-TC-5A-1	50.6	51.13	53.31	54.32	55.12	55.82	56.06	56.55	56.96	57.2	57.2	57.66
TMA-TC-5A-2	58.21	62.22	62.75	64.01	64.88	65.68	65.68	66.28	66.55	66.79	67.03	67.22
TMA-TC-5A-3	68.91	70.41	71.44	72.81	74.04	74.9	74.52	75.84	76.25	76.59	76.68	77.14
TMA-TC-5A-4	83.6	84.42	86.23	87.72	88.99	89.86	90.27	91.64	91.33	92.54	92.37	92.49
TMA-TC-5A-5	94.35	94.95	96.11	97.29	98.24	98.99	99.06	99.61	100.02	100.75	100.82	101.43
TMA-TC-5A-6	99.88	100.58	102.03	103.55	105.32	106.89	107.5	109.27	110.63	111.68	111.92	112.86
TMA-TC-5A-7	109	110.44	112.43	114.2	116.15	117.88	118.1	120.1	121.17	121.98	121.93	123.17
TMA-TC-5A-8	106.02	107.23	108.86	111.04	112.89	114.22	114.25	116.05	117.12	117.78	117.73	118.93
TMA-TC-5A-9	102.68	104.11	105.36	106.92	108.25	109.2	108.98	110.56	111.26	111.77	111.87	113.11
TMA-TC-5A-10	96.23	97.29	98.55	100	101.18	102.1	101.81	103.29	103.91	104.32	104.25	105.22
TMA-TC-5B-1	86.23	87.45	88.29	89.76	90.85	91.55	91.28	92.66	93.24	93.65	93.55	94.35
TMA-TC-5B-2	73.27	74.9	75.02	76.35	77.26	77.84	77.6	78.75	79.25	79.61	79.69	80.39
TMA-TC-5B-3	61.09	62.78	62.68	63.82	64.59	64.93	64.64	65.68	65.97	66.38	66.55	67.08
TMA-TC-5B-4	51.81	53.45	53.21	54.13	54.78	55.12	54.85	55.77	56.06	56.52	56.79	57.25

NA: Not available.

\* Suspected failed gages.

Table C-2 Thermal Data Obtained from the SHT Block

Gage	Location (m)				Days after Startup								
					0	14	28	42	56	70	84	98	112
	x	y	z	r	°C								
TMA-TC-5B-5	-0.011	0.225	0.683	3.683	24.56	32.47	37.89	40.56	41.85	42.94	43.71	44.2	44.95
TMA-TC-6-1	0.617	5.417	-0.016	0.617	23.05	77.89	89.25	96.01	99.52	102.87	106.12	108.81	111.24
TMA-TC-6-2	0.757	5.418	-0.015	0.757	23.17	67.32	79.5	86.61	91.16	94.15	96.55	98.09	99.54
TMA-TC-6-3	0.917	5.419	-0.014	0.917	22.94	57.56	69.88	76.83	81.4	84.88	88.2	90.39	92.03
TMA-TC-6-4	1.257	5.421	-0.012	1.257	23.56	45.07	56.53	62.73	67.49	70.53	73.46	75.55	76.95
TMA-TC-6-5	1.507	5.423	-0.011	1.507	23.02	37.92	48.39	54.42	58.65	61.79	64.59	66.55	68.14
TMA-TC-6-6	1.737	5.424	-0.01	1.737	23.34	33.78	42.86	48.51	52.83	55.77	58.36	60.31	61.81
TMA-TC-6-7	2.257	5.428	-0.007	2.257	22.9	27.76	34.71	39.63	43.23	46.05	48.46	50.29	51.57
TMA-TC-6-8	3.257	5.434	-0.001	3.257	22.87	24.56	27.41	30.42	33.14	35.32	37.21	38.8	39.93
TMA-TC-6-9	4.257	5.441	0.005	4.257	23.37	24.01	24.98	26.5	28.23	29.9	31.23	32.5	33.48
TMA-TC-6-10	5.257	5.447	0.01	5.257	23.94	24.01	24.33	25.05	26.11	27.17	28.13	29.09	29.66
TMA-TC-7-1	-0.96	3.4	0.007	0.96	23.19	56.59	76.44	78.94	82.34	85.94	89.54	91.98	93.31
TMA-TC-7-2	-1.1	3.401	0.008	1.1	23.17	50.58	65.63	71.51	75.43	78.92	82.03	84.23	85.99
TMA-TC-7-3	-1.26	3.402	0.008	1.26	23.29	45.29	58.53	65.05	69.13	72.55	75.48	77.64	79.42
TMA-TC-7-4	-1.6	3.403	0.009	1.6	22.92	37.08	48.34	54.73	58.72	61.91	64.59	66.64	68.38
TMA-TC-7-5	-1.85	3.404	0.01	1.85	23.32	32.87	42.38	48.34	52.29	55.34	57.87	59.81	61.47
TMA-TC-7-6	-2.08	3.406	0.01	2.08	23.19	30.02	38.48	43.93	47.63	50.65	53.04	54.98	56.57
TMA-TC-7-7	-2.6	3.408	0.011	2.6	23.19	26.33	32.11	36.62	39.93	42.52	44.71	46.44	47.9
TMA-TC-7-8	-3.6	3.413	0.014	3.6	23.34	24.18	27.5	29.06	31.32	33.43	35.07	36.57	37.74
TMA-TC-7-9	-4.6	3.418	0.016	4.6	23.66	23.91	24.68	25.91	27.32	28.79	29.93	30.91	31.74
TMA-TC-7-10	-5.6	3.423	0.019	5.6	23.74	24.03	24.21	24.75	25.57	26.53	27.44	28.15	28.84
TMA-BX-1-TC-1	0.131	6.863	0.31	0.337	24.03	33.31	38.24	40.29	40.85	42.06	42.57	43.18	43.45
TMA-BX-1-TC-2	0.136	6.023	0.309	0.338	22.8	96.18	107.18	113.91	119.61	124.71	128.08	130.69	129.38
TMA-BX-1-TC-3	0.142	5.023	0.307	0.338	23	102.1	118.71	131.03	138.17	142.02	146.29	149.1	148.43
TMA-BX-1-TC-4	0.148	4.023	0.306	0.34	23.29	99.66	118.93	131.1	138.39	143.6	148.01	150.3	150.4
TMA-BX-1-TC-5	0.154	3.023	0.304	0.341	23.27	96.93	112.62	122.46	128.35	132.99	136.61	139.38	139.48
TMA-BX-1-TC-6	0.161	2.023	0.303	0.343	23.69	96.23	98.16	102.95	106.8	110.9	112.99	115.19	113.69
TMA-BX-1-TC-7	0.164	1.543	0.302	0.344	23.76	74.59	78.7	79.38	80.65	84.3	84.2	86.44	84.25
TMA-BX-1-TC-8	0.167	1.043	0.301	0.344	23.86	61.04	67.42	68.24	67.03	69.4	68.29	69.44	67.44
TMA-BX-1-TC-9*	0.17	0.543	0.301	0.346	23.96	47.12	56.09	57.71	57.42	59.9	58.94	60.17	58.33
TMA-BX-2-TC-1	-0.631	7.093	0.281	0.691	22.62	43.13	53.31	61.01	67.08	71.88	75.55	77.98	80.07
TMA-BX-2-TC-2	-0.63	6.543	0.278	0.689	22.87	55.53	65.65	72.79	78.8	82.44	85.29	87.04	88.13
TMA-BX-2-TC-3	-0.63	6.023	0.274	0.687	22.65	63.5	74.57	81.47	85.99	88.41	90.43	91.74	92.68
TMA-BX-2-TC-4	-0.629	5.473	0.271	0.685	22.8	69.9	82.29	89.09	92.97	95.34	97.25	98.62	100.17
TMA-BX-2-TC-5	-0.628	4.883	0.267	0.682	22.92	71.42	83.99	90.51	93.84	96.45	97.1	98.48	104.08
TMA-BX-2-TC-6	-0.628	4.333	0.263	0.681	23.09	71.83	87.09	94.44	98.24	102.34	105.9	108.13	110.1
TMA-BX-2-TC-7	-0.627	3.773	0.259	0.678	22.57	70.19	85.99	92.42	97.08	100.75	104.08	106.09	108.2
TMA-BX-2-TC-8	-0.626	3.223	0.256	0.676	23.05	69.4	83.67	89.86	93.89	97.37	100.29	102.32	104.01
TMA-BX-2-TC-9	-0.626	2.623	0.252	0.675	23.49	66.33	78.53	84.81	88.99	92.42	94.86	97.03	98.41
TMA-BX-2-TC-10	-0.625	2.073	0.248	0.672	23.27	58.58	69.59	76.35	80.07	82.42	83.48	83.94	84.71
TMA-BX-2-TC-11	-0.625	1.513	0.245	0.671	23.37	49.34	58.96	65.17	68.91	71.95	73.25	74.09	74.3
TMA-BX-2-TC-12	-0.624	0.963	0.241	0.669	23.59	38.58	45.49	49.73	52.61	55.19	56.23	57.61	58.09
TMA-BX-2-TC-13	-0.623	0.39	0.237	0.667	23.69	32.35	37.35	40.46	42.26	43.88	44.98	45.85	46.81
TMA-BX-3-TC-1*	0.768	6.887	1.314	1.522	22.65	30.81	37.72	42.28	45.71	48.49	50.92	52.66	54.13
TMA-BX-3-TC-2*	0.765	6.047	1.309	1.516	22.6	34.26	43.08	48.51	52.51	55.58	58.16	59.93	61.5
TMA-BX-3-TC-3	0.762	5.047	1.302	1.509	22.65	37.08	47.95	54.54	59.11	62.37	65.27	67.13	68.6
TMA-BX-3-TC-4	0.759	4.047	1.295	1.501	22.77	37.74	48.93	55.94	60.72	64.11	66.96	68.94	70.55
TMA-BX-3-TC-5	0.756	3.047	1.288	1.493	23.02	37.16	47.63	54.28	58.77	62.27	64.86	66.57	68.04
TMA-BX-3-TC-6	0.753	2.047	1.281	1.486	23.66	34.97	43.3	48.76	52.37	55.27	57.42	58.99	60.31
TMA-BX-3-TC-7*	0.752	1.567	1.277	1.482	23.74	32.35	39.63	44.25	47.49	50.02	51.93	53.36	54.59
TMA-BX-3-TC-8	0.75	1.067	1.274	1.478	24.06	30.25	36.52	40.65	43.28	45.46	47	48.27	49.46
TMA-BX-3-TC-9*	0.749	0.567	1.27	1.474	24.01	28.42	33.92	37.28	39.46	41.29	42.67	NA	NA
TMA-BX-4-TC-1	0.788	3.46	-0.176	0.807	24.88	72.38	89.38	89.25	94.88	96.52	96.86	96.91	97.56
TMA-BX-4-TC-2	1.108	3.46	-0.171	1.121	24.43	57.39	72.26	80.68	93.65	96.74	96.76	96.76	97.2

NA: Not available.

\* Suspected failed gages.

Table C-2 Thermal Data Obtained from the SHT Block

Gage	Days after Startup											
	126	140	154	168	182	196	210	224	238	252	266	275
	°C											
TMA-TC-5B-5	44.2	45.49	45.42	46.07	46.58	46.85	46.81	47.54	47.9	48.46	49.1	49.46
TMA-TC-6-1	110.85	112.62	113.93	116.32	118.27	119.81	119.89	121.93	122.9	123.58	123.46	124.85
TMA-TC-6-2	99.13	100.46	101.64	103.79	105.75	107.28	107.31	109.2	110.15	110.78	110.87	111.82
TMA-TC-6-3	90.53	93.33	93.62	95.11	96.26	96.96	96.59	98.02	98.62	99.13	99.3	99.81
TMA-TC-6-4	76.08	78.68	79.11	80.56	81.86	82.63	82.57	83.86	84.52	84.83	85.14	85.36
TMA-TC-6-5	67.51	69.69	70.22	71.54	72.74	73.56	73.46	74.81	75.36	75.84	76.23	76.39
TMA-TC-6-6	61.64	63.45	64.01	65.29	66.47	67.25	67.32	68.45	69.03	69.49	69.95	70.07
TMA-TC-6-7	52.25	53.41	54.18	55.17	56.23	56.93	57.39	58.14	58.67	59.08	59.61	59.78
TMA-TC-6-8	40.99	41.77	42.67	43.35	44.08	44.76	45.32	45.76	46.27	46.78	47.22	47.49
TMA-TC-6-9	34.39	35.1	35.93	36.49	37.01	37.57	38.09	38.55	38.99	39.49	39.95	40.22
TMA-TC-6-10	30.49	31.1	31.86	32.3	32.74	33.21	33.63	34.09	34.49	34.93	35.42	35.71
TMA-TC-7-1	91.91	93.94	94.78	96.52	97.61	98.36	98.16	99.23	99.73	100.1	100.1	100.75
TMA-TC-7-2	84.52	87.04	87.79	89.28	90.39	91.26	90.97	92.63	93.45	93.82	94.01	94.64
TMA-TC-7-3	78.22	80.82	81.26	82.8	83.89	84.69	84.37	85.84	86.51	86.88	87.19	87.57
TMA-TC-7-4	67.75	69.93	70.36	71.73	72.76	73.56	73.49	74.64	75.31	75.77	76.08	76.37
TMA-TC-7-5	61.26	63.09	63.55	64.83	65.82	66.59	66.67	67.58	68.24	68.72	69.08	69.37
TMA-TC-7-6	56.64	58.16	58.72	59.85	60.82	61.55	61.84	62.56	63.21	63.7	64.08	64.3
TMA-TC-7-7	48.49	49.61	50.27	51.13	51.98	52.68	53.12	53.62	54.2	54.66	55.07	55.36
TMA-TC-7-8	38.58	39.41	40.1	40.75	41.33	41.92	42.38	42.79	43.3	43.74	44.13	44.44
TMA-TC-7-9	32.57	33.24	34.04	34.51	34.95	35.42	35.88	36.28	36.72	37.13	37.53	37.87
TMA-TC-7-10	29.29	29.78	30.47	30.88	31.2	31.54	31.94	32.38	32.74	33.14	33.58	33.9
TMA-BX-1-TC-1	42.94	44.08	44.51	45.15	45.63	45.85	45.49	46.17	46.61	47.22	47.81	48.27
TMA-BX-1-TC-2	134.8	120.15	137.4	138.89	141.06	142.66	143.1	144.75	145.6	146.24	145.85	147.64
TMA-BX-1-TC-3	151.91	138.19	154.38	156.74	158.66	160.5	160.57	162.75	163.82	164.43	163.73	165.82
TMA-BX-1-TC-4	153.18	141.13	155.8	157.76	159.85	161.38	161.23	163.57	164.43	164.85	164.07	166.2
TMA-BX-1-TC-5	141.87	131.27	144.38	146.34	148.28	149.75	149.53	151.72	152.51	153.01	152.31	154.35
TMA-BX-1-TC-6	116.19	106.33	117.98	119.71	121.22	122.29	122.17	123.78	124.44	124.78	124.42	125.91
TMA-BX-1-TC-7	85.05	81.57	86.64	88.08	88.97	89.57	89.35	90.53	90.99	91.28	91.3	92.13
TMA-BX-1-TC-8	67.25	65.72	68.26	69.98	70.48	70.36	69.64	70.46	70.67	70.67	70.67	71.25
TMA-BX-1-TC-9*	57.54	57.46	58.94	60.46	60.85	60.51	59.73	0	0	0	0	0
TMA-BX-2-TC-1	78.65	78.39	81.18	83.6	85.07	85.96	85.29	86.8	86.8	86.25	85.31	86.3
TMA-BX-2-TC-2	87.33	86.66	89.23	90.77	91.35	91.69	91.3	92.78	92.73	92.49	91.76	92.58
TMA-BX-2-TC-3	92.32	91.69	94.35	95.75	96.62	97.29	97.17	98.45	98.36	98.5	98.48	99.03
TMA-BX-2-TC-4	100.07	102.73	101.96	103.12	103.19	105.22	107.48	110.95	113.79	115.19	115.46	116.61
TMA-BX-2-TC-5	105.65	108.37	109.68	111.65	113.57	115.17	115.51	117.29	118.54	119.32	119.29	120.44
TMA-BX-2-TC-6	109.51	110.87	112.52	114.47	116	117.27	117.22	119.1	120.12	120.83	120.83	121.98
TMA-BX-2-TC-7	107.4	103.88	110.68	112.52	113.93	115.15	114.59	116.95	117.05	117.9	117.58	119.29
TMA-BX-2-TC-8	103.29	104.4	105.85	107.52	109.05	110.15	109.93	111.68	112.48	113.08	112.96	114.08
TMA-BX-2-TC-9	97.68	98.53	99.88	101.33	102.63	103.5	103.31	104.81	105.61	106.12	105.95	107.04
TMA-BX-2-TC-10	83.84	85.5	85.77	87.02	87.98	88.51	88.17	89.4	89.95	90.31	90.19	90.99
TMA-BX-2-TC-11	72.81	75.22	74.93	76.06	76.59	76.71	75.96	76.78	76.97	76.97	76.73	77.28
TMA-BX-2-TC-12	56.62	58.96	58.99	60.19	61.06	61.45	60.97	62.15	62.44	62.8	62.9	63.43
TMA-BX-2-TC-13	46.17	47.63	48.07	49.07	49.73	50.22	50.22	51.26	51.59	52.17	52.68	53.12
TMA-BX-3-TC-1*	71.49	129.78	281.14	610.07	NA							
TMA-BX-3-TC-2*	61.26	63.09	63.89	65.24	67.05	68.09	70.14	NA	NA	NA	NA	NA
TMA-BX-3-TC-3	67.97	70.07	70.7	72.11	73.34	74.11	74.06	75.19	75.86	76.35	76.68	76.92
TMA-BX-3-TC-4	70.07	72.19	72.86	74.3	75.46	76.25	76.18	77.33	78	78.41	78.77	79.04
TMA-BX-3-TC-5	67.44	69.3	69.88	71.11	72.09	72.86	72.89	73.87	74.52	74.98	75.39	75.65
TMA-BX-3-TC-6	60.02	61.52	62.2	63.33	64.23	64.93	65.02	65.89	66.45	66.96	67.32	67.68
TMA-BX-3-TC-7*	54.25	55.53	NA									
TMA-BX-3-TC-8	49.24	50.34	51.04	51.93	52.68	53.21	53.36	53.99	54.44	55	55.31	55.65
TMA-BX-3-TC-9*	NA	NA	NA	NA	NA	NA	NA	NA	NA	NA	NA	NA
TMA-BX-4-TC-1	97.39	97.71	99.03	99.73	100.6	100.97	100.75	101.4	101.79	101.81	101.59	103.29
TMA-BX-4-TC-2	96.5	96.4	97.05	97.25	97.32	97.56	97.25	97.66	97.75	97.87	97.83	98.12

NA: Not available.

\* Suspected failed gages.

Table C-2 Thermal Data Obtained from the SHT Block

Gage	Location (m)				Days after Startup								
	x	y	z	r	0	14	28	42	56	70	84	98	112
					°C								
TMA-BX-4-TC-3*	1.448	3.46	-0.165	1.457	NA	NA	NA	NA	NA	NA	NA	NA	NA
TMA-BX-4-TC-4	1.928	3.461	-0.156	1.934	24.06	33.24	42.01	48.02	52.63	56.64	60.07	59.81	61.01
TMA-BX-4-TC-5	2.448	3.461	-0.147	2.452	23.94	28.3	35.88	41.58	46.19	49.88	53.31	53.67	54.81
TMA-BX-4-TC-6	2.928	3.461	-0.139	2.931	23.89	26.7	29.93	33.9	37.26	39.93	42.16	43.59	44.98
TMA-BX-4-TC-7	3.447	3.461	-0.13	3.449	23.91	24.75	27.51	30.69	33.53	35.93	37.99	39.51	40.85
TMA-BX-4-TC-8	3.927	3.461	-0.122	3.929	24.06	24.41	25.71	27.96	30.15	32.08	33.78	35.22	36.35
TMA-BX-4-TC-9	4.447	3.461	-0.112	4.448	23.96	24.18	24.83	26.55	28.3	30.05	31.52	32.74	33.78
TMA-BX-4-TC-10*	4.927	3.462	-0.104	4.928	23.84	24.41	24.53	25.57	26.85	28.3	29.46	30.56	31.52
TMA-BX-4-TC-11	5.447	3.462	-0.095	5.448	24.41	24.31	23.99	24.53	25.02	25.59	26.21	26.6	27.27
TMA-BX-4-TC-12	5.927	3.462	-0.087	5.928	24.03	24.31	24.01	24.38	24.9	25.59	26.28	26.6	27.22
TMA-RTD-15-1	-1.592	4.245	2.768	3.193	23.97	24.41	27.78	31.31	34.23	36.71	38.65	40.47	42.36
TMA-RTD-15-2	-1.309	4.246	2.679	2.982	23.81	24.72	28.79	32.65	35.78	38.26	40.31	41.99	43.39
TMA-RTD-15-3	-1.022	4.246	2.589	2.783	24.38	25.41	30.23	34.54	37.95	40.57	42.72	44.46	45.91
TMA-RTD-15-4	-0.738	4.247	2.5	2.607	23.92	25.98	31.34	35.99	39.53	42.25	44.46	46.24	47.67
TMA-RTD-15-5	-0.452	4.247	2.411	2.453	23.87	26.7	32.76	37.75	41.42	44.22	46.53	48.32	49.79
TMA-RTD-15-6	-0.165	4.248	2.321	2.327	23.66	27.24	33.99	39.28	43.08	45.96	48.32	50.21	51.67
TMA-RTD-15-7	0.12	4.248	2.231	2.234	23.76	27.99	35.28	40.83	44.72	47.69	50.08	51.98	53.46
TMA-RTD-15-8	0.409	4.249	2.141	2.18	23.79	28.12	35.54	41.01	44.97	47.98	50.39	52.27	53.78
TMA-RTD-15-9	0.694	4.249	2.052	2.166	23.74	28.5	35.85	41.42	45.44	48.42	50.88	52.79	54.06
TMA-RTD-15-10	0.983	4.25	1.961	2.194	23.89	28.22	35.52	41.01	44.97	47.95	50.42	52.32	53.83
TMA-RTD-15-11	1.268	4.25	1.872	2.261	23.79	27.66	34.72	40.1	43.99	46.94	49.35	51.25	52.76
TMA-RTD-15-12	1.552	4.251	1.783	2.364	23.84	27.19	33.76	38.96	42.72	45.62	48.01	49.87	51.35
TMA-RTD-15-13	1.841	4.251	1.692	2.5	23.92	26.44	32.35	37.18	40.8	43.63	45.91	47.75	49.2
TMA-RTD-15-14	2.129	4.252	1.602	2.664	24.2	25.85	30.98	35.49	38.91	41.66	43.89	45.7	47.07
TMA-RTD-15-15	2.416	4.252	1.512	2.85	23.92	25.13	29.46	33.53	36.76	39.35	41.5	43.21	44.56
TMA-RTD-15-16	2.7	4.253	1.423	3.052	24.46	24.9	28.48	32.14	35.15	37.67	39.77	41.37	42.69
TMA-RTD-15-17	2.984	4.253	1.334	3.269	24.1	24.49	27.42	30.7	33.51	35.91	37.88	39.43	40.67
TMA-RTD-15-18	3.269	4.254	1.245	3.498	24.54	24.43	26.57	29.41	31.93	34.12	35.99	37.46	38.65
TMA-RTD-15-19	3.558	4.254	1.154	3.74	24.43	24.25	25.85	28.3	30.62	32.65	34.38	35.75	36.92
TMA-RTD-15-20*	3.844	4.255	1.065	3.989	24.36	24.12	25.33	27.47	30.49	36.92	33.14	39.72	40.88
TMA-RTD-15-21	4.125	4.255	0.977	4.239	24.43	24.1	24.9	26.6	28.5	30.18	31.65	32.89	33.89
TMA-RTD-15-22	4.412	4.256	0.887	4.5	24.56	24.12	24.59	26	27.63	29.15	30.46	31.65	32.58
TMA-RTD-15-23*	4.699	4.256	0.797	4.766	24.84	24.33	24.56	25.72	27.17	27.42	29.67	27.6	30.7
TMA-RTD-15-24	4.985	4.257	0.707	5.035	24.84	24.25	24.28	25.23	26.55	27.71	28.74	29.77	30.54
TMA-RTD-15-25	5.267	4.258	0.619	5.303	25.21	24.36	24.28	25.08	26.24	27.24	28.17	29.07	29.82
TMA-RTD-15-26	5.555	4.258	0.529	5.58	25.13	24.33	24.17	24.9	25.88	26.75	27.55	28.33	29
TMA-RTD-15-27	5.842	4.259	0.439	5.858	25.31	24.51	24.28	24.95	25.83	26.52	27.27	27.89	28.53
TMA-TEMP-16-1	5.258	4.271	0.187	5.261	24.9	24.73	25.03	26	27.18	28.3	29.29	30.25	30.93
TMA-TEMP-16-2	4.565	4.274	0.28	4.574	24.28	24.34	25.16	26.67	28.36	29.92	31.25	32.45	33.38
TMA-TEMP-16-3	3.873	4.277	0.372	3.891	24.22	24.55	26.44	28.89	31.22	33.26	34.98	36.31	37.47
TMA-TEMP-16-4	3.181	4.28	0.464	3.215	24.13	25.1	28.67	32.57	35.92	38.38	40.83	41.66	43.36
TMA-RTD-17-1	-1.767	4.275	-1.438	2.278	23.76	27.53	34.9	40.21	44.01	46.87	49.22	51.07	52.53
TMA-RTD-17-2	-1.475	4.275	-1.401	2.034	24.17	30.31	39.09	44.92	48.86	51.9	54.43	56.33	57.84
TMA-RTD-17-3	-1.184	4.274	-1.364	1.806	23.84	32.71	42.77	49.01	53.15	56.3	58.93	60.83	62.37
TMA-RTD-17-4	-0.879	4.274	-1.325	1.59	23.58	36.27	47.56	54.22	58.46	61.8	64.53	66.41	67.98
TMA-RTD-17-5	-0.521	4.273	-1.279	1.381	23.63	40.8	53.23	60.26	64.71	68.11	70.86	72.78	74.35
TMA-RTD-17-6	-0.284	4.273	-1.249	1.281	23.56	43.63	56.51	63.72	68.3	71.54	74.27	76.2	77.83
TMA-RTD-17-7	0.017	4.273	-1.21	1.21	23.69	45.93	59.12	66.39	71.02	74.14	76.86	78.87	80.52
TMA-RTD-17-8	0.316	4.272	-1.172	1.214	24.43	45.93	59.01	66.28	70.86	74	76.73	78.82	80.55
TMA-RTD-17-9	0.613	4.272	-1.134	1.289	23.89	43.01	55.78	62.71	67.25	70.44	73.14	75.16	76.89
TMA-RTD-17-10	0.904	4.271	-1.096	1.421	23.81	39.33	51.54	58.23	62.68	65.86	68.53	70.52	72.2
TMA-RTD-17-11	1.207	4.271	-1.058	1.605	23.81	35.91	48.63	54.51	58.7	62.16	64.56	66.39	67.98
TMA-RTD-17-12	1.499	4.27	-1.02	1.813	23.74	32.47	42.51	48.6	52.89	56.02	58.59	60.44	62.01
TMA-RTD-17-13	1.796	4.27	-0.982	2.047	23.56	29.59	38.24	43.96	48.03	51.09	53.57	55.39	56.88

NA: Not available.

\* Suspected failed gages.

Table C-2 Thermal Data Obtained from the SHT Block

Gage	Days after Startup											
	126	140	154	168	182	196	210	224	238	252	266	275
	°C											
TMA-RTD-17-14	52.89	54.04	55.03	56.04	56.98	57.79	58.2	58.8	59.43	59.9	60.31	60.47
TMA-RTD-17-15	49.22	50.21	51.22	52.16	53.05	53.8	54.3	54.79	55.42	55.88	56.28	56.48
TMA-RTD-17-16	45.99	46.87	47.95	48.76	49.53	50.28	50.88	51.3	51.88	52.37	52.79	52.94
TMA-RTD-17-17	43.5	44.35	45.03	45.78	46.53	47.2	47.8	48.19	48.76	49.22	49.66	49.9
TMA-RTD-17-18	40.78	41.55	42.25	42.95	43.65	44.26	44.85	45.28	45.8	46.27	46.68	46.89
TMA-RTD-17-19	38.65	39.38	40.1	40.7	41.32	41.97	42.51	42.93	43.42	43.91	44.33	44.53
TMA-RTD-17-20	36.71	37.41	38.13	38.71	39.3	39.87	40.39	40.85	41.29	41.76	42.2	42.41
TMA-RTD-17-21	35.15	35.83	36.55	37.1	37.64	38.16	38.68	39.12	39.58	40	40.44	40.7
TMA-RTD-17-22	33.71	34.36	35	35.52	36.06	36.55	37.02	37.46	37.9	38.37	38.78	39.04
TMA-RTD-17-23	32.35	32.96	33.53	34.02	34.51	35	35.49	35.88	36.29	36.79	37.2	37.49
TMA-RTD-17-24	31.29	31.86	32.42	32.89	33.3	33.79	34.25	34.67	35.05	35.54	35.93	36.27
TMA-RTD-17-25	30.26	30.8	31.31	31.78	32.14	32.6	33.07	33.45	33.79	34.33	34.74	35.08
TMA-RTD-17-26*	741.83	409.36	848.39	666.31	627.96	569.48	667.05	406.8	609.56	159.41	177.46	329.89
TMA-RTD-17-27	28.45	28.87	29.33	29.64	29.92	30.36	30.83	31.11	31.55	32.06	32.65	33.07
TMA-RTD-17-28	25.44	24.97	25.8	25.9	26.08	26.37	26.7	26.75	27.37	27.66	28.94	29.54
TMA-RTD-17-29	24.95	24.36	25.28	25.41	25.59	25.88	26.19	26.29	26.88	27.32	28.58	29.05
TMA-TEMP-18-1	31.75	-20	32.87	33.36	33.8	34.27	34.73	35.18	35.55	36.03	36.46	36.78
TMA-TEMP-18-2	34.79	-20	36.06	36.59	37.13	37.65	38.17	38.6	39.04	39.51	39.95	40.22
TMA-TEMP-18-3	39.18	-20	40.57	41.16	41.8	42.39	42.96	43.4	43.9	44.37	44.83	45.03
TMA-TEMP-18-4	44.99	-20	46.55	47.28	48.12	48.85	49.38	49.85	50.44	50.98	51.42	51.54
TMA-RTD-22-1	64.61	66.49	66.78	68.04	69.11	69.92	70.13	71.1	71.81	72.28	72.72	72.91
TMA-RTD-22-2	58.8	60.29	60.63	61.85	62.81	63.33	63.83	64.71	65.29	65.76	66.23	66.31
TMA-RTD-22-3	53.8	55.03	55.37	56.59	57.32	58.18	58.49	59.22	59.92	60.26	60.7	60.91
TMA-RTD-22-4	49.38	50.49	50.76	51.95	52.58	53.49	53.8	54.24	54.9	55.21	55.63	55.88
TMA-RTD-22-5	46.04	47.23	47.64	48.5	49.3	49.66	50.47	50.91	51.38	51.64	52.24	52.55
TMA-RTD-22-6	42.54	43.5	43.91	44.64	45.36	46.14	46.61	47.18	47.54	47.88	48.42	48.52
TMA-RTD-22-7	40.1	40.96	41.42	42.02	42.75	43.32	43.86	44.25	44.72	45.23	45.65	45.93
TMA-RTD-22-8	37.77	38.5	38.99	39.61	40.15	40.78	41.27	41.68	42.12	42.59	43.01	43.24
TMA-RTD-22-9	35.8	36.71	37.07	37.64	37.85	38.81	39.28	39.58	40.1	40.6	40.88	41.11
TMA-RTD-22-10	34.2	35.03	35.54	35.99	36.53	37.02	37.49	37.9	38.32	38.76	39.17	39.46
TMA-RTD-22-11	32.78	33.51	33.89	34.33	34.85	35.23	35.78	36.19	36.55	36.99	37.36	37.67
TMA-RTD-22-12	31.44	32.27	32.5	32.94	33.38	33.89	34.23	34.64	35.03	35.47	35.93	36.17
TMA-RTD-22-13	30.36	31.13	31.42	31.88	32.24	32.63	33.04	33.45	33.84	34.2	34.59	35.03
TMA-RTD-22-14	29.49	30.39	30.49	30.93	31.24	31.39	32.04	32.42	32.78	33.2	33.66	33.99
TMA-RTD-22-15	28.58	29.38	29.3	29.95	30.26	30.72	31.03	31.42	31.7	32.14	32.63	32.96
TMA-RTD-22-16	28.25	28.74	28.76	29.15	29.36	29.61	30.1	30.46	30.75	31.29	31.52	32.09
TMA-RTD-22-17	27.34	27.99	27.99	28.43	28.56	28.89	29.05	29.69	30	30.51	31.06	31.44
TMA-RTD-23-1	76.18	78.46	78.67	80.26	81.52	82.28	82.28	83.64	84.4	84.92	84.97	85.58
TMA-RTD-23-2	68.93	70.94	71.13	72.57	73.77	74.66	74.79	75.79	76.62	77.09	77.54	77.75
TMA-RTD-23-3	62.5	64.38	64.22	65.81	66.83	67.72	67.91	68.87	69.5	69.87	70.55	70.84
TMA-RTD-23-4	57.06	58.59	58.8	59.92	60.76	61.67	62.08	62.89	63.49	63.96	64.35	64.69
TMA-RTD-23-5	52.37	53.8	53.78	55.18	55.86	56.69	57.11	57.73	58.33	58.85	59.27	59.48
TMA-RTD-23-6	48.58	49.97	49.87	51.02	51.82	52.55	53.07	53.62	54.19	54.66	55.08	55.34
TMA-RTD-23-7	45.03	46.27	46.32	47.25	48.11	48.76	49.25	49.74	50.26	50.76	51.17	51.43
TMA-RTD-23-8	41.94	43.21	43.24	44.38	44.72	45.42	45.96	46.4	46.89	47.46	47.82	48.06
TMA-RTD-23-9	39.64	40.75	41.01	41.68	42.25	42.95	43.39	43.86	44.33	44.79	45.28	45.47
TMA-RTD-23-10	37.62	38.73	38.91	39.48	40.1	40.72	41.17	41.66	41.99	42.51	42.9	43.19
TMA-RTD-23-11*	33.56	34.51	36.17	NA	13.49	NA	37.98	38.89	39.01	39.43	39.95	40.28
TMA-RTD-23-12	34.12	34.97	35.1	35.75	36.27	36.71	37.2	37.56	37.95	38.45	38.86	39.12
TMA-RTD-23-13	32.68	33.74	33.87	34.54	35	35.42	35.96	36.14	36.76	37.25	37.56	37.88
TMA-RTD-23-14	31.42	32.4	32.53	32.86	33.45	33.87	34.23	34.77	35.13	35.54	35.93	36.27
TMA-RTD-23-15	30.33	31.29	31.39	31.83	32.22	32.6	32.99	33.81	33.79	34.25	34.72	34.97
TMA-RTD-23-16	29.51	30.46	30.54	31.03	31.31	31.67	31.96	32.63	32.83	33.27	33.71	34.07
TMA-RTD-23-17	28.71	29.64	29.67	30.08	30.33	30.67	31.08	31.42	31.8	32.04	32.73	33.09

NA: Not available.

\* Suspected failed gages.

Table C-2 Thermal Data Obtained from the SHT Block

Gage	Location (m)				Days after Startup								
					0	14	28	42	56	70	84	98	112
	x	y	z	r	°C								
TMA-RTD-23-18	-6.193	4.39	0.078	6.193	25	24.23	24.15	24.51	25.21	25.83	26.47	27.01	27.58
TMA-RTD-23-19*	-6.474	4.392	0.042	6.474	21.55	21.57	21.67	21.91	22.27	22.42	23.04	23.87	8.33
TMA-STC-1	1	0	2	2.236	24.08	25.54	28.84	31.54	33.14	34.63	35.93	36.72	37.57
TMA-STC-2	1	0	0	1	24.03	28.23	31.67	33.9	34.73	35.98	37.23	38.19	39.19
TMA-STC-3	0.5	0	-1	1.118	23.56	26.18	26.7	27.64	27.93	30.17	32.13	32.62	33.48
TMA-STC-4	0.5	0	1	1.118	24.48	29.09	33.87	36.69	37.89	39.09	40.19	40.8	41.67
TMA-STC-5	-1	0	0	1	23.76	28.67	32.13	34.56	36.01	37.28	38.36	39.09	40.31
TMA-STC-6	3	0	0.75	3.092	24.13	24.31	25.54	27.36	28.65	30	31	31.81	32.72
TMA-STC-19	0	0	1.25	1.25	24.18	29.46	34.56	37.65	39.41	40.8	41.92	42.45	43.37
TMA-STC-20	4	0	0	4	24.13	24.01	24.36	25.39	26.33	27.22	28	28.72	29.33
TMA-STC-21	3	0	-0.75	3.092	23.86	24.08	25.15	26.43	27.34	28.15	29.01	29.51	29.88
TMA-STC-22	-3	0	0.75	3.092	24.03	24.26	25.3	27.02	28.35	29.36	30.34	31	31.52
TMA-STC-23	-4	0	0	4	23.94	23.86	24.28	25.05	25.91	26.48	27.19	27.66	27.98
TMA-STC-24	0	0	-1.25	1.25	23.24	24.93	23.89	25.17	25.37	27.09	27.86	28	28.6
TMA-STC-13	-6.593	3.463	0.493	6.611	24.11	24.16	24.26	24.6	25.02	25.39	26.03	26.33	26.85
TMA-STC-14	-6.593	3.463	-0.007	6.593	23.96	24.11	24.01	24.33	24.68	25.32	25.84	26.21	26.72
TMA-STC-15	-6.593	3.463	-1.007	6.669	23.81	23.76	23.59	23.81	24.38	24.78	25.15	25.44	25.96
TMA-STC-16	-6.593	5.463	0.993	6.667	24.01	24.18	24.18	24.53	24.6	25.12	25.69	25.86	26.45
TMA-STC-17	-6.593	5.463	-0.007	6.593	23.66	23.76	23.54	23.91	24.26	25.05	25.67	25.94	26.48
TMA-STC-18	-6.593	5.463	-0.507	6.612	23.69	23.66	23.61	23.84	24.28	24.88	25.52	25.71	26.28
TMA-STC-25	-6.593	1.963	1.993	6.888	26.11	29.31	29.68	29.85	29.53	29.26	29.63	29.38	29.7
TMA-STC-26	-6.593	1.963	-0.007	6.593	24.26	24.16	24.11	24.41	24.73	25.07	25.49	25.79	26.18
TMA-STC-27	-6.593	1.963	1.493	6.76	24.78	26.33	26.63	26.77	26.53	26.67	27.04	27.02	27.49
TMA-STC-34	-6.593	4.463	-0.007	6.593	23.71	23.96	24.03	24.33	24.8	25.22	25.84	26.03	26.65
TMA-STC-35	-6.593	6.963	-0.007	6.593	23.74	23.76	23.69	23.99	24.16	24.83	25.2	25.52	26.06
TMA-STC-36	-6.593	6.963	1.493	6.76	23.99	25.07	25.25	25.44	25.05	24.53	24.8	24.28	25.05
TMA-STC-7	6.264	3.489	0.488	6.283	24.38	24.23	24.23	24.63	25.2	25.81	26.45	26.8	27.29
TMA-STC-8	6.264	3.489	-0.012	6.264	24.43	24.16	24.18	24.65	25.17	25.69	26.28	26.67	27.12
TMA-STC-9	6.264	3.489	-0.488	6.283	24.13	24.01	24.06	24.53	24.83	25.34	25.86	26.38	26.77
TMA-STC-10	6.264	5.489	0.988	6.341	24.21	23.94	23.91	24.48	25.25	25.71	26.45	26.97	27.34
TMA-STC-11	6.264	5.489	-0.012	6.264	24.13	24.06	24.11	24.58	25.22	25.79	26.55	27.12	27.56
TMA-STC-12	6.264	5.489	-1.012	6.345	23.84	24.03	24.36	24.8	25.07	25.54	26.11	26.65	26.85
TMA-STC-28	6.264	1.989	1.988	6.572	24.9	24.83	24.95	25.42	25.94	26.11	26.45	26.75	26.97
TMA-STC-29	6.264	1.989	-0.012	6.264	24.45	24.41	24.18	24.48	24.98	25.34	25.91	26.26	26.72
TMA-STC-30	6.264	1.989	1.488	6.438	24.7	24.6	24.63	24.9	25.67	25.91	26.33	26.63	26.87
TMA-STC-31	6.264	4.489	-0.012	6.264	24.41	24.11	24.21	24.88	25.17	25.89	26.58	27.17	27.66
TMA-STC-32	6.264	6.989	-0.012	6.264	23.91	23.76	24.11	24.5	25.07	25.57	26.16	26.6	26.9
TMA-STC-33	6.264	6.989	1.488	6.438	23.74	23.84	24.03	24.5	24.7	25.54	26.08	26.45	26.85
TMA-IN-THRM-1	1	-0.076	2	2.236	25.53	26.73	28.51	29.51	29.59	29.33	29.99	29.59	29.85
TMA-IN-THRM-2	-3	-0.076	1.5	3.354	25.31	25.71	26.3	27.23	27.62	27.57	28.1	27.96	28.18
TMA-IN-THRM-3	0.5	-0.076	-1	1.118	24.93	26.68	26.69	27.47	27.35	28.04	29.09	28.82	29.25
TMA-IN-THRM-4	4	-0.076	0	4	25.32	25.59	25.89	26.58	26.8	26.68	27.13	26.97	27.26
TMA-IN-THRM-5	-1	-0.076	0	1	24.56	27.58	29.63	31.24	31.84	32.13	32.9	32.9	33.47
TMA-IN-THRM-11	-6.67	2	2	6.963	25.87	26.65	26.79	26.96	26.83	26.21	26.51	26.17	25.61
TMA-IN-THRM-12	-6.67	3.5	0.5	6.689	25.13	25.33	25.3	25.53	25.72	25.35	25.73	25.72	25.76
TMA-IN-THRM-13	-6.67	4.5	0	6.67	24.67	25.29	25.09	25.34	25.62	25.04	25.45	25.19	25.19
TMA-IN-THRM-14	-6.67	5.5	-0.5	6.689	24.79	24.81	24.81	25	25.18	24.94	25.3	25.2	25.43
TMA-IN-THRM-15	-6.67	3.5	-1	6.745	24.67	24.67	24.61	24.88	25.24	25.1	25.4	25.4	25.59
TMA-IN-THRM-6	6.34	5.5	1	6.418	25.19	25.51	25.43	26	26.17	26.09	26.53	26.38	26.52
TMA-IN-THRM-7	6.34	4.5	0	6.34	25.26	25.59	25.69	26.26	26.17	26.16	26.58	26.4	26.48
TMA-IN-THRM-8	6.34	3.5	-0.5	6.36	25.19	25.51	25.47	26.01	25.94	25.89	26.31	26.09	26.16
TMA-IN-THRM-9	6.34	5.5	-1	6.418	24.94	25.36	25.47	26.01	25.9	25.94	26.33	26.25	26.4
TMA-IN-THRM-10	6.34	7	-2	6.648	25.17	25.62	25.68	26.25	26.02	26.14	26.51	26.23	26.2
TMA-BX-1-1-THRM	0.173	0.043	0.3	0.346	25.8	27.02	27.64	28.02	27.61	26.76	26.99	26.1	26.14

NA: Not available.

\* Suspected failed gages.

Table C-2 Thermal Data Obtained from the SHT Block

Gage	Days after Startup											
	126	140	154	168	182	196	210	224	238	252	266	275
°C												
TMA-BX-4-TC-3*	NA	NA	NA	NA	NA	NA	NA	NA	NA	NA	NA	NA
TMA-BX-4-TC-4	60.7	63.07	62.92	64.06	64.81	65.34	65.56	66.26	66.84	67.27	67.61	67.85
TMA-BX-4-TC-5	54.82	57.15	57.29	58.41	59.18	59.76	59.98	60.6	61.06	61.38	61.67	62.08
TMA-BX-4-TC-6	45.63	46.54	47.46	48.27	48.02	48.76	49.22	50.68	51.3	51.76	52.22	52.37
TMA-BX-4-TC-7	41.85	42.33	43.35	43.96	44.73	45.35	45.9	46.32	46.93	47.44	47.85	48.02
TMA-BX-4-TC-8	37.13	37.79	38.8	39.41	39.9	40.56	41.09	41.53	42.01	42.45	42.89	43.11
TMA-BX-4-TC-9	34.49	35.2	36.13	36.69	37.16	37.74	38.24	38.65	39.17	39.56	40.02	40.29
TMA-BX-4-TC-10*	NA	NA	NA	NA	NA	NA	NA	NA	NA	NA	NA	NA
TMA-BX-4-TC-11	27.66	28	28.87	29.11	29.41	29.9	30.32	30.74	31.1	31.67	32.16	32.53
TMA-BX-4-TC-12	27.64	28.03	28.82	29.14	29.48	29.9	30.34	30.76	31.1	31.64	32.16	32.55
TMA-RTD-15-1	44.95	45.26	47.9	48.03	48.13	48.65	48.45	48.76	49.09	49.4	49.48	49.48
TMA-RTD-15-2	44.35	45.18	45.85	46.63	47.38	48.06	48.65	49.09	49.66	50.21	50.63	50.94
TMA-RTD-15-3	46.84	47.72	48.32	49.17	50	50.68	51.25	51.72	52.27	52.76	53.15	53.38
TMA-RTD-15-4	48.58	49.48	50.49	51.38	52.24	52.97	53.46	53.96	54.45	54.95	55.34	55.57
TMA-RTD-15-5	50.6	51.59	52.55	53.54	54.4	55.1	55.63	56.15	56.67	57.16	57.58	57.79
TMA-RTD-15-6	52.37	53.41	54.35	55.39	56.28	57.03	57.5	58.05	58.57	59.06	59.48	59.69
TMA-RTD-15-7	54.09	55.21	56.09	57.16	58.07	58.83	59.27	59.84	60.34	60.81	61.17	61.38
TMA-RTD-15-8	54.38	55.49	56.41	57.47	58.44	59.17	59.61	60.21	60.73	61.22	61.62	61.85
TMA-RTD-15-9	53.15	54.77	55.63	56.51	57.47	58.33	58.83	59.53	60.05	60.52	60.49	60.55
TMA-RTD-15-10	54.38	55.52	56.41	57.5	58.44	59.22	59.63	60.23	60.76	61.25	61.64	61.85
TMA-RTD-15-11	53.31	54.45	55.34	56.38	57.34	58.1	58.49	59.12	59.63	60.1	60.49	60.7
TMA-RTD-15-12	51.98	53.02	53.93	54.97	55.91	56.64	57.08	57.66	58.18	58.65	59.01	59.24
TMA-RTD-15-13	49.9	50.86	51.82	52.79	53.67	54.43	54.9	55.39	55.91	56.38	56.77	57.01
TMA-RTD-15-14	47.88	48.76	49.74	50.65	51.48	52.21	52.73	53.2	53.67	54.17	54.56	54.82
TMA-RTD-15-15	45.44	46.27	47.33	48.13	48.91	49.61	50.1	50.57	51.04	51.54	51.95	52.19
TMA-RTD-15-16	43.63	44.46	45.49	46.22	46.94	47.64	48.19	48.63	49.09	49.58	50.05	50.23
TMA-RTD-15-17	41.68	42.46	43.55	44.17	44.87	45.52	46.06	46.53	46.94	47.46	47.9	48.08
TMA-RTD-15-18	39.66	40.42	41.48	42.05	42.69	43.32	43.89	44.33	44.74	45.23	45.7	45.85
TMA-RTD-15-19	37.85	38.6	39.66	40.21	40.83	41.45	41.99	42.44	42.85	43.29	43.76	43.96
TMA-RTD-15-20*	79.87	90.61	39.74	41.27	42.07	72.33	58.05	47.67	48.99	50.26	52.27	48.16
TMA-RTD-15-21	34.79	35.47	36.53	37.05	37.59	38.13	38.65	39.12	39.46	39.92	40.36	40.6
TMA-RTD-15-22	33.4	34.05	35.08	35.62	36.11	36.63	37.15	37.56	37.9	38.37	38.81	39.07
TMA-RTD-15-23*	NA	24.79	34.02	34.28	NA	31.99	33.97	29.05	29.17	NA	37.64	21.39
TMA-RTD-15-24	31.26	31.88	32.81	33.35	33.79	34.3	34.79	35.21	35.44	35.93	36.37	36.68
TMA-RTD-15-25	30.46	31.08	31.99	32.47	32.91	33.38	33.81	34.25	34.54	35.03	35.47	35.78
TMA-RTD-15-26	29.64	30.18	31.08	31.55	31.93	32.37	32.81	33.25	33.51	34.05	34.46	34.79
TMA-RTD-15-27	29.15	29.67	30.46	30.85	31.21	31.65	32.11	32.53	32.78	33.33	33.81	34.15
TMA-TEMP-16-1	31.69	-19.99	32.81	33.31	33.75	34.2	34.63	35.1	35.47	35.97	36.4	36.74
TMA-TEMP-16-2	34.22	-19.99	35.5	36.03	36.55	37.06	37.56	38.02	38.44	38.91	39.36	39.61
TMA-TEMP-16-3	38.42	-19.99	39.83	40.34	40.98	41.54	42.13	42.57	43.09	43.58	44.03	44.19
TMA-TEMP-16-4	44.64	-20	46.45	45.99	47.3	47.7	48.73	49.3	49.99	50.64	51.1	50.05
TMA-RTD-17-1	53.05	54.17	55.08	56.12	56.93	57.63	58.1	58.26	58.8	59.27	59.56	59.82
TMA-RTD-17-2	58.13	59.51	60.39	61.59	62.55	63.33	63.7	64.43	65.11	65.6	66	66.2
TMA-RTD-17-3	62.4	64.01	64.84	66.13	67.15	67.96	68.25	69.08	69.79	70.31	70.71	70.94
TMA-RTD-17-4	67.72	69.53	70.37	71.73	72.78	73.64	NA	NA	NA	NA	76.41	76.65
TMA-RTD-17-5	73.82	75.81	76.65	78.06	79.14	80	80.08	81.18	81.89	82.36	82.72	83.01
TMA-RTD-17-6	77.17	79.24	80.08	81.57	82.7	83.56	83.59	84.71	85.42	85.87	86.16	86.5
TMA-RTD-17-7	79.87	82.04	82.88	84.4	85.55	86.34	86.26	87.42	88.05	88.42	88.63	88.95
TMA-RTD-17-8	79.87	82.09	82.93	84.42	85.5	86.24	86.11	87.34	87.95	88.29	88.53	88.82
TMA-RTD-17-9	76.31	78.46	79.27	80.76	81.96	82.75	82.67	83.87	84.5	84.92	85.21	85.45
TMA-RTD-17-10	71.73	73.77	74.58	76.05	77.28	78.11	78.09	79.29	79.97	80.42	80.76	80.97
TMA-RTD-17-11	67.64	69.42	70.31	71.68	72.85	73.69	73.74	74.82	75.5	76	76.36	76.49
TMA-RTD-17-12	62.01	63.59	64.48	65.76	66.86	67.7	67.88	68.8	69.45	69.95	70.34	70.47
TMA-RTD-17-13	57.16	58.49	59.4	60.55	61.59	62.37	62.68	63.44	64.09	64.56	64.97	65.11

NA: Not available.

\* Suspected failed gages.

Table C-2 Thermal Data Obtained from the SHT Block

Gage	Location (m)				Days after Startup								
	x	y	z	r	0	14	28	42	56	70	84	98	112
					°C								
TMA-RTD-17-14	2.097	4.27	-0.543	2.299	23.56	27.45	34.74	40.03	43.83	46.76	49.17	50.94	52.4
TMA-RTD-17-15	2.39	4.269	-0.906	2.556	23.61	26.03	32.01	36.74	40.34	43.11	45.42	47.12	48.55
TMA-RTD-17-16	2.689	4.269	-0.868	2.826	23.63	25.08	29.79	34.02	37.31	39.95	42.12	43.81	45.21
TMA-RTD-17-17	2.992	4.268	-0.829	3.105	24.17	24.82	28.53	32.19	35.18	37.67	39.69	41.32	42.64
TMA-RTD-17-18	3.29	4.268	-0.791	3.384	24.07	24.25	27.09	30.21	32.86	35.15	37.07	38.6	39.87
TMA-RTD-17-19	3.582	4.268	-0.753	3.66	24.3	24.15	26.26	28.87	31.26	33.33	35.08	36.53	37.72
TMA-RTD-17-20	3.885	4.267	-0.715	3.95	24.38	24.15	25.64	27.81	29.9	31.78	33.35	34.72	35.83
TMA-RTD-17-21	4.173	4.267	-0.678	4.228	24.51	24.36	25.26	27.04	28.87	30.54	31.99	33.27	34.28
TMA-RTD-17-22	4.469	4.266	-0.64	4.515	25.21	24.33	24.95	26.39	28.01	29.51	30.77	31.93	32.91
TMA-RTD-17-23	4.771	4.266	-0.601	4.809	26.75	24.3	24.67	25.85	27.22	28.53	29.69	30.75	31.62
TMA-RTD-17-24	5.072	4.265	-0.562	5.103	25.21	24.33	24.56	25.54	26.73	27.86	28.87	29.82	30.62
TMA-RTD-17-25	5.367	4.265	-0.525	5.393	25.13	24.3	24.43	25.23	26.24	27.19	28.09	28.89	29.64
TMA-RTD-17-26*	0	0	0	0	75.79	56.17	49.4	116.19	130.19	301.6	674.9	742.81	397.23
TMA-RTD-17-27	5.953	4.264	-0.45	5.97	25.39	24.67	24.51	25.16	25.7	26.29	26.96	27.37	27.89
TMA-RTD-17-28	6.255	4.264	-0.411	6.268	26.13	26.21	26.16	26.75	26.55	26.03	25.57	25.1	25.1
TMA-RTD-17-29	6.545	4.263	-0.374	6.556	26.24	26.47	26.7	27.11	26.52	25.85	25.98	25.21	24.67
TMA-TEMP-18-1	5.12	4.255	-0.205	5.124	24.53	24.47	24.84	25.83	27.07	28.24	29.26	30.27	31
TMA-TEMP-18-2	4.422	4.254	-0.215	4.427	24.25	24.35	25.33	26.98	28.73	30.35	31.74	32.96	33.9
TMA-TEMP-18-3	3.723	4.252	-0.224	3.73	24	24.43	26.67	29.34	31.77	33.87	35.64	37.07	38.21
TMA-TEMP-18-4	3.025	4.25	-0.234	3.034	23.95	25.26	29.3	33.16	36.35	38.98	41.17	42.78	44.07
TMA-RTD-22-1	-1.584	4.358	-0.711	1.736	23.4	34.25	44.92	51.17	55.37	58.54	61.2	63.1	64.77
TMA-RTD-22-2	-1.879	4.36	-0.706	2.007	23.66	30.85	39.74	45.62	49.58	52.58	55.13	57.06	58.59
TMA-RTD-22-3	-2.179	4.362	-0.701	2.289	23.84	28.27	35.67	40.99	44.77	47.54	49.92	51.77	53.23
TMA-RTD-22-4	-2.479	4.364	-0.696	2.575	23.97	26.44	32.42	37.15	40.65	43.29	45.6	47.23	48.65
TMA-RTD-22-5	-2.777	4.366	-0.691	2.862	24	25.67	30.41	34.64	37.59	40.13	42.12	43.86	45.31
TMA-RTD-22-6	-3.081	4.368	-0.686	3.156	23.89	24.67	28.17	31.8	34.54	36.84	38.71	40.39	41.61
TMA-RTD-22-7	-3.377	4.37	-0.681	3.445	23.61	24.17	27.14	29.84	32.42	34.46	36.35	37.82	39.04
TMA-RTD-22-8	-3.68	4.372	-0.676	3.742	23.97	23.89	25.93	28.33	30.59	32.45	34.23	35.65	36.68
TMA-RTD-22-9	-3.98	4.374	-0.671	4.036	24.1	24.02	25.33	27.34	29.25	31.03	32.47	33.94	34.87
TMA-RTD-22-10	-4.28	4.376	-0.666	4.332	24.17	23.92	24.92	26.57	28.22	29.79	31.16	32.4	33.38
TMA-RTD-22-11	-4.578	4.378	-0.661	4.625	23.81	23.94	24.69	26.08	27.29	28.81	29.87	31	31.88
TMA-RTD-22-12	-4.876	4.38	-0.657	4.92	23.48	23.92	24.2	25.36	26.52	27.71	28.89	29.92	30.64
TMA-RTD-22-13	-5.175	4.382	-0.652	5.216	24.25	23.89	24.12	25.03	26.03	27.09	28.14	29	29.72
TMA-RTD-22-14	-5.48	4.384	-0.647	5.518	24.28	24.05	24.43	24.92	25.77	26.6	27.45	28.25	28.89
TMA-RTD-22-15	-5.775	4.386	-0.642	5.811	30.44	24	24.02	24.41	25.26	26.13	26.78	27.55	28.12
TMA-RTD-22-16	-6.078	4.388	-0.637	6.111	24.41	24.1	24.12	24.2	24.95	25.83	26.26	26.91	27.45
TMA-RTD-22-17	-6.386	4.39	-0.632	6.417	24.46	24.1	23.87	24.25	24.92	25.36	25.8	26.34	26.86
TMA-RTD-23-1	-1.404	4.35	0.694	1.566	23.97	43.29	55.7	62.79	66.91	70.16	73.06	75.05	76.6
TMA-RTD-23-2	-1.682	4.352	0.659	1.806	24.33	37.41	48.63	55.49	59.63	62.73	65.5	67.46	69.11
TMA-RTD-23-3	-1.967	4.355	0.622	2.063	24.05	33.17	42.8	49.12	53.26	56.22	58.91	60.81	62.37
TMA-RTD-23-4	-2.247	4.357	0.586	2.322	23.76	29.84	38.16	43.91	47.77	50.68	53.18	55.1	56.64
TMA-RTD-23-5	-2.53	4.359	0.549	2.589	23.66	27.47	34.54	39.61	43.32	46.04	48.39	50.34	51.72
TMA-RTD-23-6	-2.813	4.362	0.513	2.859	25.03	26.21	31.8	36.35	39.79	42.41	44.56	46.37	47.8
TMA-RTD-23-7	-3.092	4.364	0.477	3.129	23.69	25	29.46	33.53	36.55	39.04	41.11	42.85	44.12
TMA-RTD-23-8	-3.376	4.366	0.44	3.405	23.79	24.38	27.76	31.13	33.94	36.22	38.06	39.72	40.96
TMA-RTD-23-9	-3.656	4.369	0.404	3.678	24	24.23	26.73	29.59	32.11	34.23	35.91	37.38	38.65
TMA-RTD-23-10	-3.938	4.371	0.368	3.955	24.36	24.1	26.03	28.38	30.54	32.53	34.12	35.49	36.63
TMA-RTD-23-11*	-4.224	4.373	0.331	4.237	24.23	23.97	25.28	27.24	28.66	30.36	32.14	33.45	32.71
TMA-RTD-23-12	-4.501	4.376	0.296	4.511	24.54	23.92	24.97	26.52	28.09	29.77	31.19	32.06	33.14
TMA-RTD-23-13	-4.783	4.378	0.259	4.79	24.36	23.92	24.36	25.51	26.91	28.33	29.67	30.83	31.88
TMA-RTD-23-14	-5.067	4.38	0.223	5.072	24.51	24.02	24.43	25.41	26.65	27.83	28.94	29.9	30.72
TMA-RTD-23-15	-5.342	4.383	0.187	5.345	24.49	23.97	24.2	25	26.08	27.14	28.09	28.94	29.69
TMA-RTD-23-16	-5.624	4.385	0.151	5.626	25.05	24.12	24.33	24.92	25.8	26.73	27.53	28.3	29
TMA-RTD-23-17	-5.906	4.387	0.115	5.907	24.51	24.07	24.12	24.67	25.44	26.21	26.93	27.6	28.25

NA: Not available.

\* Suspected failed gages.

Table C-2 Thermal Data Obtained from the SHT Block

Gage	Days after Startup											
	126	140	154	168	182	196	210	224	238	252	266	275
	°C											
TMA-RTD-23-18	27.96	28.87	28.92	29.2	29.43	29.79	30.23	30.49	30.88	31.47	31.91	32.35
TMA-RTD-23-19*	6.26	2.15	5.56	-12.13	-21.34	-11.24	-13.02	-16.43	-24.42	-28.6	-33.48	-58.09
TMA-STC-1	37.74	38.41	38.85	39.39	39.85	40.34	40.73	41.12	41.51	42.06	42.55	42.94
TMA-STC-2	39.22	40.1	40.68	41.14	41.65	42.16	42.57	43.23	43.64	44.27	45	45.49
TMA-STC-3	33.65	33.99	34.66	35.15	35.56	36.15	36.67	36.99	37.55	38.09	39.02	39.44
TMA-STC-4	41.33	42.38	42.86	43.42	43.91	44.35	44.51	45.12	45.56	46.15	46.78	47.15
TMA-STC-5	40.24	40.99	41.65	42.31	42.86	43.49	43.91	44.61	45.07	45.63	46.27	46.71
TMA-STC-6	33.24	33.95	34.58	34.93	35.39	35.86	36.37	36.74	37.13	37.62	38.19	38.65
TMA-STC-19	42.89	43.98	44.22	44.95	45.44	45.88	46	46.58	47.02	47.54	48.12	48.46
TMA-STC-20	29.85	30.47	30.96	31.25	31.64	32.01	32.43	32.82	33.24	33.65	34.12	34.61
TMA-STC-21	30.49	30.93	31.42	31.76	32.08	32.13	32.57	32.92	33.43	33.9	34.53	35.24
TMA-STC-22	32.18	32.55	33.11	33.43	33.78	34.19	34.66	35	35.39	35.93	36.59	37.06
TMA-STC-23	28.65	28.97	29.48	29.56	29.85	30.27	30.66	30.98	31.35	31.81	32.5	33.11
TMA-STC-24	28.65	28.1	29.46	30.15	30.42	30.98	31.57	31.69	32.5	32.92	34.12	34.58
TMA-STC-13	27.09	27.59	28.33	28.62	28.74	29.04	29.56	29.9	30.29	30.71	31.3	31.67
TMA-STC-14	26.92	27.27	28.03	28.25	28.45	28.89	29.31	29.7	30.07	30.44	31.15	31.45
TMA-STC-15	26.26	26.58	27.24	27.49	27.73	28.08	28.5	28.79	29.24	29.66	30.25	30.59
TMA-STC-16	26.55	27	27.56	27.83	28.05	28.42	28.72	29.16	29.56	30	30.56	31.05
TMA-STC-17	26.55	26.63	27.44	27.59	28.0	28.15	28.74	28.84	29.38	29.78	30.61	31.08
TMA-STC-18	26.43	26.85	27.61	27.83	28.1	28.37	28.79	29.11	29.56	29.95	30.61	31
TMA-STC-25	29.09	27.91	30.02	28.92	29.85	30.22	30.61	30.83	31.37	30.51	31.81	30.29
TMA-STC-26	26.4	26.8	27.39	27.64	27.88	28.18	28.62	28.97	29.36	29.75	30.37	30.81
TMA-STC-27	27.14	27.29	28.08	27.91	28.28	28.65	29.11	29.36	29.83	30	31.05	30.71
TMA-STC-34	26.53	26.92	27.61	27.78	28.03	28.25	28.87	29.11	29.63	29.9	30.91	31.5
TMA-STC-35	26.03	26.35	27.07	27.27	27.49	27.73	28.18	28.52	28.97	29.38	29.98	30.32
TMA-STC-36	24.38	24.45	25.12	25.05	25.25	25.42	25.94	26.26	26.87	27.39	28.28	28.79
TMA-STC-7	27.96	28.42	29.04	29.36	29.7	30.12	30.56	30.93	31.35	31.84	32.47	32.84
TMA-STC-8	27.68	28.13	28.69	29.06	29.36	29.75	30.2	30.54	31	31.45	32.08	32.43
TMA-STC-9	27.36	27.83	28.4	28.65	28.94	29.36	29.78	30.15	30.51	30.98	31.64	31.89
TMA-STC-10	28.25	28.82	29.53	29.93	30.37	30.78	31.25	31.69	32.06	32.53	33.14	33.51
TMA-STC-11	28.25	28.74	29.33	29.75	30.1	30.56	31	31.4	31.81	32.26	32.79	33.21
TMA-STC-12	27.49	27.91	28.55	28.87	29.14	29.53	30.02	30.34	30.71	31.23	31.72	32.03
TMA-STC-28	27.39	27.78	28.37	28.62	28.92	29.26	29.68	30.07	30.39	30.93	31.5	31.91
TMA-STC-29	27.19	27.73	28.25	28.62	28.92	29.36	29.78	30.2	30.54	30.98	31.54	31.96
TMA-STC-30	27.36	27.81	28.45	28.79	29.09	29.48	29.93	30.32	30.66	31.2	31.76	32.16
TMA-STC-31	28.35	28.87	29.48	29.78	30.1	30.56	31.03	31.45	31.81	32.35	32.94	33.31
TMA-STC-32	27.68	28.1	28.77	29.11	29.43	29.83	30.34	30.71	31.08	31.52	32.08	32.38
TMA-STC-33	27.46	27.88	28.67	28.97	29.33	29.73	30.17	30.64	30.96	31.45	32.01	32.3
TMA-IN-THRM-1	29.72	29.42	30.11	30.29	30.5	30.9	31.23	31.39	32	32.28	33.48	33.7
TMA-IN-THRM-2	28.46	28.35	28.87	28.87	29.17	29.53	29.95	30.08	30.68	31.09	32.23	32.54
TMA-IN-THRM-3	29.25	29.02	29.66	29.98	30.28	30.74	31.26	31.34	32.06	32.43	33.63	34.02
TMA-IN-THRM-4	27.33	27.25	27.76	27.95	28.16	28.55	28.96	29.16	29.64	29.97	30.91	31.34
TMA-IN-THRM-5	33.42	33.54	34.03	34.37	34.73	35.22	35.62	35.96	36.57	36.97	38.04	38.37
TMA-IN-THRM-11	26.04	25.85	26.45	26.25	26.75	26.94	27.5	27.6	28.37	28.46	30.06	29.75
TMA-IN-THRM-12	25.92	26.02	26.43	26.43	26.77	26.97	27.51	27.68	28.37	28.56	29.83	30.05
TMA-IN-THRM-13	25.52	25.21	26.1	26.04	26.4	26.61	27.2	27.2	28.02	28.16	29.63	29.85
TMA-IN-THRM-14	25.57	25.77	26.09	26.11	26.47	26.67	27.14	27.35	27.97	28.29	29.39	29.67
TMA-IN-THRM-15	25.92	26.14	26.36	26.51	26.75	27.03	27.46	27.68	28.25	28.58	29.53	29.8
TMA-IN-THRM-6	27.04	27.25	27.65	27.92	28.19	28.54	28.93	29.2	29.65	30.11	31	31.55
TMA-IN-THRM-7	26.9	27	27.5	27.73	27.95	28.3	28.7	28.91	29.43	29.82	30.76	31.28
TMA-IN-THRM-8	26.52	26.64	27.04	27.25	27.45	27.83	28.17	28.42	28.86	29.26	30.17	30.7
TMA-IN-THRM-9	26.71	26.84	27.27	27.5	27.71	28.09	28.5	28.72	29.16	29.56	30.36	30.9
TMA-IN-THRM-10	26.68	26.87	27.22	27.45	27.7	28.04	28.43	28.67	29.13	29.58	30.44	30.93
TMA-BX-1-1-THRM	25.81	25.38	26.37	26.3	26.5	26.81	27.39	27.2	28.12	28.29	29.94	29.93

NA: Not available.

\* Suspected failed gages.

Table C-2 Thermal Data Obtained from the SHT Block

Gage	Location (m)				Days after Startup								
	x	y	z	r	0	14	28	42	56	70	84	98	112
					°C								
TMA-BX-3-1-THRM	0.747	0.067	1.267	1.471	26.01	26.79	27.57	28.29	27.96	27.28	27.76	27.09	26.63
TMA-BX-4-1-THRM	6.427	3.462	-0.078	6.427	25.43	26.05	26.27	26.7	26.28	25.8	26.06	25.51	25.28

NA: Not available.

\* Suspected failed gages.

Table C-2 Thermal Data Obtained from the SHT Block

Gage	Days after Startup											
	126	140	154	168	182	196	210	224	238	252	266	275
	°C											
TMA-BX-3-1-THRM	26.94	26.67	27.35	27.46	27.59	27.94	28.19	28.2	28.94	29.08	30.61	30.53
TMA-BX-4-1-THRM	25.53	25.44	25.91	26.08	26.28	26.57	26.69	26.81	27.4	27.72	28.92	29.45

NA: Not available.

\* Suspected failed gages.

Table C-3. Multiple Point Borehole Extensometer Displacement Data Obtained from the SHT Block, Uncorrected for Thermal Expansion of Rods (Extension Positive)

MPBX Gage	Location (m)			Days after Startup								
				0	14	28	42	56	70	84	98	112
	x	y	z	mm								
TMA-BX-1-1	0.130	6.883	0.310	-0.0903	0.8491	.2904	1.5386	1.7070	1.7723	1.7967	1.7414	1.7478
TMA-BX-1-2*	0.136	6.043	0.309	-0.0797	0.9609	1.3925	1.6606	1.5712	0.9974	0.6131	0.3272	0.1345
TMA-BX-1-3	0.142	5.043	0.307	-0.0808	0.8471	1.3092	1.5377	1.6929	1.8491	1.9417	2.0075	2.0275
TMA-BX-1-4	0.148	4.043	0.306	-0.0582	0.6777	1.0119	1.2224	1.2910	1.2626	1.2471	1.2077	0.9563
TMA-BX-1-5*	0.154	3.043	0.304	-0.0373	0.4603	0.7178	0.8613	0.8949	0.8592	0.7615	0.7694	0.6772
TMA-BX-1-6*	0.161	2.043	0.303	-0.0176	0.2194	0.3621	0.4187	0.3690	-0.0035	-0.3849	-0.7106	-1.0241
TMA-BX-2-1	-0.631	7.093	0.281	-0.0002	-0.0057	-0.0156	-0.0155	-0.0166	-0.0141	-0.0125	-0.0112	0.0352
TMA-BX-2-2	-0.630	6.023	0.274	0.0014	0.1126	0.0586	0.0748	0.0880	0.0944	0.0975	0.1003	0.1538
TMA-BX-2-3	-0.628	4.883	0.267	-0.0007	0.0431	0.0470	0.0498	0.0540	0.0596	0.0648	0.0683	0.0904
TMA-BX-2-4	-0.627	3.773	0.259	0.0024	0.2343	0.1135	0.1260	0.1330	0.1339	0.1368	0.1395	0.2827
TMA-BX-2-5	-0.626	2.623	0.252	-0.0012	-0.0283	0.0258	0.0363	0.0423	0.0461	0.0513	0.0497	0.0075
TMA-BX-2-6	-0.625	1.513	0.245	0.0006	-0.0384	0.0300	0.0371	0.0417	0.0470	0.0485	0.0518	-0.0116
TMA-BX-3-1	0.768	6.907	1.315	0.0006	0.6725	1.1419	1.4522	1.6686	1.8499	1.9501	1.9921	1.8026
TMA-BX-3-2	0.765	6.067	1.309	-0.0248	0.6602	1.1455	1.4494	1.6866	1.8644	1.9107	1.8489	1.8607
TMA-BX-3-3	0.762	5.067	1.302	-0.025	0.6663	1.1372	1.4323	1.6633	1.7348	1.6754	1.4331	1.3920
TMA-BX-3-4*	0.759	4.067	1.295	-0.025	0.5430	0.9215	1.1811	1.3545	1.4465	1.4083	1.4171	1.4754
TMA-BX-3-5*	0.756	3.067	1.288	-2.4889	0.4198	0.7824	0.9812	1.1223	1.2094	1.2433	1.2240	1.2039
TMA-BX-3-6	0.753	2.067	1.281	-0.0252	0.3247	0.5973	0.7617	0.8715	1.0047	1.1112	1.0895	1.0166
TMA-BX-4-1	0.768	3.460	-0.177	0.0256	-0.1472	-0.1107	-0.0329	0.0727	0.1417	0.2313	0.2881	0.3986
TMA-BX-4-2	1.428	3.460	-0.165	0.0006	-0.1772	-0.1796	-0.1073	-0.0613	0.0049	0.0936	0.1503	0.2092
TMA-BX-4-3	2.428	3.461	-0.148	0.0259	-0.0965	-0.1139	-0.1017	-0.0655	-0.0300	0.0041	0.0607	0.0924
TMA-BX-4-4	3.427	3.461	-0.130	0.0005	-0.0499	-0.0734	-0.0675	-0.0364	-0.0306	-0.0001	0.0293	0.0589
TMA-BX-4-5	4.427	3.461	-0.113	0.0004	-0.0252	-0.0255	-0.0231	-0.0207	-0.0178	0.0102	0.0121	0.0399
TMA-BX-4-6	5.427	3.462	-0.095	0.0003	0.0000	-0.0004	0.0004	0.0011	0.0274	0.0283	0.0289	0.0299

Table C-4. Rock Bolt Load Cell Data Obtained from the SHT Block

Gage	Location (m)			Days after Startup								
				0	14	28	42	56	70	84	98	112
	x	y	z	lbs								
TMA-RB-LC-1-AVG	0.180	-0.300	-0.370	22662	22262.8	22158	21732.3	21537.1	21444.1	21407.5	21380.8	21340.3
TMA-RB-LC-2-AVG	0.180	-0.300	-0.370	14859.4	14739.7	14708.6	14680.1	14643.7	14597	14559.8	14522.5	14496.5
TMA-RB-LC-3-AVG	0.620	-0.300	-0.210	22428	22402.2	22378.7	22348.4	22317.5	22281	22262.3	22243.2	22231
TMA-RB-LC-4-AVG	0.620	-0.300	-0.210	16663.9	16602.8	16580.3	16558.8	16522.1	16496.6	16467.4	16446.3	16424.2
TMA-RB-LC-5-AVG	-0.180	-4.700	-0.370	25971.9	25928.5	25887	25856.6	25829.3	25802.6	25783.4	25765.5	25748.7
TMA-RB-LC-6-AVG	-0.180	-4.700	-0.370	14642.7	14633.2	14632.7	14627.3	14619.4	14609.5	14601.2	14595.9	14589.2
TMA-RB-LC-7-AVG	0.620	-4.700	-0.290	4932.6	4921.1	4919.7	4911.8	4904.3	4893.6	4890.9	4883.8	4877.5
TMA-RB-LC-8-AVG	0.620	-4.700	-0.290	16862.8	16818.5	16783.6	16758.7	16738.7	16605	16592.7	16575.4	16566

NA: Not available.

\* Suspected failed gages.

Table C-3. Multiple Point Borehole Extensometer Displacement Data Obtained from the SHT Block, Uncorrected for Thermal Expansion of Rods (Extension Positive)

MPBX Gage	Days after Startup										
	126	140	154	168	182	196	210	224	238	252	266
	mm										
TMA-BX-1-1	1.8076	1.8731	1.8790	1.9726	2.0128	2.0494	2.4287	2.4180	2.4503	2.4292	2.4020
TMA-BX-1-2*	0.1877	0.2518	0.2566	0.2726	0.3112	0.2959	0.2565	NA	NA	NA	NA
TMA-BX-1-3	2.0914	2.1798	2.1819	2.2459	2.2815	2.2891	2.3125	2.3228	2.3275	2.3302	2.3285
TMA-BX-1-4	0.8047	0.6376	0.5601	0.3681	0.3500	0.2027	0.2768	0.2839	0.2111	0.2130	0.1613
TMA-BX-1-5*	0.4892	0.3710	NA								
TMA-BX-1-6*	-1.3237	-1.5200	-1.7773	-1.8235	-1.8471	-1.8461	-1.8495	NA	NA	NA	NA
TMA-BX-2-1			-0.0029	0.0004	0.0015	0.0034	0.0059	0.0076	0.0096	0.0114	0.0126
TMA-BX-2-2			0.1070	0.1083	0.1095	0.1104	0.1124	0.1134	0.1153	0.1162	0.1154
TMA-BX-2-3			0.0781	0.0847	0.0878	0.0886	0.0856	0.0851	0.0852	0.0971	0.0920
TMA-BX-2-4			0.1426	0.2119	0.1468	0.1483	0.1430	0.1474	0.1482	0.1490	0.1479
TMA-BX-2-5			0.0471	0.0479	0.0460	0.0467	0.0451	0.0467	0.0474	0.0467	0.0465
TMA-BX-2-6			-0.0122	0.0593	0.0602	0.0616	0.0611	0.0634	0.0638	0.0652	0.0644
TMA-BX-3-1	1.4568	1.3378	1.3199	1.2558	1.4447	1.4780	1.5079	1.5446	1.6006	1.6811	1.7097
TMA-BX-3-2	1.8332	1.8212	1.8784	1.8889	1.9232	1.9805	2.0079	2.0700	2.1006	2.0541	2.0828
TMA-BX-3-3	1.3902	1.4264	1.5078	1.5670	1.6246	1.6552	1.7065	1.7386	1.7682	1.7972	1.7999
TMA-BX-3-4*	1.4742	-0.5758	1.4864	1.4926	1.5231	1.4255	1.2483	1.2533	1.2560	NA	NA
TMA-BX-3-5*	1.2286	1.2589	NA								
TMA-BX-3-6	0.9909	1.0447	1.0724	1.1258	1.1534	1.1805	1.1810	1.2084	1.2352	1.2368	1.2634
TMA-BX-4-1	0.4000	0.5081	0.5141	0.5447	0.5489	0.5788	0.6067	0.6107	0.6399	0.6433	0.6718
TMA-BX-4-2	0.2111	0.2425	0.1970	0.2017	0.2309	0.2605	0.2885	0.2920	0.3209	0.3495	0.3780
TMA-BX-4-3	0.1202	0.1495	0.1544	0.0816	0.0337	0.0117	0.0397	0.0423	0.0452	0.0733	0.1015
TMA-BX-4-4	0.0860	0.1138	0.1175	0.1196	0.1214	0.1237	0.1258	0.1530	0.1550	0.1571	0.1847
TMA-BX-4-5	0.0660	0.0674	0.0696	-0.0055	-0.0553	-0.0792	-0.0779	-0.0767	-0.0755	-0.0487	-0.0725
TMA-BX-4-6	0.0304	0.0564	0.0574	0.0833	0.0838	0.0844	0.0850	0.0856	0.0862	0.0870	0.0878

Table C-4. Rock Bolt Load Cell Data Obtained from the SHT Block

Gage	Days after Startup										
	126	140	154	168	182	196	210	224	238	252	266
	lbs										
TMA-RB-LC-1-AVG	21308.5	21279.7	21254.3	21206.3	21176.9	21161.2	21145.9	21127.1	21112.2	21100.9	21102.1
TMA-RB-LC-2-AVG	14449.6	14422.7	14405.6	14389.9	14378.6	14369.9	14365.5	14353.4	14349	14342	14341.1
TMA-RB-LC-3-AVG	22224.1	22214.2	22206.8	22201.1	22194.3	22189.6	22183.4	22176.4	22171.7	22165.3	22158.4
TMA-RB-LC-4-AVG	16407.5	16394.3	16377.4	16361.5	16350.8	16340.4	16331	16320.2	16316.8	16312.1	16310.9
TMA-RB-LC-5-AVG	25738.1	25728.1	25722.2	25714.1	25705.1	25698.3	25692.7	25683.1	25676	25665.6	25652
TMA-RB-LC-6-AVG	14573.7	14567.1	14563.5	14562.3	14557.4	14553.9	14551.2	14549.3	14543.8	14543.4	14538.9
TMA-RB-LC-7-AVG	4873	4866.9	4866.7	4867.2	4866.6	4868.2	4865.2	4863.2	4863.9	4864.1	4867.1
TMA-RB-LC-8-AVG	16561.5	16552.8	16544.8	16538	16533.3	16528.6	16522.3	16516.4	16514	16503.2	16501.5

NA: Not available.

\* Suspected failed gages.

Table C-5. Wire Extensometer Data Obtained from the SHT Block

Gage	Location (m)			Days after Startup								
				0	14	28	42	56	70	84	98	112
	x	y	z	mm								
TMA-WX-1 (top)	2.098	0.000	2.230	0	-0.1	0.08	0.02	0.03	0.27	0.2	0.33	0.49
TMA-WX-1 (bottom)	1.983	0.000	-1.240									
TMA-WX-2 (top)	-2.040	0.000	2.591	0	-0.14	-0.15	-0.12	3.16	3.21	3.26	3.27	3.29
TMA-WX-2 (bottom)	-2.085	0.000	-0.914									
TMA-WX-3 (top)	6.264	3.612	2.752	0	-0.03	-0.09	0.01	0.01	0.2	0.25	0.31	0.33
TMA-WX-3 (bottom)	6.264	3.582	-0.978									
TMA-WX-4 (top)	6.264	5.633	2.759	0	-0.83	-0.78	-0.78	-0.78	-0.58	-0.49	-0.66	-0.63
TMA-WX-4 (bottom)	6.264	5.613	-1.041									
TMA-WX-5 (top)	-6.593	3.622	1.477	0	-0.61	-0.66	-0.58	-0.52	-0.5	-0.44	-0.67	-0.4
TMA-WX-5 (bottom)	-6.593	3.712	-1.558									
TMA-WX-6 (top)	-6.593	5.735	1.216	0	-2.45	-2.46	-1.98	-1.88	-1.89	-1.83	-2.95	-2.97
TMA-WX-6 (bottom)	-6.593	5.735	-1.784									

NA: Not available.

\* Suspected failed gages.

Table C-5. Wire Extensometer Data Obtained from the SHT Block

Gage	Days after Startup										
	126	140	154	168	182	196	210	224	238	252	266
	mm										
TMA-WX-1 (top)	0.47	0.39	0.66	0.66	0.55	0.55	0.55	0.55	0.55	0.44	0.59
TMA-WX-1 (bottom)											
TMA-WX-2 (top)	3.27	3.17	3.52	3.51	3.51	3.51	3.5	3.5	3.5	3.41	3.38
TMA-WX-2 (bottom)											
TMA-WX-3 (top)	0.41	0.28	0.69	-23.92	-23.92	-23.84	-23.99	-24.08	-24.08	-24	-24.03
TMA-WX-3 (bottom)											
TMA-WX-4 (top)	-0.31	-0.59	-0.2	-0.21	-0.04	-0.04	-0.09	-0.09	-0.1	-0.1	-0.12
TMA-WX-4 (bottom)											
TMA-WX-5 (top)	-0.58	-0.89	-0.48	-0.59	-0.65	-0.78	-0.82	-0.82	-0.83	-0.81	-0.82
TMA-WX-5 (bottom)											
TMA-WX-6 (top)	-2.97	-3.21	-2.75	-2.91	-2.74	-2.74	-3.06	-3.06	-3.06	-2.96	-2.92
TMA-WX-6 (bottom)											

NA: Not available.

\* Suspected failed gages.

Table C-6. Tape Extensometer Measurements for the SHT (Extension Positive)

Tape Extensometer Gage	Location (m)			Initial Reading (m)	$\Delta$ Displ. 9/24/96 (mm)	$\Delta$ Displ. 10/21/96 (mm)	$\Delta$ Displ. 12/19/96 (m)
	x	y	z				
TMA-WXM-1	2.008	0.000	-0.295	5.40439	-0.58	-0.88	0
TMA-WXM-2	-1.960	0.000	0.121	5.08575	-3.2	-3.15	-1.14
TMA-WXM-3	6.264	3.702	0.012	4.6731	-0.71	-0.38	+24.59*
TMA-WXM-4	6.264	5.603	-0.056	4.33635	-0.56	-0.31	-0.66
TMA-WXM-5	-6.593	3.722	0.012	5.87639	-0.14	-0.47	-0.61
TMA-WXM-6	-6.593	5.735	-0.019	5.83158	-0.39	-0.29	-0.08

\* Note: Data for WXM-3 on 12/19/96 likely erroneous reading.

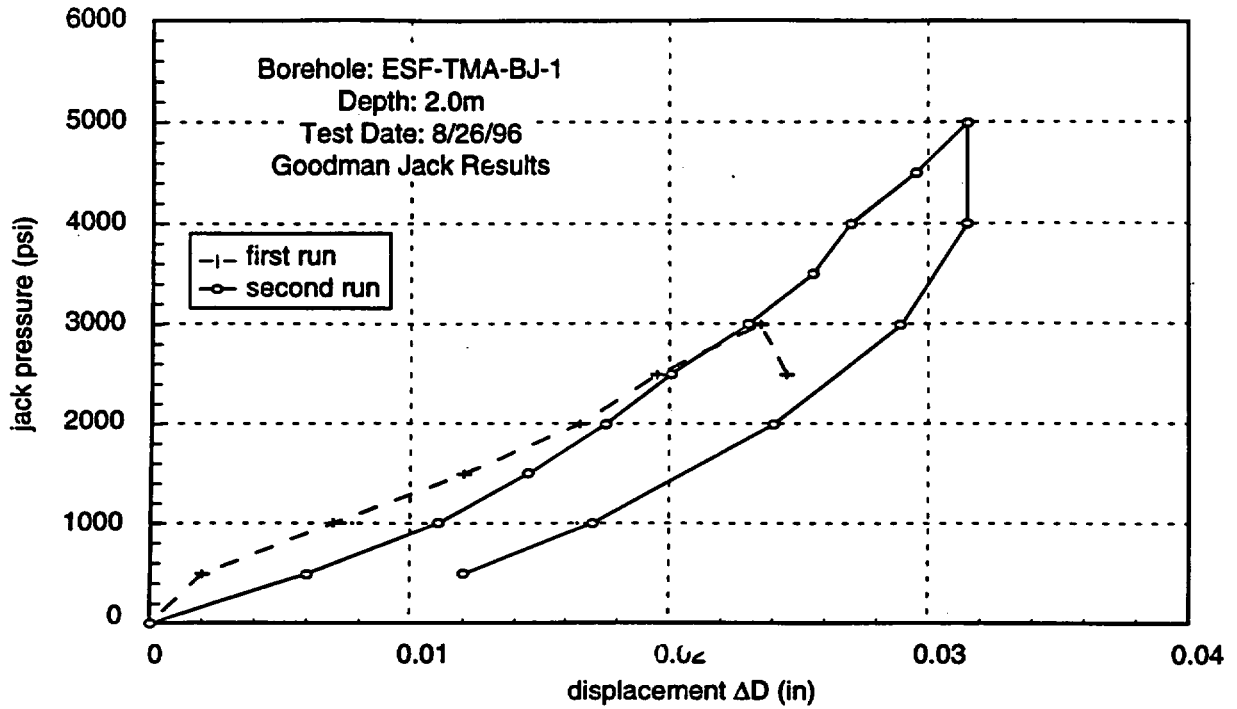
Table C-6. Tape Extensometer Measurements for the SHT (Extension Positive)

Tape Extensometer Gage	Location (m)			$\Delta$ Displ. 1/7/97 (mm)	$\Delta$ Displ. 2/11/97 (mm)	$\Delta$ Displ. 6/25/97 (mm)
	x	y	z			
TMA-WXM-1	2.008	0.000	-0.295	-0.86	-1.24	-1.49
TMA-WXM-2	-1.960	0.000	0.121	-3.78	-3.83	-4.29
TMA-WXM-3	6.264	3.702	0.012	-0.63	-2.64	-0.89
TMA-WXM-4	6.264	5.603	-0.056	-0.74	-0.94	-1.27
TMA-WXM-5	-6.593	3.722	0.012	-0.69	-0.48	-0.98
TMA-WXM-6	-6.593	5.735	-0.019	-0.48	-0.81	-1.25

\* Note: Data for WXM-3 on  
12/19/96 likely erroneous reading.

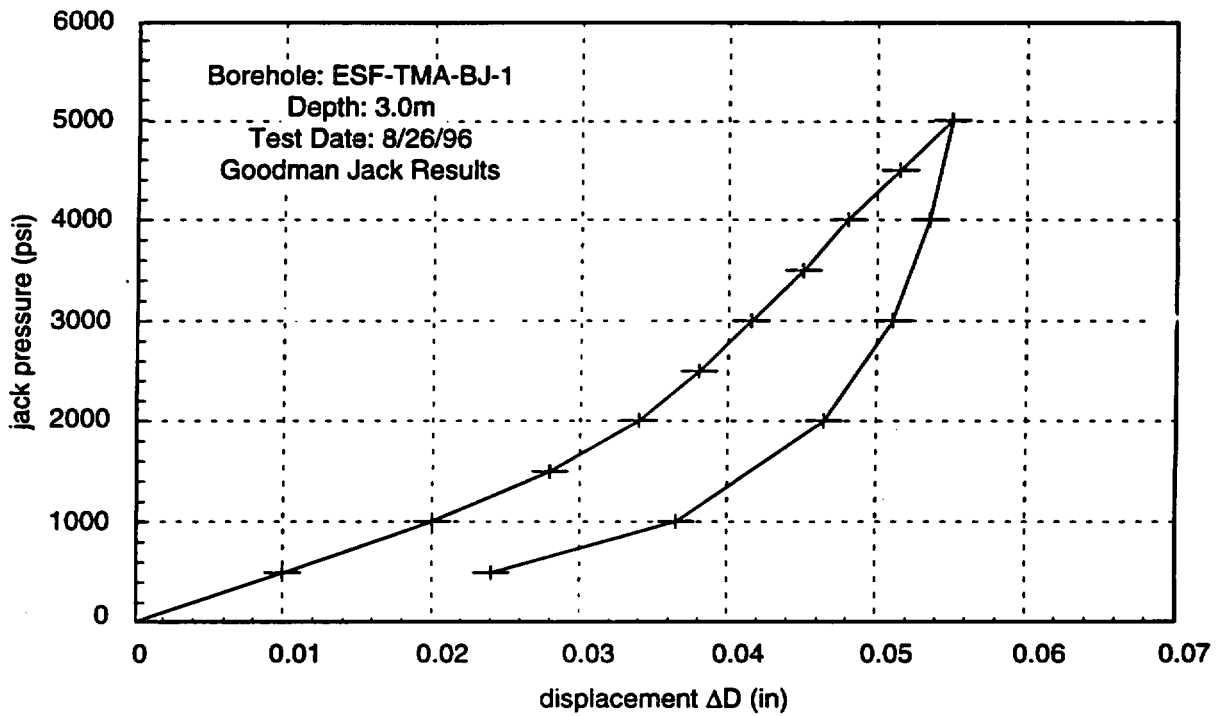
**Page intentionally blank**

**Appendix D**  
**Borehole Jack Data for Measurements Taken on**  
**26 August 1996, 10 October 1996,**  
**26 November 1996, and 18 March 1997**



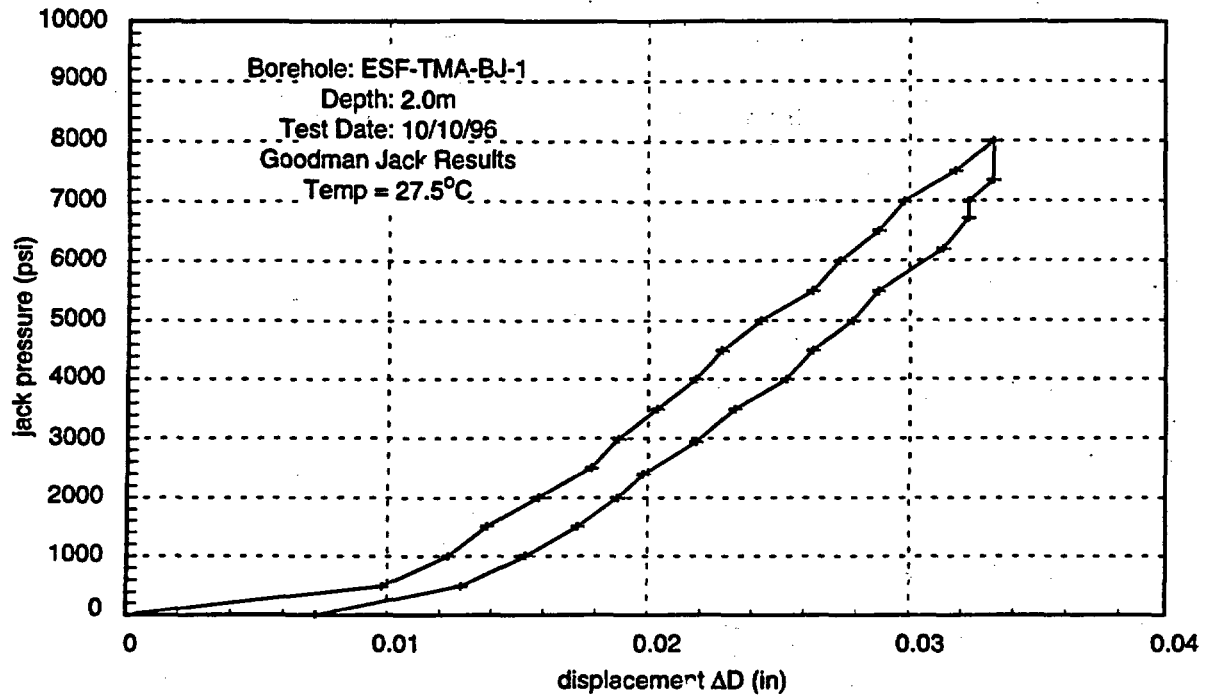
TRI-8117-14-0

Figure D-1. Pressure/displacement history for borehole jack, test date 8/26/96, 2.0 m from collar.



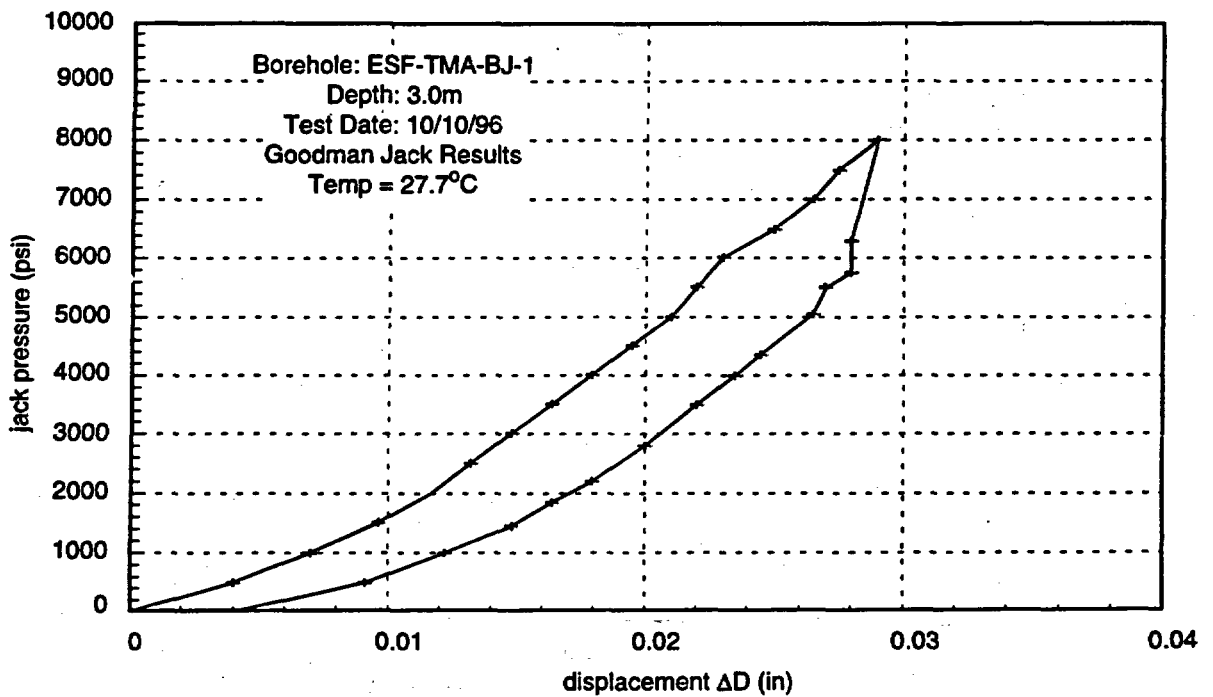
TRI-8117-15-0

Figure D-2. Pressure/displacement history for borehole jack, test date 8/26/96, 3.0 m from collar.



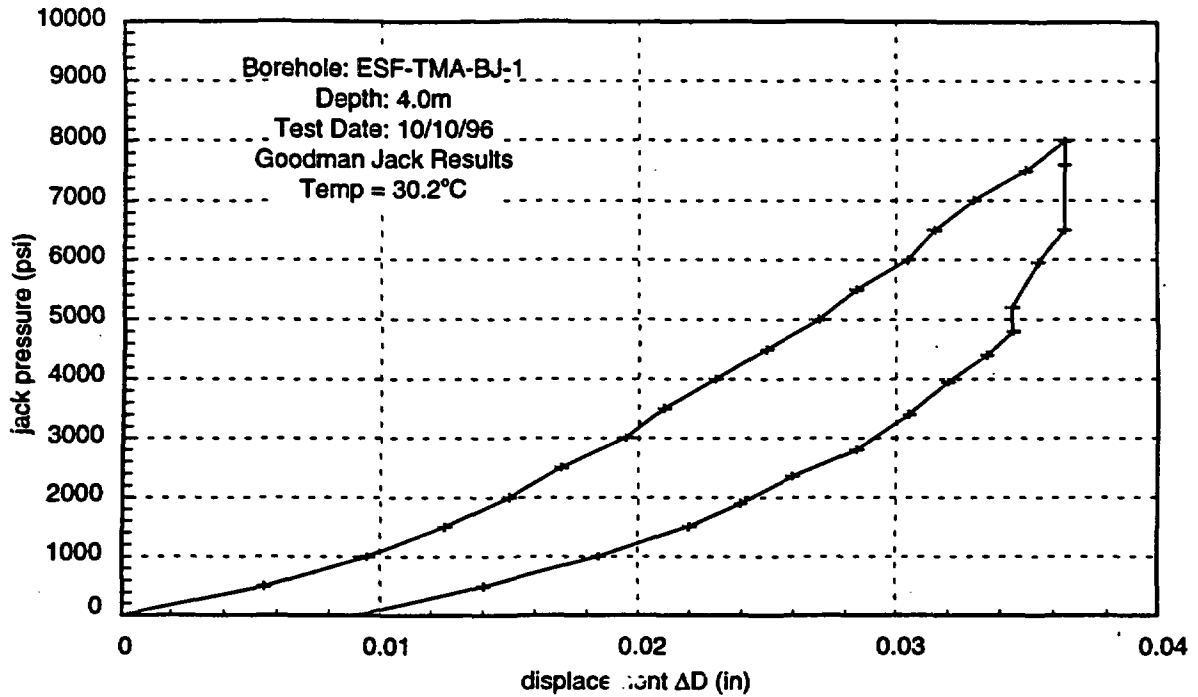
TRI-6117-16-0

Figure D-3. Pressure/displacement history for borehole jack, test date 10/10/96, 2.0 m from collar.



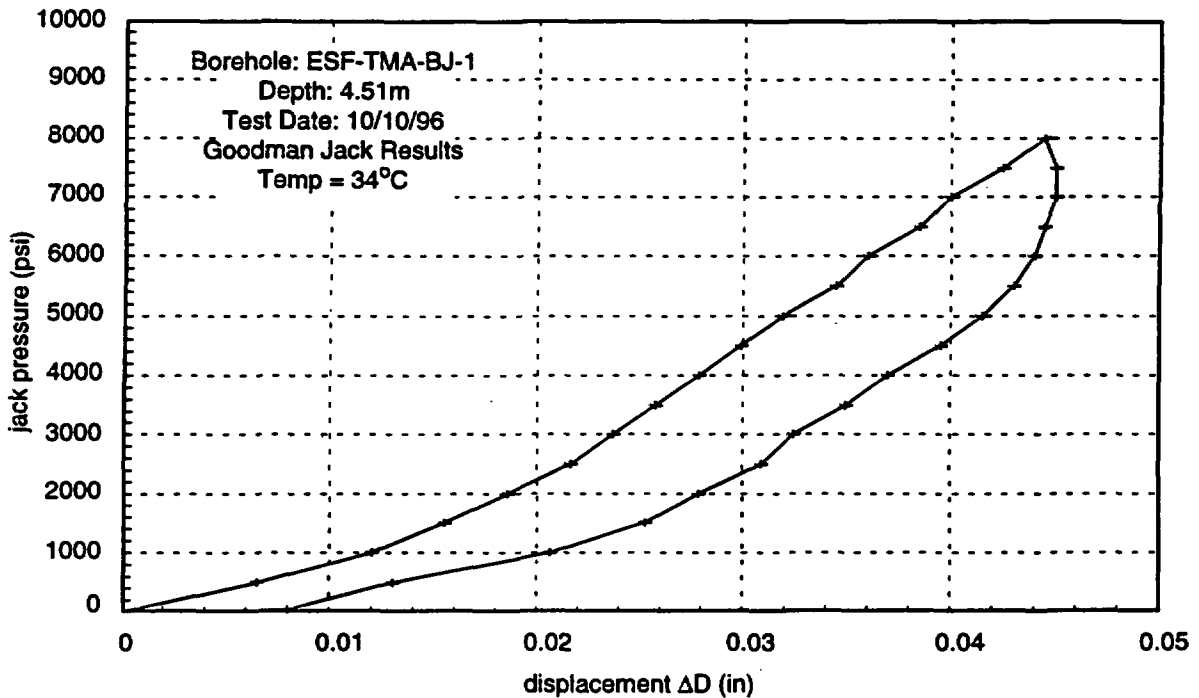
TRI-6117-17-0

Figure D-4. Pressure/displacement history for borehole jack, test date 10/10/96, 3.0 m from collar.



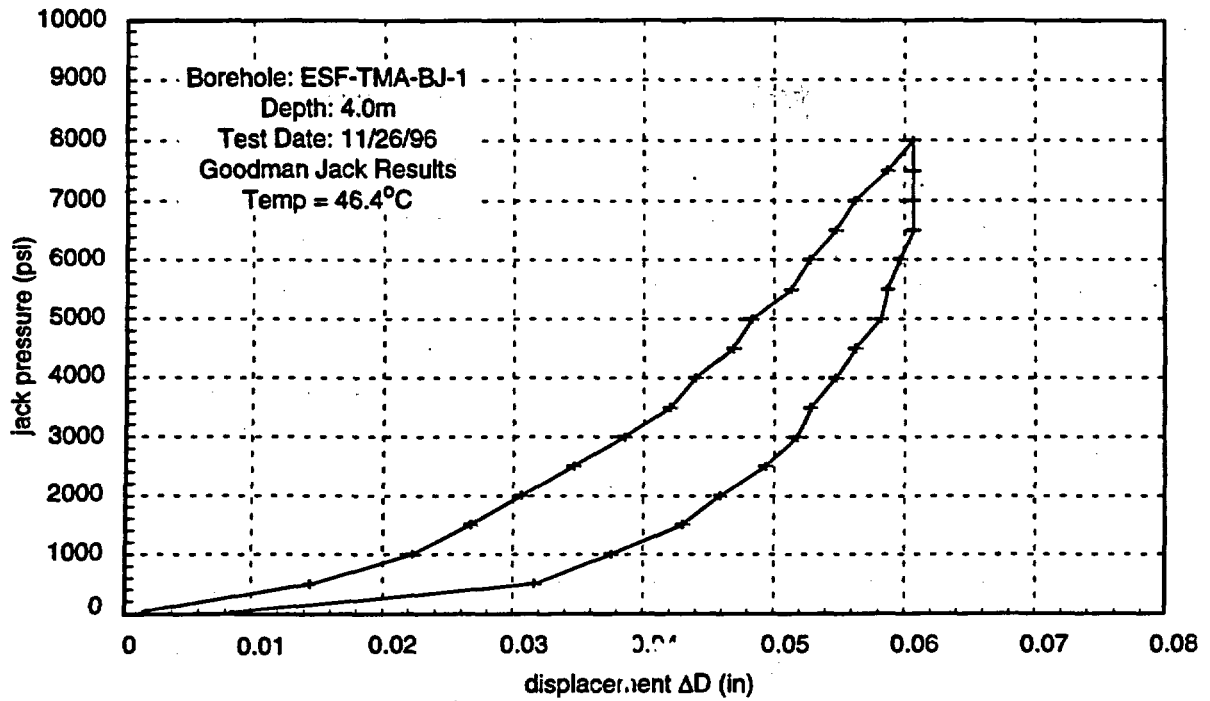
TRI-6117-18-0

Figure D-5. Pressure/displacement history for borehole jack, test date 10/10/96, 4.0 m from collar.



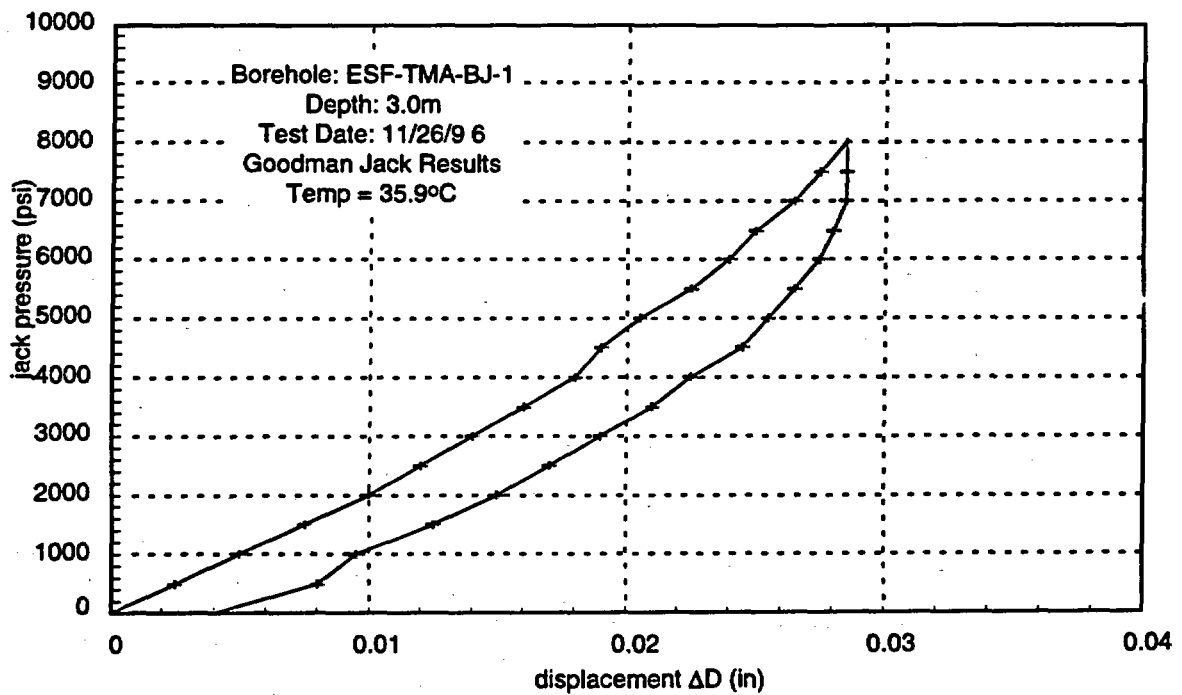
TRI-6117-19-0

Figure D-6. Pressure/displacement history for borehole jack, test date 10/10/96, 4.51 m from collar.



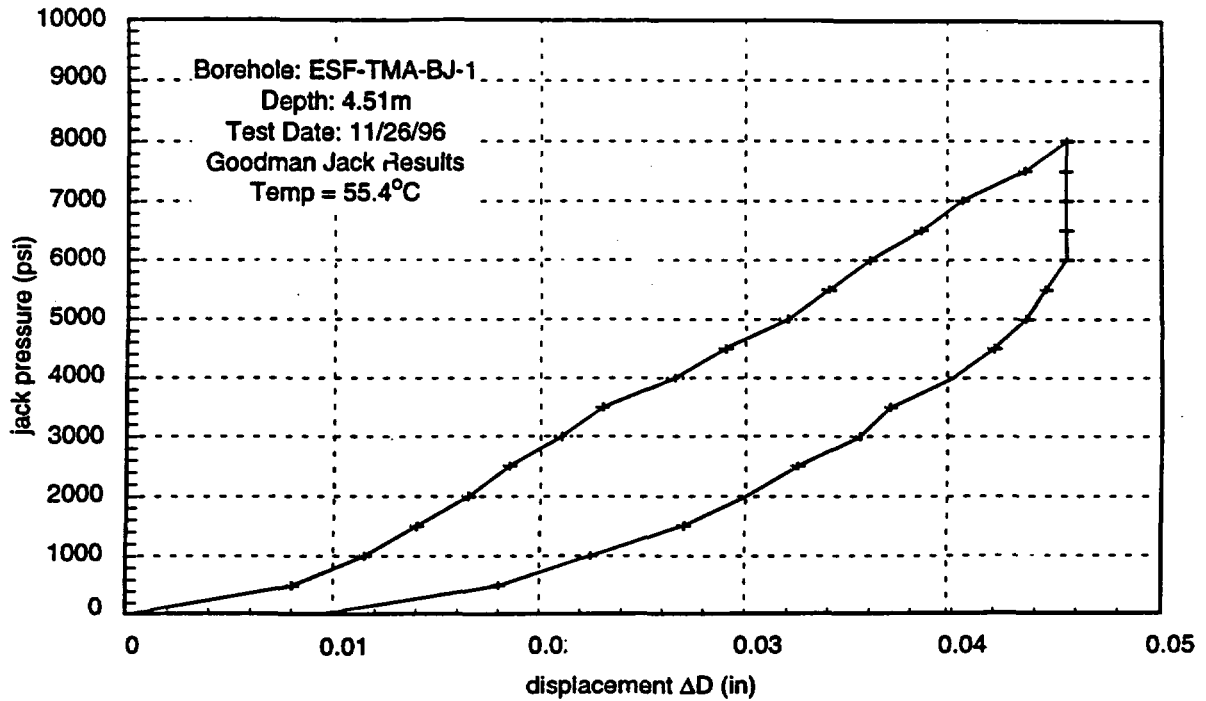
TRI-8117-20-0

Figure D-7. Pressure/displacement history for borehole jack, test date 11/26/96, 3.0 m from collar.



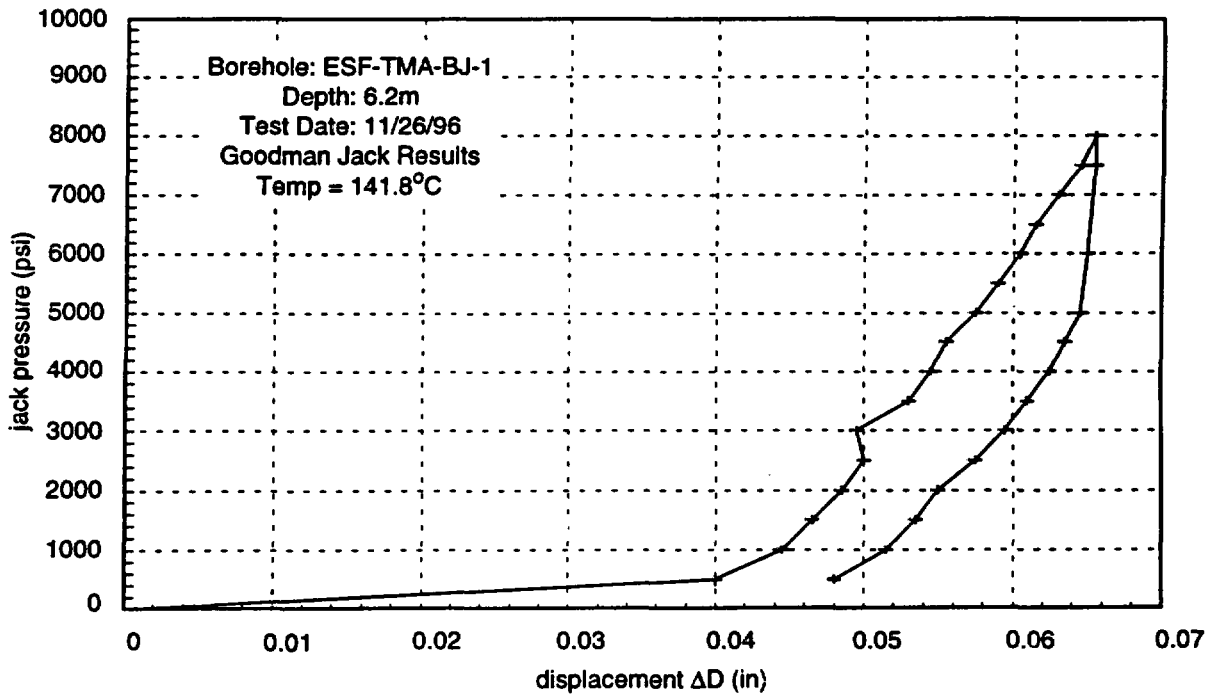
TRI-8117-20-0

Figure D-8. Pressure/displacement history for borehole jack, test date 11/26/96, 4.0 m from collar.



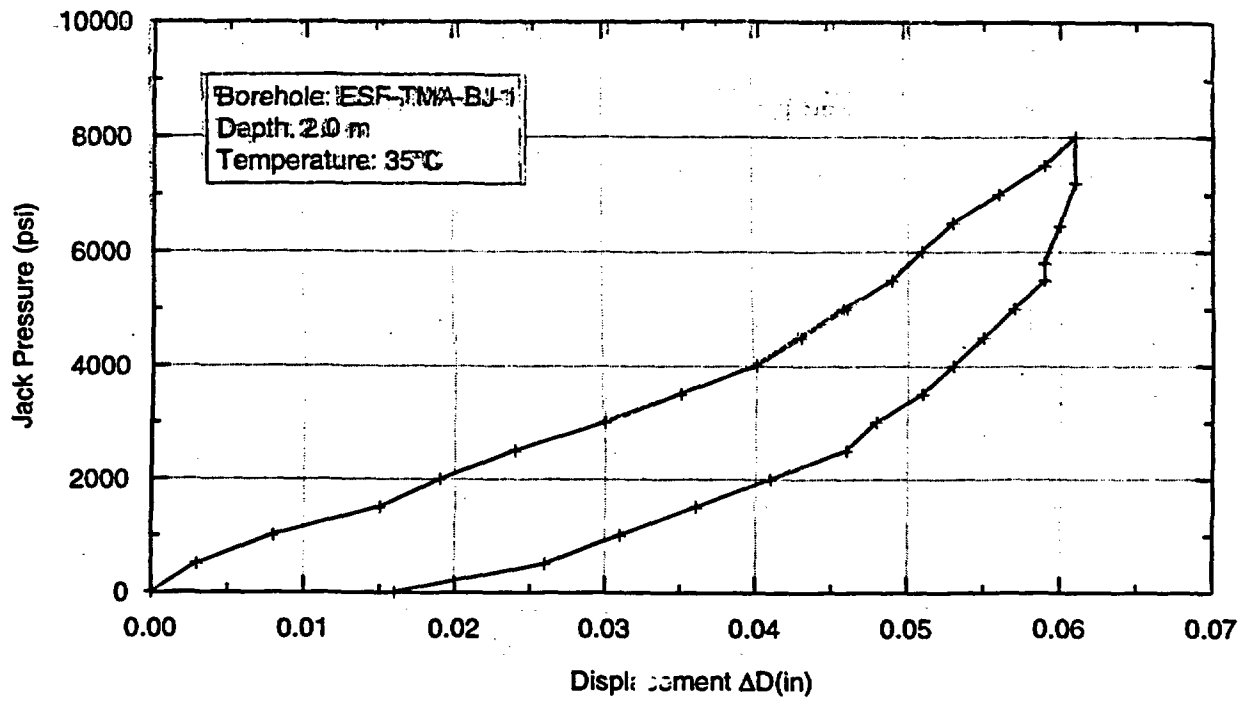
TRI-81:7-21-0

Figure D-9. Pressure/displacement history for borehole jack, test date 11/26/96, 4.51 m from collar.



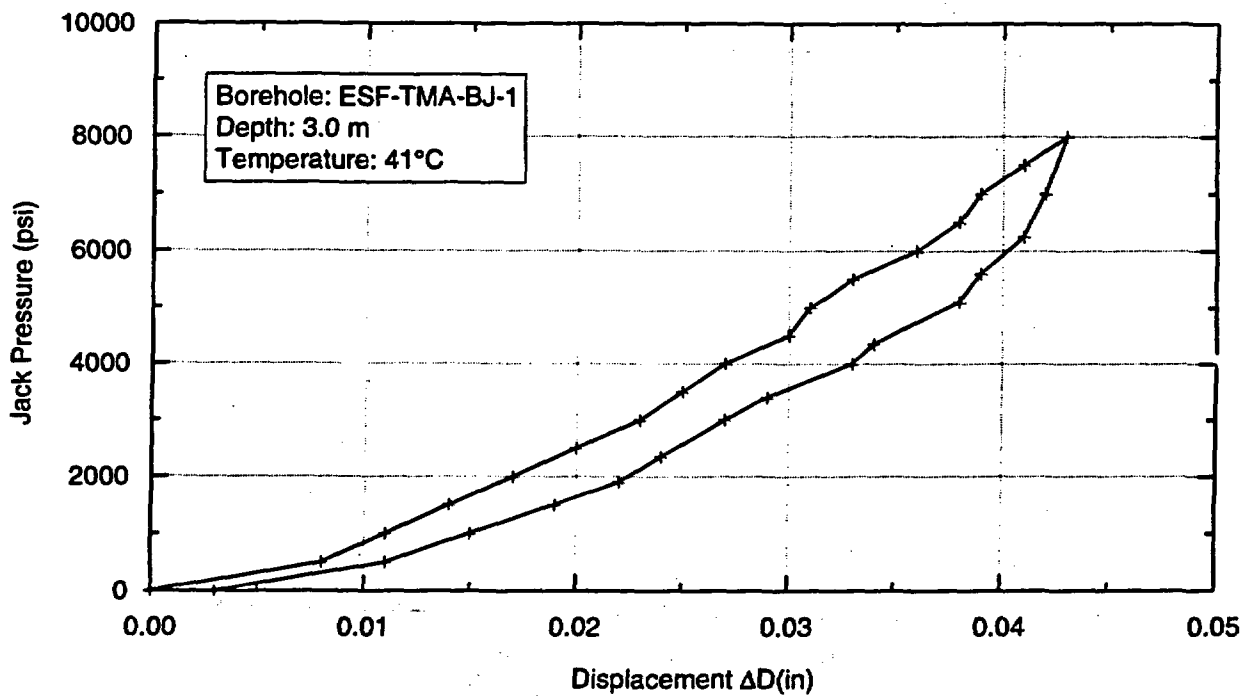
TRI-8117-22-0

Figure D-10. Pressure/displacement history for borehole jack, test date 11/26/96, 6.2 m from collar.



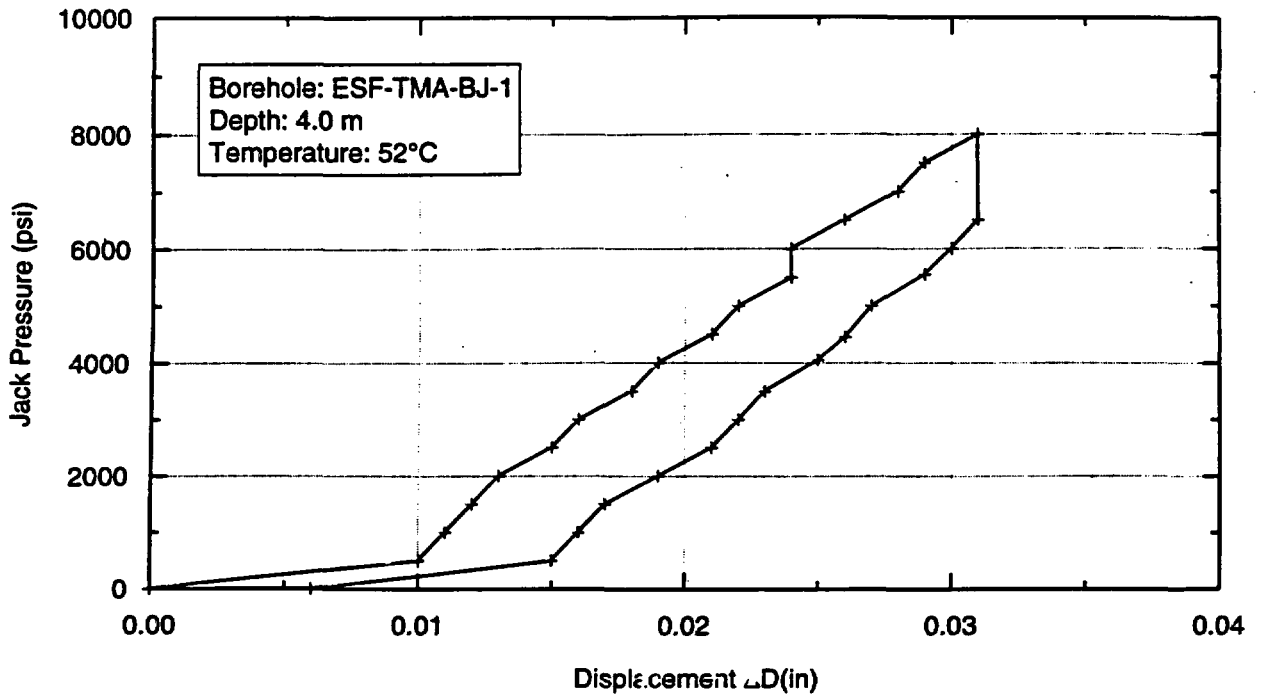
TRI-6117-14-1

Figure D-11. Pressure/displacement history for borehole jack, test date 3/18/97, 2.0 m from collar.



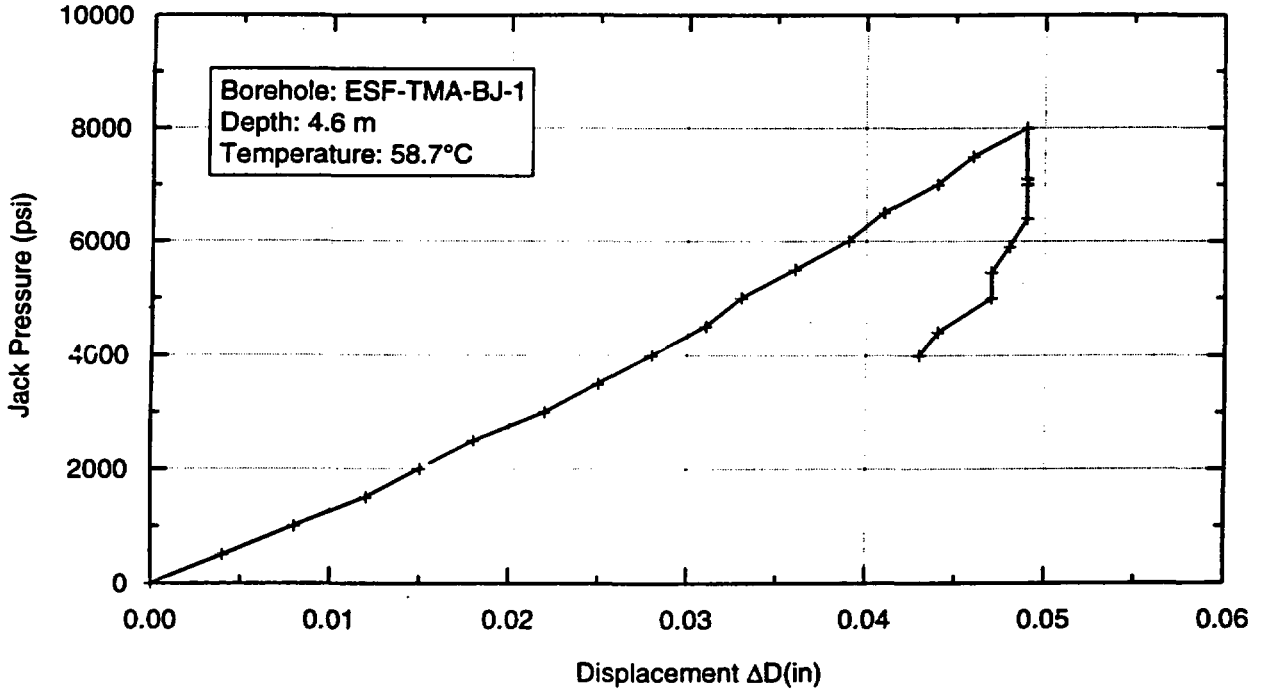
TRI-6117-15-1

Figure D-12. Pressure/displacement history for borehole jack, test date 3/18/97, 3.0 m from collar.



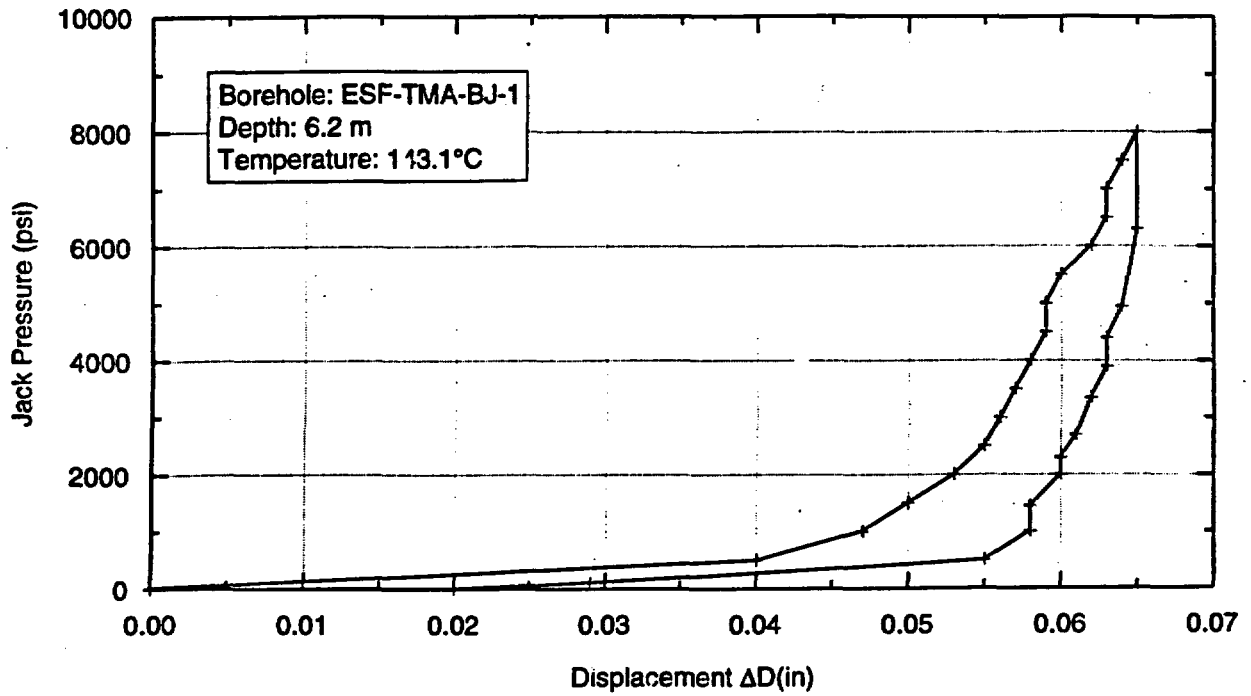
TRI-6117-18-1

Figure D-13. Pressure/displacement history for borehole jack, test date 3/18/97, 4.0 m from collar.



TRI-6117-19-1

Figure D-14. Pressure/displacement history for borehole jack, test date 3/18/97, 4.6 m from collar.



TRI-6117-22-1

Figure D-15. Pressure/displacement history for borehole jack, test date 3/18/97, 6.2 m from collar.

**Page intentionally blank**

## **DRAFT DISCLAIMER**

**This contractor document was prepared for the U.S. Department of Energy (DOE), but has not undergone programmatic, policy, or publication review, and is provided for information only. The document provides preliminary information that may change based on new information or analysis, and is not intended for publication or wide distribution; it is a lower level contractor document that may or may not directly contribute to a published DOE report. Although this document has undergone technical reviews at the contractor organization, it has not undergone a DOE policy review. Therefore, the views and opinions of authors expressed do not necessarily state or reflect those of the DOE. However, in the interest of the rapid transfer of information, we are providing this document for your information.**